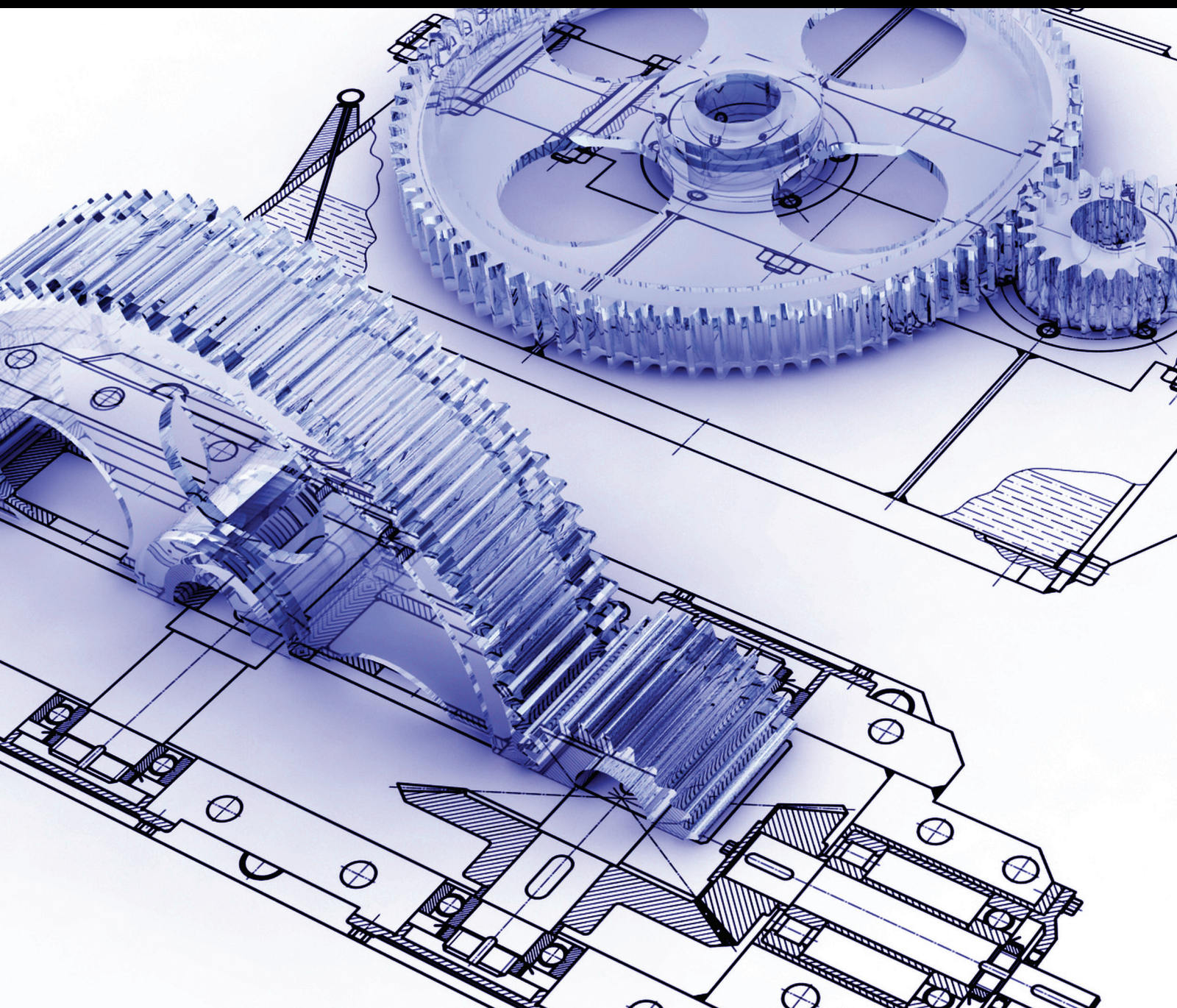


# Multiphase Flow System with Suspended Particles

Guest Editors: Guan Heng Yeoh, Dirk Lucas, Sherman Chi Pok Cheung, and Jiyuan Tu





---

# **Multiphase Flow System with Suspended Particles**

Advances in Mechanical Engineering

---

## **Multiphase Flow System with Suspended Particles**

Guest Editors: Guan Heng Yeoh, Dirk Lucas,  
Sherman Chi Pok Cheung, and Jiyuan Tu



---

Copyright © 2014 Hindawi Publishing Corporation. All rights reserved.

This is a special issue published in “Advances in Mechanical Engineering.” All articles are open access articles distributed under the Creative Commons Attribution License, which permits unrestricted use, distribution, and reproduction in any medium, provided the original work is properly cited.

## Editorial Board

Mehdi Ahmadian, USA  
Rehan Ahmed, UK  
M. T. Akhtar, Japan  
Nacim Alilat, France  
M. Affan Badar, USA  
Luis Baeza, Spain  
R. Balachandran, UK  
Adib Becker, UK  
Filippo Berto, Italy  
N. Brunetière, France  
Mustafa Canakci, Turkey  
Marco Ceccarelli, Italy  
Fakher Chaari, Tunisia  
Chin-Lung Chen, Taiwan  
Lingen Chen, China  
Qizhi Chen, Australia  
Long Cheng, China  
Kai Cheng, UK  
H. H. Cho, Republic of Korea  
S.-B. Choi, Republic of Korea  
A. S. Dalkilic, Turkey  
J. P. Davim, Portugal  
Kangyao Deng, China  
Francisco D. Denia, Spain  
T. S. Dhanasekaran, USA  
Nihad Dukhan, USA  
Farzad Ebrahimi, Iran  
Ali Fatemi, USA  
M. L. Ferrari, Italy  
Luís Godinho, Portugal  
Tian Han, China  
Ishak Hashim, Malaysia

Davood Jalali-Vahid, Iran  
Jiin Y. Jang, Taiwan  
Xiaodong Jing, China  
Mitjan Kalin, Slovenia  
S.-W. Kang, Republic of Korea  
Michal Kuciej, Poland  
Yaguo Lei, China  
Zili Li, The Netherlands  
Yangmin Li, Macau  
Jun Li, China  
Zhijun Li, China  
Jianguo Lin, UK  
Ch.-X. Lin, USA  
Jian Liu, China  
Chen-Chi M. Ma, Taiwan  
S. N. Mahmoodi, USA  
Oronzio Manca, Italy  
Ramiro Martins, Portugal  
Francesco Massi, Italy  
Hua Meng, China  
Roslinda Nazar, Malaysia  
T.H. New, Singapore  
C. T. Nguyen, Canada  
Hirosi Noguchi, Japan  
Takahito Ono, Japan  
Hakan F. Oztop, Turkey  
Duc T. Pham, UK  
Ioan Pop, Romania  
Jurij Prezelj, Slovenia  
Xiaotun Qiu, USA  
Pascal Ray, France  
R. L. Reuben, UK

P. A. R. Rosa, Portugal  
E. de Sá Caetano, Portugal  
David R. Salgado, Spain  
M. R. Salimpour, Iran  
Sunetra Sarkar, India  
Pietro Scandura, Italy  
A.S. Sekhar, India  
Liyuan Sheng, China  
Xi Shi, China  
Seiichi Shiga, Japan  
Chow-Shing Shin, Taiwan  
Anand Thite, UK  
Shan-Tung Tu, China  
Sandra Velarde-Surez, Spain  
Junwu Wang, China  
Moran Wang, China  
Jia-Jang Wu, Taiwan  
Hongwei Wu, UK  
Gongnan Xie, China  
Hui Xie, China  
Ruey-Jen Yang, Taiwan  
Jianqiao Ye, UK  
Ch.-L. Yeh, Taiwan  
Boming Yu, China  
Bo Yu, China  
Jianbo Yu, China  
Yufeng Zhang, China  
Min Zhang, China  
Ling Zheng, China  
Zhaowei Zhong, Singapore

**Multiphase Flow System with Suspended Particles**, Guan Heng Yeoh, Dirk Lucas, Sherman Chi Pok Cheung, and Jiyuan Tu  
Volume 2014, Article ID 792050, 2 pages

**Modeling of Interfacial Component for Two-Phase Frictional Pressure Gradient at Microscales**, M. M. Awad and Y. S. Muzychka  
Volume 2014, Article ID 492435, 16 pages

**A Robust Asymptotically Based Modeling Approach for Two-Phase Flows**, M. M. Awad and Y. S. Muzychka  
Volume 2014, Article ID 327653, 10 pages

**Bounds on Two-Phase Frictional Pressure Gradient and Void Fraction in Circular Pipes**, M. M. Awad and Y. S. Muzychka  
Volume 2014, Article ID 438428, 9 pages

**Heat Transfer Coefficient during Evaporation of R-1234yf, R-134a, and R-22 in Horizontal Circular Small Tubes**, Kwang-Il Choi, Nguyen-Ba Chien, and Jong-Taek Oh  
Volume 2013, Article ID 132397, 8 pages

**Flow Characterization of Dense-Phase Pneumatic Conveying System of Pulverized Coal through Electrostatic Sensor Arrays**, Feifei Fu, Ming Kong, Chuanlong Xu, Cai Liang, and Shimin Wang  
Volume 2013, Article ID 656194, 12 pages

**Particle Dispersion Behaviors of Dense Gas-Particle Flows in Bubble Fluidized Bed**, Sihao Lv, Guohui Li, and Xue Liu  
Volume 2013, Article ID 616435, 14 pages

**Solid Suspension by an Upflow Mixture of Fluid and Larger Particles**, Renzo Di Felice and Marco Rotondi  
Volume 2013, Article ID 859756, 8 pages

**Modeling and Experimental Investigation of Pressure Field in the Grinding Zone with Nanoparticle Jet of MQL**, C. H. Li, Z. L. Han, Q. Zhang, and S. Wang  
Volume 2013, Article ID 169807, 11 pages

**Experimental Characterisation and Modelling of Homogeneous Solid Suspension in an Industrial Stirred Tank**, Sébastien Calvo, Angélique Delafosse, Marie-Laure Collignon, Michel Crine, and Dominique Toye  
Volume 2013, Article ID 329264, 9 pages

**Large-Eddy Simulation of Particle-Laden Turbulent Flows over a Backward-Facing Step Considering Two-Phase Two-Way Coupling**, Wang Bing, Zhang Hui Qiang, and Wang Xi Lin  
Volume 2013, Article ID 325101, 11 pages

## Editorial

# Multiphase Flow System with Suspended Particles

Guan Heng Yeoh,<sup>1,2</sup> Dirk Lucas,<sup>3</sup> Sherman Chi Pok Cheung,<sup>4</sup> and Jiyuan Tu<sup>4</sup>

<sup>1</sup> Australian Nuclear Science Technology Organisation (ANSTO), Locked Bag 2001, Kirrawee, NSW 2233, Australia

<sup>2</sup> School of Mechanical and Manufacturing Engineering, University of New South Wales, Sydney, NSW 2052, Australia

<sup>3</sup> Computational Fluid Dynamics Division, Helmholtz-Zentrum Dresden-Rossendorf Institute of Fluid Dynamics, P.O. Box 510 119, 01314 Dresden, Germany

<sup>4</sup> School of Aerospace, Mechanical and Manufacturing Engineering, RMIT University, P.O. Box 71, Bundoora, VIC 3083, Australia

Correspondence should be addressed to Guan Heng Yeoh; [guan.yeoh@ansto.gov.au](mailto:guan.yeoh@ansto.gov.au)

Received 18 December 2013; Accepted 18 December 2013; Published 14 April 2014

Copyright © 2014 Guan Heng Yeoh et al. This is an open access article distributed under the Creative Commons Attribution License, which permits unrestricted use, distribution, and reproduction in any medium, provided the original work is properly cited.

Industrial system that comprises flow of suspended particles in fluid generally requires an understanding of the multiscale physics occurring from micro/nanoscale to mesoscale and eventually to the macroscale phenomena. Because of the inherent complexities that are prevalent in such flow, investigations are certainly at the crossroads of intense research and development in the environment of significant advancements in experimentation as well as in computing power and performance. Much concerted development is nonetheless still needed to gain a better understanding of the complicated physics through the advancement of experimental techniques and computational methodologies and models and to specifically meet the increasing demand of improving efficiency of industrial multiphase flow system.

This special issue consists of nine papers. The advances of experimental and modelling investigation of multiphase flow system are detailed in the following.

The paper, “Heat transfer coefficient during Evaporation of R-1234yf, R-134a, and R-22 in Horizontal Circular Small Tubes,” by K. I. Choi et al. provided an experimental study where convective boiling heat transfer coefficients were obtained. Effect of heat flux, inner tube diameters, and saturation temperatures was investigated. Heat transfer coefficients were found to increase with increasing heat flux due to the presence of nucleate boiling augmenting the heat transfer process. Heat transfer coefficients were also found to increase with increasing saturation temperature and decreasing inner tube diameter. Correlations obtained in this study can be applied with sufficiently good accuracy to improve the compact heat exchanger design.

The paper, “Flow characterisation of dense-phase pneumatic conveying system of pulverized coal through electrostatic sensor arrays,” by F. Fu et al. focused on experiment investigation being performed on dense-phase pneumatic conveying powder utilising electrostatic sensor array (ESA) and electrical capacitance tomography (ECT). Distribution images over the cross section of the pipeline were obtained for different superficial gas velocities. Measurements obtained through the experiment demonstrated that characteristic of particles motion and its change with increasing superficial gas velocity were different in the dense and dilute phase region of the pipe.

The paper, “Particle dispersion behaviors of dense gas-particle flows in bubble fluidized bed,” by S. Lv et al. depicted the application of Euler-Euler two-fluid model, an improved momentum transfer empirical coefficient and wavelet analysis method as well as large eddy simulation (LES) for complex dense gas-particle flow system. The study revealed that particle collision frequencies at bubble vibrant movement regions along axial direction were found to be much higher than those of radial direction and attenuated along height increase. Also, representing bubble movement, low frequency components of pressure signal in the centre were stronger than wall regions.

The paper, “Solid suspension by an upflow mixture of fluid and larger particles,” by R. Di Felice and M. Rotondi provided an experimental investigation to shed light on the fluid dynamic interactions between the solid and the fluid phases in binary solid mixture suspensions, with the smaller particles fluidized by a mixture of larger neutrally

buoyant particles and fluid. The experimental information reported can be used to determine a proper relationship for the drag force in binary-solid suspensions and relationship of relevant importance when computational fluid dynamics (CFD) simulations can be performed.

The paper, “*Modeling and experimental investigation of pressure field in the grinding zone with nanoparticle jet of MQL*,” by C. H. Li et al. focused on solid nanoparticles being added in minimum quantity lubrication (MQL) to make nanofluids and injected in the grinding zone in the form of jet flow. A mathematical model of two-phase flow pressure field of grinding zone with nanoparticle jet flow of MQL was established. The speed of grinding wheel, the gap between work piece and grinding wheel, jet flow velocity, and spraying angles of nozzles on the pressure field of grinding zone were explored. Experimental results were found to be generally consistent with theoretical simulations.

The paper, “*Experimental characterisation and modelling of homogeneous solid suspension in an industrial stirred tank*,” by S. Calvo et al. depicted a numerical study based on the development of a CFD model to describe the particle distribution of aluminium salts in an industrial scale tank. This model, validated against experimental data, was further applied to formulate scale-up and scale-down correlations to predict the minimum impeller speed needed to reach homogeneous solid distribution of aluminium salts. Results obtained from different scales allowed correlating values of aluminium salts with the volumetric power consumption of the multiphase flow system.

The paper, “*Large-eddy simulation of particle-laden turbulent flows over a backward-facing step considering two-phase two-way coupling*,” by W. Bing et al. provided a fundamental numerical study of two-phase turbulent particle-laden flows over a backward-facing step. Particle dispersions in large-scale eddy coherent structures and statistical mean and fluctuating velocities were presented to illustrate particle modulations to turbulence. Influences of particle size and material density on changes in turbulence were analysed.

The paper, “*A robust asymptotically based modeling approach for two-phase flows*,” by M. M. Awad and Y. S. Muzychka focused on a theoretical study based upon an asymptotic modelling method. A robust compact model was developed by taking into account the important frictional interactions that occur at the interface between liquid and gas as the liquid and gas phases have been assumed to flow dependently of each other. The only unknown parameter in the asymptotic modelling method in the two-phase flow is the fitting parameter which corresponds to the minimum root mean square (RMS) error for any data set.

The paper, “*Bounds of two-phase frictional pressure gradient and void fraction in circular pipes*,” by M. M. Awad and Y. S. Muzychka depicted a theoretical study based on simple expressions to determine the bounds of two-phase frictional pressure gradient and void fraction in circular pipes. Such an approach was found to be useful for practical design and analysis of system performance. Also, the knowledge of the upper and lower bounds of two-phase frictional pressure

gradient and void fraction can assist in the development of new experiments since it can provide a reasonable envelope for the data to fall within.

Guan Heng Yeoh  
Dirk Lucas  
Sherman Chi Pok Cheung  
Jiyuan Tu

## Research Article

# Modeling of Interfacial Component for Two-Phase Frictional Pressure Gradient at Microscales

M. M. Awad<sup>1</sup> and Y. S. Muzychka<sup>2</sup>

<sup>1</sup> Mechanical Power Engineering Department, Faculty of Engineering, Mansoura University, Mansoura 35516, Egypt

<sup>2</sup> Faculty of Engineering and Applied Science, Memorial University of Newfoundland, St. John's, NL, Canada A1B 3X5

Correspondence should be addressed to M. M. Awad; [m\\_m.awad@mans.edu.eg](mailto:m_m.awad@mans.edu.eg)

Received 6 May 2013; Revised 26 February 2014; Accepted 27 February 2014; Published 9 April 2014

Academic Editor: Guan Heng Yeoh

Copyright © 2014 M. M. Awad and Y. S. Muzychka. This is an open access article distributed under the Creative Commons Attribution License, which permits unrestricted use, distribution, and reproduction in any medium, provided the original work is properly cited.

A simple approach for calculating the interfacial component of frictional pressure gradient in two-phase flow at microscales is presented. This approach is developed using superposition of three pressure gradients: single-phase liquid, single-phase gas, and interfacial pressure gradient. The proposed model can be transformed in two different ways: first, two-phase interfacial multiplier for liquid flowing alone ( $\phi_{l,i}^2$ ) as a function of two-phase frictional multiplier for liquid flowing alone ( $\phi_l^2$ ) and the Lockhart-Martinelli parameter,  $X$ , and, second, two-phase interfacial multiplier for gas flowing alone ( $\phi_{g,i}^2$ ) as a function of two-phase frictional multiplier for gas flowing alone ( $\phi_g^2$ ) and the Lockhart-Martinelli parameter,  $X$ . This proposed model allows for the interfacial pressure gradient to be easily modeled. Comparisons of the proposed model with experimental data for microchannels and minichannels and existing correlations for both  $\phi_l$  and  $\phi_g$  versus  $X$  are presented.

## 1. Introduction

This paper presents the results of modeling of interfacial component for two-phase frictional pressure gradient in microchannels and minichannels. This paper contains three major sections. The first section presents a review of the data and correlations, which are recently available in the open literature. Next, a discussion on the development of a simple model for the prediction of the interfacial component for two-phase frictional pressure gradient in microchannels and minichannels is presented. Finally, a discussion of the proposed models and a comparison with published data are presented.

## 2. Literature Review

The literature review on two-phase frictional pressure gradient in microchannels and minichannels can be found in tabular form in a number of textbooks [1–5].

Also, Awad and Muzychka [6] covered the literature review on two-phase frictional pressure gradient in

microchannels and minichannels that was published until 2006.

A number of recent studies on two-phase frictional pressure gradient in microchannels and minichannels, especially that presented the Chisholm parameter ( $C$ ) as a function of many factors like mass flux, have been reviewed for this work.

There are two basic models in two-phase pressured drop: homogeneous flow model and separated flow model. Many previous researchers have developed correlations for two-phase pressure drop in microchannels and minichannels. Most correlations were the modified Lockhart-Martinelli correlation [7] that was based on the separated flow model.

Qu and Mudawar [8] studied hydrodynamic instability and pressure drop in a water-cooled two-phase microchannel heat sink containing 21 parallel  $231 \times 713 \mu\text{m}$  microchannels. The researchers identified two types of two-phase hydrodynamic instability: severe pressure drop oscillation and mild parallel channel instability. They found that the severe pressure drop oscillation that could trigger premature critical heat flux could be eliminated simply by throttling

the flow upstream of the heat sink. Various methods for predicting two-phase pressure drop were assessed for suitability for microchannel heat-sink design. First, generalized two-phase pressure drop correlations were examined that included 10 correlations developed for both macro- and mini/microchannels. A new correlation incorporating the effects of both channel size and coolant mass flux was proposed as follows:

$$C = 21 \left( 1 - e^{-319d_h} \right) (0.00418G + 0.0613). \quad (1)$$

Their new correlation showed better accuracy than prior correlations. The second method consisted of a theoretical annular two-phase flow model that aside from excellent predictive capability possessed the unique attributes of providing a detailed description of the different transport processes occurring in the microchannel, as well as fundamental appeal and broader application range than correlations.

Yue et al. [9] presented preliminary experimental results on pressure drop characteristics of single- and two-phase flows through two T-type rectangular microchannel mixers with  $d_h = 528$  and  $333 \mu\text{m}$ , respectively. For  $\text{N}_2$ -water two-phase flow in micromixers, the researchers analyzed and compared the obtained pressure drop data with existing flow pattern-independent models. They found that the Lockhart-Martinelli method [7] generally underpredicted the frictional pressure drop. As a result, a modified correlation of  $C$  value in Chisholm's equation [10] based on linear regression of experimental data was proposed to provide a better prediction of the two-phase frictional pressure drop. Their correlation was

$$C = 0.411822X^{-0.0305} \text{Re}_{lo}^{0.600428}, \quad (2)$$

$$\text{Re}_{lo} = \frac{Gd_h}{\mu_l}. \quad (3)$$

The range of variables in (2) is  $X = 0.67$ – $6.16$  and  $\text{Re}_{lo} = 88$ – $461$ . In addition, among the homogeneous flow models investigated, the viscosity correlation of McAdams et al. [11] indicated the best performance in correlating the frictional pressure drop data (mean deviations within  $\pm 20\%$  for two T-type rectangular microchannel mixers).

Cubaud and Ho [12] investigated experimentally liquid/gas flows in 200 and 525  $\mu\text{m}$  square microchannels made of glass and silicon. Two-phase flow pressure drop was measured and compared to single liquid flow pressure drop. It showed two flow regimes, one in which the liquid was essentially pushing the bubbles and another in which the liquid was flowing in the corners. Taking into account the homogeneous liquid fraction along the channel, an expression for the two-phase frictional multiplier was developed over the range of liquid and gas flow rates investigated. For the bubbly and the wedging flows, their pressure drop correlation could be written as follows:

$$\phi_l^2 = \beta_l^{-1}. \quad (4)$$

For smaller liquid fraction, their pressure drop correlation could be written as follows:

$$\begin{aligned} \phi_l^2 &= \beta_l^{-1/2}, \\ \beta_l &= \frac{Q_l}{Q_l + Q_g}. \end{aligned} \quad (5)$$

Lee and Mudawar [13] measured two-phase pressure drop across a microchannel heat sink, which served as an evaporator in a refrigeration cycle. The microchannels were formed by machining  $231 \mu\text{m}$  wide  $\times$   $713 \mu\text{m}$  deep grooves into the surface of a copper block. They performed experiments with refrigerant R134a, which spanned the following conditions: inlet pressure of  $p_{in} = 1.44$ – $6.60$  bar, mass flux of  $G = 127$ – $654 \text{ kg/m}^2\cdot\text{s}$ , inlet quality of  $x_{e,in} = 0.001$ – $0.25$ , outlet quality of  $x_{e,out} = 0.49$ -superheat, and heat flux of  $q = 31.6$ – $93.8 \text{ W/cm}^2$ . Predictions of the homogeneous equilibrium flow model and prior separated flow models and correlations yielded relatively poor predictions of pressure drop. They suggested a new correlation scheme, which incorporated the effect of liquid viscosity and surface tension in the separated flow model's two-phase pressure drop multiplier. To enhance the predictive capability of the new correlation, both their R134a data and prior microchannel water data of Qu and Mudawar [8] were examined. Large differences between the thermophysical properties of R134a and water were deemed highly effective at broadening the application range of the new correlation. Another key difference between the two data sets was the fact that both the liquid and vapor flows were laminar for the water data, while low viscosity rendered the vapor flow turbulent for R134a. Typical microchannel operating conditions rarely produced turbulent liquid flow. Two separate correlations were derived for  $C$  based on the flow states of the liquid and vapor as follows:

$$\begin{aligned} C &= \begin{cases} 2.16\text{Re}_{lo}^{0.047} \text{We}_{lo}^{0.6}, & \text{LL}, \\ 1.45\text{Re}_{lo}^{0.25} \text{We}_{lo}^{0.23}, & \text{LT}, \end{cases} \\ \text{Re}_{lo} &= \frac{Gd_h}{\mu_l}, \\ \text{We}_{lo} &= \frac{G^2 d_h}{\rho_l \sigma}. \end{aligned} \quad (6)$$

The stronger effect of surface tension should be noted where both liquid and vapor were laminar. Their correlation showed excellent agreement with the R134a data as well as previous microchannel water data.

Ide et al. [14] reported on the results of investigations into the characteristics of an air-water isothermal two-phase flow in minichannels, that was in capillary tubes with  $d = 1 \text{ mm}$ ,  $2.4 \text{ mm}$ , and  $4.9 \text{ mm}$  and also in capillary rectangular channels with  $\text{AR} = 1$ – $9$ . The directions of flow were vertical upward, horizontal and vertical downward. The researchers investigated the effects of the tube diameters and aspect ratios of the channels on these flow parameters and the flow patterns. Also, they proposed the correlations of the holdup and the frictional pressure drop. Their frictional pressure drop correlations were as follows.

For the LT region in a capillary circular tube,

$$\phi_l = 0.0837 \left[ \frac{(U_g + U_l)}{U_l} \right]^{0.425} \text{Re}_l^{3/8}. \quad (7)$$

For the LL region in a capillary rectangular channel,

$$\phi_l = 0.2485 \text{AR}^{-0.355} \left[ \frac{U_l}{\sqrt{g d_h}} \right]^{-0.233} \text{Re}_l^{3/8}. \quad (8)$$

For the LT region in a capillary rectangular channel,

$$\phi_l = 0.0848 \text{AR}^{-0.145} \left[ \frac{(U_g + U_l)}{U_l} \right]^{0.425} \text{Re}_l^{3/8}. \quad (9)$$

In their study, the critical Reynolds number from laminar flow to turbulent flow was taken as 2400. The predictions obtained from their frictional pressure drop correlations had sufficient accuracy for both the vertical and the horizontal cases.

Yue et al. [15] investigated experimental hydrodynamics and mass transfer characteristics in cocurrent gas-liquid flow through a horizontal rectangular microchannel of  $d_h = 667 \mu\text{m}$ . They obtained and analyzed two-phase flow patterns and pressure drop data. For both physical and chemical mass transfer experiments, they found that two-phase frictional pressure drop in the microchannel could be well predicted by the Lockhart-Martinelli method [7] if a new correlation of  $C$  value in Chisholm's equation [10] was used. Their new correlation was

$$C = 0.815 X^{-0.0942} \text{Re}_{lo}^{0.711}. \quad (10)$$

Harirchian and Garimella [16] studied microchannel size effects on two-phase local heat transfer and pressure drop in silicon microchannel heat sinks with the dielectric fluid Fluorinert FC-77 for  $G = 250\text{--}1600 \text{ kg/m}^2\cdot\text{s}$ . The test sections consisted of parallel microchannels with nominal widths of 100, 250, 400, 700, and 1000  $\mu\text{m}$ , all with a depth of 400  $\mu\text{m}$ , cut into 12.7 mm  $\times$  12.7 mm silicon substrates. 25 microheaters embedded in the substrate allowed local control of the imposed heat flux, while 25 temperature microsensors integrated into the back of the substrates enabled local measurements of temperature. The results of their study served to quantify the effectiveness of microchannel heat transport while simultaneously assessing the pressure drop trade-offs.

Lee and Garimella [17] investigated flow boiling in arrays of parallel microchannels using a silicon test piece with imbedded discrete heat sources and integrated local temperature sensors. The microchannels considered range in width from 102  $\mu\text{m}$  to 997  $\mu\text{m}$ , with the channel depth being nominally 400  $\mu\text{m}$  in each case ( $d_h = 160\text{--}538$ ). They conducted the experiments with deionized water that entered the channels in a purely liquid state. Results were presented in terms of temperatures and pressure drop as a function of imposed heat flux. They found that the Lockhart and Martinelli correlation gave poor predictions in microchannels

two-phase flow of imposed heat flux because it was developed for adiabatic flow. After a critical assessment of 5 correlations available in the literature, they developed a new correlation to predict the two-phase pressure drop by considering the effect of mass flux and hydraulic diameter as follows:

$$C = 2566 G^{0.5466} d_h^{0.8819} (1 - e^{-319 d_h}). \quad (11)$$

Saisorn and Wongwises [18] provided a literature review of recent research on two-phase flow in microchannels in their study. They discussed researches on the microhydrodynamics concerned with two-phase gas-liquid adiabatic flow characteristics in both circular and noncircular microchannels. Their review aimed to survey and identify new findings obtained from this attractive area that might contribute to optimum design and process control of high performance miniature devices comprising extremely small channels. The results obtained from a number of previous studies showed that the flow behaviors in the microchannels deviated significantly from those in ordinarily sized channels. Similar to the ordinarily sized channels, it was expected that the flow pattern, pressure drop, and void fraction would affect the two-phase pressure drop, holdup, system stability, exchange rates of momentum, heat, and mass during the phase-change heat transfer processes.

C. Y. Lee and S. Y. Lee [19] investigated the pressure drop of two-phase plug flows in round minichannels in this experimental study for three different tube materials, that is, glass, polyurethane, and Teflon, respectively, with  $d = 1.62\text{--}2.16 \text{ mm}$ . The researchers used air and water as the test fluids. In the wet-plug flow regime (wet wall condition at the gas portions), the pressure drop was reasonably predicted by the homogeneous flow model or by the correlations of Mishima and Hibiki [20] and Chisholm [10]. On the other hand, in the dry-plug flow regime (dry wall condition at the gas portions), the role of the moving contact lines affected the interface curvature and dynamic contact angles. As the contact lines moved faster, the advancing angles of the interfaces increased while receding angles decreased [21], and eventually, the change of the dynamic contact angles resulted in the increase of the pressure drop. As a result, they proposed a modified Lockhart-Martinelli type correlation in order to take into account the effect of the moving contact lines. They modified the Chisholm constant ( $C$ ) as follows:

$$C = 2.161 \times 10^{-21} \lambda^{-3.703} \psi^{-0.995} \text{Re}_{lo}^{0.486} \quad (12)$$

$$\lambda = \frac{\mu_l^2}{\rho_l \sigma_{lg} d}. \quad (13)$$

$$\psi = \frac{U \mu_l}{\sigma_{lg}} \quad (14)$$

$$\text{Re}_{lo} = \frac{G d}{\mu_l} \quad (15)$$

According to the dynamic contact angle models [22–24], the capillary number ( $Ca$ ), equivalent to the group which represents the relative importance of the viscosity and

the surface tension effects ( $\Psi = U\mu_l/\sigma_{lg}$ ), was considered as an important dimensionless parameter in predicting the pressure drop. They obtained the appropriate values for the coefficient and the exponents in (12) for dry-plug flows with the polyurethane and Teflon tubes based on their current experiments. Their correlation fitted the measured pressure drop data within the mean deviation of 6%.

Yue et al. [25] studied two-phase flow pattern and pressure drop characteristics during the absorption of CO<sub>2</sub> into water in three horizontal microchannel contactors that consisted of Y-type rectangular microchannels of  $d_h = 667$ , 400 and 200  $\mu\text{m}$ , respectively. With the help of a high-speed photography system, the observed flow patterns in these microchannels were bubbly flow, slug flow (including two subregimes, the Taylor flow and unstable slug flow), slug-annular flow, churn flow, and annular flow. They found that two-phase frictional pressure drop in microchannels should be described by different models depending on the flow pattern investigated. The homogeneous flow model might be only applicable to bubbly flow. However, the deviation from the homogenous flow assumption could be seen in the Taylor flow. Also, the Taylor flow could not be regarded as a separated flow due to the alternate movement of the Taylor bubbles and liquid slugs down the channel. Actually the Taylor flow was eliminated from consideration in the separated flow model developed by Lockhart and Martinelli [7]. As a result, detailed flow analysis should be performed in order to formulate reasonable correlations for the prediction of pressure drop in the Taylor flow. For flow patterns like slug-annular flow, churn flow, and annular flow, the separated flow model seemed to be more realistic because the two-phase interface configuration in these flow patterns was close to the model assumption where a continuous gas flow was seen in the center part of the microchannel while liquid film flowed adjacently to the microchannel wall. For the square microchannel with  $d_h = 400 \mu\text{m}$ , the following correlation was proposed:

$$\phi_l^2 = 0.217\beta_l^{-0.5}\text{Re}_l^{0.3} \quad (16)$$

$$\beta_l = \frac{U_l}{U_l + U_g}. \quad (17)$$

The constant and the exponent associated with  $\text{Re}_l$  at the right side of (16) were derived based on the linear least square regression analysis of the obtained data, where the standard deviation was 9.68%. For the square microchannel with  $d_h = 200 \mu\text{m}$ , (16) seemed to be further corroborated by little data already obtained. For the rectangular microchannel with  $d_h = 667 \mu\text{m}$ , (16) could not be applied directly due to the inherently higher aspect ratio in this case. However, the aspect ratio effect on  $\phi_l^2$  in this microchannel could be resolved by simply placing a different constant in (16) as follows:

$$\phi_l^2 = 0.284\beta_l^{-0.5}\text{Re}_l^{0.3}. \quad (18)$$

Using (18), the standard deviation of 21.5% was achieved.

Niu et al. [26] studied flow pattern, pressure drop, and mass transfer characteristics for the gas-liquid two-phase flow in a circular quartz-glass and stainless steel

microchannel reactor of  $d = 1.0 \text{ mm}$ . They used a mixture of CO<sub>2</sub>, N<sub>2</sub>, and polyethylene glycol dimethyl ether to represent the gas and liquid phases, respectively. The observed flow patterns in their work were bubbly, slug, churn, and slug-annular. They analyzed and compared their two-phase pressure drop data with the homogeneous model and the separate flow model to assess their predictive capabilities. Considering the effect of the mass flux, the tube diameter, and other physical properties, they correlated the  $C$  value as follows:

$$C = 0.0049\text{Re}_g^{0.98}\text{Re}_l^{1.08}\text{We}^{-0.86} \quad (19)$$

$$\text{Re}_g = \frac{Gxd}{\mu_g} \quad (20)$$

$$\text{Re}_l = \frac{G(1-x)d}{\mu_l} \quad (21)$$

$$\text{We} = \frac{G^2d}{\rho\sigma} \quad (22)$$

$$\rho = \left( \frac{x}{\rho_g} + \frac{1-x}{\rho_l} \right)^{-1}. \quad (23)$$

They tested the validity of (19) for the prediction of the two-phase frictional pressure gradient for a quartz-glass and stainless steel microchannel reactor. They found that the agreement between their experimental data and the separated flow model with the  $C$  value of (19) was generally good, with an absolute mean deviation of 3.45%, and 6.8%, respectively.

Dutkowski [27] presented results of experimental investigations of pressure drop in two-phase adiabatic flow in tubular minichannels. The researcher used air-water mixture as a working fluid. He used eight tubular minichannels with internal diameter of 1.05–2.30 mm and the test section length of 300 mm made from stainless steel. His investigations were conducted within the range: mass flow rate of water 0.65–59 kg/h, mass flow rate of air 0.011–0.72 kg/h, mass fraction of air in the two-phase mixture ( $x$ ) = 0.0003–0.22, and total mass flux ( $G$ ) = 139–8582 kg/(m<sup>2</sup>·s). On the basis of his experimental investigations, he found that the application of commonly used methods to evaluation of pressure drop in two-phase flow provided poor results. Therefore, it was necessary to make some corrections and modifications for the two-phase flow in minichannels correlations.

Kawahara et al. [28] conducted an adiabatic experiment to investigate the effects of liquid properties on the characteristics of two-phase flows in a horizontal circular microchannel. Distilled water, aqueous solutions of ethanol with two different mass concentrations (49 wt% and 4.8 wt%), and pure ethanol were used as the test liquids. The researchers varied the ethanol concentration to change the surface tension and the viscosity. They injected nitrogen gas with one of the four liquids together through a T-junction mixer to the test microchannel. Two mixers with different inner diameters of 250  $\mu\text{m}$  and 500  $\mu\text{m}$  were used at a fixed microchannel diameter of 250  $\mu\text{m}$  to study flow contraction effects at the channel inlet. Liquid was injected into the main channel (line

1), while the gas was injected into the branch (line 2). When 500  $\mu\text{m}$  inner diameter mixer was used, flow contraction occurred at the inlet of the test section because the T-junction was directly connected to the 250  $\mu\text{m}$  inner diameter microchannel. The observed types of flow pattern were the quasi-homogeneous flow [29, 30] and the quasi-separated flow [29, 30]. Also, flows with the contraction had longer bubbles even at the same gas and liquid flow rates condition. They found that bubble velocity data correlated with the drift-flux model showed that the distribution parameter ( $C_0$ ) increased with increasing of liquid viscosity and/or decreasing of surface tension, and  $C_0$  for flows with the contraction was higher. Also, the pressure drop data correlated with the Lockhart-Martinelli method [7] showed that the two-phase friction multiplier ( $\phi_l^2$ ) for flows with the contraction was lower. From data analysis, new correlations of  $C_0$  and  $\phi_l^2$  were developed with some dimensionless numbers. For two-phase frictional pressure drop, they correlated their resulting  $C$  data with three dimensionless numbers, that is, the Bond number (Bo), the liquid Reynolds number ( $Re_l$ ), and the gas Weber number ( $We_g$ ), as follows:

$$C = \begin{cases} 1.38\text{Bo}^{0.04}\text{Re}_l^{0.25}\text{We}_g^{0.12} & \text{flow without the contraction} \\ 0.55\text{Bo}^{0.04}\text{Re}_l^{0.25}\text{We}_g^{0.12} & \text{flow with the contraction.} \end{cases} \quad (24)$$

They found that their two-phase frictional pressure drop correlation agreed well with their present data within 20% rms errors, irrespective of the test liquids.

Choi et al. [31] studied the wettability effect on pressure drop and flow pattern of two-phase flow in rectangular microchannel. The researchers fabricated a hydrophilic rectangular microchannel using a photosensitive glass and prepared a hydrophobic rectangular microchannel using silanization of glass surfaces with OTS (octa-dethyl-trichloro-silane). They conducted experiments of two-phase flow in the hydrophilic and the hydrophobic rectangular microchannels using water and nitrogen gas. Their visualization results showed that the wettability was important for two-phase flow pattern in rectangular microchannel. Also, two-phase frictional pressure drop was highly related with flow patterns. Finally, two-phase frictional pressure drop was analyzed with flow patterns.

Megahed and Hassan [32] investigated experimentally the pressure drop characteristics and flow visualization of a two-phase flow in a silicon microchannel heat sink. The microchannel heat sink consisted of a rectangular silicon chip in which 45 rectangular microchannels were chemically etched with a depth of 276  $\mu\text{m}$ , width of 225  $\mu\text{m}$ , and a length of 16 mm. Experiments were carried out for  $G = 341\text{--}531 \text{ kg/m}^2\text{-s}$  and  $q = 60.4\text{--}130.6 \text{ kW/m}^2$  using FC-72 as the working fluid. They observed bubble growth and flow regimes using high-speed visualization. Three major flow regimes were identified: bubbly, slug, and annular. The frictional two-phase pressure drop increased with exit quality for a constant mass flux. An assessment of different pressure drop correlations reported in the literature was conducted for validation. They obtained a new general correlation to predict

the two-phase pressure drop in microchannel heat sinks for five different refrigerants from their present work employing different values of  $d_h = 70\text{--}304 \mu\text{m}$  and its applicability extended to five different refrigerants as follows:

$$C = \begin{cases} \frac{0.0053\text{Re}_{lo}^{0.934}}{\text{Co}^{0.73}(X^2)^{0.175}}, & \text{LL,} \\ \frac{0.0002\text{Re}_{lo}^{1.7}}{\text{Co}^{0.7}(X^2)^{1.24}}, & \text{LT,} \end{cases} \quad (25)$$

$$\text{Co} = \frac{[\sigma/g(\rho_l - \rho_g)]^{1/2}}{d_h},$$

$$\text{Re}_{lo} = \frac{Gd_h}{\mu_l}.$$

Their new correlation showed a good agreement with the experimental data and predicted the evaporative pressure drop data in microchannels for laminar-liquid laminar-vapor and laminar-liquid turbulent-vapor flow with mean absolute errors of 10.4% and 14.5%, respectively.

C. Y. Lee and S. Y. Lee [33] investigated experimentally the pressure drop of the two-phase dry-plug flow (dry wall condition at the gas portions) in round minichannels. The air-water mixtures were flowed through the round minichannels made of polyurethane and Teflon, respectively, with  $d = 1.62\text{--}2.16 \text{ mm}$ . In the dry-plug flow regime, the pressure drop measured became larger either by increasing the liquid superficial velocity ( $U_l$ ) or by decreasing the gas superficial velocity ( $U_g$ ) due to the increase of the number of the moving contact lines in the test section. In such a case, the role of the moving contact lines turned out to be significant. As a result, they proposed a pressure drop model of dry-plug flow through modification of the dynamic contact angle analysis taking account of the energy dissipation by the moving contact lines that represented the experimental data within the mean deviation of 4%.

Based on the separated flow model and drift-flux model, Zhang et al. [34] explored alternative correlations of two-phase friction pressure drop and void fraction for minichannels. By applying the artificial neural network (ANN), dominant parameters to correlate the two-phase friction multiplier and void fraction were picked out. It was found that in minichannels the nondimensional Laplace constant ( $Lo^*$ ) was a main parameter to correlate the Chisholm parameter ( $C$ ) as well as the distribution parameter. By noting the asymptotic values as  $C = 21$  for conventional channels and  $C = 0$  for extremely narrow gaps, they correlated the Chisholm parameter ( $C$ ) by the following equation:

$$C = 21 \left( 1 - e^{-358/Lo^*} \right), \quad (26)$$

$$Lo^* = \frac{[\sigma/g(\rho_l - \rho_g)]^{0.5}}{d_h}. \quad (27)$$

The applicable ranges of this correlation were as follows:  $0.014 \leq d_h \leq 6.25 \text{ mm}$ ,  $Re_l \leq 2000$ , and  $Re_g \leq 2000$ .

Both previous correlations and the newly developed correlations were extensively evaluated with a variety of data sets collected from the literature. They did not recommend the application of the newly developed correlation out of the verified range. Furthermore, although the newly developed correlation could predict all the data for the flows of three groups, that is, adiabatic liquid-gas flow, adiabatic liquid-vapor flow, and flow boiling, within an acceptable margin of error, it was found from that most of the averages of the Chisholm parameter,  $C$ , for liquid-gas flow were above the curve depicted by the newly developed equation; however, those for liquid-vapor flow were below the curve. For liquid-gas two-phase flow, (26) might work better if the constant of 358 was replaced with 674. For liquid-vapor flow, however, the constant of 142 would be better.

For adiabatic liquid-gas two-phase flow

$$C = 21 \left(1 - e^{-674/Lo^*}\right). \quad (28)$$

For adiabatic liquid-vapor two-phase flow

$$C = 21 \left(1 - e^{-142/Lo^*}\right). \quad (29)$$

Choi et al. [35] conducted experiments for adiabatic liquid water and nitrogen gas flow in rectangular microchannels to investigate two-phase pressure drop in the rectangular microchannels. The researchers found that two-phase frictional pressure drop in the rectangular microchannels was highly related with flow regime. They assessed homogeneous model with six two-phase viscosity models and six separated flow models with their experimental data. The best two-phase viscosity model was Beattie and Whalley's model [36]. The best separated flow model was Qu and Mudawar's correlation [8]. Flow regime dependency in both homogeneous and separated flow models was observed. As a result, they proposed individually new flow pattern based correlations for both homogeneous and separated flow models. Their new flow pattern based correlations for homogeneous model were

$$\text{Bubble regime: } f_m = 6.51 \text{Re}_m^{-0.838},$$

$$\text{Transition regime: } f_m = 4.17 \text{Re}_m^{-0.807},$$

$$\text{Liquid ring regime: } f_m = \begin{cases} 1.40 \text{Re}_m^{-0.6}, & d_h = 490 \mu\text{m}, \\ 0.97 \text{Re}_m^{-0.97}, & d_h = 322 \mu\text{m}, \\ 0.60 \text{Re}_m^{-0.6}, & d_h = 143 \mu\text{m}. \end{cases} \quad (30)$$

Their new flow pattern based correlations for separated flow model were

$$\text{Bubble regime: } \frac{C_{\text{new}}}{C} = 0.0027G + 2.767, \quad (31)$$

$$\text{Multiple regime: } \frac{C_{\text{new}}}{C} = 0.0027G + 1.199,$$

Liquid ring regime

$$\frac{C_{\text{new}}}{C} = \begin{cases} 0.0042G + 1.3509, & d_h = 490 \mu\text{m}, \\ 0.0027G + 0.8075, & d_h = 322 \mu\text{m}, \\ 0.0014G + 0.3664, & d_h = 143 \mu\text{m}, \end{cases} \quad (32)$$

where  $C$  is defined by (26), (28), and (29) [34].

Lee et al. [37] reviewed the existing databases and correlations in the literature on the microchannel pressure drop and heat transfer. Based on this review, the researchers found that none of the existing correlations could cover the wide range of working fluids, operational conditions, and different microchannel dimensions. As a result, they revealed the importance of the Bond number that related the nominal bubble dimension or capillary parameter with the channel size. Using the Bond number, improved correlations of pressure drop and heat transfer were established. To consider the effect of the exit mass quality ( $x_e$ ) with the Bond number in the Chisholm parameter, a monomial function was determined using least square fitting with experimental data. Therefore, a new correlation was established in terms of both the Bond number and exit mass quality as follows:

$$C = 121.6 \left(1 - e^{-22.7Bo}\right) x_e^{1.85}. \quad (33)$$

This new correlation was a continuous function. As a reference, when the Bond number (Bo) was very large (extreme condition of the conventional channel), the Chisholm parameter ( $C$ ) would be 5, 10, 12, and 20 at the corresponding exit quality ( $x_e$ ) of 0.18, 0.26, 0.29, and 0.39 by this new correlation, respectively. Therefore, this new correlation at the condition of an extremely large channel dimension did not conflict with the traditional understanding of the Chisholm parameter in a macrochannel.

Pamitran et al. [38] presented an experimental investigation into the characteristics of two-phase flow pattern transitions and pressure drop of R-22, R-134a, R-410A, R-290, and R-744 in horizontal small stainless steel tubes of  $d = 0.5, 1.5$  and  $3.0$  mm. The researchers obtained experimental data over a heat flux range of 5–40 kW/m<sup>2</sup>, mass flux range of 50–600 kg/(m<sup>2</sup>·s), saturation temperature range of 0–15°C, and mass quality up to 1.0. The effects of heat flux, mass flux, saturation temperature, and inner tube diameter on the pressure drop of the working refrigerants were reported. The researchers compared experimental pressure drop with the predictions from some existing correlations. They presented a new two-phase pressure drop model that was based on a superposition model for two-phase flow boiling of refrigerants in small tubes. They developed their new pressure drop correlation on the basis of the Lockhart-Martinelli method [7] as a function of the Weber number (We) and the Reynolds number (Re) by considering the laminar-turbulent flow conditions. Using a regression method with 812 data points, a new factor  $C$  was developed as follows:

$$C = 0.003 \text{We}^{-0.433} \text{Re}^{1.23}. \quad (34)$$

They found that this correlation provided mean and average deviations of 21.66% and –2.47%, respectively, based

on comparison. This correlation would contribute to the design of heat exchangers with small tubes.

Kaji et al. [39] measured simultaneously heat transfer, pressure drop, and void fraction for upward heated air-water nonboiling two-phase flow in a Pyrex glass tube of  $d = 0.51$  mm to investigate thermohydrodynamic characteristics of two-phase flow in microchannels. They found that frictional pressure drop agreed with Mishima-Hibiki's correlation [20] at low liquid superficial velocity ( $U_l$ ), whereas it agreed with Chisholm-Laird's correlation [40] at relatively high liquid superficial velocity ( $U_l$ ). Heat transfer coefficient fairly agreed with the data for  $d = 1.03$  and  $2.01$  mm when  $U_l$  was relatively high. But it became lower than that for larger diameter tubes when  $U_l$  was low. Analogy between heat transfer and frictional pressure drop was proved to hold roughly for the two-phase flow in microchannel as follows:

$$\frac{h_{tp}}{h_l} \left( \frac{1}{1-\alpha} \right) = \phi_l^2. \quad (35)$$

Li and Wu [41] obtained experimental results of adiabatic two-phase pressure drop in micro/minichannels for both multi- and single-channel configurations from the literature. Their collected database contained 769 data points and covered 12 fluids, for a wide range of operational conditions and channel dimensions. The researchers analyzed the whole database using eleven existing correlations to verify their respective accuracies. Also, they introduced the Bond number and the Reynolds number to modify the Chisholm parameter of two-phase multipliers to develop new generalized correlations. A particular trend was observed with the Bond number that distinguished the data in three ranges, indicating the relative importance of surface tension. When  $1.5 \leq Bo$ , in the region dominated by surface tension, inertia and viscous forces could be neglected. When  $1.5 < Bo \leq 11$ , surface tension, inertia force, and viscous force were all important in the micro/minichannels. However, when  $11 < Bo$ , the effect of surface tension could be ignored. Their newly proposed correlations were

$$C = \begin{cases} 11.9Bo^{0.45} & 1.5 \leq Bo \\ 109.4(BoRe_l^{0.5})^{-0.56} & 1.5 < Bo \leq 11. \end{cases} \quad (36)$$

The Chisholm parameter had no obvious relationship with the Bond number when  $Bo > 11$  that was not drawn in their present paper. They found that their newly proposed correlations could predict the datasets accurately for different working fluids at various operational conditions for different dimensions of micro/minichannels in the range where  $Bo \leq 11$ . Their newly proposed correlation could predict 72.6% and 89.7% of the data points within the  $\pm 30\%$  and  $\pm 50\%$  error band, respectively, in the region  $1.5 < Bo \leq 11$ . Their newly proposed correlation attributed the predictive improvement to the combined number  $BoRe_l^{0.5}$ . Thus, except for surface tension, inertia force and viscous force also presented non-ignorable effects in the region  $1.5 < Bo \leq 11$ . For the range where  $11 < Bo$ , the Beattie and Whalley correlation [36] was adopted to predict the datasets. It predicted 60.0% and 88.9% of the data points within the  $\pm 30\%$  and  $\pm 50\%$  error band, respectively.

Maqbool et al. [42] performed experiments to investigate two-phase pressure drop in a circular vertical minichannel made of stainless steel (AISI 316) with internal diameter of 1.70 mm and a uniformly heated length of 245 mm using  $NH_3$  as working fluid. The researchers conducted the experiments for the following ranges:  $q = 15\text{--}350$  kW/m<sup>2</sup> and  $G = 100\text{--}500$  kg/m<sup>2</sup>·s. A uniform heat flux was applied to the test section by DC power supply. They determined two-phase frictional pressure drop variation with mass flux ( $G$ ), mass quality ( $x$ ), and heat flux ( $q$ ). They compared their experimental results to predictive methods available in the literature for frictional pressure drop. They found that the homogeneous model and the Müller-Steinhagen and Heck [43] correlation were in good agreement with their experimental data with mean absolute deviation (MAD) of 27% and 26%, respectively.

Choi et al. [44] conducted experiments of adiabatic liquid water and nitrogen gas two-phase flow in rectangular microchannels to study the aspect ratio effect on the flow pattern, pressure drop, and void fraction. The widths and heights of rectangular microchannels were  $510 \mu\text{m} \times 470 \mu\text{m}$ ,  $608 \mu\text{m} \times 410 \mu\text{m}$ ,  $501 \mu\text{m} \times 237 \mu\text{m}$ , and  $503 \mu\text{m} \times 85 \mu\text{m}$ . As a result, the aspect ratios (AR) of these rectangular microchannels were 0.92, 0.67, 0.47, and 0.16, and the hydraulic diameters ( $d_h$ ) of the rectangular microchannels were 490, 490, 322, and 143  $\mu\text{m}$ , respectively. Experimental ranges were liquid superficial velocities ( $U_l$ ) = 0.06–1.0 m/s and gas superficial velocities ( $U_g$ ) = 0.06–71 m/s. The researchers fabricated visible rectangular microchannels using a photosensitive glass and measured pressure drop in these microchannels directly through embedded ports. Typical flow patterns in the rectangular microchannels observed in their study were bubbly flow, slug bubble flow, elongated bubble flow, transitional flow (multiple flow), and liquid ring flow. As the aspect ratio decreased, the bubble flow regime became dominant due to the confinement effect and the thickness of liquid film in corner was decreased. In addition, the two-phase flow became homogeneous with decreasing aspect ratio owing to the reduction of the liquid film thickness. They proposed the transitions of slug, elongated, and multiple regimes in the following equation form.

For transition of slug between elongated bubble regimes

$$\frac{U_l}{U_g} = 0.817U_g^{-0.374}. \quad (37)$$

For transition of elongated bubble between multiple regimes

$$\frac{U_l}{U_g} = 0.0103 \exp(0.00784 \times 10^{-6} d_h) U_g^{4.576}. \quad (38)$$

They found that the  $C$  value in the Lockhart and Martinelli correlation decreased like the Zhang et al. [34] correlation (28) as the nondimensional Laplace constant ( $Lo^*$ ) increased. The frictional pressure drop in the rectangular microchannels was highly related with the flow pattern. Also, the void fraction in the rectangular microchannels ( $\alpha$ ) had a linear relation with the volumetric quality ( $\beta$ ).

Choi et al. [45] studied behaviors and pressure drop for a single bubble in a rectangular microchannel. Based on the experiments in [44, Part I], the researchers analyzed data for liquid superficial velocities ( $U_l$ ) = 0.06–0.8 m/s, gas superficial velocities ( $U_g$ ) = 0.06–0.66 m/s, and aspect ratios (AR) = 0.92, 0.67, 0.47 and 0.16. The pressure drop for the single bubble in the rectangular microchannels was evaluated using the information of the bubble behavior. The pressure drop in the single elongated bubble was proportional to the bubble velocity. As the aspect ratio decreased, the pressure drop in the single elongated bubble in the rectangular microchannel increased.

Saisorn and Wongwises [46] studied experimentally adiabatic two-phase air-water flow. The researchers used two channels, made of fused silica, with  $d = 0.53$  and  $0.15$  mm as test sections. They compared the measured frictional pressure drop data with the predictions regarding the homogeneous flow assumption. Many well-known two-phase viscosity models were subsequently evaluated for applicability to microchannels.

Table 1 presents a summary of previous studies.

### 3. Proposed Methodology

Recently, Muzychka and Awad [47] developed an alternative approach for predicting two-phase frictional pressure drop using superposition of three pressure gradients, single-phase liquid, single-phase gas, and interfacial pressure drop, as follows:

$$\left(\frac{dp}{dz}\right)_{f,tp} = \left(\frac{dp}{dz}\right)_{f,l} + \left(\frac{dp}{dz}\right)_{f,i} + \left(\frac{dp}{dz}\right)_{f,g}. \quad (39)$$

When there is no contribution to the pressure gradient through phase interaction, the second term of the right hand side in (39) is equal to zero. The case can be represented with the Chisholm constant ( $C$ ) = 0 [6, 48]. This can also be obtained using the asymptotic model for two-phase frictional pressure gradient with linear superposition ( $n = 1$ ) [6].

Rearranging (39), we obtain

$$\left(\frac{dp}{dz}\right)_{f,i} = \left(\frac{dp}{dz}\right)_{f,tp} - \left(\frac{dp}{dz}\right)_{f,l} - \left(\frac{dp}{dz}\right)_{f,g}. \quad (40)$$

From (40), it is clear that we can calculate the two-phase interfacial pressure gradient,  $(dp/dz)_{f,i}$ , by subtracting the sum of single-phase liquid pressure gradient,  $(dp/dz)_{f,l}$ , and single-phase gas pressure gradient,  $(dp/dz)_{f,g}$ , from the two-phase frictional pressure gradient,  $(dp/dz)_{f,tp}$ . Dividing both sides of (40) by the single-phase liquid frictional pressure gradient, we obtain

$$\phi_{l,i}^2 = \phi_l^2 - 1 - \frac{1}{X^2}. \quad (41)$$

On the other hand, dividing both sides of (40) by the single-phase gas frictional pressure gradient, we obtain

$$\phi_{g,i}^2 = \phi_g^2 - X^2 - 1. \quad (42)$$

Comparing (41)-(42) with the Chisholm [10] formulation gives

$$\phi_{l,i}^2 = \frac{C}{X} \quad (43)$$

for the liquid multiplier formulation or

$$\phi_{g,i}^2 = CX \quad (44)$$

for the gas multiplier formulation.

This represents a simple one-parameter model, whereby closure can be found with comparison with experiment. If the interfacial effects can be modeled by Chisholm's proposed model [10], then all of the reduced data should show trends indicated by (43) or (44). However, if data do not scale according to (43) or (44), that is, a slope of  $-1$  or  $+1$ , then a two-parameter model is clearly required. This will be shown in Figures 2 and 3, which show that all interfacial effects have the same slope but their intensity is governed by the value of  $C$ .

Equations (43) and (44) may be extended to develop a simple two-parameter power law model such that

$$\phi_{l,i}^2 = \frac{A}{X^m} \quad (45)$$

for the liquid multiplier formulation or

$$\phi_{g,i}^2 = AX^m \quad (46)$$

for the gas multiplier formulation.

Equations (45) and (46) can lead to the following equations:

$$\phi_l^2 = 1 + \frac{A}{X^m} + \frac{1}{X^2} \quad (47)$$

or

$$\phi_g^2 = 1 + AX^m + X^2. \quad (48)$$

These forms have the advantage that experimental data for a particular flow regime can be fitted to the simple power law after the removal of the single-phase pressure gradients from the experimental data. Additional modifications may be introduced if the coefficients  $A$  and  $m$  can be shown to depend on other variables like mass flow rate, fluid properties, and mass quality or void fraction. These issues will be examined next considering a few data sets from the open literature.

### 4. Results and Discussion

In this section, we will apply the approach outlined above to recent selected correlations and data sets. Given that two-phase flow data are widely reported using the Lockhart-Martinelli parameters  $\phi_l$  or  $\phi_g$  versus  $X$ , we can present two-phase flow data simply as an interfacial two-phase multiplier using (41) and (42).

Figure 1 shows  $\phi_{l,i}$  versus  $X$  for the Zhang et al. [34] correlation at the different values of the nondimensional

TABLE 1: Summary of previous studies.

Author	$d$	Fluids	Orientation/conditions	Range/applicability	Techniques, basis, and observations
Qu and Mudawar [8]	$231 \times 713 \mu\text{m}$	Water			A new correlation incorporating the effects of both channel size and coolant mass flux was proposed.
Yue et al. [9]	528 and $333 \mu\text{m}$	$\text{N}_2$ -water		$X = 0.67\text{--}6.16$ $\text{Re}_{i0} = 88\text{--}461$	A modified correlation of $C$ value in Chisholm's equation [10] based on linear regression of experimental data was proposed.
Cubaud and Ho [12]	200 and 525 mm				$\phi_l^2 = \beta_l^{-1}$ (the bubbly and the wedging flows) $\phi_l^2 = \beta_l^{-1/2}$ (smaller liquid fraction)
Lee and Mudawar [13]	$231 \times 713 \mu\text{m}$	R134a		$p_{\text{in}} = 1.44\text{--}6.60 \text{ bar}$ $G = 127\text{--}654 \text{ kg/m}^2\cdot\text{s}$ $x_{e,\text{in}} = 0.001\text{--}0.25$ $x_{e,\text{out}} = 0.49\text{--}$ superheat $q = 31.6\text{--}93.8 \text{ W/cm}^2$	Two separate correlations were derived for $C$ based on the flow states of the liquid and vapor.
Ide et al. [14]	1, 2.4, and 4.9 mm	Air-water	vertical upward, horizontal and vertical downward	$\text{AR} = 1\text{--}9$ (capillary rectangular channels)	They proposed the correlations of the holdup and the frictional pressure drop for both capillary circular tube and capillary rectangular channel.
Yue et al. [15]	$667 \mu\text{m}$		Horizontal		A new correlation of $C$ value in Chisholm's equation [10] was proposed.
Harirchian and Garimella [16]	$12.7 \times 12.7 \text{ mm}$	Dielectric fluid Fluorinert FC-77		$G = 250\text{--}1600 \text{ kg/m}^2\cdot\text{s}$	Their study served to quantify the effectiveness of microchannel heat transport while simultaneously assessing the pressure drop trade-offs.
Lee and Garimella [17]	$160\text{--}538 \mu\text{m}$	Deionized water			They developed a new correlation to predict the two-phase pressure drop by considering the effect of mass flux and hydraulic diameter ( $C = f(G, d_h)$ ).
C. Y. Lee and S. Y. Lee [19]	$1.62\text{--}2.16 \text{ mm}$	Air-water			They proposed a modified Lockhart-Martinelli type correlation to take into account the moving contact lines effect ( $C = f(\lambda, \Psi, \text{Re}_{i0})$ ).
Yue et al. [25]	667, 400, and $200 \mu\text{m}$	$\text{CO}_2$ -water			$\phi_l^2 = 0.217\beta_l^{0.5}\text{Re}_l^{0.3}$ ( $d_h = 400 \mu\text{m}$ ) $\phi_l^2 = 0.284\beta_l^{0.5}\text{Re}_l^{0.3}$ ( $d_h = 200 \mu\text{m}$ )
Niu et al. [26]	1.0 mm	A mixture of $\text{CO}_2$ , $\text{N}_2$ , and polyethylene glycol dimethyl			$C = 0.0049 \text{Re}_g^{0.98} \text{Re}_l^{1.08} \text{We}^{-0.86}$

TABLE I: Continued.

Author	$d$	Fluids	Orientation/conditions	Range/applicability	Techniques, basis, and observations
Dutkowski [27]	1.05–2.30 mm	Air-water	$x = 0.0003–0.22$ $G = 139–8582 \text{ kg}/(\text{m}^2\cdot\text{s})$		It was found that the application of commonly used methods to evaluation of pressure drop in two-phase flow provided poor results.
Kawahara et al. [28]	250 $\mu\text{m}$	Distilled water, aqueous solutions of ethanol with two different mass concentrations (49 wt% and 4.8 wt%), and pure ethanol	Horizontal		They correlated their resulting $C$ data with three dimensionless numbers, that is, the Bond number ( $Bo$ ), the liquid Reynolds number ( $Re_l$ ), and the gas Weber number ( $We_g$ ).
Choi et al. [31]		$\text{N}_2$ -water			Two-phase frictional pressure drop was analyzed with flow patterns.
Megahed and Hassan [32]		FC-72		$G = 341–531 \text{ kg}/\text{m}^2\cdot\text{s}$ $q = 60.4–130.6 \text{ kW}/\text{m}^2$	$C = f(Re_{lo}, Co, X)$
C. Y. Lee and S. Y. Lee [33]	1.62–2.16 mm	Air-water			They proposed a pressure drop model of dry-plug flow through modification of the dynamic contact angle analysis taking account of the energy dissipation by the moving contact lines.
Zhang et al. [34]	0.014–6.25 mm			$Re_l \leq 2000$ $Re_g \leq 2000$	$C = f(Lo^*)$
Choi et al. [35]		$\text{N}_2$ -water			They proposed individually new flow pattern based correlations for both homogeneous and separated flow models.
Lee et al. [37]					$C = f(Bo, x_e)$
Pamitran et al. [38]	0.5, 1.5, and 3.0 mm	R-22, R-134a, R-410A, R-290, and R-744	Horizontal	$q = 5–40 \text{ kW}/\text{m}^2$ $G = 50–600 \text{ kg}/(\text{m}^2\cdot\text{s})$ Saturation temperature = 0–15°C	$C = 0.003We^{-0.433}Re^{1.23}$
Kaji et al. [39]	0.51 mm	Air-water	Vertical upward		Analogy between heat transfer and frictional pressure drop was proved to hold roughly for the two-phase flow in microchannel.
Li and Wu [41]					They introduced the Bond number and the Reynolds number to modify the Chisholm parameter of two-phase multipliers to develop new generalized correlations.

TABLE I: Continued.

Author	$d$	Fluids	Orientation/conditions	Range/applicability	Techniques, basis, and observations
Maqbool et al. [42]	1.70 mm	Ammonia (NH <sub>3</sub> )		$q = 15\text{--}350 \text{ kW/m}^2$ $G = 100\text{--}5 \text{ kg/m}^2\cdot\text{s}$	They found that the homogeneous model and the Müller-Steinhagen and Heck [43] correlation were in good agreement with their experimental data.
Choi et al. [44]	490, 490, 322, and 143 $\mu\text{m}$	N <sub>2</sub> -water		AR = 0.92, 0.67, 0.47 and 0.16 $U_l = 0.06\text{--}1.0 \text{ m/s}$ $U_g = 0.06\text{--}71 \text{ m/s}$	The frictional pressure drop in the rectangular microchannels was highly related with the flow pattern.
Choi et al. [45]	490, 490, 322, and 143 $\mu\text{m}$	N <sub>2</sub> -water		AR = 0.92, 0.67, 0.47 and 0.16 $U_l = 0.06\text{--}0.8 \text{ m/s}$ $U_g = 0.06\text{--}0.66 \text{ m/s}$	The pressure drop in the single elongated bubble was proportional to the bubble velocity. As the aspect ratio decreased, the pressure drop in the single elongated bubble in the rectangular microchannel increased.
Saisorn and Wongwises [46]	0.53 and 0.15 mm	Air-water			They investigated the viscosity models for pressure drop prediction for two-phase flow in microchannels.

Laplace constant ( $Lo^*$ ) = 0.01, 0.1, 1, 10, and 100, respectively. Figure 1 is obtained by substituting (26) into (41). It is clear that  $\phi_{l,i}$  decreases with increasing  $X$  for the different values of the nondimensional Laplace constant ( $Lo^*$ ) = 0.01, 0.1, 1, 10, and 100, respectively. Also,  $\phi_{l,i}$  decreases with increasing  $Lo^*$  for the same value of  $X$ .

Figure 2 shows  $\phi_{l,i}$  versus  $X$  for the Lee et al. [37] correlation at the exit quality ( $x_e$ ) of 0.18 and different values of the Bond number ( $Bo$ ) = 0.01, 0.1, 1, and 10, respectively. Figure 2 is obtained by substituting (33) into (41). It is clear that  $\phi_{l,i}$  decreases with increasing  $X$  for the different values of the Bond number ( $Bo$ ) = 0.01, 0.1, 1, and 10, respectively. Also,  $\phi_{l,i}$  increases with increasing  $Bo$  for the same value of  $X$ .

Figure 3 shows  $\phi_{l,i}$  versus  $X$  for the Niu et al. [26] data in  $d = 1 \text{ mm}$  at  $U_l = 0.15, 0.2, 0.3, 0.4, 0.5, 0.6,$  and  $0.7 \text{ m/s}$ , respectively.  $U_l$  can be nondimensionalized using  $Fr_l = U_l/(gd)^{0.5}$ . As a result, the corresponding values of  $Fr_l = 1.515, 2.020, 3.029, 4.039, 5.049, 6.059,$  and  $7.069$ , respectively. Figure 3 is obtained by using (41). Solving for  $A$  and  $m$  for each data set of  $U_l$ , we obtain  $A = 9.955, 11.053, 18.456, 32.679, 38.237, 37.124,$  and  $39.653$ , respectively, while  $m = -1.242, -1.277, -1.597, -1.931, -1.946, -1.855,$  and  $-1.845$ , respectively. Table 2 shows comparison of one- (the best Chisholm constant and the asymptotic model) and two- ( $A$  and  $m$ ) parameter models for  $\phi_l$  of the Niu et al. [26] data. It is clear from Table 2 that the two-parameter model for  $\phi_l$  is better than the one-parameter model (the best Chisholm constant,  $C = 8$ , and the asymptotic model,  $n = 1/3.15$ ) for  $\phi_l$ . The corresponding values of %rms are 1.96%, 5.67%, and 7.31%, respectively.

Figure 4 shows  $\phi_{l,i}$  versus  $X$  for the Kaji et al. [39] data in  $d = 0.51 \text{ mm}$  (vertical heated flow) at  $U_l = 1.567\text{--}0.077 \text{ m/s}$

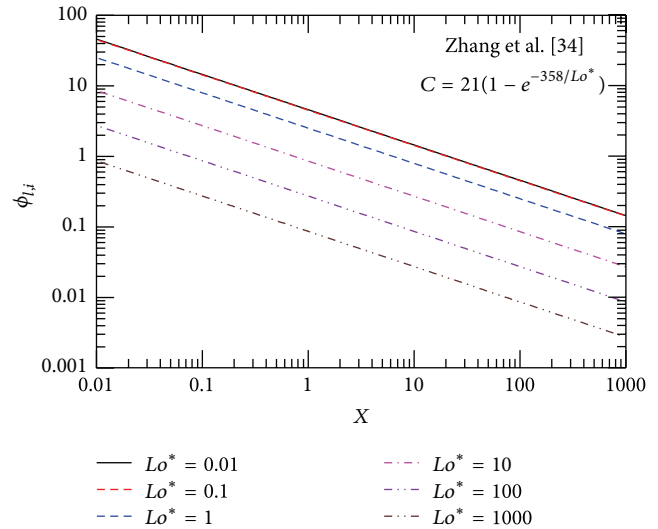


FIGURE 1: Interfacial two-phase multiplier for the Zhang et al. [34] correlation.

TABLE 2: Comparison of one- and two-parameter models for  $\phi_l$  of the Niu et al. [26] data.

%rms using $A$ and $m$	$C$	%rms	$n$	%rms
1.96%	8	5.67%	1/3.15	7.31%

( $Fr_l = 22.158\text{--}1.089$ ), respectively. Figure 5 shows  $\phi_{l,i}$  versus  $X$  for the Kaji et al. [39] data in  $d = 0.514 \text{ mm}$  (horizontal adiabatic flow) at  $U_l = 2.409\text{--}0.086 \text{ m/s}$  ( $Fr_l = 33.931\text{--}1.211$ ), respectively. Figure 6 shows  $\phi_{l,i}$  versus  $X$  for the Kaji et al.

TABLE 3: Summary of the Kaji et al. [39] data.

$d$ (mm)	$U_l$ (m/s)	$Fr_l$	$A$	$m$	Orientation	Condition
0.51	1.567, 1.045, 0.865, 0.814, 0.455, 0.423, 0.241, 0.212, 0.146, 0.118, and 0.077	22.158, 14.776, 12.231, 11.510, 6.434, 5.981, 3.408, 2.998, 2.064, 1.669, and 1.089	23.118, 19.436, 13.666, 17.089, 8.566, 4.534, 3.848, 4.677, 4.667, 4.230, and 2.982	-1.263, -1.706, -0.986, -1.674, -1.726, -0.497, -0.220, -0.747, -0.870, -0.159, and -0.452	Vertical	Heated
0.514	2.409, 1.606, 0.803, 0.630, 0.400, 0.248, and 0.086	33.931, 22.621, 11.310, 8.874, 5.634, 3.493, and 1.211	54.545, 27.617, 18.970, 11.385, 7.504, 5.509, and 3.251	-1.668, -1.414, -1.370, -1.656, -1.528, -1.229, and -1.114	Horizontal	Adiabatic
1.03	1.874, 1.205, 0.796, 0.523, and 0.200	18.647, 11.994, 7.924, 5.206, and 1.990	117.872, 37.520, 20.977, 18.605, and 11.881	-1.894, -1.402, -1.142, -1.404, and -0.580	Vertical	Heated
2.01	1.126, 0.866, 0.573, 0.301, and 0.105	8.020, 6.169, 4.081, 2.144, and 0.749	25.320, 23.890, 24.208, 18.259, and 9.203	-1.071, -1.074, -1.106, -1.121, and -1.080	Vertical	Heated

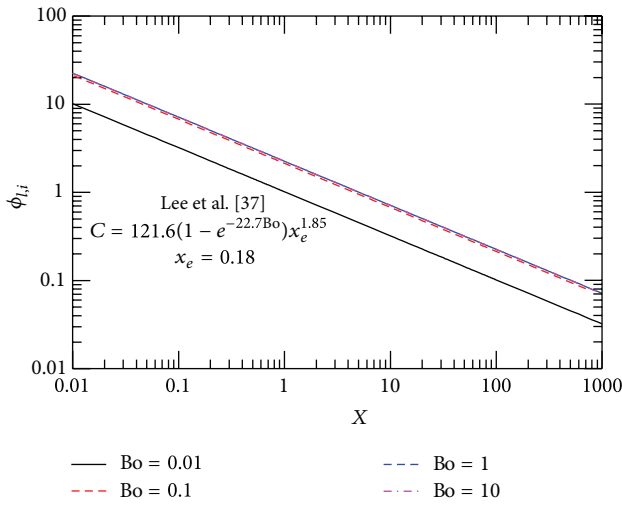
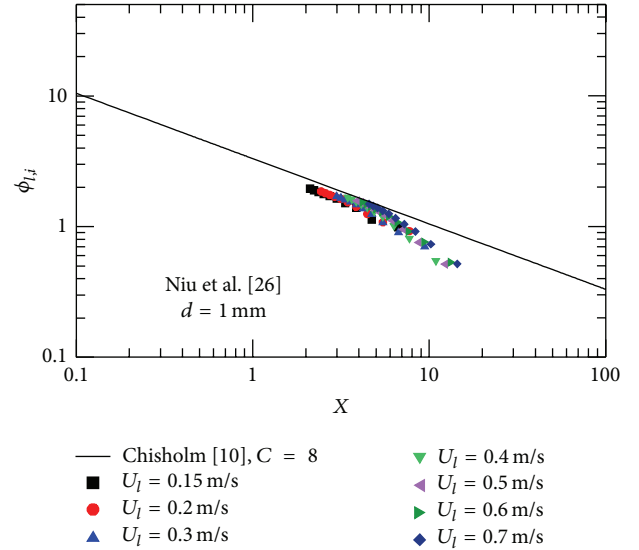


FIGURE 2: Interfacial two-phase multiplier for the Lee et al. [37] correlation.

TABLE 4: Comparison of one- and two-parameter models for  $\phi_l$  of the Kaji et al. [39] data.

%rms using $A$ and $m$	$C$	%rms	$n$	%rms
6.59%	7	20.88%	1/3.05	20.06%
4.43%	7	23.32%	1/3.1	23.06%
8.69%	16	14.04%	1/3.95	15.71%
9.23%	15	20.02%	1/4	19.70%

[39] data in  $d = 1.03$  mm (vertical heated flow) at  $U_l = 1.874$ – $0.200$  m/s ( $Fr_l = 18.647$ – $1.990$ ), respectively. Figure 7 shows  $\phi_{l,i}$  versus  $X$  for the Kaji et al. [39] data in  $d = 2.01$  mm (vertical heated flow) at  $U_l = 1.126$ – $0.105$  m/s ( $Fr_l = 8.020$ – $0.749$ ), respectively. Figures 4–7 are obtained by using (41). Solving for  $A$  and  $m$  for each data set of  $U_l$  in Figures 4–7, we can obtain the different values of the constant ( $A$ ) and the exponent ( $m$ ) for each data set of  $U_l$  in Figures 4–7. Table 3 presents a summary of the Kaji et al. [39] data. Table 4 shows comparison of one- (the best Chisholm constant and the asymptotic model) and two- ( $A$  and  $m$ ) parameter models for  $\phi_l$  of the Kaji et al. [39] data in  $d = 0.51$  mm (vertical heated flow),  $d = 0.514$  mm (horizontal adiabatic flow),  $d =$

FIGURE 3: Interfacial two-phase multiplier for the Niu et al. [26] data in  $d = 1$  mm.

1.03 mm (vertical heated flow), and  $d = 2.01$  mm (vertical heated flow), respectively. Based on the corresponding values of %rms in Table 4 using the simple models (either one- or two-parameter correlation schemes), it is clear that the two-parameter model for  $\phi_l$  is better than the one-parameter model (the best Chisholm constant ( $C$ ) and the asymptotic model ( $n$ )) for  $\phi_l$ . Also, as  $d$  increases from 0.51 mm for vertical heated flow and 0.514 mm for horizontal adiabatic flow to 1.03 and 2.01 mm for vertical heated flow, the best Chisholm constant ( $C$ ) increases while the fitting parameter of the asymptotic model ( $n$ ) decreases because the flow goes from laminar to turbulent.

Based on the results for the comparison of one- (the best Chisholm constant and the asymptotic model) and two- ( $A$  and  $m$ ) parameter models for  $\phi_l$  of the Niu et al. [26] data shown in Table 2 and the results for the comparison of one- (the best Chisholm constant and the asymptotic model) and two- ( $A$  and  $m$ ) parameter models for  $\phi_l$  of the Kaji et al. [39] data shown in Table 4, it is obvious that the two- ( $A$  and  $m$ ) parameter model works better than the one- (the best

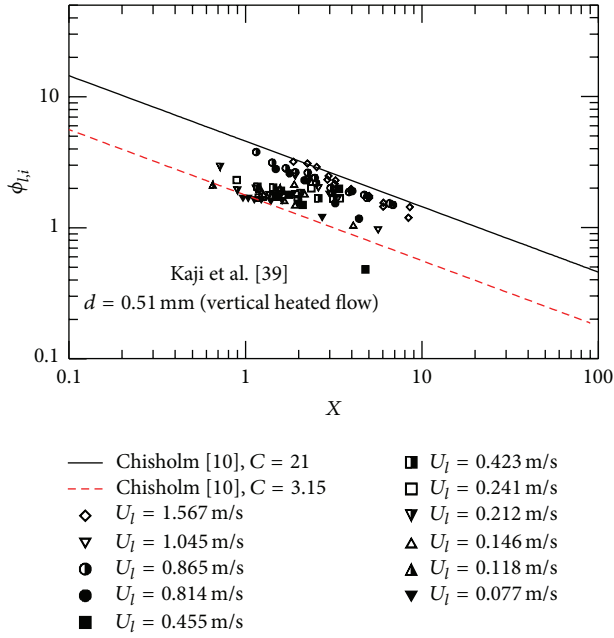


FIGURE 4: Interfacial two-phase multiplier for the Kaji et al. [39] data in  $d = 0.51$  mm (vertical heated flow).

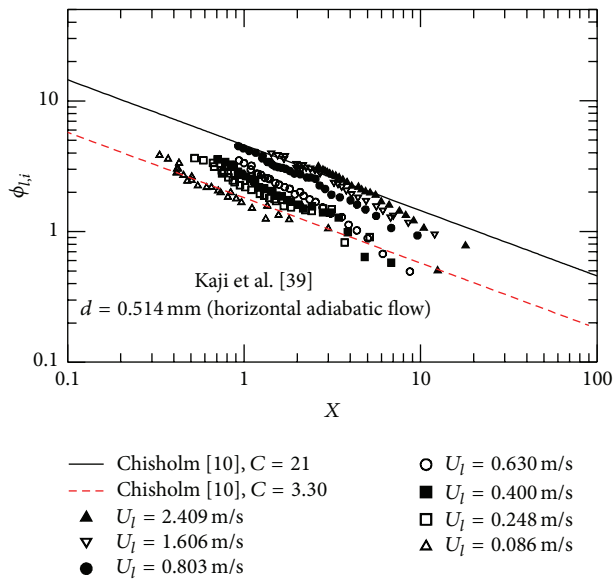


FIGURE 5: Interfacial two-phase multiplier for the Kaji et al. [39] data in  $d = 0.514$  mm (horizontal adiabatic flow).

Chisholm constant and the asymptotic model) parameter model for examining data with strong interfacial effects. Therefore, decomposing the Lockhart-Martinelli approach into single-phase and interfacial components would appear to provide better understanding of experimental data and leads to better model/correlation development.

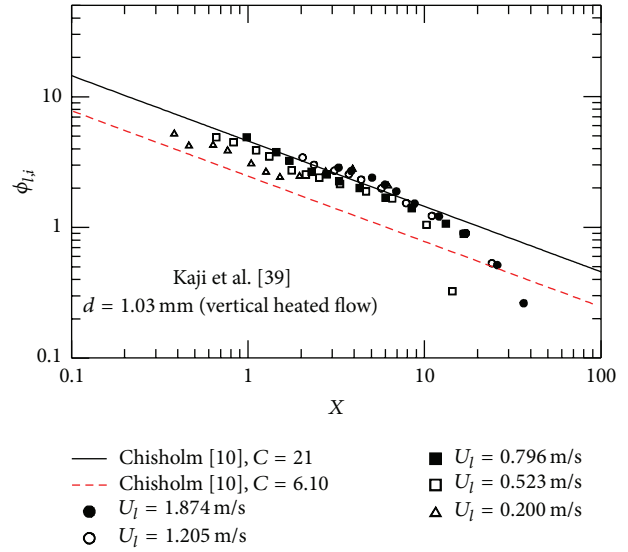


FIGURE 6: Interfacial two-phase multiplier for the Kaji et al. [39] data in  $d = 1.03$  mm (vertical heated flow).

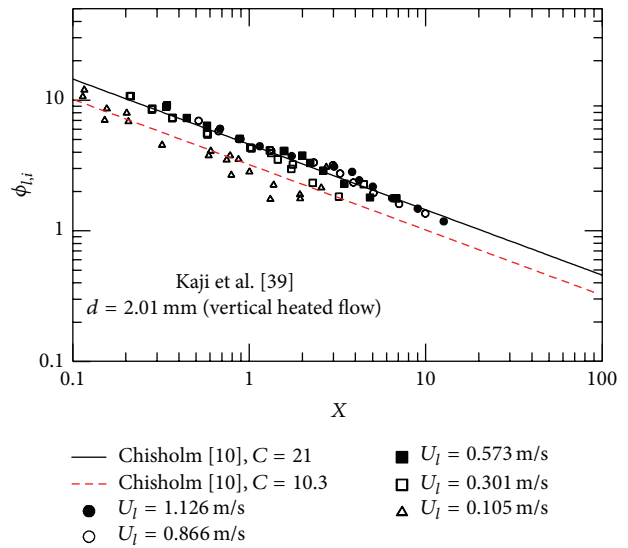


FIGURE 7: Interfacial two-phase multiplier for the Kaji et al. [39] data in  $d = 2.01$  mm (vertical heated flow).

## 5. Summary and Conclusions

In the present study, modeling of interfacial component for two-phase frictional pressure gradient in microchannels and minichannels was considered. A review of the classic Lockhart-Martinelli method and other representations of two-phase flow that were recently available in the open literature was examined. These approaches can all be considered one- (the best Chisholm constant and the asymptotic model) and two-parameter models. The two-parameter models offer more flexibility for developing empirical models for specific flow regimes when the simple Chisholm model fails to

capture the slope of the interfacial two-phase multiplier. The above approaches were compared for a few selected data sets and it was found that the proposed two-parameter modeling approach is the best and offers the greatest flexibility.

Two-phase flow modeling from the viewpoint of interfacial phenomena is deemed to be a better approach from the standpoint of understanding what variables will affect the data in the interfacial region. The true impact of the two-phase flow interfacial effects is more clearly seen, only after the removal of the single-phase flow contributions from the Lockhart-Martinelli two-phase multiplier. This is evident where the assumed Chisholm model clearly does not model the interfacial effects adequately. Decomposing the Lockhart-Martinelli approach into single-phase and interfacial components would appear to provide better understanding of experimental data and lead to better model/correlation development.

## Nomenclature

A:	Constant
AR:	Aspect ratio of cross section of rectangular channel
Bo:	The Bond number
C:	The Chisholm constant
$C_0$ :	Distribution parameter
Ca:	Capillary number
Co:	Confinement number
$d$ :	Diameter, m
Fr:	The Froude number
G:	Mass flux, $\text{kg}/\text{m}^2 \cdot \text{s}$
$g$ :	Gravitational acceleration, $\text{m}/\text{s}^2$
$h$ :	Heat transfer coefficient, $\text{W}/\text{m}^2 \cdot \text{K}$
$Lo^*$ :	The nondimensional Laplace constant
$m$ :	Exponent
$n$ :	Blending parameter in the asymptotic model
$p$ :	Pressure, Pa
$dp/dz$ :	Pressure gradient, $\text{Pa}/\text{m}$
Q:	Volumetric flow rate, $\text{m}^3/\text{s}$
$q$ :	Heat flux, $\text{W}/\text{m}^2$
Re:	The Reynolds number
We:	The Weber number
X:	The Lockhart-Martinelli parameter
$x$ :	Mass quality
$x_e$ :	Thermodynamic equilibrium quality.

## Greek Symbols

$\alpha$ :	Void fraction
$\beta$ :	Holdup
$\phi^2$ :	Two-phase frictional multiplier
$\lambda$ :	The Lee and Lee parameter (13)
$\mu$ :	Dynamic viscosity, $\text{kg}/\text{m} \cdot \text{s}$
$\rho$ :	Density, $\text{kg}/\text{m}^3$
$\sigma$ :	Surface tension, $\text{N}/\text{m}$
$\Psi$ :	The Lee and Lee parameter (14).

## Subscripts

$g$ :	Gas phase
$h$ :	Hydraulic
$i$ :	Interfacial
in:	Inlet
$l$ :	Liquid phase
$lg$ :	Liquid-gas
$lo$ :	All flow is liquid
new:	New
out:	Outlet
tp:	Two-phase.

## Acronyms

ANN:	Artificial neural network
LL:	Laminar-laminar
LT:	Laminar-turbulent
MAD:	Mean absolute deviation

## Conflict of Interests

The authors certify that they have no actual or potential conflict of interests including any financial, personal, or other relationships with other people or organizations within three years of beginning the submitted work that could inappropriately influence, or be perceived to influence, their work.

## Acknowledgment

The authors acknowledge the financial support of the Natural Sciences and Engineering Research Council of Canada (NSERC) through the Discovery Grants program.

## References

- [1] G. P. Celata, *Heat Transfer and Fluid Flow in Microchannels*, Begell House, Redding, Conn, USA, 2004.
- [2] S. G. Kandlikar, S. Garimella, D. Li, S. Colin, and M. R. King, *Heat Transfer and Fluid Flow in Minichannels and Microchannels*, Elsevier, Oxford, UK, 2006.
- [3] C. T. Crowe, *Multiphase Flow Handbook*, Taylor & Francis, Boca Raton, Fla, USA, 2006.
- [4] S. M. Ghiaasiaan, *Two-Phase Flow, Boiling and Condensation in Conventional and Miniature Systems*, Cambridge University Press, New York, NY, USA, 2008.
- [5] L. P. Yarin, A. Mosyak, and G. Hetsroni, *Fluid Flow, Heat Transfer and Boiling in Micro-Channels*, Springer, Berlin, Germany, 2009.
- [6] M. M. Awad and Y. S. Muzychka, "Bounds on two-phase frictional pressure gradient in minichannels and microchannels," *Heat Transfer Engineering*, vol. 28, no. 8-9, pp. 720-729, 2007.
- [7] R. W. Lockhart and R. C. Martinelli, "Proposed correlation of data for isothermal two-phase, two-component flow in pipes," *Chemical Engineering Progress Symposium Series*, vol. 45, no. 1, pp. 39-48, 1949.
- [8] W. Qu and I. Mudawar, "Measurement and prediction of pressure drop in two-phase micro-channel heat sinks," *International*

- Journal of Heat and Mass Transfer*, vol. 46, no. 15, pp. 2737–2753, 2003.
- [9] J. Yue, G. Chen, and Q. Yuan, “Pressure drops of single and two-phase flows through T-type microchannel mixers,” *Chemical Engineering Journal*, vol. 102, no. 1, pp. 11–24, 2004.
  - [10] D. Chisholm, “A theoretical basis for the Lockhart-Martinelli correlation for two-phase flow,” *International Journal of Heat and Mass Transfer*, vol. 10, no. 12, pp. 1767–1778, 1967.
  - [11] W. H. McAdams, W. K. Woods, and L. C. Heroman, “Vaporization inside horizontal tubes. II-benzene-oil mixtures,” *Transactions of the ASME Journal of Heat Transfer*, vol. 64, no. 3, pp. 193–200, 1942.
  - [12] T. Cubaud and C.-M. Ho, “Transport of bubbles in square microchannels,” *Physics of Fluids*, vol. 16, no. 12, pp. 4575–4585, 2004.
  - [13] J. Lee and I. Mudawar, “Two-phase flow in high-heat-flux micro-channel heat sink for refrigeration cooling applications: part I-pressure drop characteristics,” *International Journal of Heat and Mass Transfer*, vol. 48, no. 5, pp. 928–940, 2005.
  - [14] H. Ide, A. Kariyasaki, and T. Fukano, “Fundamental data on the gas-liquid two-phase flow in minichannels,” *International Journal of Thermal Sciences*, vol. 46, no. 6, pp. 519–530, 2007.
  - [15] J. Yue, G. Chen, Q. Yuan, L. Luo, and Y. Gonthier, “Hydrodynamics and mass transfer characteristics in gas-liquid flow through a rectangular microchannel,” *Chemical Engineering Science*, vol. 62, no. 7, pp. 2096–2108, 2007.
  - [16] T. Harirchian and S. V. Garimella, “Microchannel size effects on two-phase local heat transfer and pressure drop in silicon microchannel heat sinks with a dielectric fluid,” in *Proceedings of the ASME International Mechanical Engineering Congress and Exposition (IMECE '07)*, pp. 437–446, Seattle, Wash, USA, November 2007.
  - [17] P.-S. Lee and S. V. Garimella, “Saturated flow boiling heat transfer and pressure drop in silicon microchannel arrays,” *International Journal of Heat and Mass Transfer*, vol. 51, no. 3–4, pp. 789–806, 2008.
  - [18] S. Saisorn and S. Wongwises, “A review of two-phase gas-liquid adiabatic flow characteristics in micro-channels,” *Renewable and Sustainable Energy Reviews*, vol. 12, no. 3, pp. 824–838, 2008.
  - [19] C. Y. Lee and S. Y. Lee, “Pressure drop of two-phase plug flow in round mini-channels: influence of surface wettability,” *Experimental Thermal and Fluid Science*, vol. 32, no. 8, pp. 1716–1722, 2008.
  - [20] K. Mishima and T. Hibiki, “Some characteristics of air-water two-phase flow in small diameter vertical tubes,” *International Journal of Multiphase Flow*, vol. 22, no. 4, pp. 703–712, 1996.
  - [21] T. D. Blake, “The physics of moving wetting lines,” *Journal of Colloid and Interface Science*, vol. 299, no. 1, pp. 1–13, 2006.
  - [22] M. Bracke, F. de Voeght, and P. Joos, “The kinetics of wetting: the dynamic contact angle,” in *Trends in Colloid and Interface Science III*, vol. 79 of *Progress in Colloid & Polymer Science*, pp. 142–149, Springer, New York, NY, USA, 1989.
  - [23] J. E. Seebergh and J. C. Berg, “Dynamic wetting in the low capillary number regime,” *Chemical Engineering Science*, vol. 47, no. 17–18, pp. 4455–4464, 1992.
  - [24] S. van Mourik, A. E. P. Veldman, and M. E. Dreyer, “Simulation of capillary flow with a dynamic contact angle,” *Microgravity Science and Technology*, vol. 17, no. 3, pp. 91–98, 2005.
  - [25] J. Yue, L. Luo, Y. Gonthier, G. Chen, and Q. Yuan, “An experimental investigation of gas-liquid two-phase flow in single microchannel contactors,” *Chemical Engineering Science*, vol. 63, no. 16, pp. 4189–4202, 2008.
  - [26] H. Niu, L. Pan, H. Su, and S. Wang, “Flow pattern, pressure drop, and mass transfer in a gas-liquid concurrent two-phase flow microchannel reactor,” *Industrial and Engineering Chemistry Research*, vol. 48, no. 3, pp. 1621–1628, 2009.
  - [27] K. Dutkowsky, “Two-phase pressure drop of air-water in minichannels,” *International Journal of Heat and Mass Transfer*, vol. 52, no. 21–22, pp. 5185–5192, 2009.
  - [28] A. Kawahara, M. Sadatomi, K. Nei, and H. Matsuo, “Experimental study on bubble velocity, void fraction and pressure drop for gas-liquid two-phase flow in a circular microchannel,” *International Journal of Heat and Fluid Flow*, vol. 30, no. 5, pp. 831–841, 2009.
  - [29] A. Kawahara, M. Sadatomi, and K. Kumagae, “Effects of gas-liquid inlet/mixing conditions on two-phase flow in microchannels,” *Progress in Multiphase Flow Research*, vol. 1, pp. 197–203, 2006.
  - [30] M. Kawaji, A. Kawahara, K. Mori, M. Sadatomi, and K. Kumagae, “Gas-liquid two-phase flow in microchannels: the effects of gas-liquid injection methods,” in *Proceedings of the 18th National and 7th ISHMT-ASME Heat and Mass Transfer Conference*, pp. 80–89, Guwahat, India, 2006.
  - [31] C.-W. Choi, D. I. Yu, and M. H. Kim, “Study of wettability effect on pressure drop and flow pattern of two-phase flow in rectangular microchannel,” *Transactions of the Korean Society of Mechanical Engineers B*, vol. 33, no. 12, pp. 939–946, 2009.
  - [32] A. Megahed and I. Hassan, “Two-phase pressure drop and flow visualization of FC-72 in a silicon microchannel heat sink,” *International Journal of Heat and Fluid Flow*, vol. 30, no. 6, pp. 1171–1182, 2009.
  - [33] C. Y. Lee and S. Y. Lee, “Pressure drop of two-phase dry-plug flow in round mini-channels: effect of moving contact line,” *Experimental Thermal and Fluid Science*, vol. 34, no. 1, pp. 1–9, 2010.
  - [34] W. Zhang, T. Hibiki, and K. Mishima, “Correlations of two-phase frictional pressure drop and void fraction in mini-channel,” *International Journal of Heat and Mass Transfer*, vol. 53, no. 1–3, pp. 453–465, 2010.
  - [35] C.-W. Choi, D. I. Yu, and M. H. Kim, “Development of new correlation and assessment of correlations for two-phase pressure drop in rectangular microchannels,” *Transactions of the Korean Society of Mechanical Engineers B*, vol. 34, no. 1, pp. 9–18, 2010.
  - [36] D. R. H. Beattie and P. B. Whalley, “A simple two-phase frictional pressure drop calculation method,” *International Journal of Multiphase Flow*, vol. 8, no. 1, pp. 83–87, 1982.
  - [37] H. J. Lee, D. Liu, Y. Alyousef, and S. C. Yao, “Generalized two-phase pressure drop and heat transfer correlations in evaporative micro/minichannels,” *Transactions of the ASME Journal of Heat Transfer*, vol. 132, no. 4, Article ID 041004, 9 pages, 2010.
  - [38] A. S. Pamitran, K.-I. Choi, J.-T. Oh, and P. Hrnjak, “Characteristics of two-phase flow pattern transitions and pressure drop of five refrigerants in horizontal circular small tubes,” *International Journal of Refrigeration*, vol. 33, no. 3, pp. 578–588, 2010.
  - [39] M. Kaji, T. Sawai, Y. Kagi, and T. Ueda, “Heat transfer and fluid dynamics of air-water two-phase flow in micro-channels,” *Experimental Thermal and Fluid Science*, vol. 34, no. 4, pp. 446–453, 2010.
  - [40] D. Chisholm and A. D. K. Laird, “Two-phase flow in rough tubes,” *Transactions of the ASME Journal of Heat Transfer*, vol. 80, no. 2, pp. 276–286, 1958.

- [41] W. Li and Z. Wu, "A general correlation for adiabatic two-phase pressure drop in micro/mini-channels," *International Journal of Heat and Mass Transfer*, vol. 53, no. 13-14, pp. 2732–2739, 2010.
- [42] M. H. Maqbool, B. Palm, R. Khodabandeh, and R. Ali, "Two-phase pressure drop of ammonia in a mini/micro-channel," in *Proceedings of the 3rd Joint US-European Fluids Engineering Summer Meeting and 8th International Conference on Nanochannels, Microchannels, and Minichannels (FEDSM-ICNMM '10)*, pp. 1731–1739, Montreal, Canada, August 2010.
- [43] H. Müller-Steinhagen and K. Heck, "A simple friction pressure drop correlation for two-phase flow in pipes," *Chemical Engineering and Processing*, vol. 20, no. 6, pp. 297–308, 1986.
- [44] C. W. Choi, D. I. Yu, and M. H. Kim, "Adiabatic two-phase flow in rectangular microchannels with different aspect ratios: part I—flow pattern, pressure drop and void fraction," *International Journal of Heat and Mass Transfer*, vol. 54, no. 1–3, pp. 616–624, 2011.
- [45] C. W. Choi, D. I. Yu, and M. H. Kim, "Adiabatic two-phase flow in rectangular microchannels with different aspect ratios: part II—bubble behaviors and pressure drop in single bubble," *International Journal of Heat and Mass Transfer*, vol. 53, no. 23–24, pp. 5242–5249, 2010.
- [46] S. Saisorn and S. Wongwises, "Two-phase air-water flow in micro-channels: an investigation of the viscosity models for pressure drop prediction," *International Communications in Heat and Mass Transfer*, vol. 38, no. 2, pp. 212–217, 2011.
- [47] Y. S. Muzychka and M. M. Awad, "Asymptotic generalizations of the lockhart-martinelli method for two phase flows," *Transactions of the ASME Journal of Fluids Engineering*, vol. 132, no. 3, Article ID 031302, 12 pages, 2010.
- [48] M. M. Awad and Y. S. Muzychka, "Two-phase flow modeling in microchannels and minichannels," *Heat Transfer Engineering*, vol. 31, no. 13, pp. 1023–1033, 2010.

## Research Article

# A Robust Asymptotically Based Modeling Approach for Two-Phase Flows

M. M. Awad<sup>1</sup> and Y. S. Muzychka<sup>2</sup>

<sup>1</sup> Mechanical Power Engineering Department, Faculty of Engineering, Mansoura University, Mansoura 35516, Egypt

<sup>2</sup> Faculty of Engineering and Applied Science, Memorial University of Newfoundland, St. John's, Newfoundland, Canada A1B 3X5

Correspondence should be addressed to M. M. Awad; m\_m.awad@mans.edu.eg

Received 6 May 2013; Accepted 11 November 2013; Published 25 February 2014

Academic Editor: Guan Heng Yeoh

Copyright © 2014 M. M. Awad and Y. S. Muzychka. This is an open access article distributed under the Creative Commons Attribution License, which permits unrestricted use, distribution, and reproduction in any medium, provided the original work is properly cited.

A simple semitheoretical method for calculating two-phase frictional pressure gradient in horizontal circular pipes using asymptotic analysis to develop a robust compact model is presented. Two-phase frictional pressure gradient is expressed in terms of the asymptotic single-phase frictional pressure gradients for liquid and gas flowing alone. The proposed model can be transformed into either a two-phase frictional multiplier for liquid flowing alone ( $\phi_l^2$ ) or two-phase frictional multiplier for gas flowing alone ( $\phi_g^2$ ) as a function of the Lockhart-Martinelli parameter,  $X$ . Single-phase friction factors are calculated using the Churchill model which allows for prediction over the full range of laminar-transition-turbulent regions and allows for pipe roughness effects. The proposed model is compared against published data to show the asymptotic behavior. Comparison with other existing correlations for two-phase frictional pressure gradient such as the Chisholm correlation, the Friedel correlation, and the Müller-Steinhagen and Heck correlation, is also presented. Comparison with experimental data for both  $\phi_l$  and  $\phi_g$  versus  $X$  is also presented. At the end of the paper, the present asymptotic model is also extended to minichannels and microchannels.

## 1. Introduction

In the present study, new two-phase flow modeling is proposed, based upon an asymptotic modeling method to overcome the disadvantages of the separate cylinders model of two-phase flow where the liquid and gas phases are assumed to flow independently of each other in two separate parallel circular cylinders. The separate cylinders model of two-phase flow was introduced first by Turner [1]. Since then, it had appeared in a number of texts such as those by Wallis [2], Carey [3], and Brennen [4]. The equations of  $\phi_l^2$  and  $\phi_g^2$  are [5, see Appendix A]

$$\phi_l^2 = \left[ 1 + (\phi_l^2)^{2(m-n)/((5-m)(5-n))} \left( \frac{1}{X^2} \right)^{2/(5-n)} \right]^{(5-m)/2}, \quad (1)$$

$$\phi_g^2 = \left[ 1 + (\phi_g^2)^{2(m-n)/((5-m)(5-n))} (X^2)^{2/(5-m)} \right]^{(5-n)/2}. \quad (2)$$

This general form of  $\phi_l^2$  in (1) and  $\phi_g^2$  in (2) has five different conditions as follows.

- (i)  $m = n = 0.25$ . This represents turbulent liquid-turbulent gas flow type ( $Re_l > 2000$  and  $Re_g > 2000$ ).
- (ii)  $m = 1, n = 0.25$ . This represents laminar liquid-turbulent gas flow type ( $Re_l < 2000$  and  $Re_g > 2000$ ).
- (iii)  $m = 0.25, n = 1$ . This represents turbulent liquid-laminar gas flow type ( $Re_l > 2000$  and  $Re_g < 2000$ ).
- (iv)  $m = n = 1$ . This represents laminar liquid-laminar gas flow type ( $Re_l < 2000$  and  $Re_g < 2000$ ).
- (v)  $m = n = 0$ . This represents constant friction factor liquid-gas flow type.

Table 1 shows the expressions of  $\phi_l^2$  and  $\phi_g^2$  for different flow conditions, respectively.

TABLE 1: Expressions of  $\phi_l^2$  and  $\phi_g^2$  for different flow conditions.

Liquid	Gas	$\phi_l^2$	$\phi_g^2$
Turbulent $m = 0.25$	Turbulent $n = 0.25$	$\phi_l^2 = \left[ 1 + \left( \frac{1}{X^2} \right)^{1/2.375} \right]^{2.375}$	$\phi_g^2 = \left[ 1 + (X^2)^{1/2.375} \right]^{2.375}$
Laminar $m = 1$	Turbulent $n = 0.25$	$\phi_l^2 = \left[ 1 + (\phi_l^2)^{(3/38)} \left( \frac{1}{X^2} \right)^{1/2.375} \right]^2$	$\phi_g^2 = \left[ 1 + (\phi_g^2)^{(-3/38)} (X^2)^{0.5} \right]^{2.375}$
Turbulent $m = 0.25$	Laminar $n = 1$	$\phi_l^2 = \left[ 1 + (\phi_l^2)^{(-3/38)} \left( \frac{1}{X^2} \right)^{0.5} \right]^{2.375}$	$\phi_g^2 = \left[ 1 + (\phi_g^2)^{(3/38)} (X^2)^{(1/2.375)} \right]^2$
Laminar $m = 1$	Laminar $n = 1$	$\phi_l^2 = \left[ 1 + \left( \frac{1}{X^2} \right)^{0.5} \right]^2$	$\phi_g^2 = \left[ 1 + (X^2)^{0.5} \right]^2$
$f = \text{constant}$ $m = n = 0$		$\phi_l^2 = \left[ 1 + \left( \frac{1}{X^2} \right)^{0.4} \right]^{2.5}$	$\phi_g^2 = \left[ 1 + (X^2)^{0.4} \right]^{2.5}$

From Table 1, it is clear that the expressions of  $\phi_l^2$  and  $\phi_g^2$  are implicit for liquid-gas laminar-turbulent flow or turbulent-laminar flow. These implicit expressions can be solved by means of computer algebra systems like Maple software [6]. The authors confirm that there is not any financial gain related to writing Maple software as [6] in the present paper.

The main disadvantage of the separate cylinders model for two-phase flow is not taking into account the important frictional interactions that occur at the interface between liquid and gas, and, needless to say, it would simply neglect the nature of two-phase flow because the liquid and gas phases are assumed to flow independently of each other in two separate parallel circular cylinders. Also, the values of the Reynolds number for the liquid and gas phases are important because these values determine the flow condition and hence the suitable expression for this flow condition. In addition, the obtained expressions are implicit for liquid-gas laminar-turbulent flow or turbulent-laminar flow [5].

In the current study, two-phase frictional pressure gradient is expressed in terms of the asymptotic single-phase frictional pressure gradients for liquid and gas flowing alone. Asymptotes appear in many engineering problems such as steady and unsteady internal and external conduction, free and forced internal and external convection, fluid flow, and mass transfer. Often, there exists a smooth transition between two asymptotic solutions [7–10]. This smooth transition indicates that there is no sudden change in slope and no discontinuity within the transition region.

The asymptotic analysis method was first introduced by Churchill and Usagi [7], in 1972. After this time, this method of combining asymptotic solutions proved quite successful in developing models in many applications [10]. Recently, it has been applied to two-phase flow in circular pipes [5, 11], minichannels, and microchannels [5, 12]. Moreover, Awad and Butt have shown that the asymptotic method works well for petroleum industry applications for flows through porous media [13], liquid-liquid flows [14], and flows through fractured media [15].

In the asymptotic model, the dependent parameter  $y$  has two asymptotes. The first asymptote is  $y_0$ , which corresponds to very small value of the independent parameter  $z$ .

The second asymptote is  $y_\infty$ , which corresponds to very large value of the independent parameter  $z$ . The two asymptotes  $y_0$  and  $y_\infty$  can be expressed as follows [7–10]:

$$\begin{aligned} y_0 &= c_0 z^i, & z &\rightarrow 0, \\ y_\infty &= c_\infty z^j, & z &\rightarrow \infty. \end{aligned} \quad (3)$$

The two asymptotes  $y_0$  and  $y_\infty$  are based on analytical solution. They consist of a constant, which has a positive real value. The two constants are called  $c_0$  as  $z \rightarrow 0$  and  $c_\infty$  as  $z \rightarrow \infty$ . The values of the two exponents  $i$  and  $j$  are often 0, 1, 1/2, 1/4, and 1/3 [7–10].

From analytical, experimental, or numerical methods, it is known that  $y$  frequently transitions in a smooth manner between the two asymptotes  $y_0$  and  $y_\infty$ .

For the case of two-phase frictional pressure gradient in horizontal pipes, the two asymptotes  $y_0$  and  $y_\infty$  increase with increasing values of  $z$ , and the solution  $y$  is concave upwards. This trend is also found in the case of external free and forced convection from single isothermal convex bodies.

Since  $y_0 > y_\infty$  as  $z \rightarrow 0$ , so the solution  $y$  is concave upwards, and the two asymptotes  $y_0$  and  $y_\infty$  can be combined in the following method [7–10]:

$$y = \left[ y_0^p + y_\infty^p \right]^{1/p}. \quad (4)$$

The parameter  $p$  is a fitting or “blending” parameter whose value can be determined in a simple method. The effect of the parameter  $p$  in (4) is only important in the transition region. The results for small and large values of the independent parameter  $z$  remain unchanged with changing the parameter  $p$ .

To determine a value of  $p$ , there are a number of methods as discussed by Churchill and Usagi [7]. For example, we can select an intermediate value of  $z = z_{\text{int}}$  corresponding or near to the intersection of the two asymptotes for which  $y(z_{\text{int}})$  is known from analytical, experimental, or numerical methods. Using (3) and (4), we can write for the intermediate value of  $z = z_{\text{int}}$ ,

$$y(z_{\text{int}}) = \left[ (c_0 z_{\text{int}}^i)^p + (c_\infty z_{\text{int}}^j)^p \right]^{1/p}. \quad (5)$$

Although the fitting or “blending” parameter  $p$  is unknown, it can be calculated by numerical methods for solving a nonlinear equation or by means of computer algebra systems like Maple release 9 software [6].

In the present study,  $p$  is chosen as the value, which minimizes the root mean square (RMS) error,  $e_{\text{RMS}}$ , between the model predictions and the available data. The fractional error ( $e$ ) in applying the model to each available data point is defined as

$$e = \left| \frac{\text{Predicted} - \text{Available}}{\text{Available}} \right|. \quad (6)$$

For groups of data, the root mean square (RMS) error,  $e_{\text{RMS}}$ , is defined as

$$e_{\text{RMS}} = \left[ \frac{1}{N} \sum_{k=1}^N e_k^2 \right]^{1/2}. \quad (7)$$

If  $p$  is a weak function of the mass flow rate, or mass flux of either the liquid phase or the gas phase, a single value may be chosen which best represents all of the available data for two-phase frictional pressure gradient.

The approximate solution  $y$  is often presented in a form, which is based on one of the two asymptotes  $y_0$  and  $y_\infty$ . For example, if the approximate solution  $y$  is presented in terms of the asymptote  $y_0$ , then the model can be expressed as follows [7–10]:

$$\frac{y}{y_0} = \left[ 1 + \left( \frac{y_\infty}{y_0} \right)^p \right]^{1/p}. \quad (8)$$

On the other hand, if the approximate solution  $y$  is presented in terms of the asymptote  $y_\infty$ , then the model can be expressed as follows [7–10]:

$$\frac{y}{y_\infty} = \left[ 1 + \left( \frac{y_0}{y_\infty} \right)^p \right]^{1/p}. \quad (9)$$

*1.1. Asymptotic Modeling in Two-Phase Flow.* Using the asymptotic analysis method, two-phase frictional pressure gradient  $(dp/dz)_f$  can be expressed in terms of single-phase frictional pressure gradient for liquid flowing alone  $(dp/dz)_{f,l}$  and single-phase frictional pressure gradient for gas flowing alone  $(dp/dz)_{f,g}$  as follows:

$$\left( \frac{dp}{dz} \right)_f = \left[ \left( \frac{dp}{dz} \right)_{f,l}^p + \left( \frac{dp}{dz} \right)_{f,g}^p \right]^{1/p}. \quad (10)$$

Equation (10) reduces to  $(dp/dz)_{f,l}$  and  $(dp/dz)_{f,g}$  as  $x = 0$  and 1, respectively. It is clear that the asymptotic analysis method arrives at the same form as the separate cylinders model formulation [1], but with a different physical approach. Rather than modeling the fluid as two distinct fluid streams flowing in separate pipes, the two-phase frictional pressure gradient can be predicted using a nonlinear superposition of the component pressure gradients that would arise from each stream flowing alone in the same pipe, through application

of the Churchill-Usagi asymptotic correlation method [7]. This form was asymptotically correct for either phase as the mass quality varied from  $0 < x < 1$ . Further, rather than approaching the Lockhart-Martinelli parameter from the point of view of the four flow regimes using simple friction models, the asymptotic analysis method uses the Churchill [16] model for the friction factor in smooth and rough pipes for all values of the Reynolds number. In this way the proposed model was most general and contained only one empirical coefficient, the Churchill-Usagi [7] blending parameter.

The principal advantages of the asymptotic analysis method over the separate cylinders model formulation [1] are twofold. First, all four Lockhart-Martinelli flow regimes can be handled with ease, since the separate cylinders model formulation [1] leads to implicit relationships for the two mixed regimes. Second, since the friction model used is only a function of Reynolds number and roughness, broader applications involving rough pipes can be easily modeled.

If the two-phase frictional pressure gradient  $(dp/dz)_f$  is presented in terms of the single-phase frictional pressure gradient for liquid flowing alone  $(dp/dz)_{f,l}$ , then the model can be expressed using the Lockhart-Martinelli parameter ( $X$ ) as follows:

$$\left( \frac{dp}{dz} \right)_f = \left( \frac{dp}{dz} \right)_{f,l} \left[ 1 + \left( \frac{1}{X^2} \right)^p \right]^{1/p}. \quad (11)$$

Equation (11) can be expressed in terms of a two-phase frictional multiplier liquid flowing alone in the pipe ( $\phi_l^2$ ) as follows:

$$\phi_l^2 = \left[ 1 + \left( \frac{1}{X^2} \right)^p \right]^{1/p}. \quad (12)$$

On the other hand, if the two-phase frictional pressure gradient  $(dp/dz)_f$  is presented in terms of the single-phase frictional pressure gradient for gas flowing alone  $(dp/dz)_{f,g}$ , then the model can be expressed using the Lockhart-Martinelli parameter ( $X$ ) as follows:

$$\left( \frac{dp}{dz} \right)_f = \left( \frac{dp}{dz} \right)_{f,g} \left[ 1 + (X^2)^p \right]^{1/p}. \quad (13)$$

Equation (13) can be expressed in terms of a two-phase frictional multiplier for gas flowing alone in the pipe ( $\phi_g^2$ ) as follows:

$$\phi_g^2 = \left[ 1 + (X^2)^p \right]^{1/p}. \quad (14)$$

It is clear that (12) and (14) are similar to the separate cylinders model formulation [1] for constant friction factor ( $1/p = 2.5$ ) or when both liquid and gas are either turbulent ( $1/p = 2.375$ ) or laminar ( $1/p = 2$ ). Also, (12) and (14) are still explicit for liquid-gas laminar-turbulent flow and turbulent-laminar flow.

**1.1.1. Single-Phase Frictional Pressure Gradient Equations.** The single-phase frictional pressure gradient can be related to the Fanning friction factor in terms of mass flow rate of both the liquid phase and the gas phase as follows:

$$\begin{aligned} \left(\frac{dp}{dz}\right)_{f,l} &= \frac{32f_l m_l^2}{\pi^2 d^5 \rho_l}, \\ \left(\frac{dp}{dz}\right)_{f,g} &= \frac{32f_g m_g^2}{\pi^2 d^5 \rho_g}. \end{aligned} \quad (15)$$

Equation (15) can be written in terms of mass flux and mass quality as follows:

$$\begin{aligned} \left(\frac{dp}{dz}\right)_{f,l} &= \frac{2f_l G^2 (1-x)^2}{d\rho_l}, \\ \left(\frac{dp}{dz}\right)_{f,g} &= \frac{2f_g G^2 x^2}{d\rho_g}. \end{aligned} \quad (16)$$

The model that was developed by Churchill [16] is introduced to define the Fanning friction factor. When a computer is used, the Churchill model equations [16] are more recommended than the Blasius equations [17] to define the Fanning friction factor [18]. The Churchill model was a correlation of the Moody chart [19]. Churchill's correlation spanned the entire range of laminar, transition, and turbulent flow in pipes. The Churchill model equations that define the Fanning friction factor are

$$\begin{aligned} f &= 2 \left[ \left( \frac{8}{Re} \right)^{12} + \frac{1}{(a+b)^{3/2}} \right]^{1/12}, \\ a &= \left[ 2.457 \ln \frac{1}{(7/Re)^{0.9} + (0.27\epsilon/d)} \right]^{16}, \\ b &= \left( \frac{37530}{Re} \right)^{16}. \end{aligned} \quad (17)$$

The Reynolds number equations can be expressed in terms of mass flow rate of both the liquid phase and the gas phase or mass flux and mass quality as follows:

$$\begin{aligned} Re_l &= \frac{4m_l}{\pi d \mu_l} = \frac{G(1-x)d}{\mu_l}, \\ Re_g &= \frac{4m_g}{\pi d \mu_g} = \frac{Gxd}{\mu_g}. \end{aligned} \quad (18)$$

## 2. Results and Discussion

Examples of two-phase frictional pressure gradient in horizontal pipes for published data of different pipe diameters are presented to show features of the asymptotes, asymptotic analysis, and the development of simple compact models. At the end of the paper, the present asymptotic model is also extended to minichannels and microchannels.

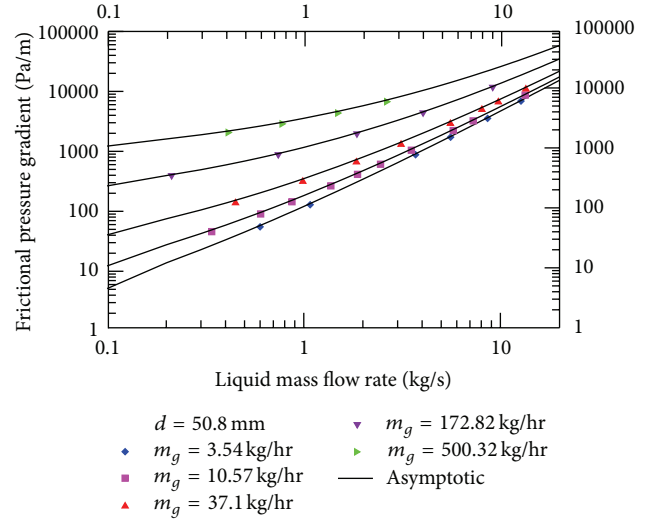


FIGURE 1: Comparison of the Asymptotic Model with Dukler's Data [20].

TABLE 2: Comparison of different models with Dukler's data [20].

Model	RMS (%)
Chisholm [21]	23.08
Chisholm [22]	63.13
Friedel [23]	83.32
Müller-Steinhagen and Heck [24]	36.20
Asymptotic [11]	12.11

**2.1. Comparison of the Present Asymptotic Model with Data.** Figure 1 shows comparison of the present asymptotic model [11] with Dukler's data [20] for air-water flow in a smooth horizontal pipe at  $d = 2$  in. (50.8 mm). The frictional pressure gradient is represented as a function of the liquid mass flow rate on log-log scale for the gas mass flow rate values of 7.8, 23.3, 81.8, 381, and 1103 lb<sub>m</sub>/hr (3.54, 10.57, 37.1, 172.82, and 500.32 kg/s), respectively. For the same value of the gas mass flow rate, the frictional pressure gradient increases with increasing liquid mass flow rate. Also, the frictional pressure gradient increases with increasing gas mass flow rate at the same value of the liquid mass flow rate. Equation (10) represents the present asymptotic model [11]. It can be seen that the present model with fitting parameter  $p = 1/3.9$  represents Dukler's data in a successful manner. The root mean square (RMS) error,  $e_{RMS}$ , is equal to 12.11%. The worst agreement is obtained for data points with an absolute error ( $e$ ) of 23.34%.

Comparison of different models such as Chisholm [21], Chisholm [22], Friedel [23], and Müller-Steinhagen and Heck [24] as well as the present asymptotic model [11] with  $p = 1/3.9$  with Dukler's data [20] is shown in Table 2.

As a brief on these different models, Chisholm [21] developed equations in terms of the Lockhart-Martinelli correlating groups for the friction pressure drop during the flow of

TABLE 3: Values of the asymptotic parameter ( $p$ ) in circular pipes at different conditions.

Author	$d$ (mm)	Working fluid	$p$	$e_{\text{RMS}}$	$e_{\text{RMS}}^*$
Dukler [20]	50.8	Air-Water	1/3.9	12.11%	29.43%
Chisholm [18]	27	Air-Water	1/4	16.73%	38.21%
Govier and Omer [25]	26.06	Air-Water	1/3.9	8.03%	19.87%
Janssen and Kervinen [26]	18.85	Steam	1/2.9	2.44%	12.90%
Hashizume [27]	10	R12	1/3	8.44%	10.80%
Hashizume [27]	10	R22	1/2.8	9.12%	16.68%
Cicchitti et al. [28]	5.1	Steam	1/3.1	8.29%	9.56%
Cheremisinoff and Davis [29]	63.5	Air-Water	1/2.85	14.21%	18.51%

\* Calculated at  $p = 1/3.25$ .

gas-liquid or vapor-liquid mixtures in pipes. His theoretical development was different from previous treatments in the method of allowing for the interfacial shear force between the phases. Also, he avoided some of the anomalies occurring in previous “lumped flow.” He gave simplified equations for use in engineering design for both two-phase frictional multiplier for liquid flowing alone in the pipe ( $\phi_l^2$ ) and two-phase frictional multiplier for gas flowing alone in the pipe ( $\phi_g^2$ ) as a function of the Chisholm constant ( $C$ ) and the Lockhart-Martinelli parameter ( $X$ ). The values of  $C$  were dependent on whether the liquid and gas phases were laminar or turbulent flow. The values of  $C$  were restricted to mixtures with gas-liquid density ratios corresponding to air-water mixtures at atmospheric pressure. The different values of  $C$  are given as  $C = 20$  for turbulent-turbulent flow,  $C = 12$  for laminar liquid-turbulent gas flow,  $C = 10$  for turbulent liquid-laminar gas flow, and  $C = 5$  for laminar-laminar flow. He compared his predicted values using these values of  $C$  and his equation with the Lockhart-Martinelli values. He obtained good agreement with the Lockhart-Martinelli empirical curves.

Chisholm [22] showed that his previous equation in [21] for predicting the friction pressure drop during two-phase flow was an unsatisfactory form for use with evaporating flows as  $(dp/dz)_f$ , in that case, varied along the flow path. Therefore, he transformed his equation with sufficient accuracy for engineering purposes to an expression for two-phase frictional multiplier for total flow assumed liquid in the pipe ( $\phi_{lo}^2$ ) as a function of physical property coefficient ( $\Gamma$ ), Chisholm parameter ( $B$ ), and mass quality ( $x$ ).

Friedel [23] proposed a method in terms of the multiplier ( $\phi_{lo}^2$ ). He developed his correlation and fit it with 25000 data points. The smallest pipe diameter in the Friedel database was 4 mm. His correlation included both the gravity effect by Froude number ( $Fr$ ) and the effect of surface tension and the total mass flux by Weber number ( $We$ ). Friedel [23] proposed a method in terms of the multiplier ( $\phi_{lo}^2$ ). He developed his correlation and fit it with 25000 data points. The smallest pipe diameter in the Friedel database was 4 mm. His correlation included both the gravity effect by Froude number ( $Fr$ ), and the effect of surface tension and the total mass flux by Weber number ( $We$ ).

Müller-Steinhagen and Heck [24] suggested a new correlation for the prediction of frictional pressure drop in two-phase flow  $(dp/dz)_f$  in pipes. Their correlation had an advantage that was simple and more convenient to use than other methods. They developed an equation for the roughly linear increase of the pressure drop with increasing quality (for  $x < 0.7$ ). In order to cover the full range of flow quality ( $0 < x < 1$ ), they used the method of superposition (at  $x = 1$ ,  $(dp/dz)_f = (dp/dz)_{f,go}$ ). It was obvious that their correlation related the frictional pressure gradient in two-phase flow  $(dp/dz)_f$  to the frictional pressure gradient if the total flow assumed liquid in the pipe  $(dp/dz)_{f,lo}$ , the frictional pressure gradient if the total flow assumed gas in the pipe  $(dp/dz)_{f,go}$ , and the mass quality ( $x$ ). To determine their reliabilities, they checked their correlation and another 14 correlations against a data bank containing 9313 measurements of frictional pressure drop for different fluids, different tube diameters (between 4 and 352 mm), and different flow conditions (horizontal flow, vertical upwards flow, and vertical downwards flow). The data bank containing only measurements with the frictional pressure gradient  $(dp/dz)_f$  was greater than 20 Pa/m to avoid uncertainties due to the scatter of data.

2.2.  $\phi_l$  and  $\phi_g$  versus Lockhart-Martinelli Parameter ( $X$ ) in Circular Pipes. Figure 2 shows  $\phi_l$  versus Lockhart-Martinelli parameter ( $X$ ) for turbulent-turbulent flow for different working fluids in a smooth horizontal pipe of different diameters at different conditions using the present asymptotic model and the first six data sets in Table 3. Equation (12) represents the present model with different values of  $p$  as shown in Table 3.

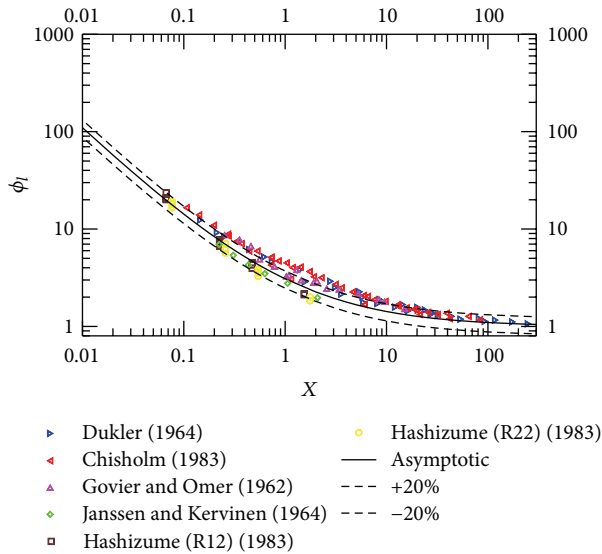
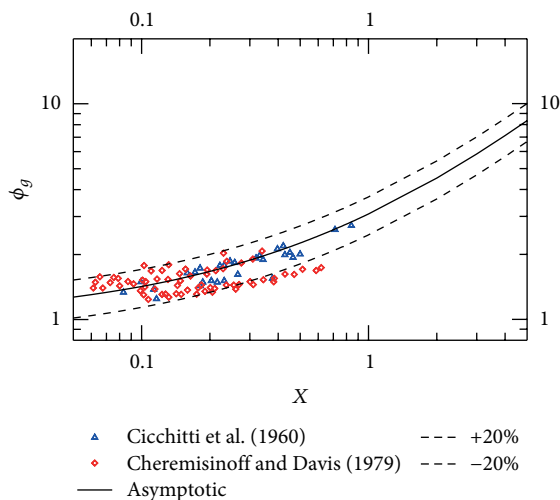
Figure 3 shows  $\phi_g$  versus Lockhart-Martinelli parameter ( $X$ ) for turbulent-turbulent flow for different working fluids in a smooth horizontal pipe of different diameters at different conditions using the present asymptotic model and the last two data sets in Table 3. Equation (14) represents the present model with different values of  $p$  as shown in Table 3.

To have a robust model, one value of the fitting parameter ( $p$ ) is chosen as  $p = 1/3.25$ . When  $p = 1/3.25$ , the root mean square (RMS) error  $e_{\text{RMS}} = 23.80\%$ . Figure 2 shows  $\phi_l$  versus  $X$  for the first six data sets in Table 4 while Figure 3

TABLE 4: Values of the asymptotic parameter ( $p$ ) in minichannels and microchannels at different conditions.

Author	$d$ (mm)	Working fluid	$p$	$e_{\text{RMS}}$	$e_{\text{RMS}}$ at $p = 1/2$
Ju Lee and Yong Lee [30]	0.78*	Air-Water	1/1.75	11.7%	14.07%
Chung and Kawaji [31]	0.1	Nitrogen-Water	1/1.7	13.44%	16.09%
Kawaji et al. [32] <sup>+</sup>	0.1	Nitrogen-Water	1/2.15	10.39%	11.34%
Kawaji et al. [32] <sup>++</sup>	0.1	Nitrogen-Water	1/2.55	11.65%	17.36%
Ohtake et al. [33]	0.32*	Argon-Water	1/1.55	19.56%	24.16%
	0.42*			16.08%**	18.24%**
	0.49*				

\*Hydraulic diameter. \*\*The two lower points are not taken into account. <sup>+</sup>Gas in the main channel and liquid in the branch. <sup>++</sup>Liquid in the main channel and gas in the branch.

FIGURE 2:  $\phi_l$  versus  $X$  for different sets of data in circular pipes.FIGURE 3:  $\phi_g$  versus  $X$  for different sets of data in circular pipes.

shows  $\phi_g$  versus  $X$  for the last two data sets in Table 3 with  $p = 1/3.25$ . It can be seen that there is a good agreement between the present asymptotic model and the different data sets in Figures 2 and 3.

2.3.  $\phi_l$  and  $\phi_g$  versus Lockhart-Martinelli Parameter ( $X$ ) in Minichannels and Microchannels. In this section, the present asymptotic model is also extended to minichannels and microchannels using the same published data sets in [34]. Figure 4 shows  $\phi_l$  versus Lockhart-Martinelli parameter ( $X$ ) for laminar-laminar flow for different working fluids in smooth minichannels and microchannels of different diameters at different conditions using the present asymptotic model and the first three data sets in Table 4. Equation (12) represents the present model with different values of  $p$  as shown in Table 4.

Figure 5 shows  $\phi_g$  versus Lockhart-Martinelli parameter ( $X$ ) for laminar-laminar flow for different working fluids in smooth minichannels and microchannels at different conditions using the present asymptotic model and the last two data sets in Table 4. Equation (14) represents the present model with different values of  $p$  as shown in Table 4.

To have a robust model, one value of the fitting parameter ( $p$ ) is chosen as  $p = 1/2$ . When  $p = 1/2$ , the root mean square (RMS) error,  $e_{\text{RMS}} = 17.14\%$  or  $15.69\%$  if the two lower points of Ohtake et al. data [33] are not taken into account. Figure 4 shows  $\phi_l$  versus  $X$  for the first three data sets in Table 4 while Figure 5 shows  $\phi_g$  versus  $X$  for the last two data sets in Table 4 with  $p = 1/2$ . It can be seen that there is a good agreement between the present asymptotic model and the different data sets in Figures 4 and 5.

### 3. Summary and Conclusions

New two-phase flow modeling is proposed, based upon an asymptotic modeling method. The main advantage of the asymptotic modeling method in two-phase flow is taking into account the important frictional interactions that occur at the interface between liquid and gas because the liquid and gas phases are assumed to flow dependently of each other in the same pipe. Also, the values of the Reynolds number for the liquid and gas phases are not important because the Churchill model [16] that spanned the entire

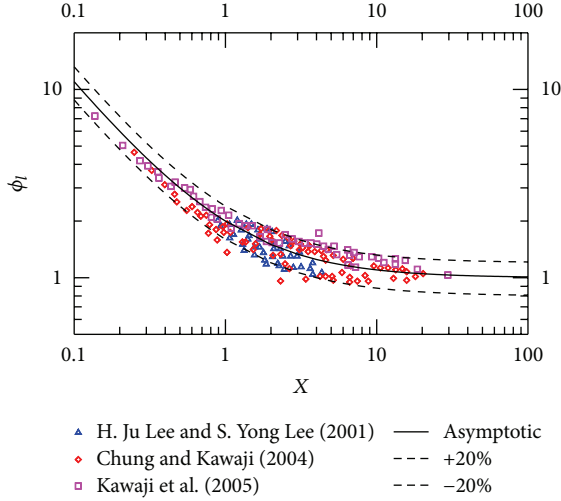


FIGURE 4:  $\phi_l$  versus  $X$  for different sets of data in minichannels and microchannels.

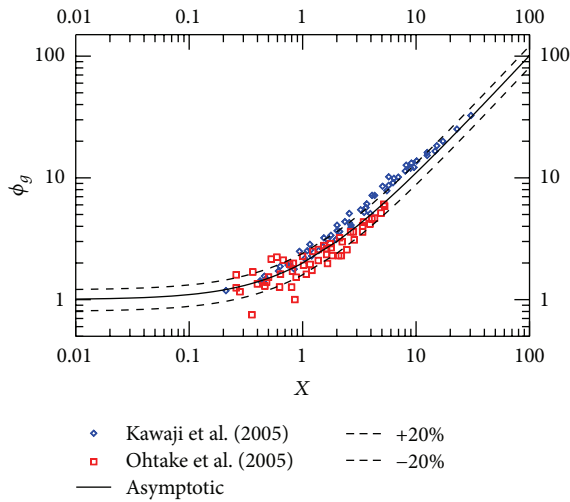


FIGURE 5:  $\phi_g$  versus  $X$  for different sets of data in minichannels and microchannels.

range of laminar, transition, and turbulent flow in pipes is introduced to define the Fanning friction factor. In addition, the obtained expressions of  $\phi_l^2$  and  $\phi_g^2$  are explicit for all flow conditions. The only unknown parameter in the asymptotic modeling method in two-phase flow is the fitting parameter ( $p$ ). The value of the fitting parameter ( $p$ ) corresponds to the minimum root mean square (RMS) error,  $e_{RMS}$ , for any data set. To have a robust model, one value of the fitting parameter ( $p$ ) is chosen as  $p = 1/3.25$  for large diameter (macroscale) and  $p = 1/2$  for small diameter (microscale). The difference between the values of  $p = 1/3.25$  for large diameter (macroscale) and  $p = 1/2$  for small diameter (microscale) can be due to the effect of diameter ( $d$ ) on  $p$ .

## Appendix

In the appendix, a generalization of the separate cylinders model of two-phase flow will be presented to include laminar liquid-turbulent gas flow and turbulent liquid-laminar gas flow that were not presented in the literature. In the separate cylinders model of two-phase flow, the liquid and gas phases are assumed to flow independently of each other in two separate parallel circular cylinders of radii  $r_{le}$  and  $r_{ge}$ , respectively. The radius of the actual pipe is  $r_o$ , and its area is the sum of the area of the separate cylinders.

The gas and liquid volumetric fractions are given as follows:

$$\alpha = \frac{A_{ge}}{A_o} = \frac{\pi r_{ge}^2}{\pi r_o^2} = \frac{r_{ge}^2}{r_o^2}, \quad (\text{A.1})$$

$$1 - \alpha = \frac{A_{le}}{A_o} = \frac{\pi r_{le}^2}{\pi r_o^2} = \frac{r_{le}^2}{r_o^2}.$$

The pressure over any cross-section of the two-phase flow is assumed to be constant so that the two-phase pressure gradient is the same for each phase. Due to this assumption, the separate cylinders model of two-phase flow is not valid for gas-liquid slug flow that gives rise to large pressure fluctuations [1]. The pressure gradients in the imagined cylinders are therefore both equal to the two-phase frictional pressure gradient in the actual pipe.

The pressure gradient in the separate cylinder of radius  $r_{ge}$  carrying the gas phase is given by

$$\left(\frac{dp}{dz}\right) = \frac{2f_{ge}}{2r_{ge}} \left[ \frac{(\pi r_o^2 G)^2 x^2 / (\pi r_{ge}^2)^2}{\rho_g} \right] = \frac{f_{ge} G^2 x^2}{\rho_g r_{ge} \alpha^2},$$

$$f_{ge} = c \text{Re}_{ge}^{-n}, \quad (\text{A.2})$$

$$\text{Re}_{ge} = \frac{(\pi r_o^2 G) x (2r_{ge}) / (\pi r_{ge}^2)}{\mu_g} = \frac{2r_{ge} G x}{\mu_g \alpha}.$$

For the gas flowing alone through the actual pipe of radius  $r_o$ , the frictional pressure gradient is given by

$$\left(\frac{dp}{dz}\right)_{f,g} = \frac{f_g G^2 x^2}{\rho_g r_o},$$

$$f_g = c \text{Re}_g^{-n}, \quad (\text{A.3})$$

$$\text{Re}_g = \frac{2r_o G x}{\mu_g}.$$

Using the assumption that the pressure gradient in the imagined cylinder of radius  $r_{ge}$  is equal to the two-phase frictional pressure gradient in the actual pipe of radius  $r_o$  and using the definition of  $\phi_g^2$ , we obtain

$$\phi_g^2 = \frac{(dp/dz)_f}{(dp/dz)_{f,g}} = \left(\frac{r_o}{r_{ge}}\right)^{5-n} = \frac{1}{\alpha^{(5-n)/2}}. \quad (\text{A.4})$$

The pressure gradient in the separate cylinder of radius  $r_{le}$  carrying the liquid phase is given by

$$\left(\frac{dp}{dz}\right) = \frac{2f_{le}}{2r_{le}} \left[ \frac{(\pi r_o^2 G)^2 (1-x)^2 / (\pi r_{le}^2)^2}{\rho_l} \right] = \frac{f_{le} G^2 (1-x)^2}{\rho_l r_{le} (1-\alpha)^2},$$

$$f_{le} = b \text{Re}_{le}^{-m},$$

$$\text{Re}_{le} = \frac{(\pi r_o^2 G) (1-x) (2r_{le}) / (\pi r_{le}^2)}{\mu_l} = \frac{2r_{le} G (1-x)}{\mu_l (1-\alpha)}. \quad (\text{A.5})$$

For the liquid flowing alone through the actual pipe of radius  $r_o$ , the frictional pressure gradient is given by

$$\left(\frac{dp}{dz}\right)_{f,l} = \frac{f_l G^2 (1-x)^2}{\rho_l r_o},$$

$$f_l = b \text{Re}_l^{-m}, \quad (\text{A.6})$$

$$\text{Re}_l = \frac{2r_o G (1-x)}{\mu_l}.$$

Using the assumption that the pressure gradient in the imagined cylinder of radius  $r_{le}$  is equal to the two-phase frictional pressure gradient in the actual pipe of radius  $r_o$  and using the definition of  $\phi_l^2$ , we obtain

$$\phi_l^2 = \frac{(dp/dz)_f}{(dp/dz)_{f,l}} = \left(\frac{r_o}{r_{le}}\right)^{5-m} = \frac{1}{(1-\alpha)^{(5-m)/2}}. \quad (\text{A.7})$$

Combining (A.4) and (A.7) to eliminate  $\alpha$ , we obtain

$$\frac{1}{\phi_l^{4/(5-m)}} + \frac{1}{\phi_g^{4/(5-n)}} = 1. \quad (\text{A.8})$$

The definition of  $X^2$  is given by

$$X^2 = \frac{(dp/dz)_{f,l}}{(dp/dz)_{f,g}} = \frac{\phi_g^2}{\phi_l^2}. \quad (\text{A.9})$$

Multiplying both sides of (A.8) by  $\phi_l^{4/(5-m)}$  and using (A.9), we obtain

$$\phi_l^2 = \left[ 1 + (\phi_l^2)^{2(m-n)/((5-m)(5-n))} \left(\frac{1}{X^2}\right)^{2/(5-n)} \right]^{(5-m)/2}. \quad (\text{A.10})$$

Multiplying both sides of (A.8) by  $\phi_g^{4/(5-n)}$  and using (A.9), we obtain

$$\phi_g^2 = \left[ 1 + (\phi_g^2)^{2(n-m)/((5-m)(5-n))} (X^2)^{2/(5-m)} \right]^{(5-n)/2}. \quad (\text{A.11})$$

## Nomenclature

$A$ :	The pipe cross-sectional area, $\text{m}^2$
$a$ :	Churchill parameter
$b$ :	Constant, Churchill parameter
$c$ :	Constant
$d$ :	Pipe diameter, m
$e$ :	Error
$f$ :	Fanning friction factor
$G$ :	Mass flux, $\text{kg}/\text{m}^2\text{-s}$
$i$ :	Exponent in asymptotic solution for $z \rightarrow 0$
$j$ :	Exponent in asymptotic solution for $z \rightarrow \infty$
$k$ :	Index for summation
$m$ :	Exponent, mass flow rate, $\text{kg}/\text{s}$
$N$ :	Number of data points
$n$ :	Exponent
$p$ :	Fitting parameter
$dp/dz$ :	Pressure gradient, $\text{Pa}/\text{m}$
$\text{Re}$ :	Reynolds number
$r_{ge}$ :	Radius of the separate circular cylinder carrying the gas phase
$r_{le}$ :	Radius of the separate circular cylinder carrying the liquid phase
$r_o$ :	Radius of the actual pipe
$X$ :	Lockhart-Martinelli parameter
$x$ :	Mass quality
$y$ :	Dependent parameter
$z$ :	Independent parameter.

## Greek Symbols

$\alpha$ :	Void fraction
$\varepsilon$ :	Pipe roughness, m
$\rho$ :	Density, $\text{kg}/\text{m}^3$
$\phi_g^2$ :	Two-phase frictional multiplier for gas alone flow
$\phi_l^2$ :	Two-phase frictional multiplier for liquid alone flow
$\mu$ :	Dynamic viscosity, $\text{kg}/\text{m}\cdot\text{s}$ .

## Subscripts

0:	Corresponding to very small value
$\infty$ :	Corresponding to very large value
$f$ :	Frictional
$g$ :	Gas
int:	Intermediate value
$l$ :	Liquid
RMS:	Root mean square.

## Conflict of Interests

The authors certify that they have no actual or potential conflict of interests including any financial, personal, or other relationships with other people or organizations within

three years of beginning the submitted work that could inappropriately influence, or be perceived to influence, their work.

## Acknowledgment

The authors acknowledge the financial support of the Natural Sciences and Engineering Research Council of Canada (NSERC) through the Discovery Grants Program.

## References

- [1] J. M. Turner, *Annular two-phase flow [Ph.D. thesis]*, Dartmouth College, Hanover, NH, USA, 1966.
- [2] G. B. Wallis, *One-Dimensional Two-Phase Flow*, McGraw-Hill Book Company, New York, NY, USA, 1969.
- [3] V. P. Carey, *Liquid-Vapor Phase-Change Phenomena : An Introduction to the Thermophysics of Vaporization and Condensation Processes in Heat Transfer Equipment*, chapter 10, Hemisphere Publishing Corporation, Washington, DC, USA, 1992.
- [4] C. E. Brennen, *Fundamentals of Multiphase Flow*, chapter 8, Cambridge University Press, Cambridge, UK, 2005.
- [5] M. M. Awad, *Two-phase flow modeling in circular pipes [Ph.D. thesis]*, Memorial University of Newfoundland, Newfoundland, Canada, 2007.
- [6] *Maple Release 9*, Waterloo Maple Software, Waterloo, Canada, 2003.
- [7] S. W. Churchill and R. Usagi, "A general expression for the correlation of rates of transfer and other phenomena," *American Institute of Chemical Engineers*, vol. 18, no. 6, pp. 1121–1128, 1972.
- [8] S. W. Churchill, *Viscous Flows: The Practical Use of Theory*, Butterworths, Boston, Mass, USA, 1988.
- [9] A. D. Kraus and A. Bar-Cohen, *Thermal Analysis and Control of Electronic Equipment*, Hemisphere Publishing Corporation, New York, NY, USA, 1983.
- [10] M. M. Yovanovich, "Asymptotes and asymptotic analysis for development of compact models for microelectronic cooling," in *Proceedings of the 19th Annual Semiconductor Thermal Measurement and Management Symposium and Exposition (SEMI-THERM '03)*, San Jose, Calif, USA, 2003.
- [11] M. M. Awad and Y. S. Muzychka, "A simple asymptotic compact model for two-phase frictional pressure gradient in horizontal pipes," in *Proceedings of the ASME International Mechanical Engineering Congress and Exposition (IMECE '04)*, paper no. IMECE2004-61410, pp. 675–685, Anaheim, Calif, USA, November 2004.
- [12] M. M. Awad and Y. S. Muzychka, "Two-phase flow modeling in microchannels and minichannels," in *Proceedings of the 6th International Conference on Nanochannels, Microchannels, and Minichannels (ICNMM '08)*, Paper no. ICNMM2008-62134, pp. 299–306, Technische Universitaet of Darmstadt, Darmstadt, Germany, June 2008.
- [13] M. M. Awad and S. D. Butt, "A robust asymptotically based modeling approach for two-phase flow in porous media," *ASME Journal of Heat Transfer*, vol. 131, no. 10, Article ID 101014, 12 pages, 2009. Also presented at ASME 27th International Conference on Offshore Mechanics and Arctic Engineering (OMAE '08), Session: Offshore Technology, Petroleum Technology II, OMAE2008-57792, Estoril, Portugal, June 2008.
- [14] M. M. Awad and S. D. Butt, "A robust asymptotically based modeling approach for two-phase liquid-liquid flow in pipes," in *Proceedings of the ASME 28th International Conference on Offshore Mechanics and Arctic Engineering (OMAE '09)*, paper no. OMAE2009-79072, pp. 409–418, Honolulu, Hawaii, USA, May–June 2009.
- [15] M. M. Awad and S. D. Butt, "A robust asymptotically based modeling approach for two-phase gas-liquid flow in fractures," in *Proceedings of the 12th International Conference on Fracture (ICF '09)*, paper no. ICF2009646Ottawa, Ottawa, Canada, July 2009.
- [16] S. W. Churchill, "Friction factor equation spans all fluid flow regimes," *Chemical Engineering*, vol. 84, no. 24, pp. 91–92, 1977.
- [17] H. Blasius, "Das ähnlichkeitsgesetz bei reibungsvorgängen in flüssigkeiten," *Forschung auf dem Gebiete des Ingenieurwesens*, vol. 131, 1913.
- [18] D. Chisholm, *Two-Phase Flow in Pipelines and Heat Exchangers*, George Godwin in Association with Institution of Chemical Engineers, London, UK, 1983.
- [19] L. F. Moody, "Friction factors for pipe flow," *Transactions of the American Society of Mechanical Engineers*, vol. 66, no. 8, pp. 671–677, 1944.
- [20] A. E. Dukler, "Pressure drop in horizontal conduits," in *Special Summer Program in Two-Phase Gas-Liquid Flow*, P. Griffith and S. W. Gouse Jr., Eds., Massachusetts Institute of Technology, Cambridge, Mass, USA, 1964.
- [21] D. Chisholm, "A theoretical basis for the Lockhart-Martinelli correlation for two-phase flow," *International Journal of Heat and Mass Transfer*, vol. 10, no. 12, pp. 1767–1778, 1967.
- [22] D. Chisholm, "Pressure gradients due to friction during the flow of evaporating two-phase mixtures in smooth tubes and channels," *International Journal of Heat and Mass Transfer*, vol. 16, no. 2, pp. 347–358, 1973.
- [23] L. Friedel, "Improved friction pressure drop correlations for horizontal and vertical two phase pipe flow," in *Proceedings of the European Two Phase Flow Group Meeting*, paper E2, Ispra, Italy, 1979.
- [24] H. Müller-Steinhagen and K. Heck, "A simple friction pressure drop correlation for two-phase flow in pipes," *Chemical Engineering and Processing*, vol. 20, no. 6, pp. 297–308, 1986.
- [25] G. W. Govier and M. M. Omer, "Horizontal pipeline flow of air-water mixtures," *The Canadian Journal of Chemical Engineering*, vol. 40, no. 3, pp. 93–104, 1962.
- [26] E. Janssen and J. A. Kervinen, "Two-phase pressure losses," Final Report GEAP-4634, General Electric Company, San Jose, Calif, USA, 1964.
- [27] K. Hashizume, "Flow pattern, void fraction and pressure drop of refrigerant two-phase flow in a horizontal pipe. I: experimental data," *International Journal of Multiphase Flow*, vol. 9, no. 4, pp. 399–410, 1983.
- [28] A. Cicchitti, C. Lombaradi, M. Silversti, G. Soldaini, and R. Zavattarlli, "Two-phase cooling experiments: pressure drop, heat transfer, and burnout measurements," *Energia Nucleare*, vol. 7, no. 6, pp. 407–425, 1960.
- [29] N. P. Cheremisinoff and E. J. Davis, "Stratified turbulent-turbulent gas-liquid flow," *AIChE Journal*, vol. 25, no. 1, pp. 48–56, 1979.
- [30] H. Ju Lee and S. Yong Lee, "Pressure drop correlations for two-phase flow within horizontal rectangular channels with small heights," *International Journal of Multiphase Flow*, vol. 27, no. 5, pp. 783–796, 2001.

- [31] P. M. Y. Chung and M. Kawaji, "The effect of channel diameter on adiabatic two-phase flow characteristics in microchannels," *International Journal of Multiphase Flow*, vol. 30, no. 7-8, pp. 735–761, 2004.
- [32] M. Kawaji, K. Mori, and D. Bolintineanu, "The effects of inlet geometry on gas-liquid two-phase flow in microchannels," in *Proceedings of the 3rd International Conference on Microchannels and Minichannels (ICMM '05)*, paper no. ICMM2005-75087, pp. 69–76, Ontario, Canada, June 2005.
- [33] H. Ohtake, Y. Koizumi, and H. Takahashi, "Frictional pressure drops of single-phase and gas-liquid two-phase flows in circular and rectangular microchannels," in *Proceedings of the 3rd International Conference on Microchannels and Minichannels (ICMM '05)*, Paper no. ICMM2005-75147, pp. 659–664, Ontario, Canada, June 2005.
- [34] M. M. Awad and Y. S. Muzychka, "Bounds on two-phase frictional pressure gradient in minichannels and microchannels," *Heat Transfer Engineering*, vol. 28, no. 8-9, pp. 720–729, 2007, Also presented at the 4th International Conference on Nanochannels, Microchannels and Minichannels (ICNMM '06), Session: Two-Phase Flow, Numerical and Analytical Modeling, ICNMM2006-96174, Stokes Research Institute, University of Limerick, Ireland, June 2006.

## Research Article

# Bounds on Two-Phase Frictional Pressure Gradient and Void Fraction in Circular Pipes

M. M. Awad<sup>1</sup> and Y. S. Muzychka<sup>2</sup>

<sup>1</sup> Mechanical Power Engineering Department, Faculty of Engineering, Mansoura University, Mansoura 35516, Egypt

<sup>2</sup> Faculty of Engineering and Applied Science, Memorial University of Newfoundland, St. John's, NL, Canada A1B 3X5

Correspondence should be addressed to M. M. Awad; [m\\_m\\_awad@mans.edu.eg](mailto:m_m_awad@mans.edu.eg)

Received 6 May 2013; Revised 10 November 2013; Accepted 10 November 2013; Published 25 February 2014

Academic Editor: Guan Heng Yeoh

Copyright © 2014 M. M. Awad and Y. S. Muzychka. This is an open access article distributed under the Creative Commons Attribution License, which permits unrestricted use, distribution, and reproduction in any medium, provided the original work is properly cited.

Simple rules are developed for obtaining rational bounds for two-phase frictional pressure gradient and void fraction in circular pipes. The bounds are based on turbulent-turbulent flow assumption. Both the lower and upper bounds for frictional pressure gradient are based on the separate cylinders formulation. For frictional pressure gradient, the lower bound is based on the separate cylinders formulation that uses the Blasius equation to represent the Fanning friction factor while the upper bound is based on the separate cylinders equation that represents well the Lockhart-Martinelli correlation for turbulent-turbulent flow. For void fraction, the lower bound is based on the separate cylinders formulation that uses the Blasius equation to predict the Fanning friction factor while the upper bound is based on the Butterworth relationship that represents well the Lockhart-Martinelli correlation. These two bounds are reversed in the case of liquid fraction ( $1 - \alpha$ ). For frictional pressure gradient, the model is verified using published experimental data of two-phase frictional pressure gradient versus mass flux at constant mass quality. The published data include different working fluids such as R-12, R-22, and Argon at different mass qualities, different pipe diameters, and different saturation temperatures. The bounds models are also presented in a dimensionless form as two-phase frictional multiplier ( $\phi_l$  and  $\phi_g$ ) versus Lockhart-Martinelli parameter ( $X$ ) for different working fluids such as R-12, R-22, and air-water and steam mixtures. For void fraction, the bounds models are verified using published experimental data of void fraction versus mass quality at constant mass flow rate. The published data include different working fluids such as steam, R-12, R-22, and R-410A at different pipe diameters, different pressures, and different mass flow rates. It is shown that the published data can be well bounded for a wide range of mass fluxes, mass qualities, pipe diameters, and saturation temperatures.

## 1. Introduction

In the present study, the lower and upper bounds for two-phase frictional pressure gradient and void fraction in circular pipes are developed. This approach is very useful in design and analysis, as engineers can then use the resulting average and bounding values in predictions of system performance. For example, comparisons of several two-phase flow models for the frictional pressure gradient [1] and the void fraction [2] show that no two models provide the same results for the frictional pressure gradient and the void fraction. Since all models were developed in conjunction with experimental data, which are prone to measurement error, it is reasonable to expect that any prediction is also subject to similar error.

The use of bounds can alleviate some of the subjectivity of the published two-phase flow models for the frictional pressure gradient and the void fraction by providing definite limits on the value of the two-phase frictional pressure gradient and the two-phase void fraction. The approach is also useful when conducting new experiments, since it provides a reasonable envelope for the data to fall within. The bounds are intended to provide the most realistic range of data not firm absolute limits. Statistically, this is unreasonable as the bounds would be far apart. The bounds are not fit to capture all data but rather a majority of data points, as some outlying points are due to experimental error. If a vast majority of data is within the bounds, then a reasonable expectation is realistically assured.

## 2. Proposed Methodology

*2.1. Development of Bounds on Two-Phase Frictional Pressure Gradient in Circular Pipes.* In this section, rational bounds for two-phase frictional pressure gradient in circular pipes will be developed. These bounds may be used to determine the maximum and minimum values that may reasonably be expected in a two-phase flow. Further, by averaging these limiting values an acceptable prediction for the pressure gradient is obtained which is then bracketed by the bounding values:

$$\left(\frac{dp}{dz}\right)_{f,lower} \leq \left(\frac{dp}{dz}\right)_f \leq \left(\frac{dp}{dz}\right)_{f,upper}. \quad (1)$$

The bounds model will be in the form of two-phase frictional pressure gradient versus mass flux at constant mass quality. The bounds model may also be presented in the form of two-phase frictional multiplier, which is often useful for calculation and comparison needs. For this reason, development of lower and upper bounds in terms of two-phase frictional multiplier ( $\phi_l$  and  $\phi_g$ ) versus the Lockhart-Martinelli parameter ( $X$ ) will also be presented.

In the present study, the bounds method is based on turbulent liquid-turbulent gas assumption [1, 2]. This assumption is suitable because, in practice, both  $Re_l$  and  $Re_g$  are most often greater than 2000 in circular pipes. On the other hand, the assumption of laminar liquid-laminar gas is suitable for the flow in minichannels and microchannels [8] because, in practice, both  $Re_l$  and  $Re_g$  are most often less than 2000 in minichannels and microchannels.

Both the lower and upper bounds are based on the separate cylinders formulation [9]. The equation of the separate cylinders model [9] is

$$\left(\frac{1}{\phi_l^2}\right)^{1/n} + \left(\frac{1}{\phi_g^2}\right)^{1/n} = 1. \quad (2)$$

The values of  $n$  were dependent on whether the liquid and gas phases were laminar or turbulent flow. The different values of  $n$  are given in Table 1. The reasons of choosing lower and upper bounds can be explained as follows.

From Table 1, it is obvious that the different values of  $n$  for turbulent-turbulent flow in separate-cylinders model can be:

- (i)  $n = 2.375$  ( $f = 0.079/Re^{0.25}$ ),
- (ii)  $n = 2.4$  ( $f = 0.046/Re^{0.2}$ ),
- (iii)  $n = 2.5$  ( $f = \text{constant}$ ),
- (iv)  $n = 3.5$  (maximum value in mixing-length analysis),
- (v)  $n = 4$  (good empirical representation of the Lockhart-Martinelli correlation [10]).

The present model is based on the minimum and maximum values of  $n$  for turbulent-turbulent flow, 2.375, and 4, respectively, from the separate-cylinders formulation [9].

Also, although the data points are in turbulent-turbulent flow, they cover different flow patterns such as stratified, wavy, slug, and annular. As the mass flow rate of the gas

TABLE 1: Values of exponent ( $n$ ) for different flow types.

Flow type	$n$
Laminar flow	2
Turbulent flows (analyzed on a basis of friction factor)	2.375–2.5
Turbulent flows (calculated on a mixing-length basis)	2.5–3.5
Turbulent-turbulent regime	4
All flow regimes	3.5

in two-phase flow increases, the flow pattern changes from stratified to wavy to slug to annular. As mentioned in the literature, the Lockhart-Martinelli correlation [10] has a good accuracy for annular flow pattern [11] but it has a poor accuracy (overprediction) for stratified and wavy flow pattern [12]. This is why it is taken as an upper bound. Further  $n = 4$  as a closure constant was arbitrarily chosen to fit the data and thus accounts for interfacial effects between phases making it an upper bound, whereas  $n = 2.375$  as a closure constant is obtained from the Blasius friction model [13] and does not account for interfacial effects and therefore represents a lower bound for the data. Faghri and Zhang [14] further commented that the advantage of the pressure drop correlations based on the separated-flow model is that they are applicable for all flow patterns. This flexibility is accompanied by low accuracy.

*2.1.1. The Lower Bound.* The lower bound is based on the separate cylinders formulation [9] that uses the Blasius equation [13] to represent the Fanning friction factor. Introducing the Lockhart-Martinelli parameter ( $X$ ) into (2), we obtain  $\phi_l^2$  and  $\phi_g^2$  for turbulent-turbulent flow ( $n = 2.375$ , Table 1), respectively, as follows:

$$\phi_l^2 = \left[1 + \left(\frac{1}{X^2}\right)^{1/2.375}\right]^{2.375}, \quad (3)$$

$$\phi_g^2 = \left[1 + (X^2)^{1/2.375}\right]^{2.375}. \quad (4)$$

For turbulent-turbulent flow, the Lockhart-Martinelli parameter ( $X$ ) can be expressed as [15]

$$X = \left(\frac{1-x}{x}\right)^{7/8} \left(\frac{\rho_g}{\rho_l}\right)^{1/2} \left(\frac{\mu_l}{\mu_g}\right)^{1/8}. \quad (5)$$

The Lockhart-Martinelli expression for the two-phase frictional multiplier ( $\phi_l^2$ ) is given by

$$\phi_l^2 = \frac{(dp/dz)_f}{(dp/dz)_{f,l}}. \quad (6)$$

The single-phase liquid frictional pressure gradient can be related to the Fanning friction factor in terms of mass flux and mass quality for liquid flowing alone as follows:

$$\left(\frac{dp}{dz}\right)_{f,l} = \frac{2f_l G^2 (1-x)^2}{d\rho_l}. \quad (7)$$

For turbulent-turbulent flow, the Fanning friction factor is defined using the Blasius equation [13] as follows:

$$f_l = \frac{0.079}{\text{Re}_l^{1/4}}. \quad (8)$$

The Reynolds number equation can be expressed in terms of mass flux and mass quality for liquid flowing alone as

$$\text{Re}_l = \frac{G(1-x)d}{\mu_l}. \quad (9)$$

Using (3) and (5)–(9), we obtain

$$\begin{aligned} \left(\frac{dp}{dz}\right)_{f,\text{lower}} &= \frac{0.158G^{1.75}(1-x)^{1.75}\mu_l^{0.25}}{d^{1.25}\rho_l} \\ &\times \left[1 + \left(\frac{x}{1-x}\right)^{0.7368} \left(\frac{\rho_l}{\rho_g}\right)^{0.4211} \left(\frac{\mu_g}{\mu_l}\right)^{0.1053}\right]^{2.375}. \end{aligned} \quad (10)$$

**2.1.2. The Upper Bound.** The upper bound is based on the separate cylinders formulation [9] that uses an equation that represents well the Lockhart-Martinelli correlation for turbulent-turbulent flow. The equation of the upper bound is similar to the lower bound case except for the definitions of  $\phi_l^2$  and  $\phi_g^2$ . Introducing the Lockhart-Martinelli parameter ( $X$ ) into (2), we obtain  $\phi_l^2$  and  $\phi_g^2$  for turbulent-turbulent flow ( $n = 4$ , Table 1), respectively, as follows:

$$\phi_l^2 = \left[1 + \left(\frac{1}{X^2}\right)^{1/4}\right]^4, \quad (11)$$

$$\phi_g^2 = \left[1 + (X^2)^{1/4}\right]^4. \quad (12)$$

Equations (11) and (12) represent well the Lockhart-Martinelli correlation [10] for turbulent-turbulent flow. Using (11) and (5)–(9), we obtain

$$\begin{aligned} \left(\frac{dp}{dz}\right)_{f,\text{upper}} &= \frac{0.158G^{1.75}(1-x)^{1.75}\mu_l^{0.25}}{d^{1.25}\rho_l} \\ &\times \left[1 + \left(\frac{x}{1-x}\right)^{0.4375} \left(\frac{\rho_l}{\rho_g}\right)^{0.25} \left(\frac{\mu_g}{\mu_l}\right)^{0.0625}\right]^4. \end{aligned} \quad (13)$$

**2.1.3. Mean Model.** A simple model may be developed by averaging the two bounds. This is defined as follows:

$$\phi_{l,\text{av}}^2 = \frac{1}{2} \left[ \left[1 + \left(\frac{1}{X^2}\right)^{1/2.375}\right]^{2.375} + \left[1 + \left(\frac{1}{X^2}\right)^{1/4}\right]^4 \right], \quad (14)$$

or

$$\begin{aligned} \phi_{g,\text{av}}^2 &= \frac{1}{2} \left[ \left[1 + (X^2)^{1/2.375}\right]^{2.375} + \left[1 + (X^2)^{1/4}\right]^4 \right], \quad (15) \\ \left(\frac{dp}{dz}\right)_{f,\text{av}} &= \frac{0.079G^{1.75}(1-x)^{1.75}\mu_l^{0.25}}{d^{1.25}\rho_l} \\ &\times \left[ \left[1 + \left(\frac{x}{1-x}\right)^{0.7368} \left(\frac{\rho_l}{\rho_g}\right)^{0.4211} \left(\frac{\mu_g}{\mu_l}\right)^{0.1053}\right]^{2.375} \right. \\ &\left. + \left[1 + \left(\frac{x}{1-x}\right)^{0.4375} \left(\frac{\rho_l}{\rho_g}\right)^{0.25} \left(\frac{\mu_g}{\mu_l}\right)^{0.0625}\right]^4 \right]. \end{aligned} \quad (16)$$

Otherwise the more accurate asymptotic model [16] should be used as follows:

$$\phi_{l,\text{asy}}^2 = \left[1 + \left(\frac{1}{X^2}\right)^{1/3.25}\right]^{3.25}, \quad (17)$$

or

$$\phi_{g,\text{asy}}^2 = \left[1 + (X^2)^{1/3.25}\right]^{3.25}, \quad (18)$$

$$\begin{aligned} \left(\frac{dp}{dz}\right)_{f,\text{asy}} &= \frac{0.158G^{1.75}(1-x)^{1.75}\mu_l^{0.25}}{d^{1.25}\rho_l} \\ &\times \left[1 + \left(\frac{x}{1-x}\right)^{0.5385} \left(\frac{\rho_l}{\rho_g}\right)^{0.3077} \left(\frac{\mu_g}{\mu_l}\right)^{0.0769}\right]^{3.25}. \end{aligned} \quad (19)$$

**2.2. Development of Bounds on Two-Phase Void Fraction in Circular Pipes.** In this section, rational bounds for two-phase void fraction in circular pipes will be developed. These bounds may be used to determine the maximum and minimum values that may reasonably be expected in a two-phase flow. Further, by averaging these limiting values an acceptable prediction for the void fraction is obtained which is then bracketed by the bounding values:

$$\alpha_{\text{lower}} \leq \alpha \leq \alpha_{\text{upper}}. \quad (20)$$

The bounds model will be in the form of two-phase void fraction against mass quality at constant mass flow rate. The bounds model may also be presented in the form of void fraction against the Lockhart-Martinelli parameter ( $X$ ).

For the case of large circular pipes, the bounds method is based on turbulent liquid-turbulent gas assumption [1, 2]. This assumption is suitable because, in practice, both  $\text{Re}_l$  and  $\text{Re}_g$  are most often greater than 2000 in large circular pipes.

**2.2.1. The Lower Bound.** The lower bound is based on the separate cylinders formulation [9] for turbulent-turbulent flow that uses the Blasius equation [13] to predict the Fanning friction factor. Using the separate cylinders analysis [9] and introducing the Blasius equation [13] to represent the Fanning friction factor for turbulent-turbulent flow,  $\alpha$  can be expressed as follows:

$$\alpha = \frac{1}{1 + X^{16/19}}. \quad (21)$$

Substituting (5) into (21), we obtain

$$\alpha = \frac{1}{1 + \left[ \left( \frac{(1-x)}{x} \right)^{7/8} (\rho_g/\rho_l)^{1/2} (\mu_l/\mu_g)^{1/8} \right]^{16/19}}. \quad (22)$$

**2.2.2. The Upper Bound.** In order to make the bounds model tight and present it in the form of void fraction ( $\alpha$ ) against the Lockhart-Martinelli parameter ( $X$ ), the Lockhart-Martinelli correlation [10] is chosen to represent the upper bound although the homogeneous model gives higher prediction of the void fraction ( $\alpha$ ) than the Lockhart-Martinelli correlation at the same mass quality ( $x$ ) except at low values of the mass quality ( $x$ ). Butterworth [17] represented the Lockhart-Martinelli correlation [10] by the relation:

$$\alpha = \frac{1}{1 + 0.28X^{0.71}}. \quad (23)$$

Substituting (5) into (23), we obtain

$$\alpha = \frac{1}{1 + 0.28 \left[ \left( \frac{(1-x)}{x} \right)^{7/8} (\rho_g/\rho_l)^{1/2} (\mu_l/\mu_g)^{1/8} \right]^{0.71}}. \quad (24)$$

Since  $(1 - \alpha)$  represents the liquid fraction, the lower and upper bounds are reversed in the case of liquid fraction data.

**2.2.3. Mean Model.** A simple model may be developed by averaging the two bounds. This is defined as follows:

$$\alpha_{av} = \frac{0.5}{1 + X^{16/19}} + \frac{0.5}{1 + 0.28X^{0.71}}, \quad (25)$$

or

$$\begin{aligned} \alpha_{av} &= \frac{0.5}{1 + \left[ \left( \frac{(1-x)}{x} \right)^{7/8} (\rho_g/\rho_l)^{1/2} (\mu_l/\mu_g)^{1/8} \right]^{16/19}} \\ &+ \frac{0.5}{1 + 0.28 \left[ \left( \frac{(1-x)}{x} \right)^{7/8} (\rho_g/\rho_l)^{1/2} (\mu_l/\mu_g)^{1/8} \right]^{0.71}}. \end{aligned} \quad (26)$$

### 3. Results and Discussion

For frictional pressure gradient, examples of two-phase frictional pressure gradient versus mass flux at constant mass

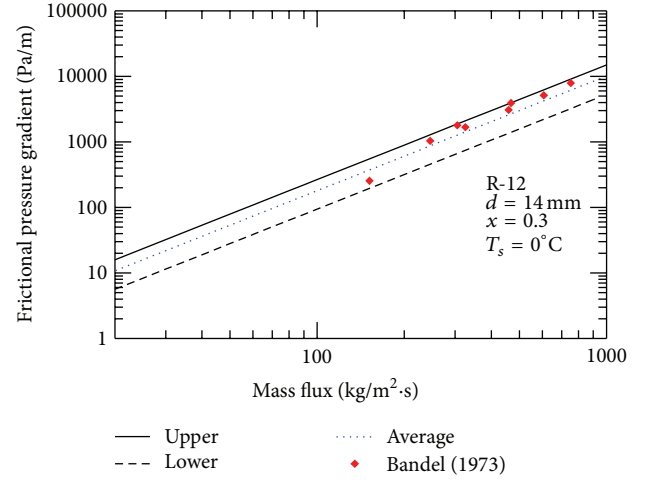


FIGURE 1: Comparison of the present model with Bandel's data [3].

quality from published experimental studies are presented to show the advantages of the bounds models. The published data include different working fluids such as R-12, R-22, and Argon at different mass qualities with different pipe diameters. Also, examples of two-phase frictional multiplier ( $\phi_l$  and  $\phi_g$ ) versus Lockhart-Martinelli parameter ( $X$ ) using published data of different working fluids such as R-12, R-22, and air-water and steam from other experimental work are presented to validate the bounds model in dimensionless form.

For void fraction, examples of two-phase void fraction versus mass quality at constant mass flow rate from published experimental studies are presented to show features of the bounds. The published data include different working fluids such as steam, R-12, R-22, and R-410A at different pipe diameters, different pressures, and different mass flow rates. Also, the model is verified using published experimental data of void fraction ( $\alpha$ ) and liquid fraction ( $1 - \alpha$ ) versus the Lockhart-Martinelli parameter ( $X$ ) for different working fluids such as R-12, R-22, and air-water mixtures in turbulent-turbulent flow.

**3.1. Two-Phase Frictional Pressure Gradient.** Figures 1–4 show the frictional pressure gradient versus mass flux in turbulent-turbulent flow. Equation (10) represents the lower bound and (13) represents the upper bound, while (16) represents the average. Figure 1 compares the present approach with Bandel's data [3] for R-12 flow at  $x = 0.3$  and  $T_s = 0^\circ\text{C}$  in a smooth horizontal pipe at  $d = 14$  mm. Figure 2 compares the present approach with Hashizume's data [4] for R-12 flow at  $x = 0.8$  and  $T_s = 50^\circ\text{C}$  in a smooth horizontal pipe at  $d = 10$  mm. Figure 3 compares the present approach with Hashizume's data [4] for R-22 flow at  $x = 0.8$  and  $T_s = 39^\circ\text{C}$  in a smooth horizontal pipe at  $d = 10$  mm. Figure 4 compares the present approach with Müller-Steinhagen's data [5] for Argon flow at  $x = 0.4$  and reduced pressure of 0.188 in a smooth horizontal pipe at  $d = 14$  mm. From Figures 1–4, it can be seen that the published data can be well bounded.

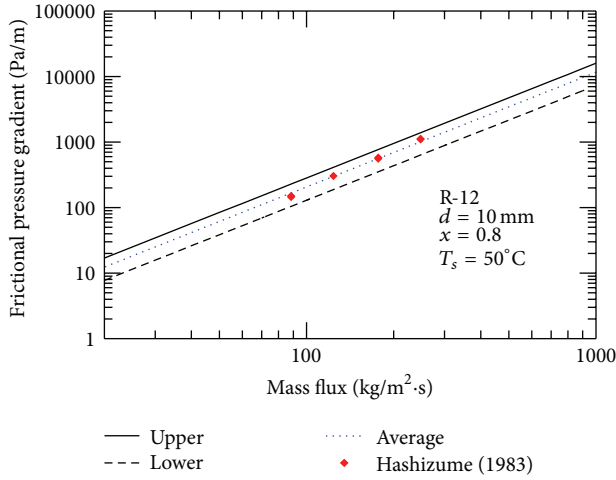


FIGURE 2: Comparison of the present model with Hashizume's data [4].

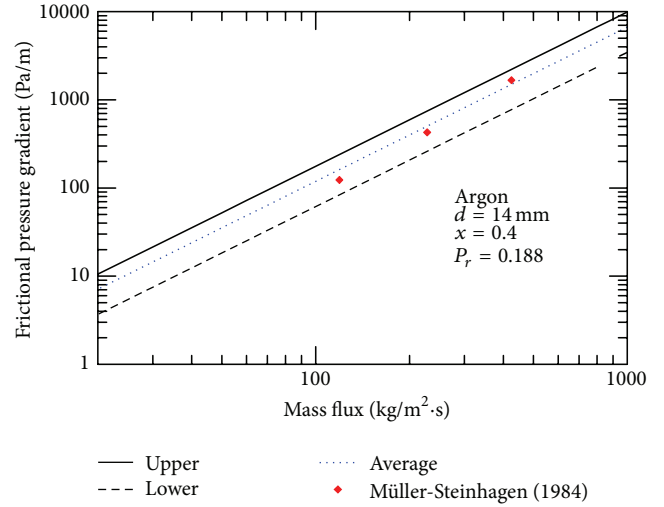


FIGURE 4: Comparison of the model with Müller-Steinhagen's data [5].

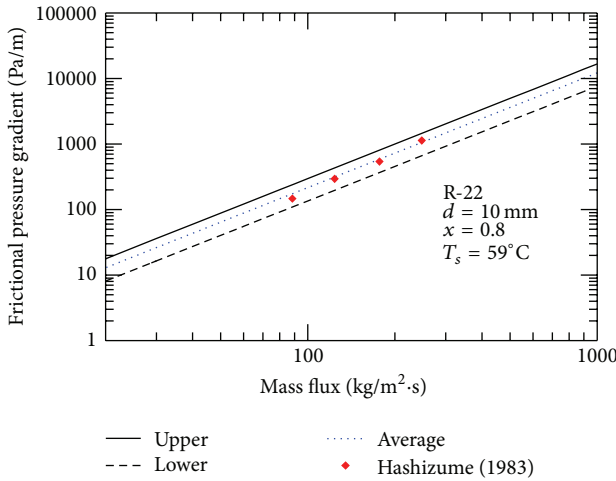


FIGURE 3: Comparison of the present model with Hashizume's data [4].

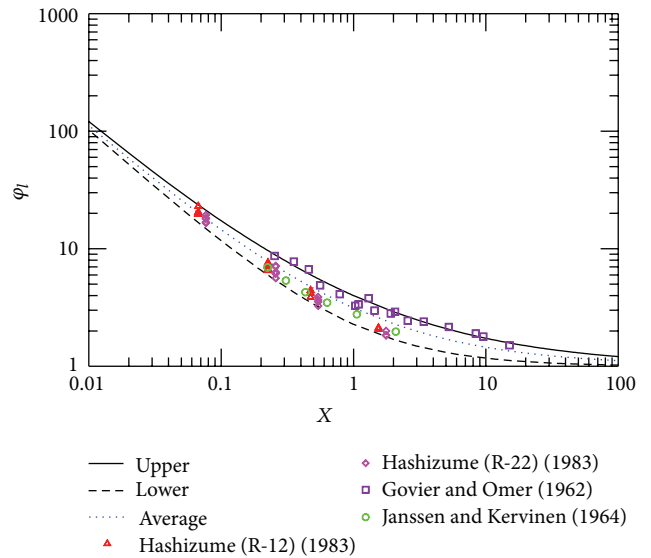


FIGURE 5:  $\phi_l$  versus  $X$  for different sets of data.

In Figures 1–4, the mean model predicts the published data with the root mean square (RMS) error of 26.41%, 8.62%, 11.23%, and 21.42%, respectively, while the asymptotic model, (19), gives the root mean square (RMS) error of 29.67%, 10.65%, 8.34%, and 15.75%, respectively. From Figures 1–4, it can be seen that the bounds on two-phase frictional pressure gradient in circular pipes are good indicators in experiments for establishing the validity of test results and other physical issues.

3.2.  $\phi_l$  and  $\phi_g$  versus Lockhart-Martinelli Parameter ( $X$ ). Figure 5 shows  $\phi_l$  versus Lockhart-Martinelli parameter ( $X$ ) for turbulent-turbulent flow. Equation (3) represents the lower bound and (11) represents the upper bound, while (14) represents the average. Figure 5 compares the present model with the data sets of Hashizume's data [4] for R-12 flow in a smooth horizontal pipe of  $d = 10$  mm at  $T_s = 20^\circ\text{C}$

and  $x = 0.1, 0.3, 0.5,$  and  $0.8$ , Hashizume's data [4] for R-22 flow in a smooth horizontal pipe of  $d = 10$  mm at  $T_s = 20^\circ\text{C}$  and  $x = 0.1, 0.3, 0.5,$  and  $0.8$ , Govier and Omer's data [18] for air-water mixtures in a smooth horizontal pipe of 1.026 in (26.06 mm) diameter, and Janssen and Kervinen's data [19] for steam-water flow in a smooth horizontal pipe at a pressure of 1066 psia (73.5 bar) and  $d = 0.742$  in (18.85 mm) for  $G = 1.68 \times 10^6$  lb<sub>m</sub>/ft<sup>2</sup> · hr (2278 kg/m<sup>2</sup> · s). The mean model predicts the published data of  $\phi_l$  with the root mean square (RMS) error of 14.41%, 21.47%, 16.19%, and 18.7%, respectively, while the asymptotic model, (17), gives the root mean square (RMS) error of 10.8%, 16.68%, 19.87%, and 12.9%, respectively. From Figure 5, it is clear that the bounds contain a vast majority of the data.

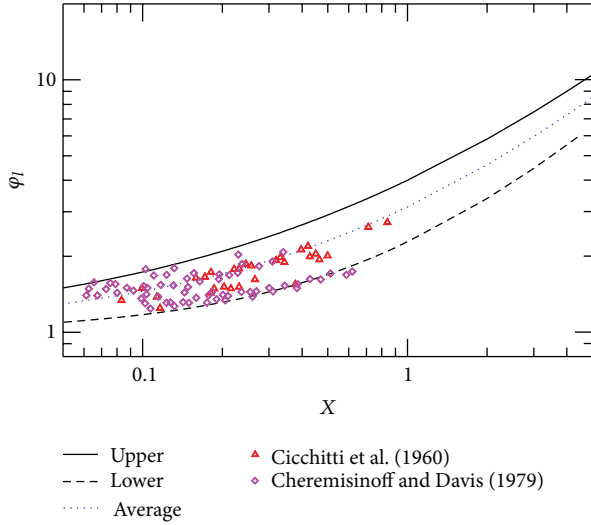


FIGURE 6:  $\phi_g$  versus  $X$  for different sets of data.

Figure 6 shows  $\phi_g$  versus Lockhart-Martinelli parameter ( $X$ ) for turbulent-turbulent flow. Equation (4) represents the lower bound and (12) represents the upper bound, while (15) represents the average. Figure 6 compares the present model with the data sets of Cicchitti et al.'s data [20] for adiabatic flow of steam in a smooth pipe of 5.1 mm diameter at a pressure of 30–60 kg/cm<sup>2</sup> (29.4–58.8) bar and Chermisinoff and Davis's [21] for stratified flow of air-water mixtures in a smooth horizontal pipe of 63.5 mm diameter. Cicchitti et al. [20] mentioned that their steam data for turbulent-turbulent flow ( $\phi_g$  versus  $X$ ) fall in the strip bounded by the Martinelli and Nelson lines [22] drawn up for atmospheric and critical pressures. The advantages of the present bound models over the Martinelli and Nelson lines [22] at atmospheric and critical pressures are as follows.

- (i) The Martinelli and Nelson lines [22] at atmospheric and critical pressures were presented in a graphical manner while the present bound models are presented in the form of simple equations.
- (ii) The Martinelli and Nelson lines [22] at atmospheric and critical pressures can be used only when steam is the working fluid while the present bound models can be used for different working fluids as in Figure 6.

The mean model predicts the published data of  $\phi_g$  with the root mean square (RMS) error of 12.84% and 22.03%, respectively, while the asymptotic model, (18), gives the root mean square (RMS) error of 9.56% and 18.51%, respectively. From Figure 6, It is clear that the bounds contain a vast majority of the data.

**3.3. Two-Phase Void Fraction.** Figures 7–10 show the void fraction versus mass quality. Equation (22) represents the lower bound and (24) represents the upper bound while (26) represents the average. Figure 7 compares the present model with Larson's data [6] for adiabatic flow of steam-water mixture at  $p_s = 1000$  psia (6 894.74 kPa). Figure 8 compares

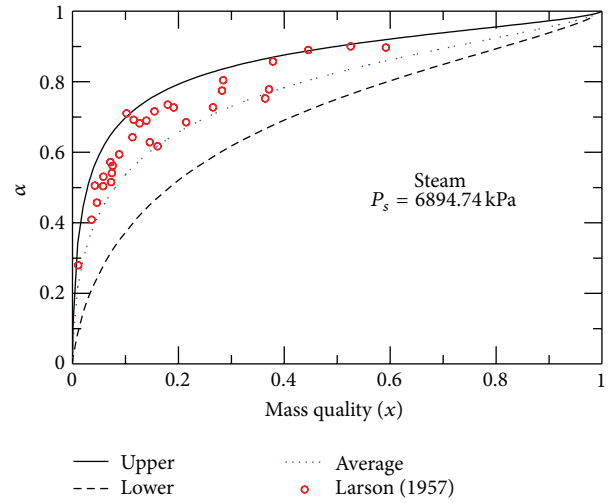


FIGURE 7: Comparison of the present model with Larson's data [6].

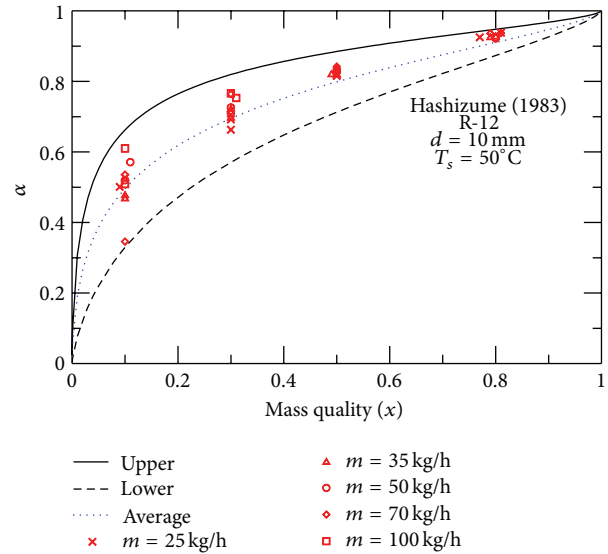


FIGURE 8: Comparison of the present model with Hashizume's data [4].

the present model with Hashizume's data [4] for R-12 flow at  $T_s = 50^\circ\text{C}$  and  $m = 25, 35, 50, 70,$  and  $100$  kg/hr, respectively, in a smooth horizontal pipe at  $d = 10$  mm. Figure 9 compares the present model with Hashizume's data [4] for R-22 flow at  $T_s = 39^\circ\text{C}$  and  $m = 25, 35, 50, 70,$  and  $100$  kg/hr, respectively, in a smooth horizontal pipe at  $d = 10$  mm. Figure 10 compares the present model with Wojtan et al.'s data [7] R-410A flow at  $T_s = 5^\circ\text{C}$  and  $G = 70, 150, 200,$  and  $300$  kg/m<sup>2</sup>·s, respectively, in a smooth horizontal pipe at  $d = 5/8$  in. (15.875 mm). In Figures 7–10, the mean model predicts the published data of  $\alpha$  with the root mean square (RMS) error of 12.17%, 9.04%, 7.39%, and 26.86%, respectively. In Figure 10, if the two lower points at  $G = 70$  kg/m<sup>2</sup>·s are not included, RMS will be 10.6% instead of 26.86%. From Figures 7–10, it can be seen that the bounds on two-phase void fraction in circular pipes are good indicators in experiments for establishing the validity of test results and other physical issues.

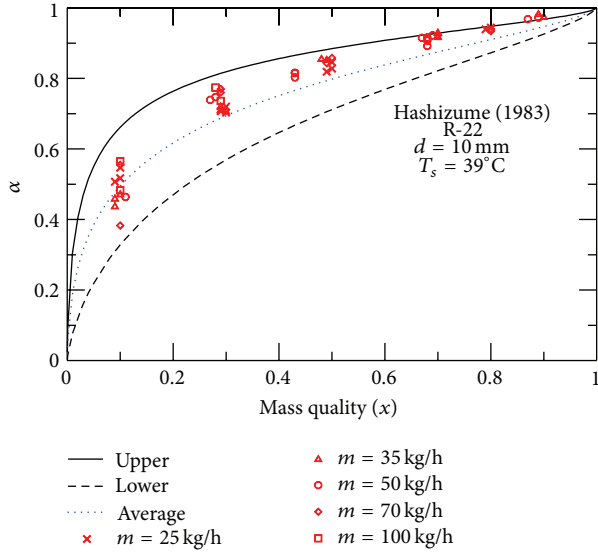


FIGURE 9: Comparison of the present model with Hashizume's data [4].

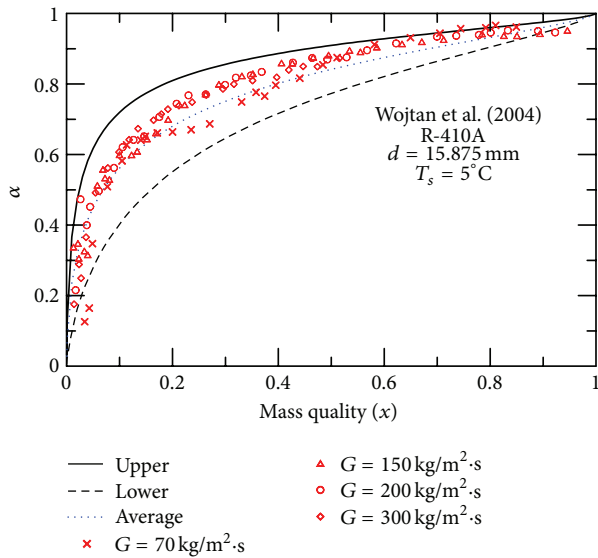


FIGURE 10: Comparison of the present model with Wojtan et al's data [7].

3.4.  $\alpha$  and  $(1-\alpha)$  versus Lockhart-Martinelli Parameter ( $X$ ). Figure 11 shows  $\alpha$  versus Lockhart-Martinelli parameter ( $X$ ) for turbulent-turbulent flow. Equation (21) represents the lower bound and (23) represents the upper bound, while (25) represents the average. Figure 11 compares the present model with the data sets of Hashizume's data [4] for R-12 flow in a smooth horizontal pipe of  $d = 10 \text{ mm}$  at  $T_s = 39^\circ \text{C}$  and  $x = 0.1, 0.3, 0.5$  and  $0.8$ , and Hashizume's data [4] for R-22 flow in a smooth horizontal pipe of  $d = 10 \text{ mm}$  at  $T_s = 50^\circ \text{C}$  and  $x = 0.1, 0.3, 0.5$ , and  $0.8$ . The mean model predicts the published data of  $\alpha$  with the root mean square (RMS) error of 9.21% and 5.78%, respectively.

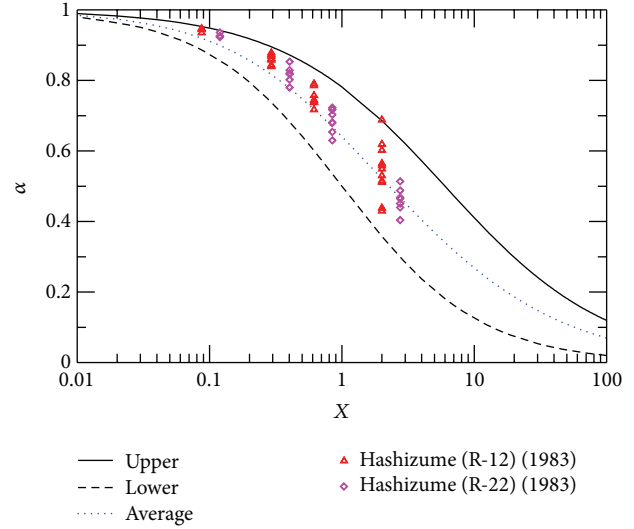


FIGURE 11:  $\alpha$  versus  $X$  for different sets of data.

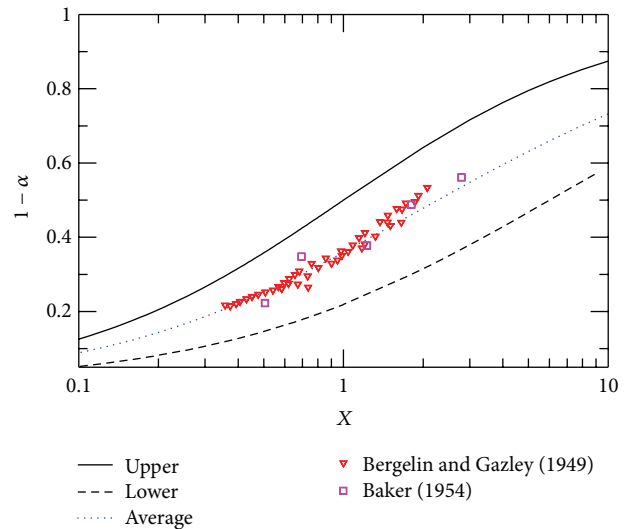


FIGURE 12:  $1 - \alpha$  versus  $X$  for different sets of data.

Figure 12 shows  $1 - \alpha$  versus Lockhart-Martinelli parameter ( $X$ ) for turbulent-turbulent flow. The lower bound is based on the Butterworth relation [17] for liquid fraction ( $1 - \alpha$ ). The upper bound is based on separate cylinders model [9] for liquid fraction ( $1 - \alpha$ ) for turbulent-turbulent flow. The average is based on the arithmetic mean of lower bound and upper bound for liquid fraction ( $1 - \alpha$ ). Figure 12 compares the present model with the data sets of Bergelin and Gazeley's data [23] for air-water flow in a smooth horizontal pipe at  $m_f = 650, 1070, 1420, 1830$ , and  $2275 \text{ lb}_m/\text{hr}$  (294.84, 485.352, 644.112, 830.088, and  $1031.94 \text{ kg/hr}$ ), and Baker's data [24] for simultaneous flow of oil and gas in pipelines of  $d = 8$ , and  $10 \text{ in.}$  (203.2 and  $254 \text{ mm}$ ), respectively. The mean model predicts the published data of  $(1 - \alpha)$  with the root mean square (RMS) error of 4.99% and 9.44%, respectively.

## 4. Summary and Conclusions

Simple expressions are developed for obtaining bounds for two-phase frictional pressure gradient and void fraction in circular pipes. The bounds approach is very useful in design and analysis, as engineers can then use the resulting average using the mean model and bounding values using the lower bound and the upper bound, respectively, in predictions of system performance. Also, the bounds approach is useful when conducting new experiments, since it provides a reasonable envelope for the data to fall within. The bounds are based on turbulent-turbulent flow assumption. Both the lower and upper bounds are based on the separate cylinders formulation. For frictional pressure gradient, the lower bound is based on the separate cylinders formulation that uses the Blasius equation to represent the Fanning friction factor while the upper bound is based on the separate cylinders equation that represents well the Lockhart-Martinelli correlation for turbulent-turbulent flow. For void fraction, the lower bound is based on the separate cylinders formulation that uses the Blasius equation to predict the Fanning friction factor while the upper bound is based on the Butterworth relationship that represents well the Lockhart-Martinelli correlation. These two bounds are reversed in the case of liquid fraction ( $1 - \alpha$ ). The mean model is based on the arithmetic mean of lower bound and upper bound. For frictional pressure gradient, the model is verified using published experimental data of two-phase frictional pressure gradient versus mass flux at constant mass quality. The published data include different working fluids such as R-12, R-22 and Argon at different mass qualities, different pipe diameters, and different saturation temperatures. The bounds models are also presented in a dimensionless form as two-phase frictional multiplier ( $\phi_l$  and  $\phi_g$ ) versus Lockhart-Martinelli parameter ( $X$ ) for different working fluids such as R-12, R-22, air-water and steam mixtures. For void fraction, the bounds models are verified using published experimental data of void fraction versus mass quality at constant mass flow rate. The published data include different working fluids such as steam, R-12, R-22, and R-410A at different pipe diameters, different pressures, and different mass flow rates. It is shown that the published data can be well bounded for a wide range of mass fluxes, mass qualities, pipe diameters, and saturation temperatures. The following conclusions can be drawn based upon the present study.

First, the present model is very successful in bounding the two-phase frictional pressure gradient and void fraction well for different working fluids over a wide range of mass fluxes, mass qualities, pipe diameters, and saturation temperatures.

Second, the present model is very successful in bounding two-phase frictional multiplier ( $\phi_l$  and  $\phi_g$ ), void fraction ( $\alpha$ ), and liquid void fraction ( $1 - \alpha$ ) versus Lockhart-Martinelli parameter ( $X$ ) well for different working fluids.

Third, the mean model provides a simple and acceptable means of predicting two-phase flow parameters.

## Nomenclature

$d$ :	Pipe diameter, m
$f$ :	Fanning friction factor
$G$ :	Mass flux, $\text{kg/m}\cdot\text{s}^2$
$m$ :	Mass flow rate, $\text{kg/s}$
$dp/dz$ :	Pressure gradient, $\text{Pa/m}$
Re:	Reynolds number
$X$ :	Lockhart-Martinelli parameter
$x$ :	Mass quality.

### Greek Symbols

$\alpha$ :	Void fraction
$\rho$ :	Density, $\text{kg/m}^3$
$\phi_g^2$ :	Two-phase frictional multiplier for gas alone flow
$\phi_l^2$ :	Two-phase frictional multiplier for liquid alone flow
$\mu$ :	Dynamic viscosity, $\text{kg/m}\cdot\text{s}$ .

### Subscripts

asy:	Asymptotic
av:	Average
$f$ :	Frictional
$g$ :	Gas
$l$ :	Liquid
lower:	Lower bound
$s$ :	Saturation
upper:	Upper bound.

## Conflict of Interests

The authors certify that they have no actual or potential conflict of interests including any financial, personal, or other relationships with other people or organizations within three years of beginning the submitted work that could inappropriately influence, or be perceived to influence, their work.

## Acknowledgment

The authors acknowledge the financial support of the Natural Sciences and Engineering Research Council of Canada (NSERC) through the Discovery Grants Program.

## References

- [1] M. M. Awad and Y. S. Muzychka, "Bounds on two-phase flow. Part I. Frictional pressure gradient in circular pipes," in *Proceedings of the IMECE, FED-11 B Numerical Simulations and Theoretical Developments for Multiphase Flows-I*, 81493, Orlando, Fla, USA, 2005.
- [2] M. M. Awad and Y. S. Muzychka, "Bounds on two-phase flow. Part II. Void fraction in circular pipes," in *Proceedings of the IMECE, FED-11 B Numerical Simulations and Theoretical Developments for Multiphase Flows-I*, 81543, Orlando, Fla, USA, 2005.

- [3] J. Bandel, *Druckverlust und wärmeübergang bei der verdampfung siedender kältemittel im durchströmten waagerechten rohr* [Ph.D. dissertation], Universität Karlsruhe, 1973.
- [4] K. Hashizume, "Flow pattern, void fraction and pressure drop of refrigerant two-phase flow in a horizontal pipe-I. Experimental data," *International Journal of Multiphase Flow*, vol. 9, no. 4, pp. 399–410, 1983.
- [5] H. Müller-Steinhagen, "Wärmeübergang und fouling beim strömungssieden von argon und stickstoff im horizontalen rohr," *Forschung im Ingenieurwesen A*, vol. 50, no. 3, p. 90, 1984.
- [6] H. C. Larson, *Void fraction of two-phase steam-water mixture* [M.S. thesis], University of Minnesota, 1957.
- [7] L. Wojtan, T. Ursenbacher, and J. R. Thome, "Interfacial measurements in stratified types of flow—part II: measurements for R-22 and R-410A," *International Journal of Multiphase Flow*, vol. 30, no. 2, pp. 125–137, 2004.
- [8] M. M. Awad and Y. S. Muzychka, "Bounds on two-phase frictional pressure gradient in minichannels and microchannels," *Heat Transfer Engineering*, vol. 28, no. 8-9, pp. 720–729, 2007, Also presented at the 4th International Conference on Nanochannels, Microchannels and Minichannels (ICNMM '06), Session: Two-Phase Flow, Numerical and Analytical Modeling, ICNMM2006-96174, Stokes Research Institute, University of Limerick, Limerick, Ireland.
- [9] J. M. Turner, *Annular two-phase flow* [Ph.D. thesis], Dartmouth College, Hanover, Germany, 1966.
- [10] R. W. Lockhart and R. C. Martinelli, "Proposed correlation of data for isothermal two-phase, two-component flow in pipes," *Chemical Engineering Progress Symposium Series*, vol. 45, no. 1, pp. 39–48, 1949.
- [11] J. G. Collier and J. R. Thome, *Convective Boiling and Condensation*, Clarendon Press, Oxford, UK, 3rd edition, 1994.
- [12] T. Johannessen, "A theoretical solution of the Lockhart and Martinelli flow model for calculating two-phase flow pressure drop and hold-up," *International Journal of Heat and Mass Transfer*, vol. 15, no. 8, pp. 1443–1449, 1972.
- [13] H. Blasius, "Das ähnlichkeitsgesetz bei reibungsvorgängen in flüssigkeiten," *Forschung auf dem Gebiete des Ingenieurwesens*, vol. 131, 1913.
- [14] A. Faghri and Y. Zhang, *Transport Phenomena in Multiphase Systems*, chapter 11, Elsevier, 2006.
- [15] A. L. de Souza and M. D. M. Pimenta, "Prediction of pressure drop during horizontal two-phase flow of pure and mixed refrigerants," in *Proceedings of the ASME/JSME Fluids Engineering and Laser Anemometry Conference and Exhibition*, vol. 210, pp. 161–171, August 1995.
- [16] M. M. Awad, *Two-phase flow modeling in circular pipes* [Ph.D. thesis], Memorial University of Newfoundland, Newfoundland, Island, 2007.
- [17] D. Butterworth, "A comparison of some void-fraction relationships for co-current gas-liquid flow," *International Journal of Multiphase Flow*, vol. 1, no. 6, pp. 845–850, 1975.
- [18] G. W. Govier and M. M. Omer, "Horizontal pipeline flow of air-water mixtures," *The Canadian Journal of Chemical Engineering*, vol. 40, no. 3, pp. 93–104, 1962.
- [19] E. Janssen and J. A. Kervinen, "Two-phase pressure losses," Final Report GEAP-4634, General Electric Company, San Jose, Calif, USA, 1964.
- [20] A. Cicchitti, C. Lombaradi, M. Silversti, G. Soldaini, and R. Zavattarlli, "Two-phase cooling experiments- pressure drop, heat transfer, and burnout measurements," *Energia Nucleare*, vol. 7, no. 6, pp. 407–425, 1960.
- [21] N. P. Cheremisinoff and E. J. Davis, "Stratified turbulent-turbulent gas-liquid flow," *AIChE Journal*, vol. 25, no. 1, pp. 48–56, 1979.
- [22] R. C. Martinelli and D. B. Nelson, "Prediction of pressure drop during forced-circulation boiling of water," *Transactions of the ASME*, vol. 70, no. 6, pp. 695–702, 1948.
- [23] O. P. Bergelin and C. Jr. Gazeley, "Cocurrent gas-liquid flow. I. Flow in horizontal tubes," in *Proceedings of the ASME Heat Transfer and Fluid Mechanics Institute*, pp. 5–18, New York, NY, USA, 1949.
- [24] O. Baker, "Simultaneous flow of oil and gas," *Oil & Gas Journal*, vol. 53, pp. 185–195, 1954.

## Research Article

# Heat Transfer Coefficient during Evaporation of R-1234yf, R-134a, and R-22 in Horizontal Circular Small Tubes

Kwang-Il Choi,<sup>1</sup> Nguyen-Ba Chien,<sup>2</sup> and Jong-Taek Oh<sup>1</sup>

<sup>1</sup> Department of Refrigeration and Air Conditioning Engineering, Chonnam National University, San 96-1, Dunduk-Dong, Yeosu, Chonnam 550-749, Republic of Korea

<sup>2</sup> Graduate School, Department of Refrigeration and Air Conditioning Engineering, Chonnam National University, San 96-1, Dunduk-Dong, Yeosu, Chonnam 550-749, Republic of Korea

Correspondence should be addressed to Jong-Taek Oh; ohjt@chonnam.ac.kr

Received 24 April 2013; Accepted 26 August 2013

Academic Editor: Guan Heng Yeoh

Copyright © 2013 Kwang-Il Choi et al. This is an open access article distributed under the Creative Commons Attribution License, which permits unrestricted use, distribution, and reproduction in any medium, provided the original work is properly cited.

Experimental data of heat transfer coefficient during evaporation of R-1234yf, R-134a, and R-22 in horizontal circular small tubes are compared. The local heat transfer coefficient is obtained for heat fluxes ranging from 10 to 35 kW m<sup>-2</sup>, mass fluxes ranging from 100 to 650 kg m<sup>-2</sup> s<sup>-1</sup>, saturation temperatures of 5, 10, and 15°C, and quality up to 1.0. The test sections are made of stainless steel tubes with inner diameters of 1.5 and 3.0 mm, the lengths of 1000 and 2000. Effects of heat flux, inner tube diameter, and saturation temperature on heat transfer coefficient are reported in the present study. Nucleate boiling heat transfer contribution is predominant, especially at low quality region, and laminar flow appears in the evaporative small tubes. The experimental results are compared against four existing heat transfer coefficients, and the modified correlation of heat transfer coefficient is developed with good prediction.

## 1. Introduction

Environmental protection is one of the most important reasons that make human develop the sustainable technologies. In the refrigeration and air-conditioning fields, besides studying the renewable and saving energy systems, developing the environmentally friendly refrigerants is a grand mission. The roadmap of phasing out HCFCs such as R-22 has been outlined under the Montreal Protocol. Controlling the greenhouse gases was proposed through the Kyoto Protocol (1997). Recently, EU regulation [1] banned the refrigerants having global warming potential (GWP) greater than 150 in new mobile air conditioners (MACs) from 2011 and all models from 2017 in the EU market. R-134a that was widely used before the need to be replaced due to its GWP is equal 1430. Review by Calm [2] showed that refrigerants are going to the fourth generation in the demands of zero/low Ozone depletion potential (ODP), low GWP, short atmospheric lifetime, and high efficiency. Natural refrigerants such as CO<sub>2</sub>, NH<sub>3</sub> are considered to be the promising candidates. The other one, R-1234yf developed by Honeywell and DuPont is also

paid a considerable attention. The thermodynamic properties of R-1234yf are similar to the ones of R-134a, while its GWP is only 4. Hence, it meets the standard of EU regulation as well as the fact that the manufacture can minimize the change of equipment when replacing R-134a by R-1234yf.

To date, numerous studies about the heat transfer characteristics and performance of R-1234yf have been published. Park and Jung [3] investigated the nucleate boiling heat transfer coefficients (HTCs) of R-134a and R-1234yf on a flat plain and low fin surfaces. The experimental data were measured at the liquid pool temperature of 7°C and the heat fluxes from 10 kW m<sup>-2</sup> to 200 kW m<sup>-2</sup>. The test results showed that the nucleate boiling HTCs of R-1234yf were similar those of R-134a. Saitoh et al. [4] performed the boiling heat transfer coefficient of R-1234yf inside a smooth small horizontal tube of 2.0 mm internal diameter. The data were measured at the heat fluxes of 6–24 kW m<sup>-2</sup>, mass fluxes of 100–400 kg m<sup>-2</sup> s<sup>-1</sup>, an evaporating of 288.15 K and the inlet vapor quality of 0–0.25. He reasoned that the effect of heat flux on the heat transfer coefficient was large at low vapor quality, while the outcome of mass flux was

large at higher vapor quality. The heat transfer coefficient of R-1234yf was almost the same as that of R-134a. He also compared the experimental HTC with his correlation proposed in previous study, and the predicted results agreed well with the experimental ones. Lee and Jung [5] reviewed the performance of R-134a and R-1234yf in a bench tester for automobile applications. His experimental results showed that the coefficient of performance and capacity of R-1234yf are up to 2.7% and 40% lower than those of R-134a, respectively. The compressor discharge temperature and amount of charge of R-1234yf are 6.5°C and 10% lower than those of R-134a. He concluded that R-1234yf can be used as a long-term environmentally friendly solution in MACs. del Col et al. [6] reported the flow boiling of R-1234yf in a 1 mm diameter channel. This study showed that HTCs of R-1234yf is highly dependent on the heat flux while the mass velocity have no effect. With regard to the vapor quality, the HTCs decreased with the vapor quality up to 0.3, then it remained pretty constant. However, the published data in open library are still limited.

The aim of this study is to determine the HTCs during evaporation of R-1234yf in horizontal circular small tubes. R-22 and R-134a, although, will be phased out in the near future, but they are still being applied in many applications nowadays, especially in developing countries. Hence, this study also discussed their HTCs based on our previous experimental data. In addition, due to the limited of heat transfer coefficient correlation for R-1234yf in minichannel have been proposed, the modified correlations are developed with the good accuracy that can be improved the calculation on designing the compact heat exchangers using this new refrigerant.

## 2. Experimental Apparatus and Method

**2.1. Experimental Test Facility.** The experimental apparatus was comprised of a refrigerant loop, three water loops, and a data acquisition system. Figure 1 shows a schematic diagram of the refrigerant loop. The refrigerant flow system consists of a condensing unit, receiver, refrigerant pump, mass flow meter, and preheater. Vapor phase refrigerant from the evaporative test section was condensed into the liquid phase in the condensing unit. The condensed refrigerant was then supplied to the receiver. The refrigerant was pumped by the refrigerant pump, which is connected to an electric motor controller used to control the flow rate of the refrigerant. The Coriolis-type mass flow meter was used to measure the refrigerant flow rate. The vapor quality at the inlet of the test section was controlled using a preheater. Temperatures of condenser, sub-cooler, and preheater were adjusted by three individual water loops.

**2.2. Test Section.** The test sections were made of circular stainless steel smooth tubes with inner diameters of 1.5 and 3.0 mm. The heated lengths were 1000 and 2000 mm in the horizontal orientation. For evaporation, power was conducted from an electric transformer to the test section. The input electric voltage and current could be adjusted to

TABLE 1: Summary of the estimated uncertainty.

Parameter	Uncertainty
$T_{wi}$ (°C)	±0.1 to ±0.35
$P$ (kPa)	±2.5
$G$ (%)	±1.85 to ±9.78
$q$ (%)	±1.67 to ±3.58
$x$ (%)	±1.79 to ±9.82
$h$ (%)	±0.03 to ±27.6

TABLE 2: Experimental conditions.

Test section	Horizontal stainless-steel circular smooth small tube
Quality	Up to 1.0
Working refrigerant	R-1234yf, R-22, and R-134a
Inlet diameter (mm)	1.5 and 3.0
Tube length (mm)	1000 and 2000
Mass flux (kg/(m <sup>2</sup> /s))	100–650
Heat flux (kW/m <sup>2</sup> )	10–35
Inlet $T_{sat}$ (°C)	5–15

control the input power. The test sections were well insulated with rubber and foam. The outside tube wall temperatures at the top, middle, and bottom sides were measured at every 100 mm axial intervals of the heated length using T-type thermocouples. The local saturation pressure, which was used to determine the saturation temperature, was measured using Bourdon tube-type pressure gauges at the inlet and the outlet of the test section. A pressure transducer was also installed to measure the pressure drop gradient of the refrigerant between the inlet and outlet of the test section. Sight glasses, having the same inner diameter as the test section and a length of 200 mm, were installed to visualize the flow and to enhance the flow stability of the fluid when entering the test section.

The physical properties of the refrigerant were obtained from REFPROP 8 [11]. The temperature and flow rate data were recorded using data acquisition and flow meter, respectively. Table 1 gives a summary of the estimated uncertainty associated with all the parameters at a 95% confidence interval. The uncertainties, obtained using the RSS method [12], included both random and systematic errors, and these changed values according to the flow conditions, so their minimum to maximum ranges were shown. The experimental conditions were also shown in Table 2.

**2.3. Data Reduction.** The local physical properties of the refrigerant were determined from the measured saturation pressure at the inlet and outlet of the test section. The mass quality  $x$  along the test section was evaluated based on the local thermodynamic properties

$$x = \frac{i - i_f}{i_{fg}}, \quad (1)$$

where  $i$  is the enthalpy [kJ kg<sup>-1</sup>],  $f$  is the saturated liquid condition, and  $g$  is the saturated vapor condition. The local

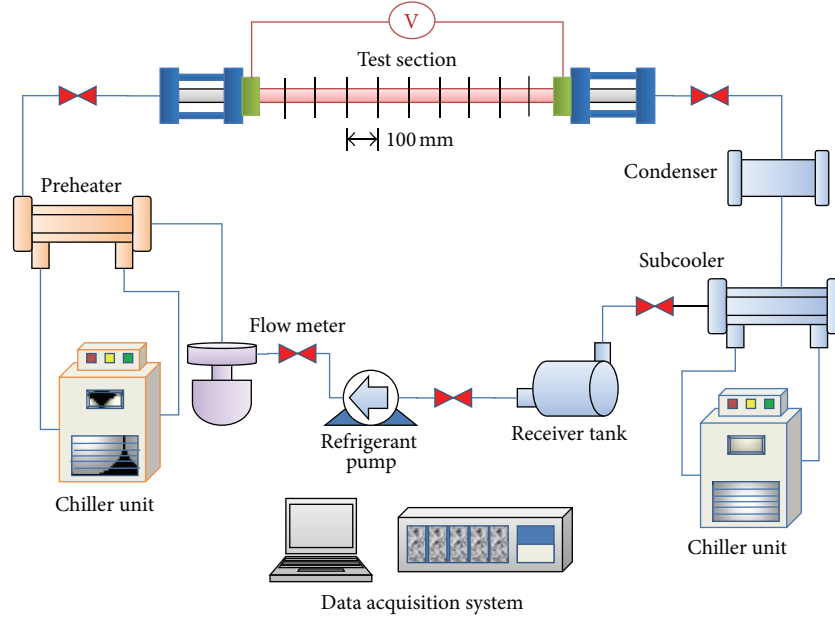


FIGURE 1: Experimental test facility.

heat transfer coefficient  $h$  along the length of the test section is defined as follows:

$$h = \frac{q}{T_{wi} - T_{sat}}, \quad (2)$$

where  $q$  is the heat flux [ $\text{kW}/\text{m}^2$ ],  $T$  is the temperature [K],  $w$  is a tube wall of the test section,  $i$  is the inner side, and  $sat$  is the saturation condition. The inside tube wall temperature  $T_{wi}$  is the average temperature of the top and bottom wall temperatures, and is determined using steady-state one-dimensional radial conduction heat transfer through the test section wall. The saturation temperature  $T_{sat}$  was obtained from the measured saturation pressure  $P_{sat}$ .

### 3. Result and Discussion

#### 3.1. Heat Transfer Coefficient

**3.1.1. Effect of Heat Flux.** Figure 2 shows that the dependence of the HTC on heat flux appeared in the low quality region for R-1234yf and R-134a. The mass flux and saturation temp. were kept constant at  $500 \text{ kg m}^{-2} \text{ s}^{-1}$  and  $10^\circ\text{C}$ , respectively. The trend depicts that in the low quality region (vapor quality  $< 0.3$ ), the HTCs increased with increasing heat flux. It means that the nucleate boiling heat transfer mechanism is dominant in the initial stage of evaporation and it was suppressed when the vapor quality increases. The result was in good agreement with the other one, represented in the study on HTCs of R-1234yf by Saitoh et al. [4].

**3.1.2. Effect of Inner Diameter.** Figure 3 illustrates the effect of the inner tube diameter on the heat transfer coefficient. In the low quality region ( $x < 0.2$ ), a smaller inner tube

diameter shows a higher heat transfer coefficient. This is due to more active nucleate boiling in the smaller diameter tube. As the tube diameter decreases, the contact surface area for heat transfer increases. More active nucleate boiling causes dry patches to appear earlier.

**3.1.3. Effect of Saturate Temperature.** The effect of saturation temperature is shown in Figure 4. The HTCs increased with increasing saturation temperature, which was due to more active nucleate boiling as shown by our experimental data. These results can also be explained by considering the physical properties of the fluid such as pressure, density ratio  $\rho_f/\rho_g$ , viscosity ratio  $\mu_f/\mu_g$ , and surface tension.

**3.1.4. Comparison between the Experimental and Predicted Value of Some Correlation.** The HTCs of R-1234yf in this study were analyzed and compared using some heat transfer coefficient correlations. Figure 5 shows comparisons of the experimental heat transfer coefficient with Gungor-Winterton [7], Shah [8], Wattlelet et al. [9], and Tran et al. [10]. Among them, Gungor-Winterton correlation gave the best results.

**3.2. Development of New Heat Transfer Correlation.** Various studies [13, 14] showed that the heat transfer coefficient correlation for conventional tube could not predict well the heat transfer coefficient of minichannel. In addition, Bertsch et al. [15] reviewed several heat transfer correlations for minichannels and microchannels. The study noted that most of them developed based on small testing conditions and, consequently, these correlations did not extrapolate well beyond their often narrow operating range. Therefore, in the present work, the modified heat transfer coefficient correlations were developed using our data. The formula was

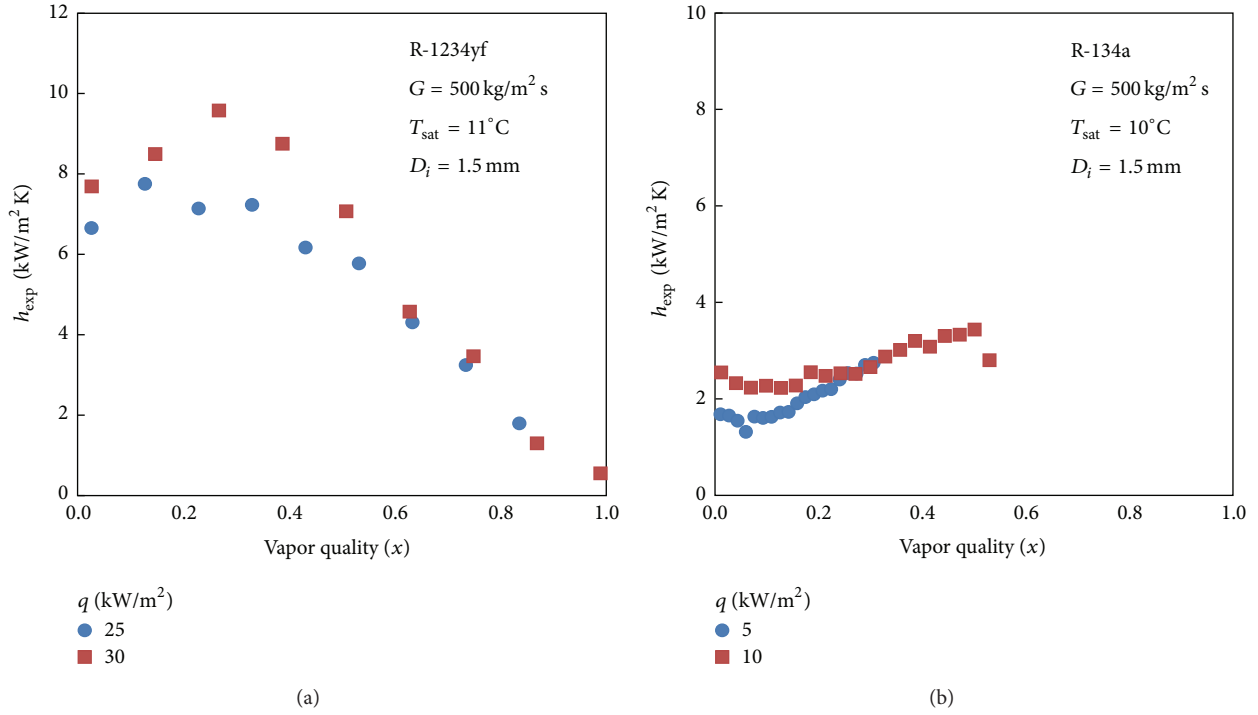


FIGURE 2: Effect of heat flux on heat transfer coefficient for R-1234yf and R-134a.

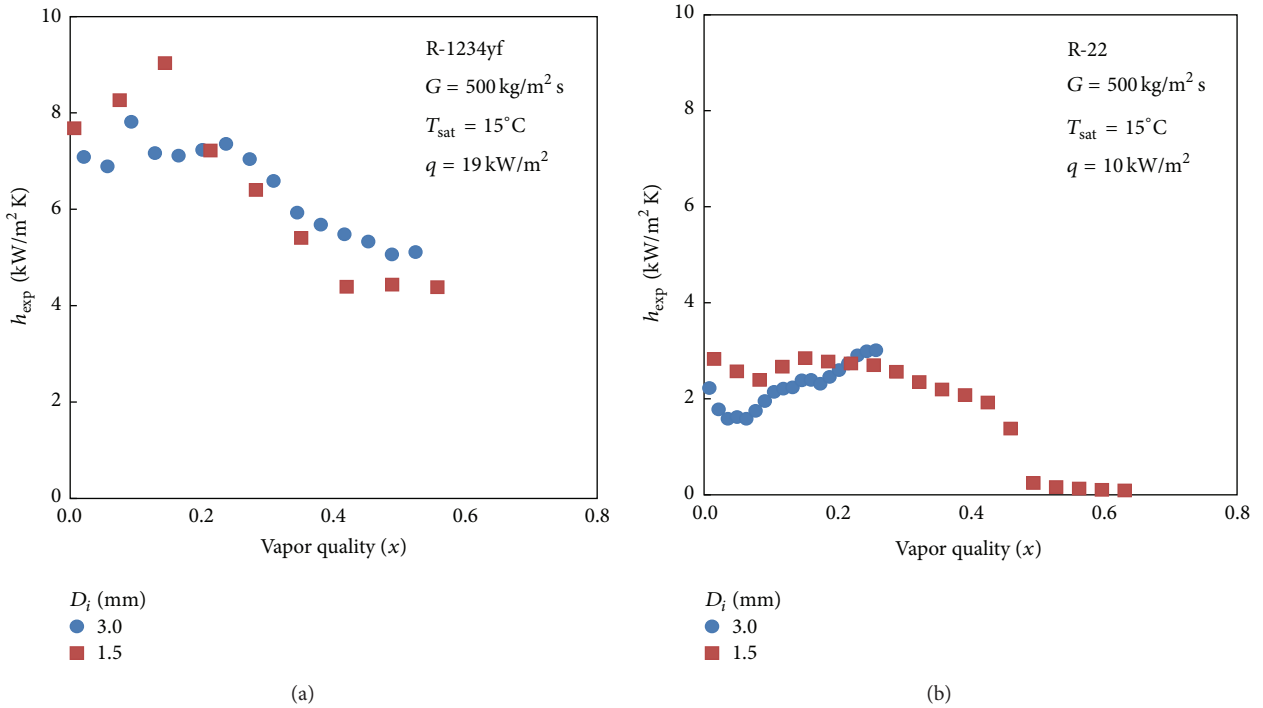


FIGURE 3: Effect of inner diameter on heat transfer coefficient for R-1234yf and R-22, respectively.

based on the Chen correlation [16] that used the physical superposition approach.

3.2.1. *Modification of Factor F.* The flow boiling heat transfer in a tube, following Zhang et al. correlation [17], mainly

consist two mechanisms: nucleate boiling and forced convective evaporation. A superposition model of the heat transfer coefficient may be written as follows:

$$h_{tp} = Fh_{lo} + Sh_{pool} \tag{3}$$

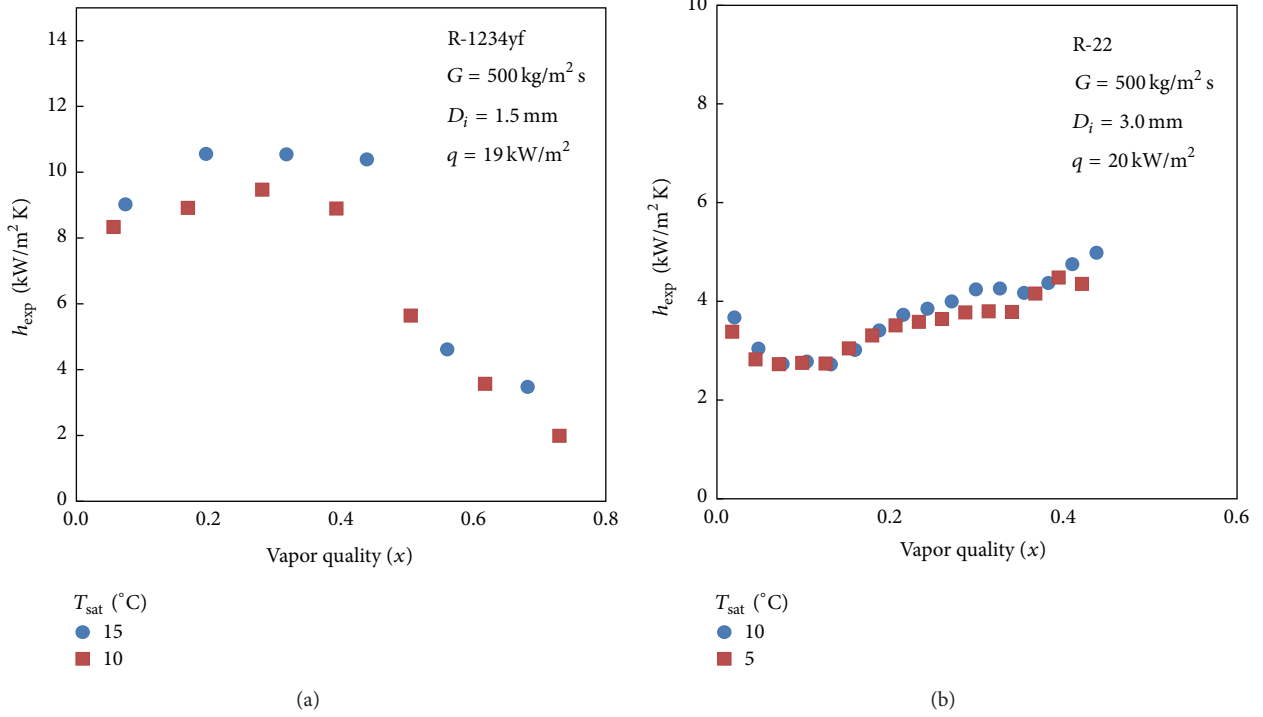


FIGURE 4: Effect of saturation temperature on heat transfer coefficient for R-1234yf and R-22.

The factor  $F$  is introduced as a convective two-phase multiplier to account for enhanced convection due to cocurrent flow of liquid and vapor by Chen, where  $F = fn(X_{tt})$ . Since the effect of small tube that make the convective heat transfer for evaporating refrigerant in small tube delayed with that in conventional tubes, the function should be physically evaluated again. Chisholm [18] introduced a relationship between the factor  $F$  and the two-phase frictional multiplier that is based on the pressure gradient for liquid alone flow,  $F = f(\phi_f^2)$  where

$$\phi_f^2 = 1 + \frac{C}{X} + \frac{1}{X^2}. \quad (4)$$

For liquid-vapor flow conditions of turbulent-turbulent ( $tt$ ), laminar-turbulent ( $vt$ ), turbulent-laminar ( $tv$ ), and laminar-laminar ( $vv$ ), the values of the Chisholm parameter  $C$  are 20, 12, 10, and 5, respectively [16]. The Lockhart-Martinelli parameter,  $X$ , is defined as follows:

$$X = \left[ \frac{(-dp/dz)_f}{(-dp/dz)_g} \right]^{1/2} = \left( \frac{f_f}{f_g} \right)^{1/2} \left( \frac{1-x}{x} \right) \left( \frac{\rho_g}{\rho_f} \right)^{1/2}, \quad (5)$$

where  $((dp/dz)_f)$  is the pressure gradient due to friction ( $\text{N m}^{-2} \text{ m}^{-1}$ ) and  $\rho$  is the density ( $\text{kg m}^{-3}$ ). The friction factor  $f$  in (5) was obtained by considering the flow conditions of laminar-turbulent flows where  $f = 16\text{Re}^{-1}$  for  $\text{Re} < 2300$  (laminar flow) and  $f = 0.079\text{Re}^{-0.25}$  for  $\text{Re} > 3000$  (turbulent

TABLE 3: Coefficients for the convective two-phase multiply factor  $F$ .

Coefficients	$a_1$	$b_1$	$c_1$
R-22	0.003	1.60	0.498
R-134a	0.010	1.30	0.100
R-1234yf	0.070	0.82	0.700

flow). The liquid heat transfer coefficient is defined by the Dittus-Boelter correlation [19]:

$$h_{lo} = 0.023 \frac{k_f}{D} \left[ \frac{G(1-x)D}{\mu_f} \right]^{0.8} \left( \frac{c_{pf}\mu_f}{k_f} \right)^{0.4}. \quad (6)$$

The  $F$  factor proposed by Zhang et al. [17] did not cover all the operating conditions in this work. Hence, a new factor  $F$  was developed from our experimental data using the regression method. Note that, the minimum value of enhancement factor equals to 1 for pure liquid or pure vapor. Hence, its formula was proposed as

$$F = \text{MAX} \left[ \left( a_1 (\phi_f)^{b_1} + c_1 \right), 1 \right]. \quad (7)$$

The  $a_1$ ,  $b_1$ , and  $c_1$  coefficients in (7) were listed in Table 3.

**3.2.2. Nucleate Boiling Contribution.** The nucleate boiling heat transfer of the experimental data was predicted using the Cooper correlation [20]. For a surface roughness of  $1.0 \mu\text{m}$ , the correlation is given as follows:

$$h_{pb} = 55P_r^{0.12} (-0.4343 \ln P_r)^{-0.55} M^{-0.5} q^{0.67}. \quad (8)$$

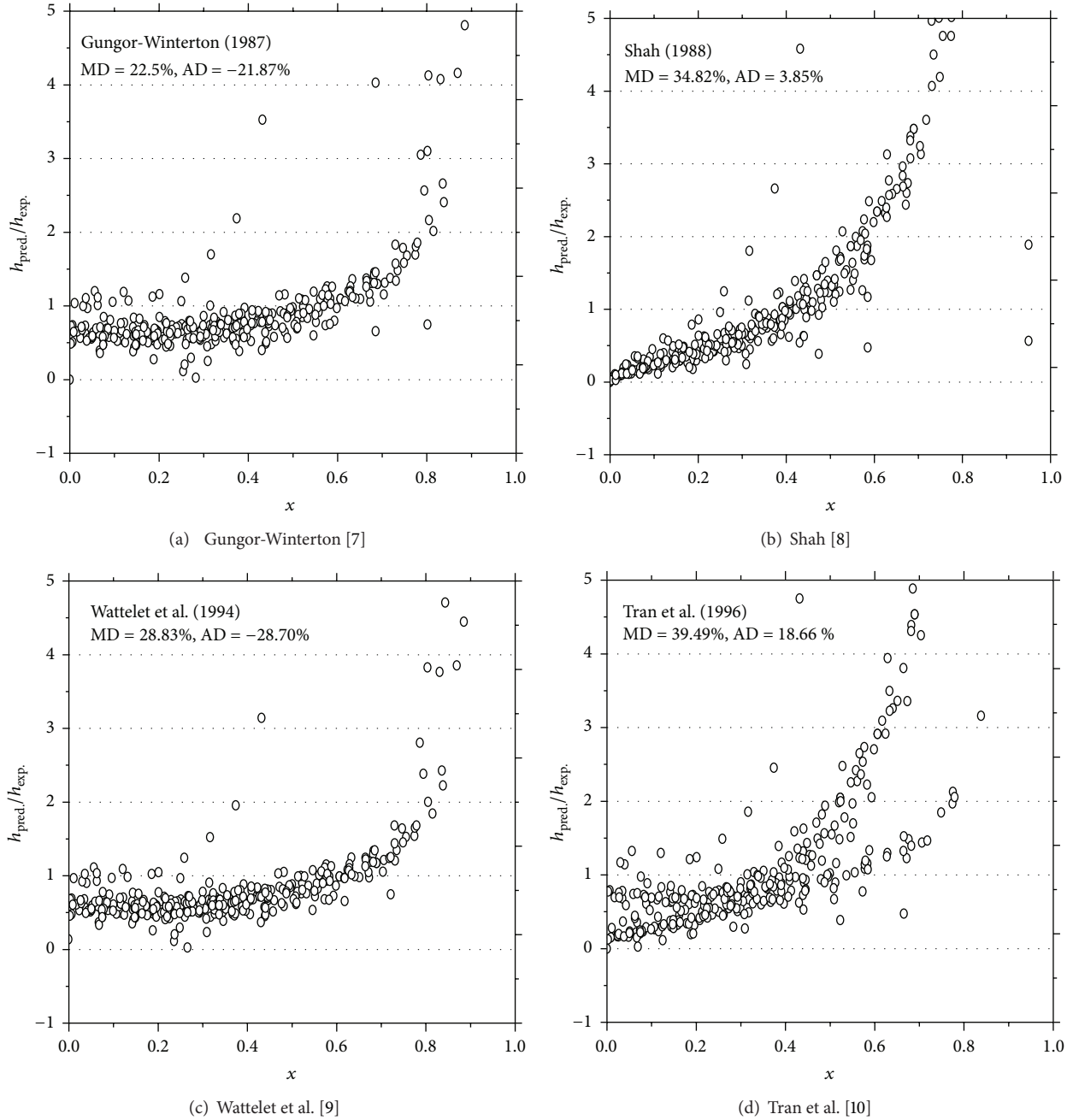


FIGURE 5: Comparison of heat transfer coefficient between the experimental data and the prediction with existing correlations.

TABLE 4: Coefficients for the nucleate boiling factor  $S$ .

Coefficients	$a_2$	$b_2$	$c_2$
R-22	0.99	0.181	0.262
R-134a	1.00	0.170	0.196
R-1234yf	15.85	-0.14	0.270

The nucleate boiling suppression factor  $S$  in our correlation is function of boiling number  $Bo$  and two-phase frictional multiplier  $\phi_f^2$ . Using the experimental data from this study,

a new nucleate boiling suppression factor, a ratio of  $h_{nbc}/h_{pb}$ , is proposed as follows:

$$S = a_2 (\phi_f^2)^{b_2} Bo^{c_2}. \quad (9)$$

The coefficients of (9) for each correlation are illustrated in Table 4. A modified heat transfer coefficient correlation was developed by the regression method with 1175 experimental data points. The whole comparison of heat transfer coefficient between the experimental data and prediction using our correlation is shown in Figure 6. The proposed correlation

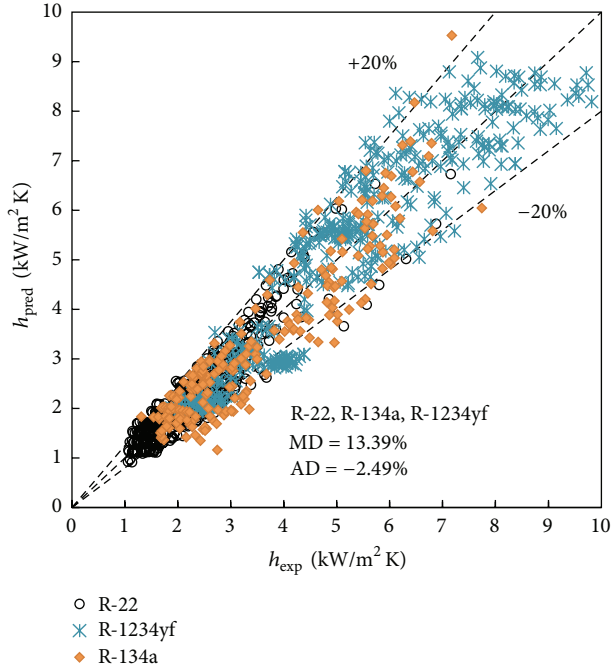


FIGURE 6: Comparison of heat transfer coefficient between the present experimental data and predicted values using newly-modified correlation.

TABLE 5: Deviation of the heat transfer coefficient comparison between the present data and the prediction using the new developed heat transfer coefficient correlations.

Deviation	R-22	R-134a	R-1234yf	Overall
Mean (%)	12.25	14.78	13.16	13.39
Average (%)	-1.25	-5.28	-0.94	-2.49

provided very good prediction with the overall mean deviation for three refrigerants of 13.39%. The deviation for each correlation is tabulated in Table 5.

#### 4. Conclusions

The convective boiling heat transfer coefficients were experimentally performed in horizontal small tubes with R-1234yf, R-134a, and R-22. The effects of heat flux, inner tube diameters, and saturation temperatures at three states of 5, 10, and 15°C on heat transfer coefficient were discussed in this study. The experimental results illustrated that the HTC's increased with increasing heat flux because nucleate boiling is dominant much more strongly in low-quality region. The HTC's also increase with increasing saturation temperature and decreasing inner tube diameter. The experimental data of R-1234yf were compared using some existing heat transfer coefficient correlations. Among them, Gungor-Winterton [7] correlation gave the best prediction with the MD of 22.5%. Other correlations were underpredicted. Finally, the modify heat transfer coefficient correlations were developed based on the superposition model of the contribution of nucleate and

boiling heat transfer with a good accuracy that can be applied to improve the compact heat exchanger design.

#### Nomenclature

- MD: Mean Deviation,  
 $MD = (1/n) \sum_1^n |(dp_{pred} - dp_{exp}) \times 100 / dp_{exp}|$
- C: Chisholm parameter  
D: Diameter (m)  
G: Mass flux ( $kg\ m^{-2}\ s^{-1}$ )  
L: Tube length (m)  
H: Heat transfer coefficient ( $kW\ m^{-2}\ K^{-1}$ )  
n: Number of data  
q: Heat flux ( $kW\ m^{-2}$ )  
T: Temperature (K)  
X: Lockhart-Martinelli parameter  
x: Vapor quality  
AD: Average Deviation,  
 $AD = (1/n) \sum_1^n ((dp_{pred} - dp_{exp}) \times 100 / dp_{exp})$
- $c_p$ : Specific heat ( $kJ\ kg^{-1}\ K^{-1}$ )  
f: Friction factor  
g: Acceleration due to gravity ( $g = 9.81\ m/s^2$ )  
 $h_{pb}$ : Nucleate boiling heat transfer coefficient ( $W\ m^{-2}\ K^{-1}$ )  
 $h_{lo}$ : Liquid heat transfer coefficient ( $W\ m^{-2}\ K^{-1}$ )  
P: Pressure (kPa)  
Re: Reynolds number, ( $Re = GD/\mu$ )  
W: Mass flow rate ( $kg\ s^{-1}$ )  
I: Enthalpy ( $kg\ kJ^{-1}$ ).

#### Greek Letters

- $\alpha$ : Void fraction  
 $\rho$ : Density ( $kg\ m^{-3}$ )  
 $\phi_f^2$ : Two-phase frictional multiplier  
 $\phi_c^2$ : New two-phase frictional multiplier  
 $\mu$ : Viscosity (Pas)  
 $\sigma$ : Surface tension ( $N\ m^{-1}$ )  
 $(dp/dz)$ : Pressure gradient ( $N\ m^{-2}\ m^{-1}$ )  
 $((dp/dz)F)$ : Pressure gradient due to friction ( $N\ m^{-2}\ m^{-1}$ ).

#### Subscripts

- crit: Critical point  
f: Saturated liquid  
g: Saturated vapor  
mom: Momentum  
o: Outer tube  
pred: Predicted value  
sat: Saturation  
t: Turbulent  
v: Laminar  
exp: Experimental value  
frict: Frictional  
i: Inner tube  
go: Vapor only

lo: Liquid only  
 pb: Pool boiling  
 r: Reduced  
 sc: Sub-cooled  
 tp: Two-phase  
 w: Wall.

## Acknowledgments

This work was supported by the Korea Institute of Energy Technology Evaluation and Planning (KETEP) Grant no. (2011T100100464) of the Energy Technology Development.

## References

- [1] Directive 2006/40/EC of the European Parliament and of the Council of 17 May 2006 Relating to Emissions from Air-conditioning Systems in Motor Vehicles and Amending.
- [2] J. M. Calm, "The next generation of refrigerants—historical review, considerations, and outlook," *International Journal of Refrigeration*, vol. 31, no. 7, pp. 1123–1133, 2008.
- [3] K. Park and D. Jung, "Nucleate boiling heat transfer coefficients of R1234yf on plain and low fin surfaces," *International Journal of Refrigeration*, vol. 33, no. 3, pp. 553–557, 2010.
- [4] S. Saitoh, C. Dang, Y. Nakamura, and E. Hihara, "Boiling heat transfer of HFO-1234yf flowing in a smooth small-diameter horizontal tube," *International Journal of Refrigeration*, vol. 34, no. 8, pp. 1846–1853, 2011.
- [5] Y. Lee and D. Jung, "A brief performance comparison of R1234yf and R134a in a bench tester for automobile applications," *Applied Thermal Engineering*, vol. 35, no. 1, pp. 240–242, 2012.
- [6] D. del Col, S. Bortolin, D. Torresin, and A. Cavallini, "Flow boiling of R1234yf in a 1 mm diameter channel," *International Journal of Refrigeration*, vol. 36, no. 2, pp. 353–362, 2013.
- [7] K. E. Gungor and R. H. S. Winterton, "Simplified general correlation for saturated flow boiling and comparisons of correlations with data," *Chemical Engineering Research and Design*, vol. 65, no. 2, pp. 148–156, 1987.
- [8] M. M. Shah, "Chart correlation for saturated boiling heat transfer: equations and further study," *ASHRAE Transactions*, vol. 88, no. 2673, pp. 185–196, 1988.
- [9] J. P. Wattlelet, J. C. Chato, A. L. Souza, and B. R. Christoffersen, "Evaporative characteristics of R-12, R-134a, and MP-39 at low mass fluxes," *ASHRAE Transactions*, vol. 100, no. 1, pp. 603–615, 1994.
- [10] T. N. Tran, M. W. Wambsganss, and D. M. France, "Small circular- and rectangular-channel boiling with two refrigerants," *International Journal of Multiphase Flow*, vol. 22, no. 3, pp. 485–496, 1996.
- [11] NIST, "NIST reference fluid thermodynamic and transport properties," REFPROP 8, National Institute of Standards and Technology, Boulder, Colo, USA, 2007.
- [12] American Society of Mechanical Engineers, "Part 1: measurement uncertainty, instrument and apparatus," ASNI/ASME PTC 19.1-1985, American Society of Mechanical Engineers, New York, NY, USA, 1985.
- [13] J. R. Thome, "Boiling in microchannels: a review of experiment and theory," *International Journal of Heat and Fluid Flow*, vol. 25, no. 2, pp. 128–139, 2004.
- [14] L. Cheng and D. Mewes, "Review of two-phase flow and flow boiling of mixtures in small and mini channels," *International Journal of Multiphase Flow*, vol. 32, no. 2, pp. 183–207, 2006.
- [15] S. S. Bertsch, E. A. Groll, and S. V. Garimella, "Review and comparative analysis of studies on saturated flow boiling in small channels," *Nanoscale and Microscale Thermophysical Engineering*, vol. 12, no. 3, pp. 187–227, 2008.
- [16] J. C. Chen, "Correlation for boiling heat transfer to saturated fluids in convective flow," *Industrial & Engineering Chemistry Process Design and Development*, vol. 5, no. 3, pp. 322–329, 1966.
- [17] W. Zhang, T. Hibiki, and K. Mishima, "Correlation for flow boiling heat transfer in mini-channels," *International Journal of Heat and Mass Transfer*, vol. 47, no. 26, pp. 5749–5763, 2004.
- [18] D. Chisholm, "A theoretical basis for the Lockhart-Martinelli correlation for two-phase flow," *International Journal of Heat and Mass Transfer*, vol. 10, no. 12, pp. 1767–1778, 1967.
- [19] F. W. Dittus and L. M. K. Boelter, "Heat transfer in automobile radiators of the turbulent type," *University of California Publication in Engineering*, vol. 2, pp. 443–461, 1930.
- [20] M. G. Cooper, "Heat flow rates in saturated nucleate pool boiling—a wide-ranging examination using reduced properties," *Advances in Heat Transfer*, vol. 16, pp. 157–239, 1984.

## Research Article

# Flow Characterization of Dense-Phase Pneumatic Conveying System of Pulverized Coal through Electrostatic Sensor Arrays

Feifei Fu,<sup>1</sup> Ming Kong,<sup>2</sup> Chuanlong Xu,<sup>1</sup> Cai Liang,<sup>1</sup> and Shimin Wang<sup>1</sup>

<sup>1</sup> Key Laboratory of Energy Thermal Conversion and Control of Ministry of Education, School of Energy and Environment, Southeast University, Nanjing 210096, China

<sup>2</sup> College of Metrology and Measurement Engineering, China Jiliang University, Hangzhou 310018, China

Correspondence should be addressed to Chuanlong Xu; [chuanlongxu@seu.edu.cn](mailto:chuanlongxu@seu.edu.cn)

Received 4 April 2013; Accepted 23 June 2013

Academic Editor: Guan Heng Yeoh

Copyright © 2013 Feifei Fu et al. This is an open access article distributed under the Creative Commons Attribution License, which permits unrestricted use, distribution, and reproduction in any medium, provided the original work is properly cited.

Experiments are performed in a dense-phase pneumatic conveying system of pulverized coal, and electrostatic signals and coal particle distribution images over cross-section of the pipeline at superficial gas velocities of 5.7 m/s, 6.9 m/s, and 8.1 m/s are obtained through use of electrostatic sensor arrays (ESA) and electrical capacitance tomography (ECT), respectively. In combination with ECT imaging results, the output signals of the ESA are analyzed by FFT and approximate entropy method. Results show that characteristic of particles motion and its change with increasing superficial gas velocity are different in the dense and dilute phase region of the pipe. With increasing the superficial gas velocity, the peak frequency of the electrostatic signal increases linearly in dense-phase region, while that in dilute phase region is nonlinear, implying that the increase of the axial particles velocity is the main dynamic change, while in dilute phase regions, the particles velocity fluctuation in the radial direction cannot be ignored. The ApEn value of the electrostatic signal in dense phase region is larger than that in dilute phase region. When the ApEn value difference of the electrostatic signals is smaller, the pulverized coal particles are better suspended.

## 1. Introduction

Dense-phase pneumatic conveying system of powder is widely applied in the chemical and industrial processes such as the pulverized coal transport of entrained flow gasifiers in chemical plants and the coal powder injection systems of blast furnaces in steel plants. However, due to the unsteady and complex nonlinear nature of the dense-phase gas-solid two-phase flow in the pneumatic transport pipelines, it is desirable to investigate the particle flow behavior for the optimized design and operation of these dense-phase pneumatic conveying systems. For the investigation into the dense-phase gas-solid flow, on the one hand, the mathematical modeling and numerical simulations for the gas-solid flow are used to predict the particle behavior [1–4]. However, no great progresses in the modeling were made to date because of the randomness and complexity of the dense-phase gas-solid flow. On the other hand the experimental time series such as the pressure, particle concentration, and acoustic

emission were obtained from the gas-solid flow system, and nonlinear processing methods including the entropy, Lyapunov exponent, and correlation dimension are employed to extract the instantaneous dynamic behavior of particles [5–8]. Approximate entropy (ApEn) method as a quantifying method for the randomness inherent in the time series, has been widely used for flow pattern identification in fluidized bed, gas-liquid two-phase flow complexity measure analysis, and fault detection in industrial process [9–11].

When particles are pneumatically transported in the conveying pipelines, charges are generated on the particles due to particles-particles and particles-wall collisions and friction [12, 13]. Based on particle charging, electrostatic technique has been widely applied to particle parameters measurement such as particle velocity and particle size due to its advantages of low cost, simple structure, and being a noncontact, highly sensitive, and robust sensor [14–16]. Recently, the ring-shaped electrostatic sensor has been used to measure particle average velocity and characterize

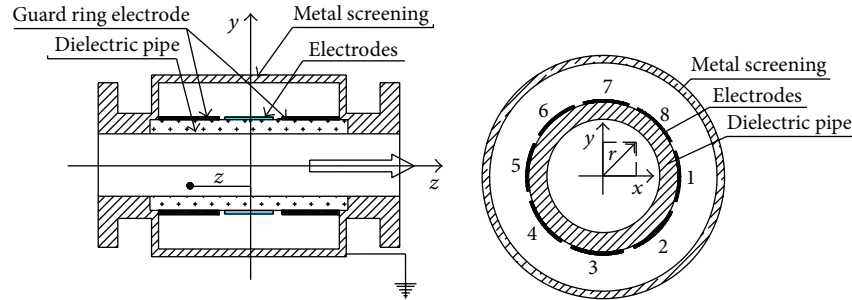


FIGURE 1: Schematic diagram of the 8 electrode electrostatic sensor arrays.

the nonlinear behavior of the particle movement in the dense-phase pneumatic transport system [7, 17]. However, it has the limitations of characterizing the local particles velocity and local motion characteristics of the gas-solid two-phase flow. This is because the output signal of the ring-shaped sensor is the superposition of the charges induced by all the charged particles in the sensing zone of the sensor [18]. In fact, an inhomogeneous particle velocity distribution and the asymmetric structure of gas-solid flow usually exist over the cross-section of the pipe. Therefore it is necessary to measure local particle velocity and motion characteristics for characterizing particle flow characteristics in a gas-solid system. Electrostatic sensor array (ESA), as an improved ring-shaped electrostatic sensor, was proposed to measure gas-solid flow because each electrode of the ESA has its localized sensitive zone [19]. In a sense, by arranging the electrodes in the axial and circumferential directions of the conveying pipeline, the output signals of those electrodes reflect local particle flow behavior of gas-solid flow in time and space. Electrical capacitance tomography (ECT) technology is capable of visualizing the spatial distribution of solid particle and determining solid concentration over the cross-section of a pipe. Up to date, ECT has been used for the visualization and characterization of particle flow [20]. Therefore, multisensor integrations including electrostatic sensor array and electrical capacitance tomography (ECT) system would be more useful for comprehensively understanding the particles behavior of gas-solid two-phase flow system.

The objective of this paper is to investigate the flow characteristics of dense-phase pneumatic conveying system of pulverized coal through electrostatic sensor arrays in conjunction with ECT. The sensitivity distribution characteristics of the electrostatic sensor arrays are firstly analyzed using finite element method and experimentally verified by the full pipe particle flow and quarter particle flow in a gravity-fed flow rig. On a dense-phase pneumatic conveying system of pulverized coal, electrostatic signals and coal particle distribution over cross-section of the pipeline in three experimental cases are then obtained, respectively, by electrostatic sensor arrays and ECT system. FFT and approximate entropy methods combined with ECT images are applied to reveal the relationship between the particle characteristics and the frequency spectrums and approximate entropy of the output signals of electrostatic sensor arrays.

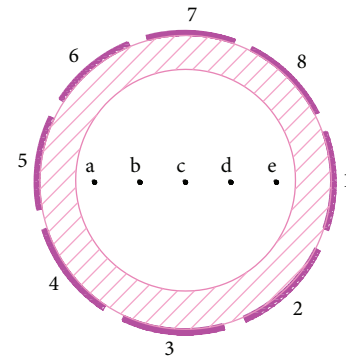


FIGURE 2: Typical flow streamlines in the ESA with 8-electrodes.

## 2. Electrostatic Sensor Arrays

A schematic of the electrostatic sensor arrays is shown in Figure 1. It mainly consists of eight arc-shaped electrodes evenly distributed along the circumference of the pipe, two grounded guard ring electrodes, one grounded metal screening to resist electromagnetic interference, and one dielectric pipe to isolate the electrode. Mathematic model of the ESA has been introduced in the literature [19]. Due to the complex 3D electrostatic field distribution of ESA, it is difficult to derive an analytical solution to its mathematical model. The recent availability of various electromagnetic field calculation software packages in conjunction with fast computing equipment has made it possible to calculate the electrostatic field. In the work presented in this paper, Ansoft (Maxwell 3D Field Simulator) is utilized to calculate the induced charge on the electrodes of the ESA.

Five typical flow streamlines denoted by a, b, c, d, and e in Figure 2 are selected to represent the axial sensitivity distribution of the ESA. The flow streamlines are uniformly located on the dielectric pipe's diameter passing through the center point of the electrodes 1 and 5. In the numerical simulations and experiments, the inner radius of the dielectric pipeline is 10 mm, and thus the spacing between the five streamlines equals 2 mm. The EAS model consists of eight electrodes with the length of 10 mm and width of 6 mm. When a unit point charge moves in a streamline, eight independent induced charge values on the eight electrodes

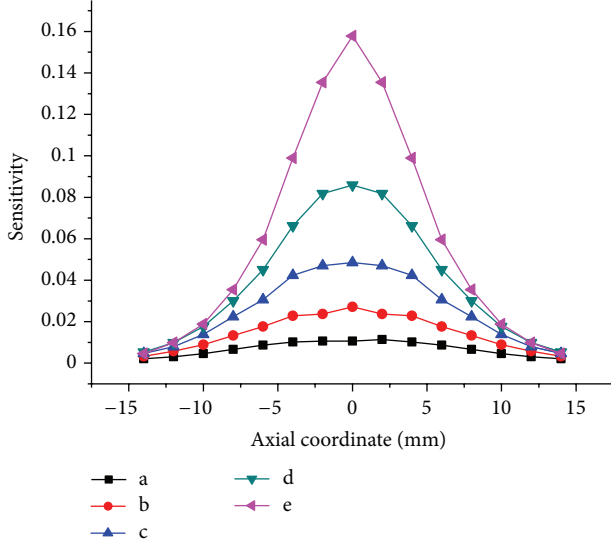


FIGURE 3: Variation of the sensitivity with the axial coordinate in different streamlines.

of the ESA can be obtained simultaneously by calculating electrostatic field, and each electrode has its own sensing zone. But the eight electrodes have the same sensing field distribution because of the axial symmetric distribution of the ESA. Therefore if the sensitivity distribution of one electrode is calculated, those of the other electrodes of the ESA can be obtained by rotation.

Figure 3 shows the variation of the sensitivity with the axial coordinate  $z$  for different streamlines. Figure 4 shows the sensitivity distribution of the electrode 1 at the central cross-section ( $z = 0$ ). From Figure 3 and Figure 4, it can be seen that the sensitivity of each electrode is three-dimensional and is inhomogeneous over the cross-section and along the axial direction of the pipe. The electrode has higher sensitivity at  $z = 0$ , and the sensitivity decreases with increasing  $|z|$  in the same streamlines. The rapid change in the sensitivity occurs when the unity point charge moves along the streamlines (d, e) close to the electrode. However the streamlines a, b, and c contribute much less to the induced charge on the electrode. As shown in Figure 4, the sensitivity in the red area near the electrode 1 is larger and decreases with the increasing distance from the electrode. The sensitivity in the blue area is only a tenth of that in the red area. This implies that the charged particles nearby the electrode make the most significant contributions to its output, and thus the sensing field is quite localized around the electrode. The local sensitivity distribution indicates that the ESA can give some information on gas-solid flow distribution.

### 3. Approximate Entropy Method

Pincus proposed the approximate entropy (ApEn) method for the analysis of random time series [21]. Now it has been widely used to quantify the randomness inherent in time

series. The computation process of ApEn for a time series  $\{x(i)\}$  with the length of  $N$  is as follows.

*Step 1.* Embedding vector  $X(i)$  is created, and it contains  $m$  consecutive values of  $x$

$$X(i) = [x(i), x(i+1), x(i+2), \dots, x(i+m-1)], \quad (1)$$

$$1 \leq i \leq N - m + 1,$$

where  $m$  is the embedding dimension.

*Step 2.* The distance  $d[X(i), X(j)]$  between two vectors  $X(i)$  and  $X(j)$  is defined as

$$d[X(i), X(j)] = \max_{k=0, \dots, m-1} \{|x(i+k-1) - x(j+k-1)|\}. \quad (2)$$

*Step 3.* For each  $i$ ,  $1 \leq i \leq N - m + 1$ ,

$$C_i^m(r) = \frac{\{\text{number of } 1 \leq j \leq N - m \text{ such that } d[X(i), X(j)] \leq r\}}{(N - m + 1)}, \quad (3)$$

where  $r$  is the tolerance deviation.  $C_i^m(r)$  denotes the probability that the distance  $d[X(i), X(j)]$  between two vectors  $X(i)$  and  $X(j)$  is less than  $r$  when  $X(i)$  is taken as the center. The average of  $C^m(r)$  is then defined by

$$C^m(r) = \frac{\sum_{i=1}^{N-m+1} \ln C_i^m(r)}{(N - m + 1)}. \quad (4)$$

*Step 4.* Increase the embedding dimension  $m$  to  $m + 1$ , and repeat Step 1 to Step 3. We have

$$C^{m+1}(r) = \frac{\sum_{i=1}^{N-m+1} \ln C_i^{m+1}(r)}{(N - m)}. \quad (5)$$

*Step 5.*  $C^m(r)$  and  $C^{m+1}(r)$  denote the probabilities of the template matching for  $m$  and  $m + 1$  points, respectively. Therefore ApEn is defined by

$$\text{ApEn}(m, r) = \lim_{N \rightarrow \infty} \{C^m(r) - C^{m+1}(r)\}. \quad (6)$$

In practice,  $N$  is a finite scalar, and so the ApEn can be approximated as

$$\text{ApEn}(m, r, N) = C^m(r) - C^{m+1}(r). \quad (7)$$

From (7), it can be seen that the ApEn value varies with the embedding dimension  $m$  and similar tolerance  $r$ . The larger ApEn value indicates that the time series is more complex and irregular.

### 4. Experimental Setup

A schematic diagram of the dense-phase pneumatic conveying system of pulverized coal at high pressure is shown in

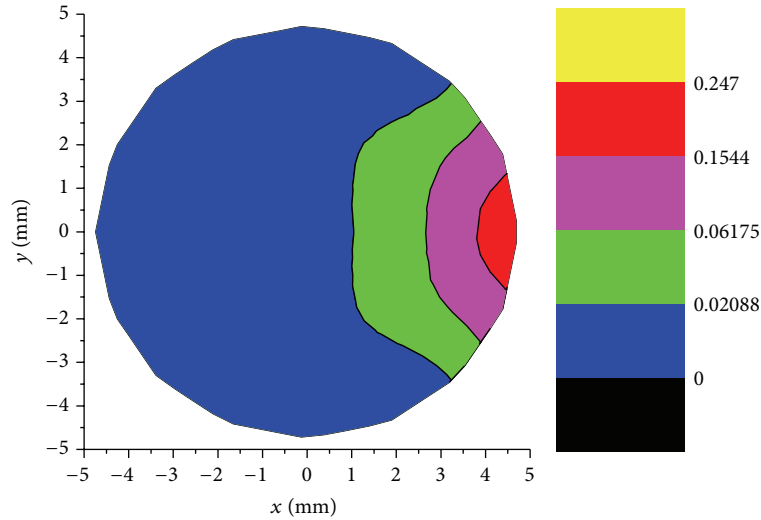


FIGURE 4: Sensitivity distribution over the central cross-section of ESA.

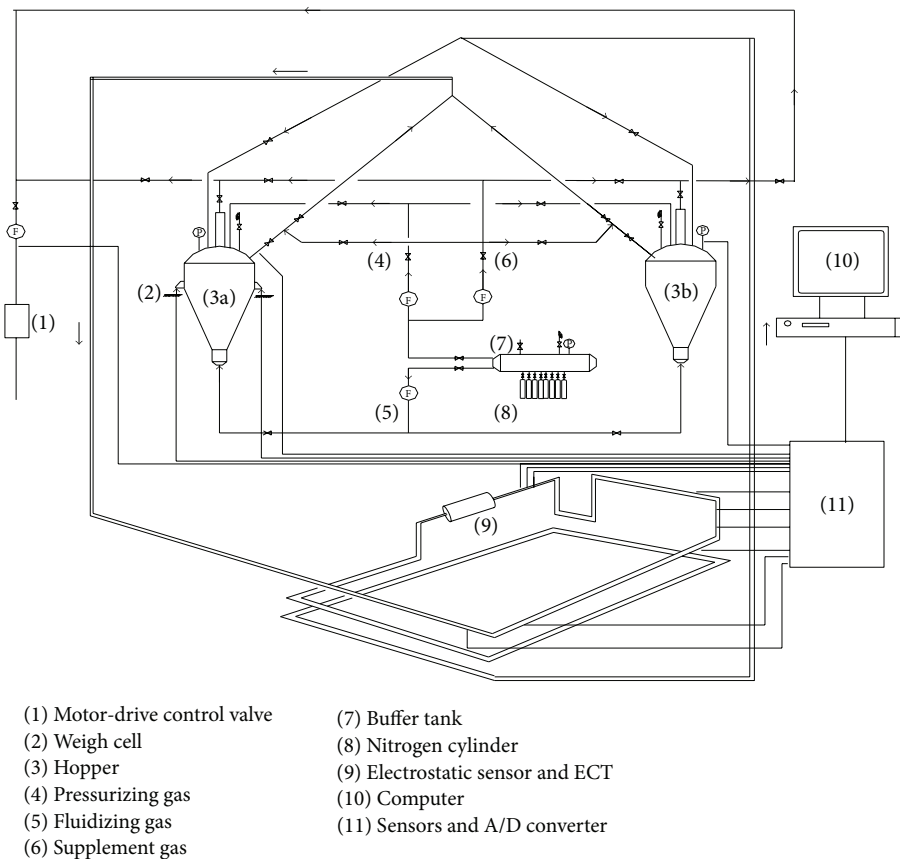


FIGURE 5: Schematic of a dense-phase pneumatic conveying system of pulverized coal at high pressure.

Figure 5. High-pressure gas supplied from the buffer tank is divided into the pressurizing gas, the fluidizing gas, and the supplement gas. The feeding hopper adopts the bottom-fluidization and top-discharge arrangements. Pulverized coal in the feeding hopper is fluidized by the fluidizing gas

and enters the conveying pipeline through an accelerating segment located in the hopper. Finally the coal particle flow reaches the receiving hopper. The rate of each gas is measured by a metal tube variable-area flow meter, and the fluctuation of solid mass flow rate is monitored by the load cells. Both

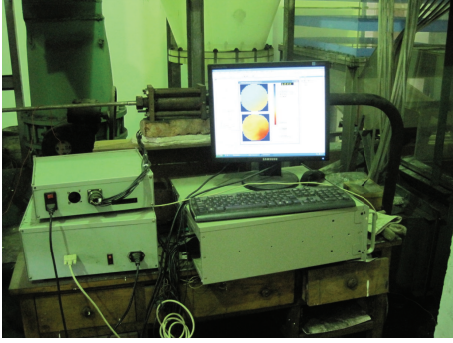


FIGURE 6: Integrated sensors including ESA and ECT.

the feeding hopper and the receiving hopper have a capacity of  $0.648 \text{ m}^3$ . The transport pipeline section consists of 45 m of  $\Phi 10$  mm bore stainless steel pipeline. The gas pressure in the buffer tank is kept at 4 Mpa. The transported material is pulverized lignite coal. The coal properties are summarized in Table 1. The transportation gas is  $\text{CO}_2$ .

Figure 6 shows a photograph of the integrated sensor including ESA and ECT. The integrated sensor head and electrodes arrangement of the ECT and the ESA is shown in Figure 7. The electrodes were tightly mounted on a quartz glass tube with length of 200 mm and diameter of 10 mm. The ECT consists of eight electrodes with the length of 100 mm and width of 6 mm, a multichannel signal conditioning, data acquisition circuit, and image reconstruction program. The ESA has the same size parameters as those in Section 2. The output signals of the conditioning circuit of the ESA were sampled by a PCI9112 acquisition card and then stored in a computer. Sampling frequency is 1000 Hz.

## 5. Results and Discussions

**5.1. Gravity-Fed Particle Flow Experiments.** Figure 8 shows a photograph of a gravity-fed flow rig. Particles from the hopper first enter the pipeline and then pass the head of the integrated sensor by gravity. During experiments, the quarter flow and full pipe flow were achieved through vertical pipe and inclining pipe at an angle of  $45^\circ$ . Particles used in the experiments were glass beads with the diameter of 1 mm.

The energies of the eight electrostatic output signals of the ESA for quarter flow and full pipe flow were calculated, and the ECT images were acquired in three consecutive seconds. Figure 9 shows the signal energy of the quarter flow on the eight electrodes and the ECT reconstruction images. It can be seen from Figure 9(a) that the grey value of the area close to the electrodes 3 and 4 is larger, implying that the particle concentration in the area is higher. The corresponding signal energy of the electrodes 3 and 4 is larger than that from the other six electrodes (in Figure 9(b)). This verifies that the sensing zone of the electrode of the ESA is localized, and the electrode has higher sensitivity close to it. Figure 10 shows the signal energy of full pipe flow on the eight electrodes of the ESA and the reconstruction images of the ECT. Compared

with Figure 9, the energy distributions from eight electrodes for the full pipe flow fluctuate around a mean value of 2.2, although the signal energy of the electrode 8 is smaller than that of the other seven electrodes for the reason that the particle concentration near the electrode 8 is low during experiments. Therefore it can be concluded that the output signals of the ESA effectively reflect the particle distribution over the cross-section of the pipe.

### 5.2. Pneumatic Conveying Experiments of Pulverized Coal.

Experiments on the dense-phase pneumatic conveying system of pulverized coal are performed. Experimental parameters are listed in Table 2. Raw differential pressure signals and mass signals in three cases are shown in Figure 11. It can be seen from Figure 11 that in three cases the coal mass in the receiving hopper has a good linear decrease, and its correlation coefficient is more than 0.9. The differential pressure fluctuations are smooth over a period of stable transport time (50 s–250 s).

In a horizontal pneumatic conveying pipeline, the pulverized coal is dense in the bottom and dilute in the top of the pipe due to gravity. Figure 12 shows the particle distribution images over the cross-section of the pipe in the three cases. It can be seen that coal particle concentration decreases, and particle distribution becomes homogeneous with increasing superficial gas velocity. From the ECT images and the average coal concentration over the cross-section of the pipeline (in Figure 13), the pulverized coal distribution and average coal concentration vary slightly with time, and thus particles conveying continuity are all in good conditions in the three cases. Especially in the case 3 with the larger superficial gas velocity, coal particles are totally suspended and homogeneous. Therefore ECT technique can distinguish particle distribution over the cross-section of the pipe, which mainly reflects the characteristics of macroscale particles distribution. However, ECT is not suitable for characterizing particles motion in micro scale.

Figures 14 and 15 show the peak frequencies and ApEn value of the eight electrode output signals of the ESA in three cases with different superficial gas velocities, respectively. The variations of ApEn value, peak frequency, and peak amplitude of the electrostatic signals with increasing superficial gas velocity are summarized in Table 3. It can be seen from Table 3 that the peak amplitudes generally decrease with increasing superficial gas velocity. The larger charge quantity contributes to the bigger amplitude of the output signal in frequency domain [16]. Collision number increase in a certain degree will lead to the increase of the particles charge quantity. As the superficial gas velocity is increased, the particles concentration decreases, and the particle-particle collision number decreases. So the particle charge decreases. However, ApEn value and peak frequency have nonlinear relations with superficial velocity. Compared with the particle distribution images shown in Figure 12, the electrodes 2 and 3 are in dense-phase region, the electrodes 6 and 7 are in dilute phase region, and the electrodes 1, 4, 5, and 8 are in the border region. From Table 3, it can be seen that the ApEn values and peak frequencies on the electrodes 1, 4, 5, and 8 are poorly

TABLE 1: Properties of lignite coal particles.

Material	Mean size $d_s$ ( $\mu\text{m}$ )	True density $\rho_s/(\text{Kg}/\text{m}^3)$	Shape factor $\Phi_s$	Moisture content %
Lignite	208.5	1350	0.64	10.39

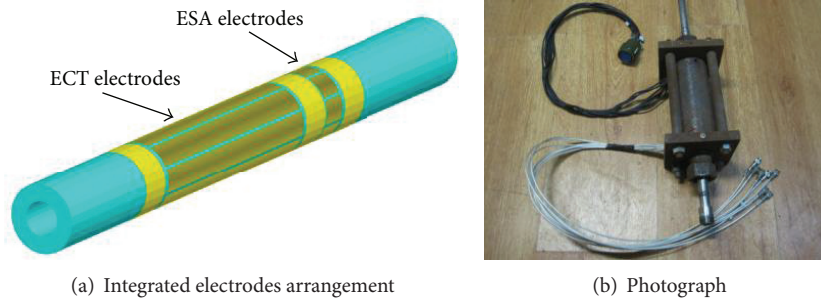


FIGURE 7: Integrated sensor head.

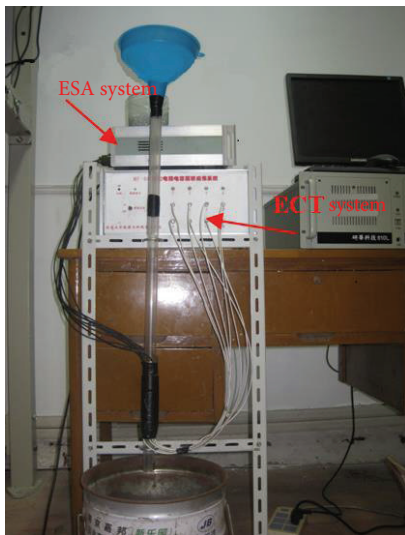


FIGURE 8: Gravity-fed flow rig.

comparable. This is because the particle flow varies randomly between dense-phase and dilute phase in the border region. Therefore the features in the frequency domain and ApEn values of the output signals on the electrodes 2 and 3 and the electrodes 6 and 7 are used to analyze and describe the particle motion characteristics in dense-phase region and dilute phase region.

Figures 16 and 17, respectively, show the frequency spectrum of the output signals on the electrodes 2, 3, 6, and 7 in three cases. The peak frequencies are shown in Figure 18. It can be seen that the peak frequencies on the electrodes 2 and 3 increase with the increase of superficial gas velocity. Previous study has proven that the frequency characteristics of the electrostatic sensor output signal are closely related to the charge carried by the particles, the velocity, and

distribution of charged particles in its sensing zone [19]. The particles velocity increases with increasing the superficial velocity, and consequently the peak frequency increases [16]. However, the peak frequencies on the electrodes 6 and 7 do not keep increasing, shown in Figure 18. The reason is that the particle distribution and velocity fluctuation in radial direction also exert nonlinear influence on frequency characteristics of electrostatic sensor output signals [16]. In the turbulent flow, particles concentration is inversely proportional to turbulent kinetic energy of particles [22]. When the superficial gas velocity is 5.7 m/s, it is turbulent flow with the Reynolds (Re) number more than  $2 \times 10^5$ . The bigger turbulent kinetic energy of particles means the particle velocity fluctuation in radial direction is stronger. So in dilute phase region, the particle velocity fluctuation in radial direction is more turbulent. Though the particle velocity increase is the main variation with increasing the superficial gas velocity in dilute phase region, the particle velocity fluctuation in radial direction is big enough that it causes an important nonlinear influence on the change of its output signal peak frequency. Therefore, as the superficial gas velocity increases, the increase of the particles velocity is the main dynamic change, while in dilute phase region the particles velocity fluctuation in the radial direction cannot be ignored.

The randomness and complexity of particles motion in the dense-phase conveying pipeline could be quantified by the ApEn value. Figure 19 shows the ApEn value of the output signals on the electrodes 2, 3, 6, and 7 in three cases. It can be seen that the ApEn values on the electrodes 2 and 3 are bigger than those on electrodes 6 and 7. As superficial gas velocity increases, the ApEn values on the electrodes 2 and 3 decrease while those on the electrodes 6 and 7 increase. The particle-particle collision frequency in dense-phase region is higher than that in dilute phase region. In fact, the ApEn value of the output signals of the ESA indicates the complexity of the electrostatic signal itself but does not completely refer to the

TABLE 2: Experimental parameters.

Case	Total transportation differential pressure/(MPa)	Fluidizing gas/(m <sup>3</sup> /h)	Supplement gas/(m <sup>3</sup> /h)	Voidage	Mass flow rate/(kg/s)	Superficial gas velocity/(m/s)
Case 1	1	0.1925	0.3904	0.503	0.4965	5.7
Case 2	1	0.1911	0.3833	0.612	0.3883	6.9
Case 3	1	0.2135	0.4166	0.704	0.2964	8.1

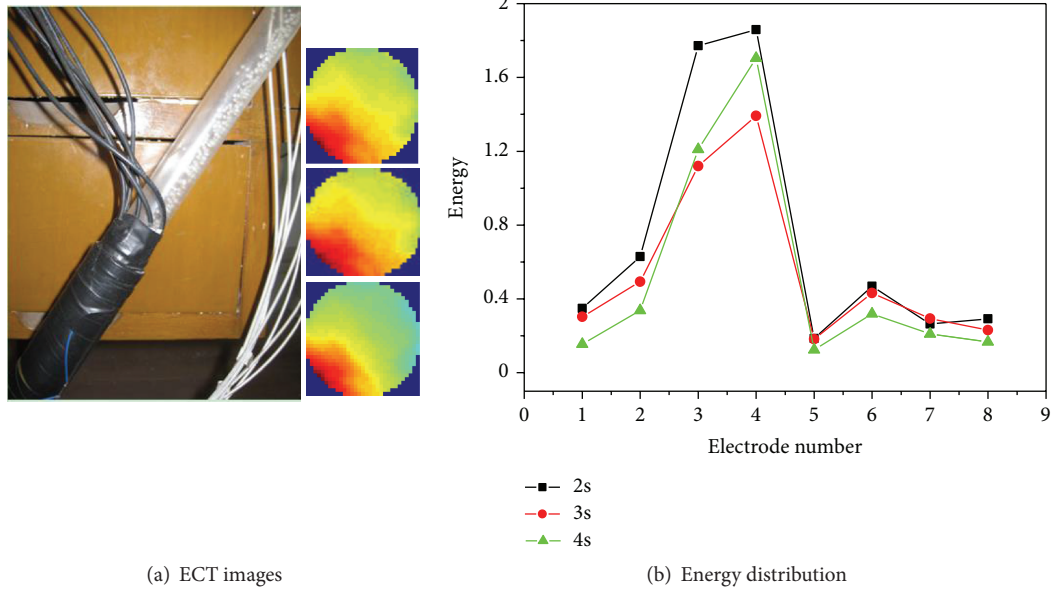


FIGURE 9: ECT images and electrostatic signal energy distribution for quarter flow (the electrode positions of the ESA are shown in Figure 2).

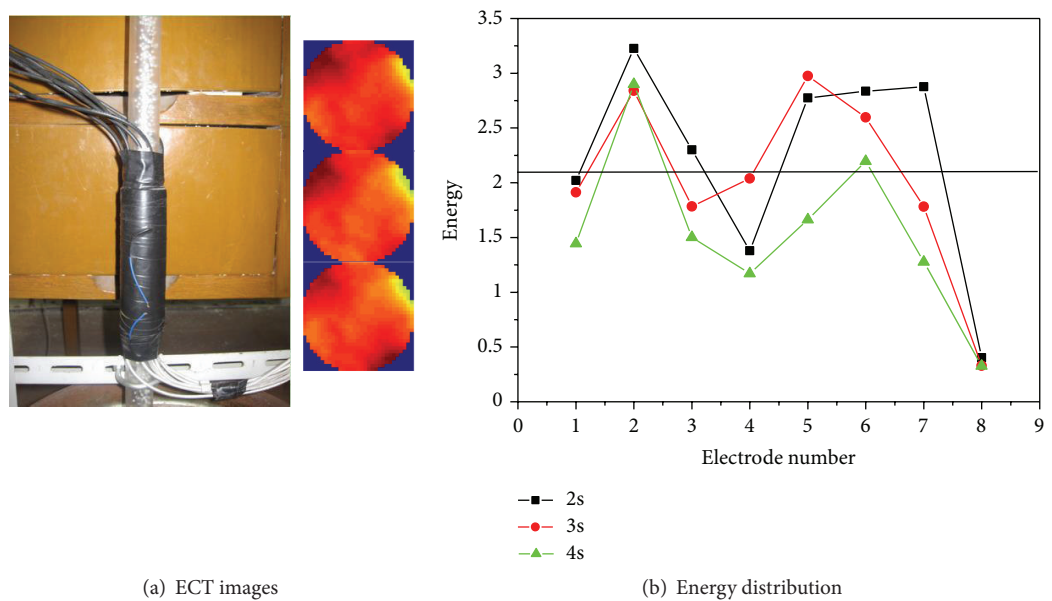
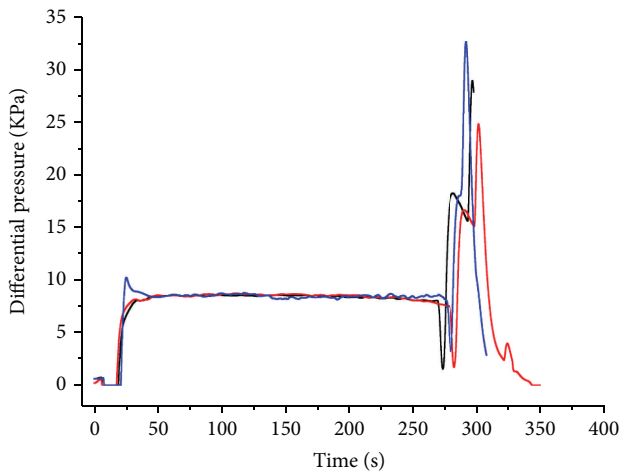


FIGURE 10: ECT images and electrostatic signal energy distribution for full pipe flow.

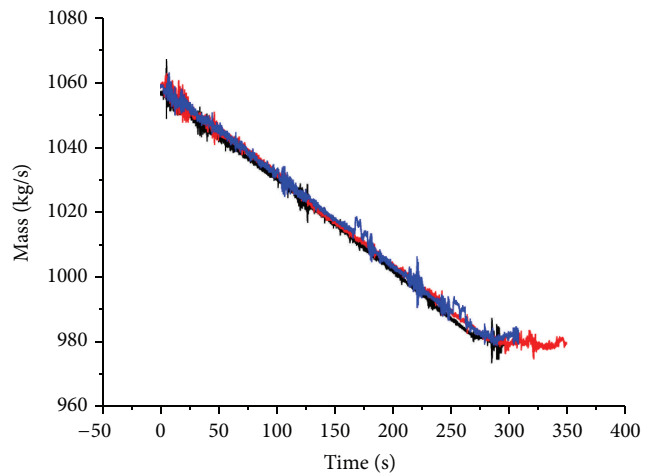
TABLE 3: Statistics of electrostatic signals of the eight electrodes with increasing superficial gas velocity.

Electrode	ApEn	Peak frequency	Amplitude of the peak frequency
Dense-phase region			
1	First increase then decrease	First increase then decrease	No obvious change
2	Decrease	Increase	No obvious change
3	Decrease	Increase	Decrease
4	First increase then decrease	Increase	Decrease
Dilute phase region			
5	Increase	First decrease then increase	Decrease
6	Increase	First decrease then increase	Decrease
7	Increase	Increase	Decrease
8	Decrease	Decrease	Decrease



— Case 1  
— Case 2  
— Case 3

(a) Differential pressure signals



— Case 1  
— Case 2  
— Case 3

(b) Mass signals

FIGURE 11: Variation of differential pressure fluctuations and coal mass with time in three cases.

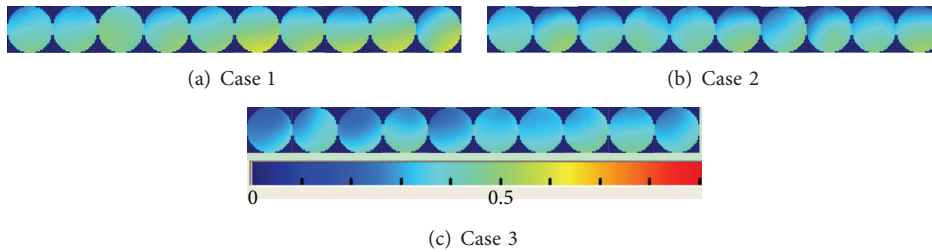


FIGURE 12: ECT images in the three cases.

randomness of the particles motion, because the electrostatic signal is influenced by other factors such as the radial and axial gradients of the particles charges and the variation of the particles charge with time. Obviously, particles charge gradient and variation are more random in the dense-phase

region. So, in the dilute phase regions the randomness of the electrostatic signals is weaker than that in the dense-phase region, though the particle velocity fluctuation in radial direction makes particles motion complex. While the superficial gas velocity increases, particle concentration

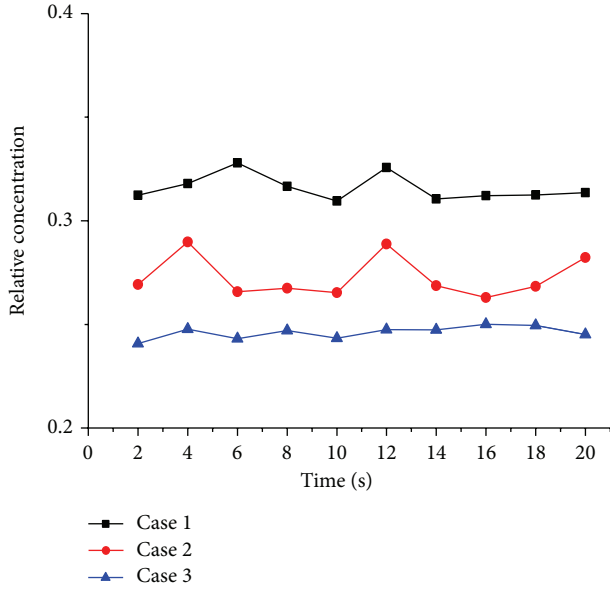


FIGURE 13: Average coal concentration over the cross-section of the pipeline in the three cases.

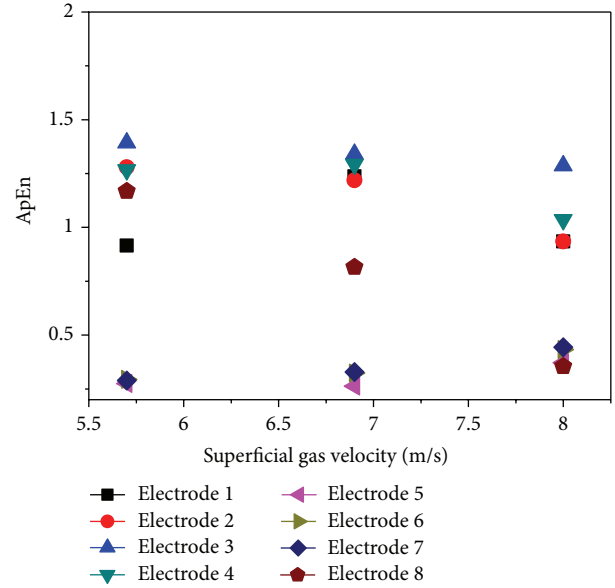


FIGURE 15: ApEn of eight electrode-electrostatic output signals.

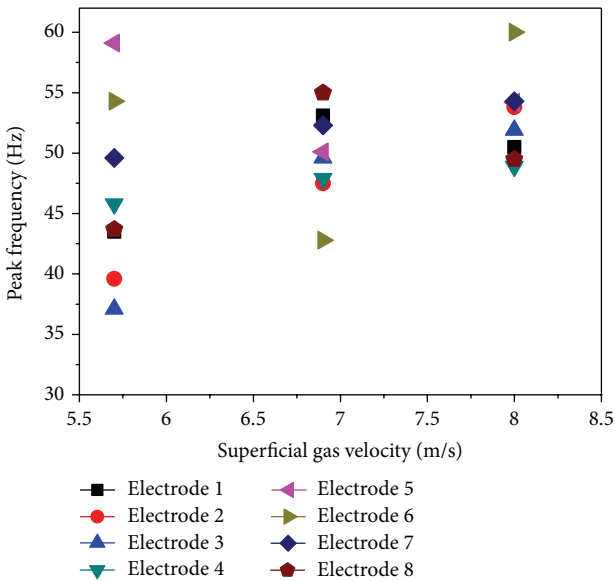


FIGURE 14: Peak frequencies of eight-electrode electrostatic output signals of the ESA.

in the dense-phase decreases. As a result, the difference of particle movement complexity in dense-phase and dilute phase region is reduced. In addition, compared with ECT images, it is found that when the difference between the ApEn values on the electrodes 2 and 3 and those on the electrodes 6 and 7 are smaller, the suspension property of coal particles is better.

## 6. Conclusions

The sensitivity of electrostatic sensor arrays (ESA) was investigated and analyzed through use of a finite element analysis software Ansoft Maxwell 3D. Experiments have been performed in a dense-phase pneumatic conveying system of pulverized coal, and electrostatic signals and coal particle distribution images over cross-section of the pipeline at superficial gas velocities of 5.7 m/s, 6.9 m/s, and 8.1 m/s were obtained through use of the ESA and ECT. The FEM modeling results indicated that the sensitivity distribution of the electrostatic sensor array is quite localized around each electrode and thus is mainly sensitive to the particles nearby it. This was also verified by the signals energy distribution of the ESA with eight electrodes under full pipe flow and quarter flow conditions in a gravity-fed flow rig. Experimental results in the dense-phase pneumatic conveying system of pulverized coal illustrated that the frequency domain features and ApEn value of the ESA output signals are useful for distinguishing the particle motion behavior in dense-phase and dilute phase regions of the conveying pipe. As the superficial gas velocity increases, the peak frequency value of the electrostatic signal increases linearly in dense-phase region, while that in dilute phase region is nonlinear. Therefore the increase of the axial particles velocity is the main dynamic change, while in dilute phase region the particles velocity fluctuation in the radial direction cannot be ignored. The ApEn value of the electrostatic signal in dense-phase region is larger than that in dilute phase region. When the ApEn value difference is smaller, the pulverized coal particles are better suspended. Therefore, the frequency domain features and ApEn value of the ESA output signals embody the difference in the characteristics of particles motion and its change rule with increasing the superficial gas velocity in dense-phase and dilute phase regions.

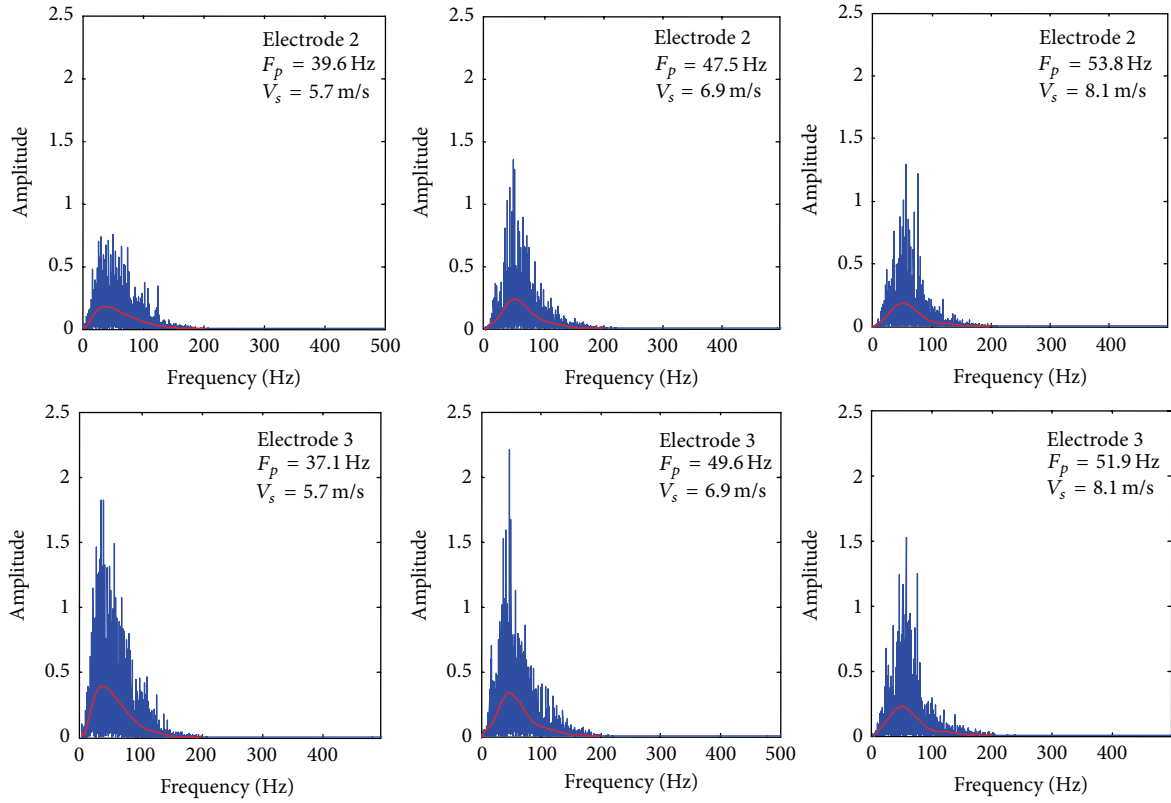


FIGURE 16: FFT spectrum of the electrostatic signals of the electrodes 2 and 3 for three superficial gas velocities.

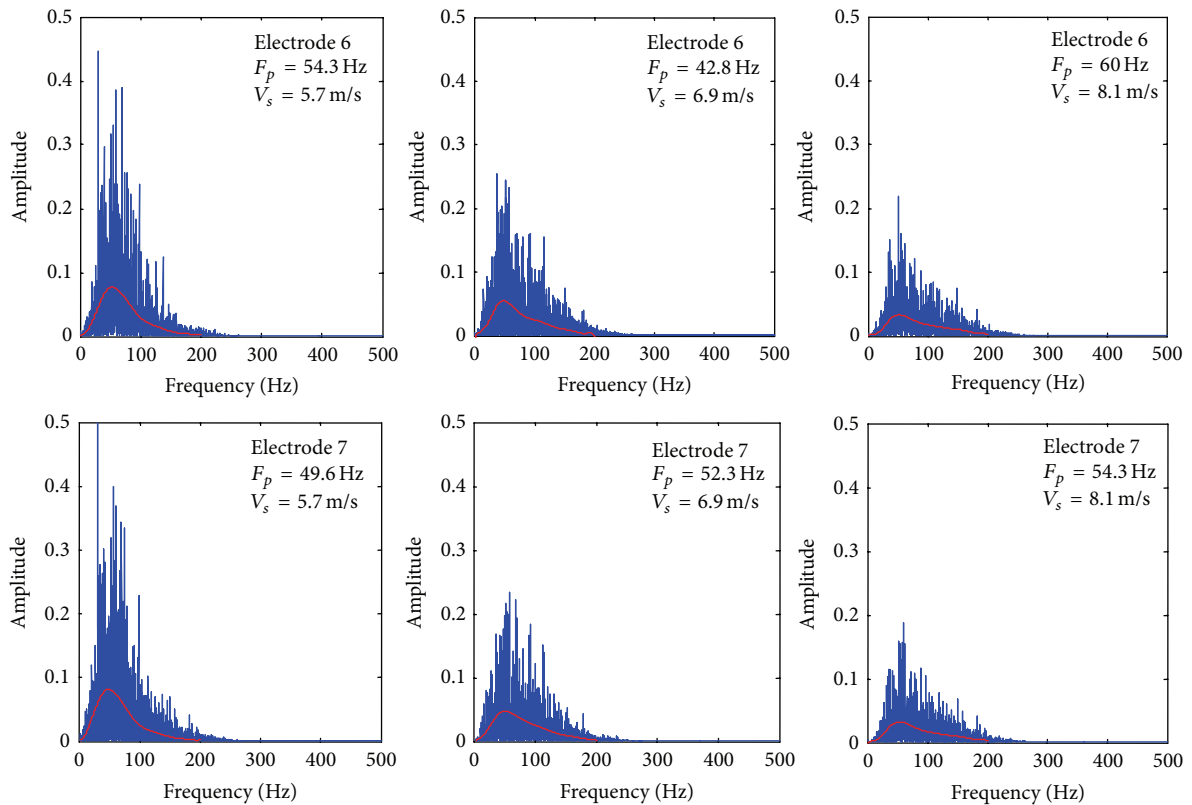


FIGURE 17: FFT spectrum of the electrostatic signals of the electrodes 6 and 7 for three superficial gas velocities.

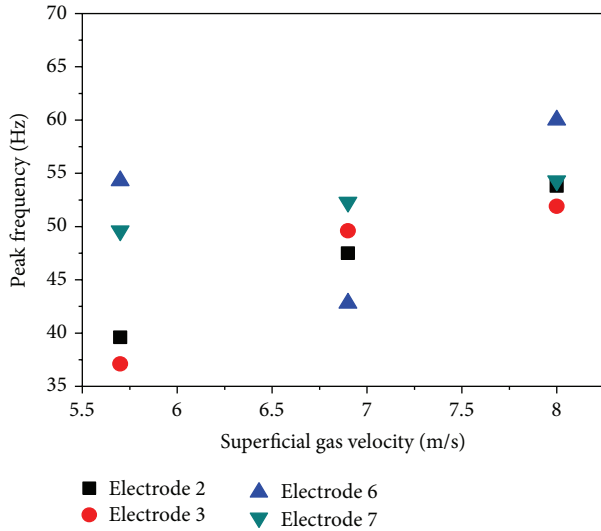


FIGURE 18: Peak frequencies of electrostatic signals of the electrodes 2, 3, 6, and 7 for three superficial gas velocities.

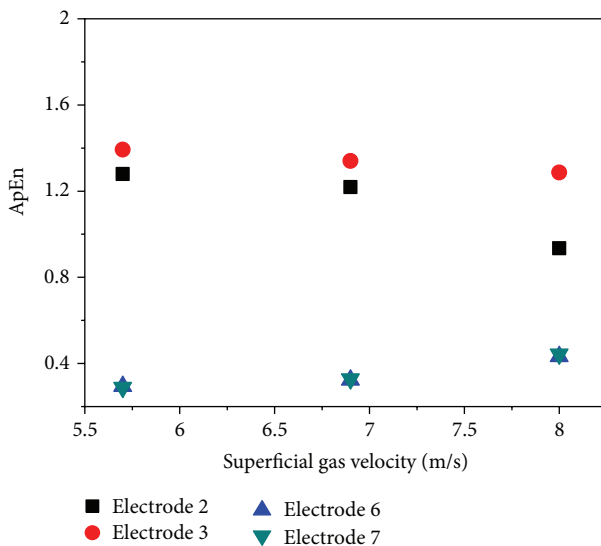


FIGURE 19: ApEn of electrostatic signals of electrodes 2, 3, 6, and 7 for three superficial gas velocities.

## Acknowledgments

The authors wish to express their gratitude to the Special Funds for the National Natural Science Foundation of China (no. 50906012), New Century Excellent Talents at Chinese Universities (NCET-12-0116), and the Major State Basic Research Projects of China (no. 2010CB227002).

## References

[1] Y. Tsuji, "Multi-scale modeling of dense phase gas-particle flow," *Chemical Engineering Science*, vol. 62, no. 13, pp. 3410–3418, 2007.

[2] J. Xiang and D. McGlinchey, "Numerical simulation of particle motion in dense phase pneumatic conveying," *Granular Matter*, vol. 6, no. 2-3, pp. 167–172, 2004.

[3] M. Sakai and S. Koshizuka, "Large-scale discrete element modeling in pneumatic conveying," *Chemical Engineering Science*, vol. 64, no. 3, pp. 533–539, 2009.

[4] W. Pu, C. Zhao, Y. Xiong et al., "Three-dimensional numerical simulation of dense pneumatic conveying of pulverized coal in a vertical pipe at high pressure," *Chemical Engineering and Technology*, vol. 31, no. 2, pp. 215–223, 2008.

[5] C. Zhao, C. Liang, X. Chen, W. Pu, P. Lu, and C. Fan, "Flow characteristics and Shannon entropy analysis of dense-phase pneumatic conveying under high pressure," *Journal of Southeast University*, vol. 23, no. 4, pp. 609–614, 2007.

[6] C. Liang, C. Zhao, X. Chen, W. Pu, P. Lu, and C. Fan, "Flow characteristics and Shannon entropy analysis of dense-phase pneumatic conveying of pulverized coal with variable moisture content at high pressure," *Chemical Engineering and Technology*, vol. 30, no. 7, pp. 926–931, 2007.

[7] Y. Yan, "Flow measurement of particulate solids in pipelines," *Flow Measurement and Instrumentation*, vol. 11, no. 3, p. 151, 2000.

[8] Y. Yan, "Mass flow measurement of bulk solids in pneumatic pipelines," *Measurement Science and Technology*, vol. 7, no. 12, pp. 1687–1706, 1996.

[9] J. Yang, Y. Wen, and P. Li, "Feature extraction and identification of leak acoustic signal in water distribution pipelines using correlation analysis and approximate entropy," *Chinese Journal of Scientific Instrument*, vol. 30, no. 2, pp. 272–279, 2009.

[10] R. Li, F. Lu, H. Xu, and L. Zhang, "Novel approach for load analysis based on local wave and approximate entropy," *Proceedings of the Chinese Society of Electrical Engineering*, vol. 30, no. 25, pp. 51–58, 2010.

[11] P. Lin, X. Wang, B. Chen, and Y. Huang, "Character of approximate entropy and its application in the complexity measurement of gas-solid fluidized bed," *Journal of Chemical Engineering of Chinese Universities*, vol. 18, no. 3, pp. 281–286, 2004.

[12] S. Matsusaka and H. Masuda, "Electrostatics of particles," *Advanced Powder Technology*, vol. 14, no. 2, pp. 143–166, 2003.

[13] M. Nifuku and H. Katoh, "A study on the static electrification of powders during pneumatic transportation and the ignition of dust cloud," *Powder Technology*, vol. 135-136, pp. 234–242, 2003.

[14] Y. Yan, B. Byrne, S. Woodhead, and J. Coulthard, "Velocity measurement of pneumatically conveyed solids using electrodynamic sensors," *Measurement Science and Technology*, vol. 6, no. 5, pp. 515–537, 1995.

[15] C. Xu, B. Zhou, D. Yang, G. Tang, and S. Wang, "Velocity measurement of pneumatically conveyed solid particles using an electrostatic sensor," *Measurement Science and Technology*, vol. 19, no. 2, Article ID 024005, pp. 167–175, 2008.

[16] C. Xu, S. Wang, G. Tang, D. Yang, and B. Zhou, "Sensing characteristics of electrostatic inductive sensor for flow parameters measurement of pneumatically conveyed particles," *Journal of Electrostatics*, vol. 65, no. 9, pp. 582–592, 2007.

[17] C. Xu, C. Liang, B. Zhou, and S. Wang, "HHT analysis of electrostatic fluctuation signals in dense-phase pneumatic conveying of pulverized coal at high pressure," *Chemical Engineering Science*, vol. 65, no. 4, pp. 1334–1344, 2010.

[18] C. Xu, S. Wang, M. Kong, Y. Zhao, and Y. Lu, "Spatial sensitivity of electrodynamic sensor for flow parameters measurement of pneumatically conveyed solids," *Acta Metrologica Sinica*, vol. 27, no. 4, pp. 335–396, 2006.

- [19] C. Xu, J. Li, H. Gao, and S. Wang, "Investigations into sensing characteristics of electrostatic sensor arrays through computational modelling and practical experimentation," *Journal of Electrostatics*, vol. 70, no. 1, pp. 60–71, 2012.
- [20] X. Cong, X. Guo, X. Gong, H. Lu, and W. Dong, "Experimental research of flow patterns and pressure signals in horizontal dense phase pneumatic conveying of pulverized coal," *Powder Technology*, vol. 208, no. 3, pp. 600–609, 2011.
- [21] S. M. Pincus, "Approximate entropy as a measure of system complexity," *Proceedings of the National Academy of Sciences of the United States of America*, vol. 88, no. 6, pp. 2297–2301, 1991.
- [22] J. L. Sinclair and R. Jackson, "Gas-particle flow in a vertical pipe with particle-particle interactions," *AIChE Journal*, vol. 35, no. 9, pp. 1473–1486, 1989.

## Research Article

# Particle Dispersion Behaviors of Dense Gas-Particle Flows in Bubble Fluidized Bed

Sihao Lv,<sup>1</sup> Guohui Li,<sup>2</sup> and Xue Liu<sup>3</sup>

<sup>1</sup> College of Chemistry and Environmental Engineering, Dongguan University of Technology, Dongguan 523808, China

<sup>2</sup> School of Electronic and Information Engineering, Dalian Jiaotong University, Dalian 116028, China

<sup>3</sup> Performance Test Center, Harbin Power System Engineering and Research Institute, Harbin 150046, China

Correspondence should be addressed to Guohui Li; [maillgh@djtu.edu.cn](mailto:maillgh@djtu.edu.cn)

Received 11 January 2013; Revised 26 April 2013; Accepted 20 May 2013

Academic Editor: Guan Heng Yeoh

Copyright © 2013 Sihao Lv et al. This is an open access article distributed under the Creative Commons Attribution License, which permits unrestricted use, distribution, and reproduction in any medium, provided the original work is properly cited.

An Euler-Euler two-fluid model incorporating a developed momentum transfer empirical coefficient is developed to study the particle dispersion behaviors of dense gas-particle flows in gas-fluidization reactor. In this model, the four-way couplings among gas-particles, particle-gas, and particle-particle collisions are fully considered based on kinetic theory of granular flows and an improved smooth continuous drag coefficient is utilized. Gas turbulent flow is solved by large eddy simulation. The particle fraction, the time-averaged axial particle velocity, the histogram of particle fluctuation velocity, and the wavelet analysis of pressure signals are obtained. The results are in good agreement with experimental measurements. The mean value and the variance of axial particle velocity are greater than those of radial particle velocities. Particle collision frequencies at bubble vibrant movement regions along axial direction are much higher than those of radial direction and attenuated along height increase. Low-frequency component of pressure signal indicating the bubble movement behaviors in the center of reactor is stronger than wall regions. Furthermore, the negative values represent the passed bubble and positive peak values disclose the continuous motion of single bubble.

## 1. Introduction

Circulating fluidized beds (CFB) have been widely applied in the chemical industry due to their practical applications, such as riser, downer, and gas-fluidized bubble bed [1]. The efficiency of systems relies primarily on their hydrodynamic behaviors, especially for particle dispersion behaviors. Thus, a better understanding of the dynamics of fluidized beds is the key problem to improve the efficiency and scale-up laboratory, which can be achieved through numerical simulation due to the rapid development of computer hardware technique. Except the traditional experimental measurement approach, the computational fluid dynamics (CFD) a powerful tool for the better understanding of physical phenomena involved in the gas-particle fluidization system [2, 3].

Generally, mathematical simulation of gas-particle bubbling fluidized bed can be divided into the Euler-Euler two-fluid model and Euler-Lagrange discrete particle model.

In the Eulerian-Lagrangian approach, numerous discrete particles are tracked and interparticle collisions are simulated using a hard-sphere or a soft-sphere model. In the framework of two-fluid model, particles and gas are described as interpenetrating continua and the two sets of conservation equations for mass, momentum, and energy are numerically solved. The Eulerian-Eulerian models require closure laws for particle interactions, interaction between gas and particle phases to close the system of equations, which are generally a set of models, either physical or empirical correlations. Comparing these two approaches, due to the huge computation consumption for discrete particle model in industry application, two-fluid model has successfully applied. So far, the most popular theory for closing particle-particle collision is the kinetic theory of granular flow (KTGF), firstly proposed by Gidaspow [4, 5]. It is analogous with the kinetic theory of gases and the macroscopic behavior of particle phase is described by the equations that account for

the energy associated with particles arising out of collisions and fluctuating motions of the particles. The kinetic and collision momentum transfer due to particle collisions can be modeled as a function of the local particle concentration and the fluctuating motion of the particles. Ding and Gidaspow 1990 [6] firstly proposed the concept of granular temperature to indicate particle collisions, which is defined as  $\theta = \langle C^2 \rangle / 3$ , where  $C$  is the random fluctuating velocity of the particulate phase. Thus, the rheologic properties of particles, the solid phase pressure, viscosity of particles, conductive energy flux, and dissipation are considered as a function of granular temperature. Simulations using kinetic theory of granular flow have been reported by many researchers in gas-particle fluidization [7–20]. In KFGT, the particle flow is assumed to be laminar flows instead of large-scale turbulent flows. In order to solve this point, Zhou et al. [21–26] research group of Tsinghua University have successfully proposed a series of kinetic energy equations for gas and particle phases ( $k-k_p$ ), second-order and unified second-order moment (SOM, USM) models for dilute and dense gas-particle turbulent flows, that is,  $k-\varepsilon-k_p$  model,  $k-\varepsilon-k_p-\theta$  four-equation model,  $k-\varepsilon-k_p-\varepsilon_p-\theta$  five-equation model, USM- $\theta$  particle temperature model, and subgrid scale USM model to simulate particle turbulent flows based on the Reynolds-averaged Navier-Stokes (RANS) method. In USM model, the anisotropy between gas and particle two-phase stresses and their interaction can be fully considered by establishing the two-phase Reynolds stresses transport equations and their stress correlations.

Besides the effects of particle and particle collision, the other very important factor on gas-particle two-phase turbulent flow behavior is the momentum transfer process between gas and particle phases. This kind of transfer behavior can be typically represented by drag force. Due to the fact that it is difficult to get an accurate value restricted to different Reynolds numbers and packing fractions, as well as in terms of homogeneity, monodispersity, and sphericity of the particles, a large number of the gas-solid drag forces have some limitations due to empirical relations from the measurements. Although the relations by Ergun and Orning [27], Wen and Yu [28], and Giblaro et al. [29] have been the most widely used, there is at present no real consensus as to what the most accurate prediction for the drag force is at given Reynolds numbers and packing fraction. Thus, so far, all correlations are all based on experimental data. In order to assure these correlations more accurately in theory, Huilin et al. 2003 [17] introduced a weighted average two-scale switch function to prevent the discontinuous behaviors when solid volume fraction is less than 0.2. Beetstra et al. 2007 [30] proposed a drag force model based on the kinetic theory of granular flows and lattice Boltzmann data for monodisperse and bidisperse systems. Even if these corrections have successfully got better results in specified cases, they should be further validated for wide applications.

As we have known, the motion of bubbles can produce the pressure fluctuations and the amplitude of the pressure fluctuations is definitely related to the particle dispersion behaviors. Successfully, wavelet analysis approach has identified the multiscale frequency wave components for bubble

upward and downward movements with different particle dispersion behaviors. Van Der Schaaf 1998 [31] demonstrated that the pressure fluctuations in a gas-solid fluidized bed could be partitioned into a fractional Brownian motion (FBM) and Gaussian white noise (GWN), caused by the jet and the formation of the small bubbles near the distributor. He et al. 1997 [32] indicated that the upward moving compression waves originate from the formation and coalesce of gas bubbles, and downward moving compression waves are caused by gas bubble eruptions at the fluidized bed surface. Lu and Li 1999 [33] found that the peak frequency of these signals can represent the bubbling frequency, and the average peak value can represent the bubble size. Although many models have been developed to describe these behaviors, a valid method to process the pressure fluctuation signals is to be further developed and validated.

To date, considering the effects of gas-particle moment transfer represented by transfer coefficient coupling KGFT theory and wavelet analysis of pressure fluctuation approaches on dense particle dispersion behaviors in bubble fluidized bed have never been reported. Compared to RANS approach using LES, the instantaneous flow information of two phases and coherent structure of particle dispersion only can be provided in detail rather than the RANS. In this study, coupled with LES, KGFT, and improved transfer coefficient model, as well as wavelet analysis approach, are used to study the particle hydrodynamics and transport characteristics.

## 2. Conservation Equations of Two-Phase Turbulent Flows

**2.1. Governing Equations.** The continuity equations, representing the mass conservation for gas and solid phases, respectively, can be written as follows:

$$\begin{aligned} \frac{\partial}{\partial t} (\varepsilon_g \rho_g) + \nabla \cdot (\varepsilon_g \rho_g v_g) &= 0, \\ \frac{\partial}{\partial t} (\varepsilon_s \rho_s) + \nabla \cdot (\varepsilon_s \rho_s v_s) &= 0, \end{aligned} \quad (1)$$

where  $v$  is the velocities,  $\rho$  is densities, and  $\varepsilon$  is the volumetric fractions of gas and solid phases, respectively. Subscript  $g$  is gas phase and  $s$  is solid phase. In relation to single-phase continuity equation, the above equations differ by the presence of the phases volumetric fractions. It is defined as follows:

$$\varepsilon_g + \varepsilon_s = 1. \quad (2)$$

The momentum equations for gas and solid phases, respectively, can be written as follows:

$$\begin{aligned} \frac{\partial}{\partial t} (\varepsilon_g \rho_g v_g) + \nabla \cdot (\varepsilon_g \rho_g v_g v_g) &= -\varepsilon_g \nabla P_g + S_{g,g} \\ &\quad + \nabla \cdot \tau_g + \beta (v_g - v_s), \\ \frac{\partial}{\partial t} (\varepsilon_s \rho_s v_s) + \nabla \cdot (\varepsilon_s \rho_s v_s v_s) &= P_s + S_{s,s} + \nabla \cdot \tau_s - \beta (v_g - v_s). \end{aligned} \quad (3)$$

TABLE 1: System geometry and properties.

Particle shape	Spherical	Reactor width	400 mm
Particle materials	Glass	Reactor height	3000 mm
Particle density	2480 kg/m <sup>3</sup>	Cell width dx	10 mm
Particle diameter	0.225 mm	Cell height dy	20 mm
Initial volume concentration	0.4	The number cell nx	40
Maximum packing volume concentration	0.6413	The number cell ny	150
Initial particle packing height	110 mm	Diameter of jet hole	40 mm
Gas dynamic viscosity	1.789e - 5 kg/m·s	Minimum jet velocity	2.0 m/s
Gas density	1.225 kg/m <sup>3</sup>	Jet velocity	27.5 m/s

In (3),  $P_g$  is the thermodynamic pressure,  $\beta$  is the interface drag coefficient between gas phase and particle phase,  $\tau_g$  is the gas phase viscous stress tensor,  $S_{g,g}$  is the gravity source term of gas phase,  $\mu_g$  is the dynamic viscosity and assumed to be constant and is set equal to  $1.8 \times 10^{-5}$ ,  $g$  is gravitational accelerations,  $I$  is the unit tensor, subscript lam is the laminar flow, and  $t$  is the turbulence flow.

2.2. *Closure for Stress Equations.* The Newtonian rheology and the Stokes hypothesis are assumed for both gas phase and particle phase; the viscous stress tensor of gas and particle phase are computed as follows:

$$\begin{aligned}\tau_g &= \mu_g \left[ \nabla \mathbf{v}_g + (\nabla \mathbf{v}_g)^T \right] - \frac{2}{3} \mu_g (\nabla \cdot \mathbf{v}_g) \mathbf{I}, \\ \mu_g &= \mu_{g,\text{lam}} + \mu_t, \\ \tau_s &= (-p_s + \varepsilon_s \xi_s \nabla \cdot \mathbf{v}_s) \delta_{ij} - 2\varepsilon_s \mu_s S_s, \\ S_s &= \frac{1}{2} \left[ \nabla v_s + (\nabla v_s)^T \right] - \frac{1}{3} \nabla v_g.\end{aligned}\quad (4)$$

The gas is assumed to be incompressible and has a constant density. Gas turbulent flow is solved by large eddy simulation; that is, the larger-scale eddy is directly solved by Navier-Stokes equations and the smaller-scale eddy is modeled by subgrid scale model. The traditional Smagorinsky's [34] eddy viscosity has a problem that there is an overlarge eddy viscosity dissipation at wall. In this paper, empirical corrected model presented by Yuu et al. 2000 [35] is utilized; it is as follows:

$$\begin{aligned}\mu_t &= C_{vt} C_\varepsilon^{1/3} \rho_g \Delta \left( \frac{-A_2 + \sqrt{A_2^2 + 4A_1(A_3 + A_4)}}{2A_1} \right), \\ \Delta &= (\Delta x \Delta y \Delta z)^{1/3}, \\ A_1 &= \frac{C_\varepsilon}{\Delta}, \\ A_2 &= \frac{6\pi D D_p^2}{\text{Re}} \left( 1 + 0.15 \overline{\text{Re}}_p^{0.687} \right) \frac{\bar{n}}{aT_L + 1}, \\ A_3 &= 2C_{vt} C_\varepsilon^{1/3} \Delta \overline{D}_D^2,\end{aligned}$$

$$A_4 = \frac{3\pi C_{vt} C_\varepsilon^{1/3} \Delta D_p D^2 \left( 1 + 0.15 \overline{\text{Re}}_p^{0.687} \right)}{\sigma \text{Re}} \frac{\partial \bar{n}}{\partial x_i} (\bar{u}_i - \bar{u}_{p_i}). \quad (5)$$

2.3. *Particle Temperature Equations.* The conservation equation of particle fluctuating energy or translational granular temperature is given as follows:

$$\begin{aligned}\frac{3}{2} \left[ \frac{\partial}{\partial t} (\varepsilon_s \rho_s \theta) + \nabla \cdot (\varepsilon_s \rho_s \theta \mathbf{v}_s) \right] &= (-\nabla P_s I + \tau_s) + \nabla \cdot (\kappa_s \nabla \theta) \\ &\quad - \gamma_s - 3\beta\theta,\end{aligned}\quad (6)$$

where  $k_s$  is the conductivity coefficient of granular temperature:

$$k_s = 2\varepsilon_s^2 \rho_s d_s g_0 (1 + e) \left( \frac{\theta}{\pi} \right)^{1/2}. \quad (7)$$

The translational fluctuation energy dissipation rate is

$$\gamma_s = 3(1 - e)^2 \varepsilon_s^2 \rho_s g_0 \theta \left[ \frac{4}{d_s} \left( \frac{\theta}{\pi} \right)^{1/2} - \nabla \cdot \mathbf{v}_s \right]. \quad (8)$$

The particle pressure is

$$P_s = \varepsilon_s \rho_s \theta [ +2(1 + e) g_0 \varepsilon_s ], \quad (9)$$

where  $\theta$  is the particle temperature and  $e$  is the restitution coefficient of particles.

The particle dynamic viscosity is simulated as follows:

$$\begin{aligned}\mu_s &= \frac{4}{5} \varepsilon_s^2 \rho_s d_s g_0 (1 + e) \sqrt{\frac{\theta}{\pi}} \\ &\quad + \frac{10\rho_s d_s \sqrt{\pi\theta}}{96(1 + e)\varepsilon_s g_0} \left[ 1 + \frac{4}{5} g_0 \varepsilon_s (1 + e) \right]^2,\end{aligned}\quad (10)$$

where  $d_s$  is the particle diameter and  $g_0$  is the radial distribution function at contact particle:

$$g_0 = \left[ 1 - \left( \frac{\varepsilon_s}{\varepsilon_{s,\text{max}}} \right)^{1/3} \right]^{-1}, \quad (11)$$

where  $\varepsilon_{s,\text{max}}$  is the particle maximum volume fraction at random packing.

The particle bulk viscosity with the effective coefficient of restitution is computed as follows:

$$\xi_s = \frac{4}{5} \varepsilon_s \rho_s d_s g_0 (1 + e) \left( \frac{\theta}{\pi} \right)^{1/2}. \quad (12)$$

**2.4. Momentum Transfer between Gas and Particle Phases.** In order to couple the momentum transfer between gas and particle phases, a model for the drag force is required. Ergun and Orning [27], Wen and Yu [28], and Giblaro et al. [29] have presented some correlations based on the experimental results, but there still are some limitations in theory. Although Beetstra et al. 2007 [30] established a drag force model based on the kinetic theory of granular flows and lattice Boltzmann data for monodisperse and bidisperse systems, it still should be further validated for applications. In this paper, based on the Huilin et al. 2003 [17] smooth function when solid volume fraction is less than 0.2 and the McKen and Pugsley 2003 [36] experimental results, a modified momentum transfer coefficient is presented.

$$\beta_1 = 0.001 \left( \frac{17.3}{\text{Re}_p} + 0.336 \right) \frac{\alpha_p \rho_g |\vec{u}_g - \vec{u}_p|}{d_p} \alpha_g^{-1.8}, \quad \alpha_g \leq 0.94,$$

$$\beta_2 = \frac{3}{4} C_D \frac{\varepsilon_s \varepsilon_g \rho_g |v_g - v_s|}{d_s} \varepsilon_g^{-2.65}, \quad 0.94 < \alpha_g \leq 0.99, \quad (13)$$

$$\beta_3 = \frac{3}{4} C_D \frac{\varepsilon_g \rho_g |v_g - v_s|}{d_s}, \quad 0.9 \leq \alpha_g \leq 0.99,$$

where  $C_D$  is the interface drag coefficient for a single particle in an infinite medium, calculated by:

$$C_D = \frac{24}{\text{Re}_p} \left[ 1 + 0.15 (\text{Re}_p)^{0.687} \right] \quad \text{Re}_p < 1000, \quad (14)$$

$$C_D = 0.44 \quad \text{Re}_p \geq 1000.$$

The Reynolds number  $\text{Re}$  based on the particle mean diameter  $d_s$  is a function of the particle sphericity  $\varphi_s$ :

$$\text{Re}_p = \frac{\varepsilon_g \rho_g |v_g - v_s| \varphi_s}{\mu_g}. \quad (15)$$

The final sooth function is

$$\beta = (1 - \varphi_1) \beta_1 + \varphi_1 ((1 - \varphi_2) \beta_2 + \varphi_2 \beta_3). \quad (16)$$

### 3. Numerical Strategy, Experiments Setup and Boundary Conditions

**3.1. Numerical Strategy.** The aforementioned governing equations are discretized using the finite differences approach with second-order upwind scheme and solved by point relaxation technique. Continuity equations are in the form

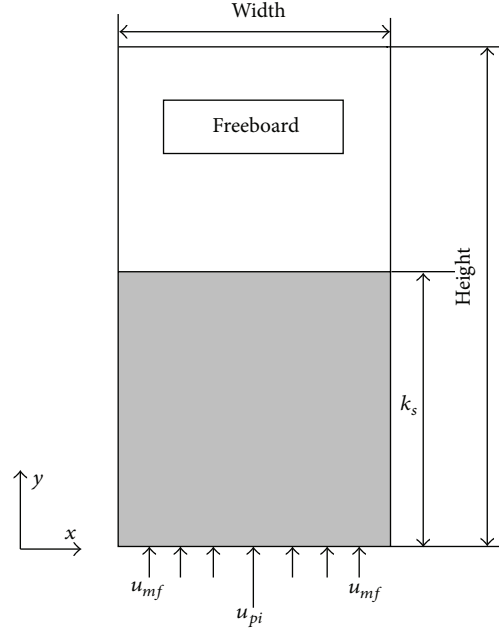


FIGURE 1: Schematic of two-dimensional bubble gas-fluidized bed.

TABLE 2: Type and flag of cells.

Flag	Type
1	Interior computational cell, no limitation of boundary conditions
3	Wall cell, no slip conditions
5	Inlet cell, specified inlet velocity
7	Outlet cell, gradient of variables is equal to zero

of implicit format and momentum equations are discretized over a staggered mesh. In the momentum equations, the convective terms are treated explicitly and all other terms are treated implicitly. The two-dimensional computational mesh is uniform staggered grid. Scalar quantity parameters such as the volume fraction of particles, density, and turbulent kinetic energy are stored at the main grid points. Staggered grid scheme is used and the velocity components are solved at the volume surfaces. A guessed pressure field is initialized for simulation start and the velocities are calculated from the momentum equations. The particulate phase continuity equation is solved using the updated velocities to compute the particulate phase volume fraction. The gas phase volume fraction is then computed. By using the gas volume fraction, the updated velocities the gas phase mass residue from continuity equation for gas phase is computed, which is used as a convergence criterion. For convergence, the gas pressure is corrected in each cell at a time until convergence is attained or the number of iterations exceeds an inner iteration limit (a number of iterations for one cell at a given time). The computations proceed until the entire computational domain is covered. At the end of such a computational sweep, if a pressure adjustment was necessary in any of the cells, the procedure

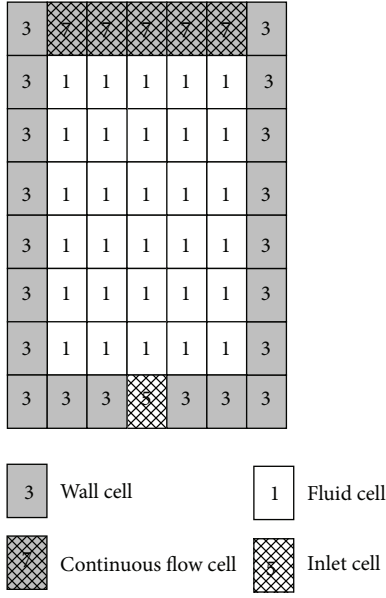


FIGURE 2: Computational cells.

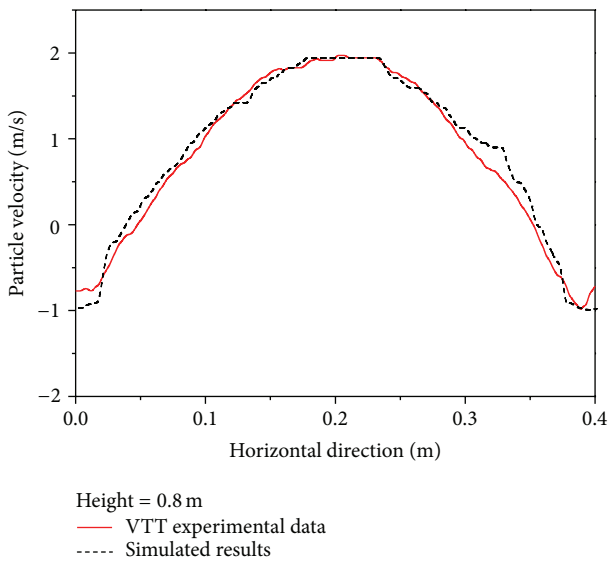


FIGURE 3: Validation of axial particle velocity and experimental data ( $h = 0.8$ ).

is repeated until simultaneous convergence in all the cells is obtained.

**3.2. Experimental Setup and Boundary Conditions.** Experimental setup is chosen from Peltola et al. 2010 [37]. The detailed geometry dimension, gas and particle property parameters are seen in Figure 1 and Table 1, respectively. Height of initial particle packing is set equal to 110 mm. Values of the volume fractions of particles at the inlet are set to 0.4 and of initial jet velocity to 27.5 m/s. At the outlet, the pressure was set to 1 atm. Cartesian coordinate system is used with 40 cells uniform computational mesh in radial direction and 150 cells uniform in axial direction. Cell flag and characters computational cells are shown in Table 2 and Figure 2.

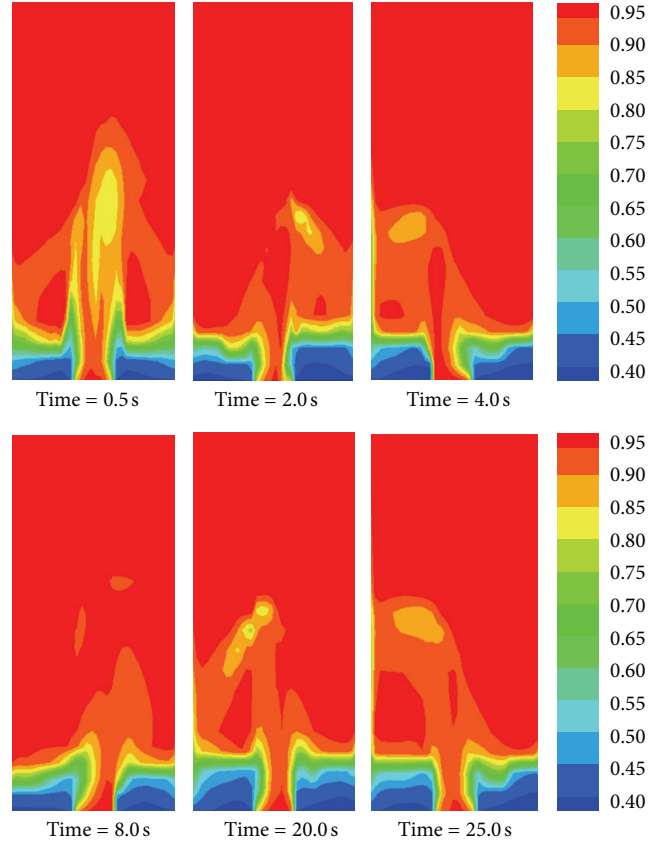


FIGURE 4: Bubbles movement behaviors in bubble gas-fluidized bed.

**3.3. Boundary Conditions.** At the wall, no slip condition is applied, in which the gas tangential and normal velocities were set to zero, and the normal velocity of particles was also set to zero. Pressure boundary condition is set to the zero for the normal gradient of pressure at the inlet and outlet. Velocity boundary condition is to provide the superficial gas velocity at the inlet cell and used to the free slip condition at the outlet profile. For temporal integration was used a fixed time step equal to  $1 \times 10^{-5}$  s based on the CFL stable criteria and the simulation running time is 25 seconds. The turbulent kinetic energy and its dissipation rate are taken by empirical expressions. The fully developed flow conditions of two-phase are taken at the outlet. At the wall, no slip condition is used for gas phase velocity and gas Reynolds stress are determined via production term including the effect of wall function for near wall grid nodes.  $\partial\varphi/\partial x = 0$  ( $\varphi = u_{g,p}, v_{g,p}, u'_{g,p}, \dots$ ). At the near-wall grid nodes, the wall-function approximation is used. At the axis, symmetric conditions are adopted for both the two phase. The convergence criteria for gas phase are mass source  $1.0 \times 10^{-5}$ .

## 4. Results and Discussion

In order to assure the accuracy of the simulation, the grid independence test for sensitivity of computed axial particle velocity distributions to spatial grid sizes is carried out. Here, coarse ( $75 \times 20$  axial by radial), medium ( $150 \times 40$ ), and

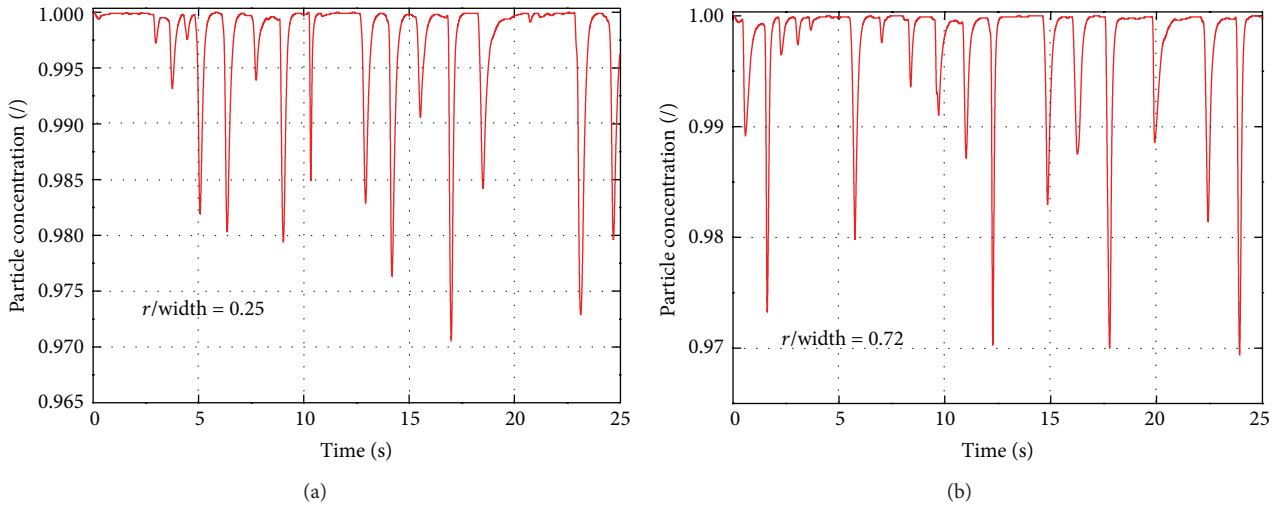


FIGURE 5: Distributions of instantaneous particle concentrations ( $h = 0.4$  m).

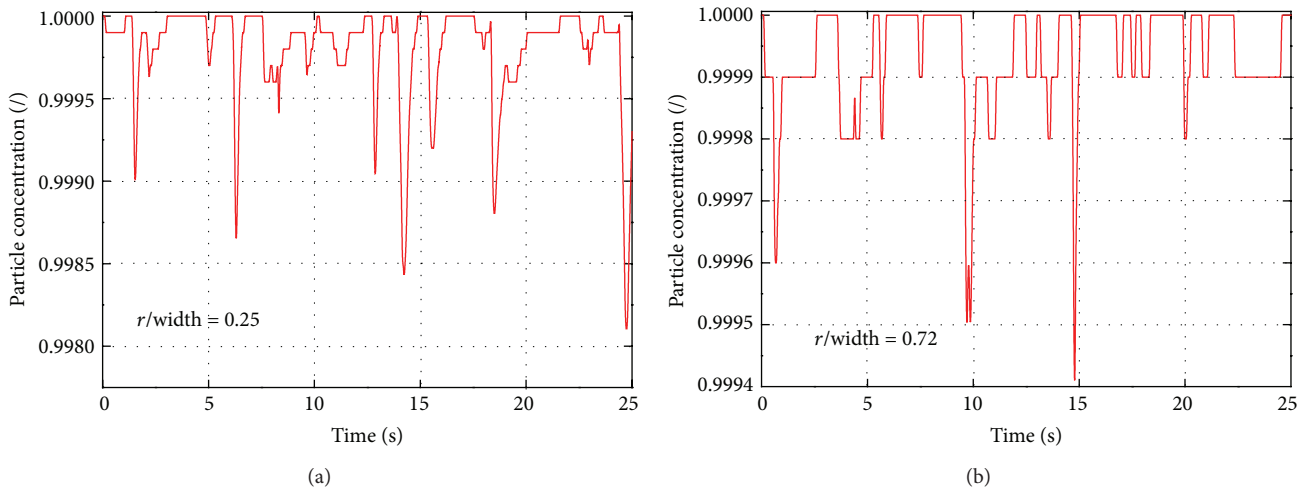


FIGURE 6: Distributions of instantaneous particle concentrations ( $h = 0.8$  m).

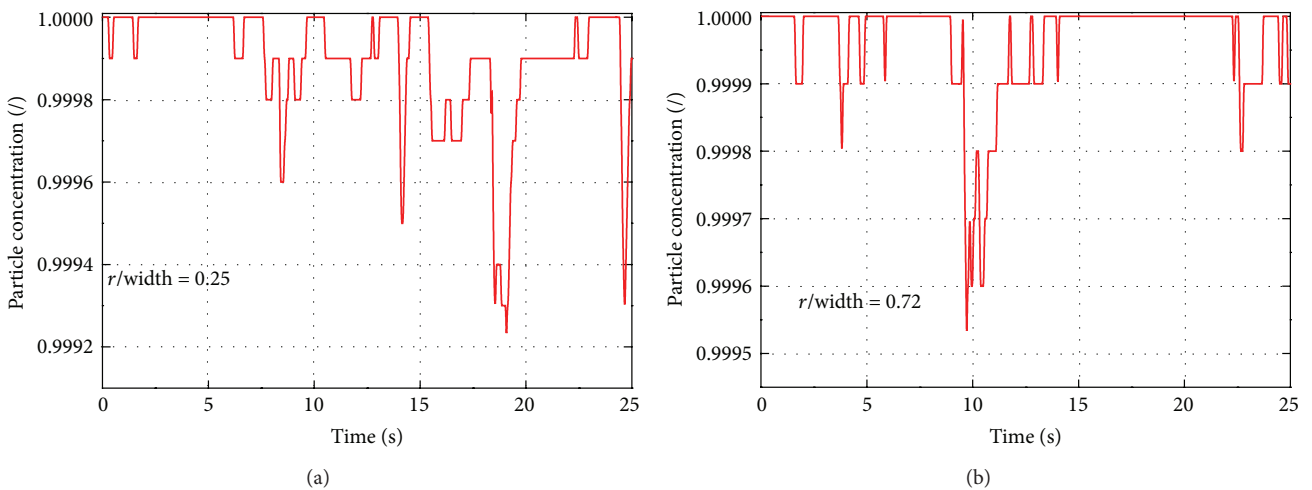


FIGURE 7: Distributions of instantaneous particle concentrations ( $h = 1.2$  m).

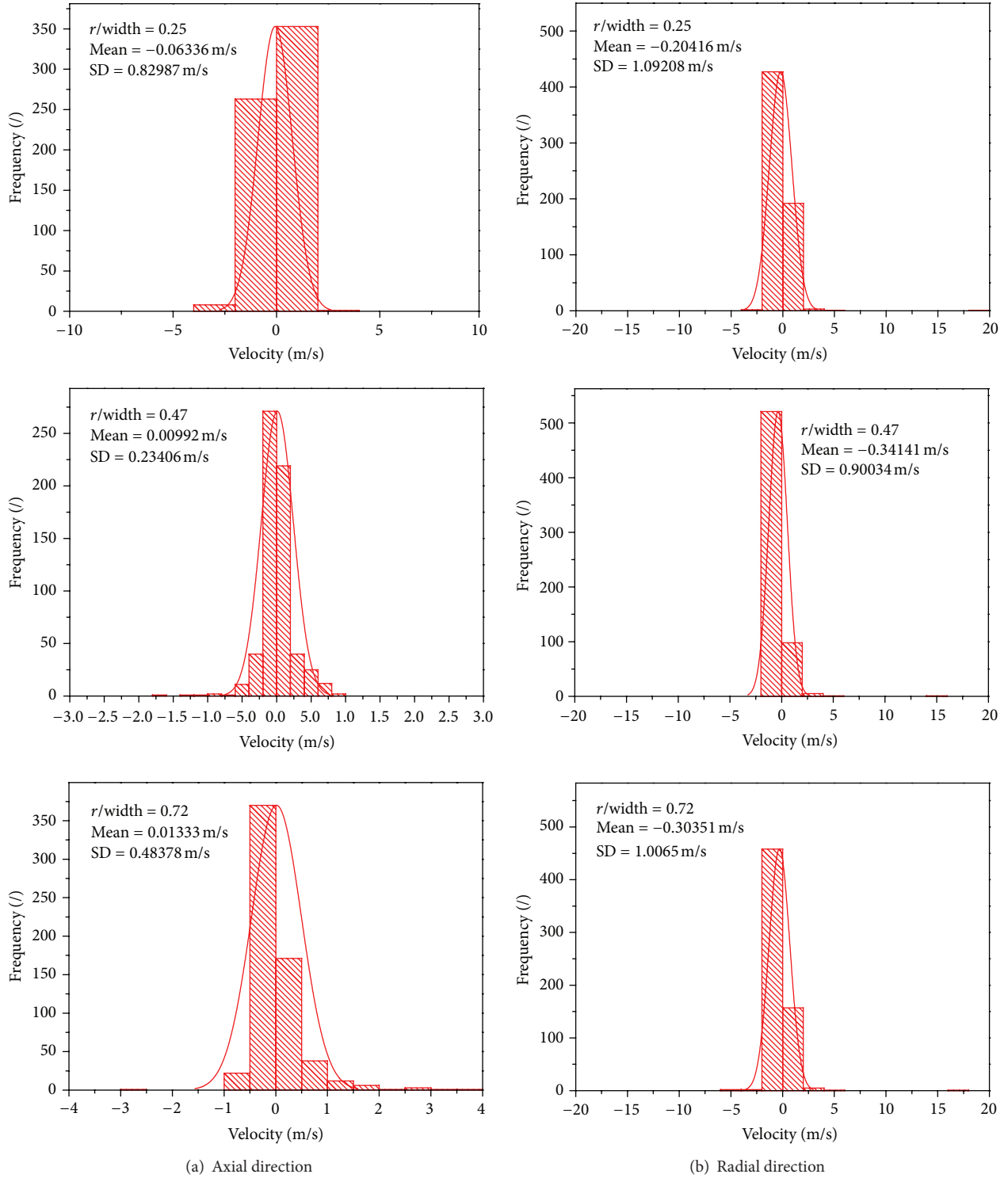


FIGURE 8: Distributions of particle velocity histogram at axial and radial directions ( $h = 0.4$  m).

fine ( $300 \times 80$ ) mesh grids are used in simulation process. Results indicated that the velocity distributions have similar trends along both axial directions, especially for medium and fine grids. So, we choose the medium grid size scheme for the simulations in order to achieve good accuracy within manageable computation time. In the meantime, the validation with experimental data also carried out for the statistical

time-averaged axial particle velocity, which is defined by the dimensionless time between 100 and 500, is determined as the sample of instantaneous velocity and is expressed by

$$\overline{u_p(x, y)} = \frac{1}{N} \sum_{i=1}^N u_{pi}(x, y, t). \quad (17)$$

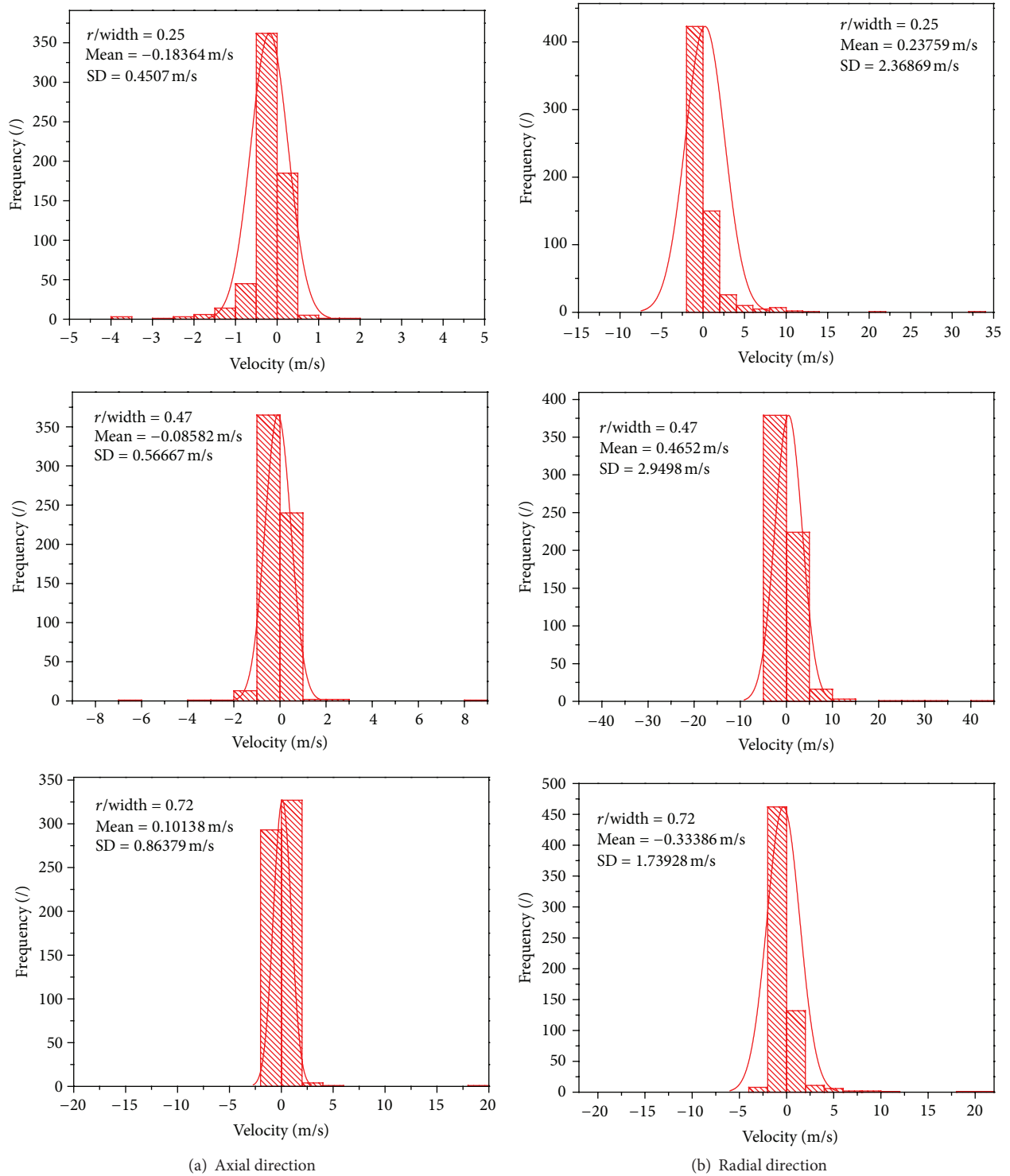


FIGURE 9: Distributions of particle velocity histogram at axial and radial directions ( $h = 0.8$  m).

The simulated results of the 0.8 m height are validated by experimental data (see Figure 4). We can see that the predicted results are in good agreement with experimental results from the literature [37]. So, this model and code in this paper have been accurately validated.

Figure 3 shows the bubbles movement behaviors in bubble gas-fluidized bed at 0.5 s, 2.0 s, 4.0 s, 8.0 s, 20.0, and 25.0 s, respectively. The bubble can be defined by the instantaneous local high porosity of particles. Two kinds of bubble behaviors named the faster and the slower are identified as the

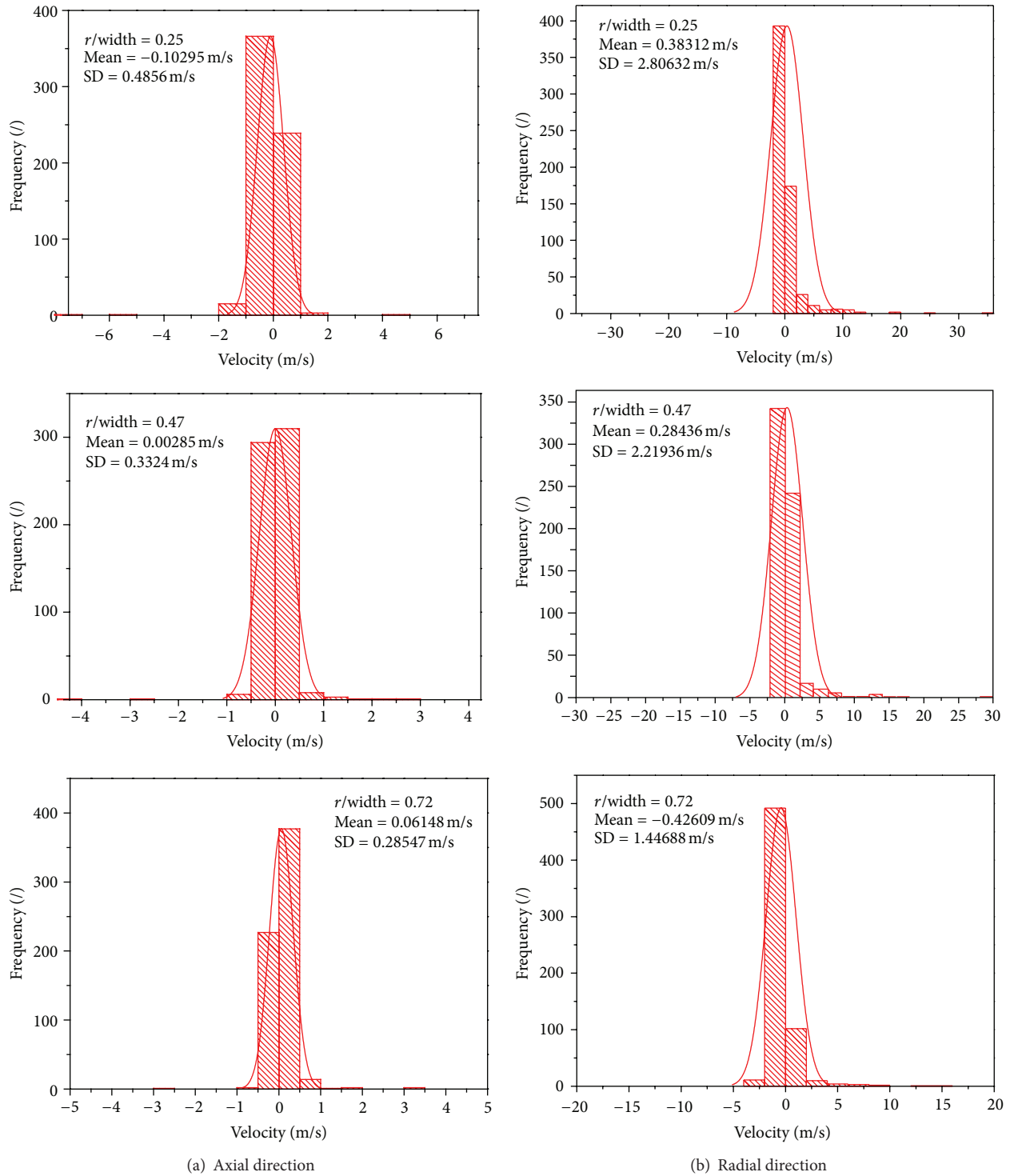


FIGURE 10: Distributions of particle velocity histogram at axial and radial directions ( $h = 1.2$  m).

halation layer around bubble, which is composed of motion circulation gas between bubble and environments. It would be affected by the bubble rising velocity. When bubble rising velocity is greater than gas gap velocity between bubble and environment, it is called the halation bubble. However, if bubble rising velocity is too fast to lead to the decrease of

halation layer, the most of gas has to circulate inside bubble. When gas gap velocity is larger than bubble rising, the gas in halation layer will penetrate the bubble; it is called non halation bubble.

When the higher jet gas passed through the interior reactor, the stronger interaction between gas and particle

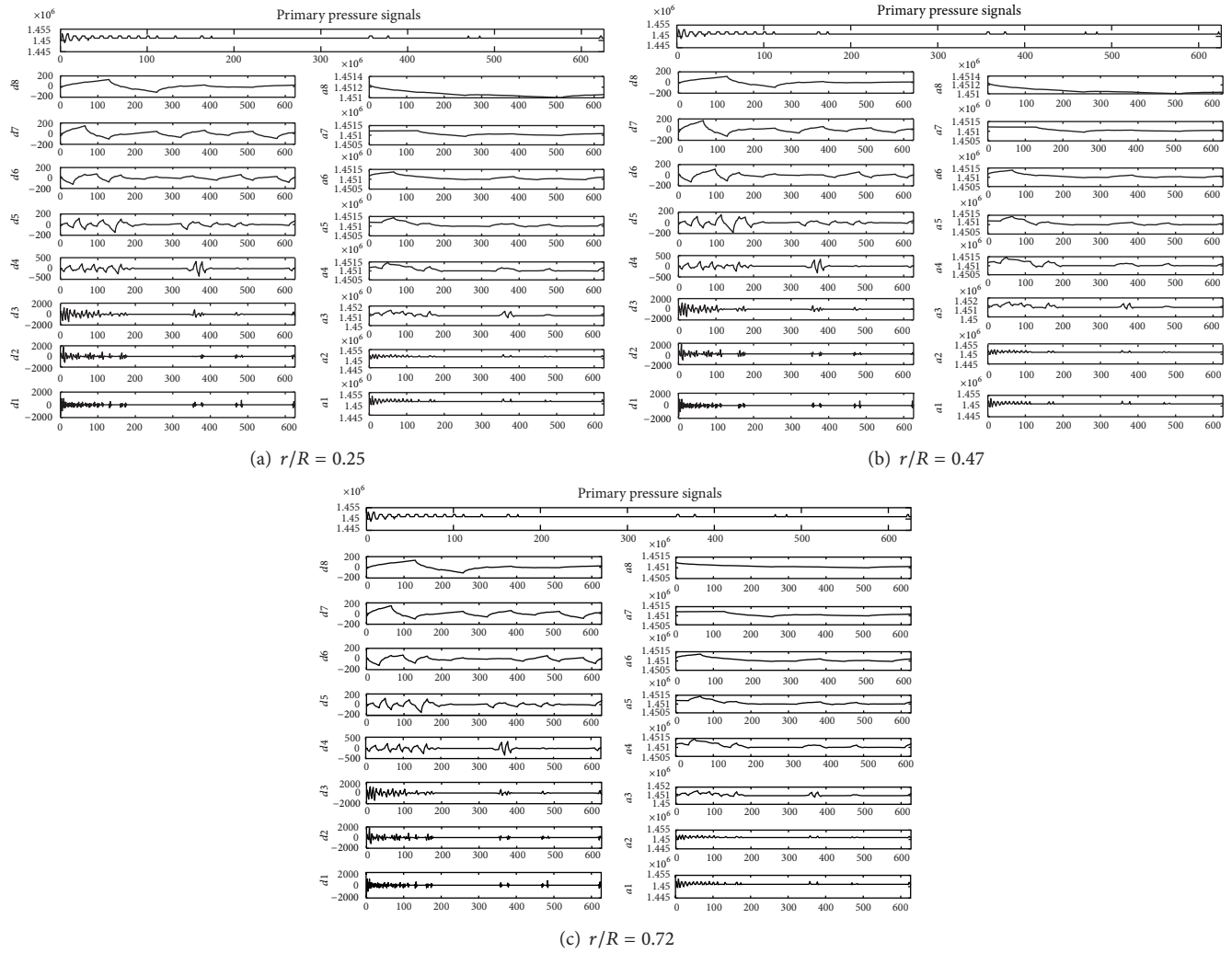


FIGURE 11: The wavelet analysis of pressure fluctuation ( $h = 0.4$  m).

phases occurred. Then, particles located at the jet inlet position are pushed upward. Thus, the local porosity will rapidly increase and the whole system begins to form the unstable stage in the gas-particle system. Once the stable system was lost, the rapidly increasing porosity is produced. At the bottom of bubble, the flow pressure is less than other positions of bubble. It leads to drive particles around bubble entered into the inner space of bubble. Thus, bubble had to leave the jet position and begin to move toward bed top surface and to grow gradually. Result of this kind of motion and development is to produce the individual bubble. When it reaches up to the top surface of bed, it will be broken up. Because of motion effects of bubble, they lead to the drastic collision of particles and accelerates the mixed process of particles. So, particle dispersions gradually become vigorous and the particle dispersions of gas-particle system shows on the intensely heterogeneous. From these figures, they clearly show the formation, the movements and the breakup of the bubbles, the movement and circulation of particle flows and dispersion and the interaction of gas and

particle phases. Some useful information, is higher particle temperature due to particle collisions, the higher porosity due to bubble movement and two-phase turbulent behaviors, and so forth.

Figures 5, 6, and 7 show the distributions of instantaneous concentration of particles at three different heights of 0.4 m, 0.8 m, and 1.2 m and at  $r/R$  of 0.25 and 0.73, respectively. The distribution of the computed concentration of particles shows uniformity in the bubbling fluidized bed, except for low values in the bubble burst region. The concentration of particles is high near the walls and in the center regime of the bed. It is low between the center and the walls. Near the bed surface, the concentrations of particles become low in the center of the bed. So, the uniformity and nonperiodicity are the main characters of particle dispersions.

Figures 8, 9, and 10 show the distributions of particles velocity histogram at axial and radial directions at three different heights of 0.4 m, 0.8 m, and 1.2 m and at  $r/R$  of 0.25, 0.47, and 0.73, respectively. We can see the distributions of the mathematical expectation and the variance of particle

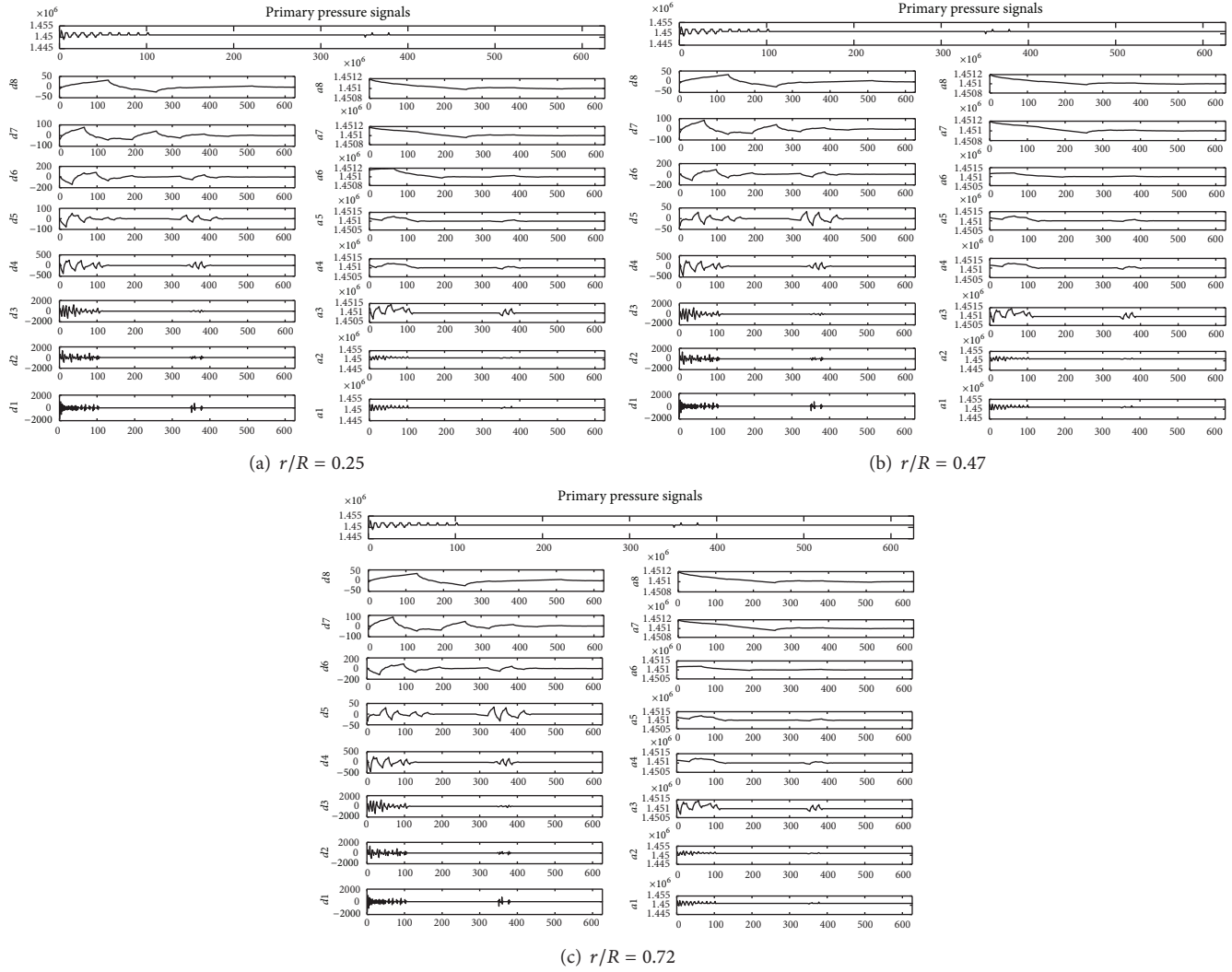


FIGURE 12: The wavelet analysis of pressure fluctuation ( $h = 0.8$  m).

velocity in radial and axial direction. Mathematical expectation represents the mean value of the random variables and the variance is the fluctuation intensity of random variables. At the height of 0.4 m, the mean values at axial direction are both less than radial directions with different radial positions. But the variance values at axial direction are larger than radial directions. With respect to the those of heights of 0.8 m and 1.2 m, they have the same trend compared to those of 0.4 m. As for the axial direction at the three heights, the mean and the variance at  $r/R$  of 0.47 and 0.72 and the middle of the 0.8 m have largest values, while at the bottom height of 0.4 m, they have the largest values at  $r/R$  of 0.25. As for the radial direction at three heights, the mean and the variance at all of  $r/R$  of 0.47 and 0.72 have the larger values than those of at  $r/R$  of 0.25. So, the larger particle collisions are often formed at the more uniform gas-particle fluid system.

To further understand the nonlinear particle dispersion behaviors, nonuniform and multiscale turbulent flows are very important to optimize design and operation for gas-fluidized bed. To great extents, the complexity degrees are

all represented by particle concentration and pressure fluctuations. Figures 11, 12, and 13 show the distributions of the wavelet analysis of pressure fluctuations at axial and radial directions at three different heights of 0.4 m, 0.8 m, and 1.2 m and at  $r/R$  of 0.25, 0.47, and 0.73, respectively. The primary pressure signal are provided in these figures, where  $d$  ( $i = 1, 8$ ) stand for the detailed information of primary signals and  $a$  ( $i = 1, 10$ ) are the approximation of signals. Results showed that the higher frequent components gradually disappeared with increasing scale and the lower frequent components are finally lost, which indicated that wavelet analysis could be stopped at the 8th layer. Pressure drops will be affected due to the variation of particle concentration or gas velocity. In the gas particle bubble fluidized bed, pressure drop have different frequencies for time behaviors. The higher frequency is mainly caused by the particle fluctuation and the lower frequency is bubble movements. In other word particle fluctuation can be considered as the higher-faster frequent components and bubble is the lower-slower frequent components.

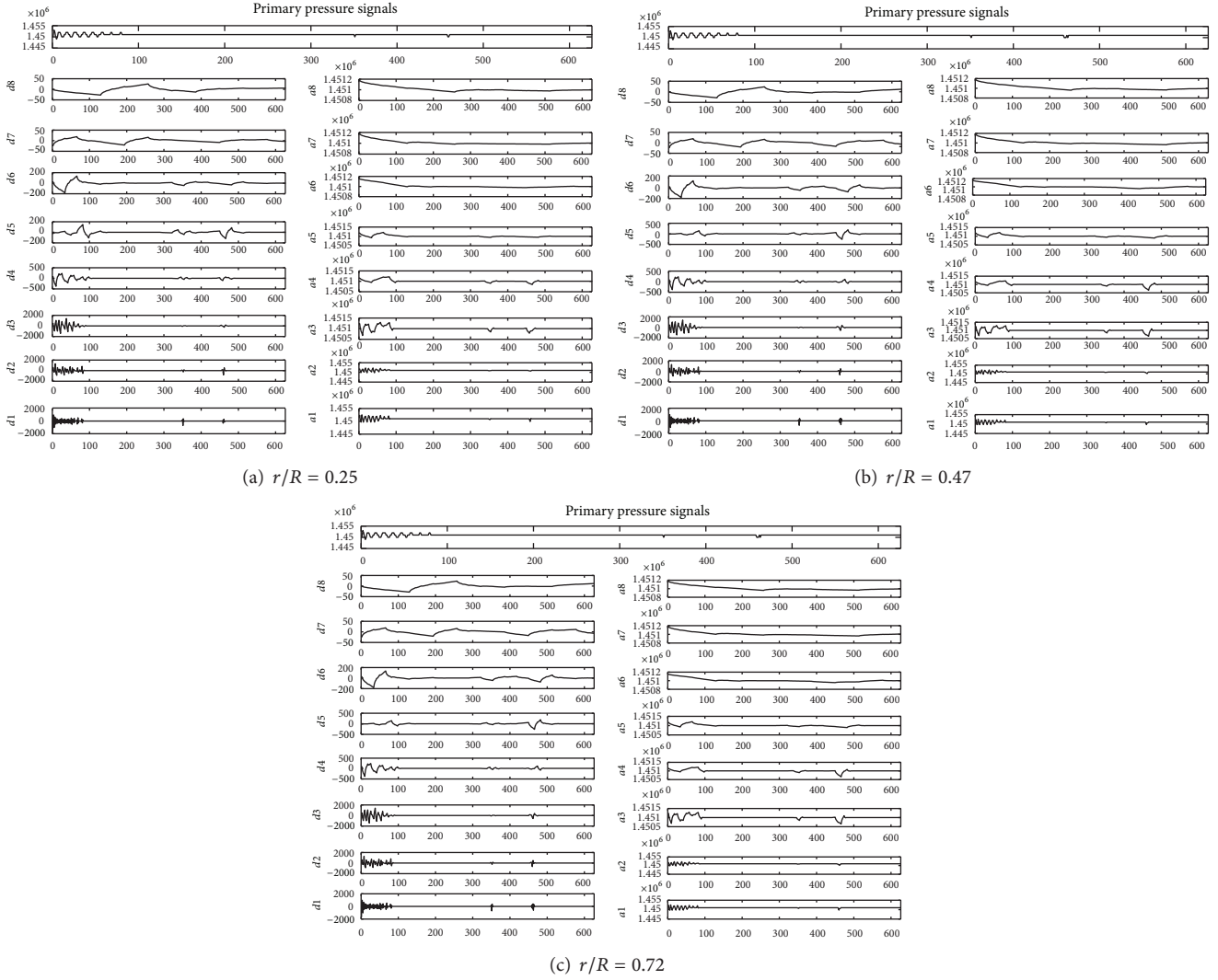


FIGURE 13: The wavelet analysis of pressure fluctuation ( $h = 1.2$  m).

As seen from these figures, regarding the same radial positions at three heights, the components fluctuations at the scale of the d1, the d2, and the d3 at height of 0.4 m will last a longer time than those of at 0.8 m and 1.2 m, in which small scale with the higher frequent component is a function of time. Particle fluctuation is a kind of the higher frequency and bubble is a kind of the lower frequency. It indicated that the random particle fluctuation will be attenuated with the height increase. As for the different radial positions at the same height, the component signal at d7 is obvious, where the peak values are larger than others. In addition, larger scale shows that the lower frequency of pressure fluctuation will be changed with the time development and the higher frequency of pressure fluctuation bubble reflected the bubble movements. At near-wall region, the bubble movements in the center bed are more vigorous. The variation of peak means the alternative formation of bubble and particle movement, where negative peaks represent the bubble passing and positive peaks are the continuous passing of the single bubble.

## 5. Conclusions

The instantaneous and statistical particle dispersions, the nonlinear hydrodynamic characteristic, multiscale flow regions, and heterogeneous characteristics in complex dense gas-particle flow system are obtained using developed Euler-Euler two-fluid model, an improved momentum transfer empirical coefficient, and wavelet analysis methods, as well as LES for solving the gas turbulent flows, which can be considered to be a novelty research approach for this study. The most important conclusions are as follows.

- (1) Particle collision frequencies at bubble vibrant movement regions along axial direction are much higher than those of radial direction and attenuated along height increase.
- (2) Representing bubble movement, low frequency components of pressure signal in the center of reactor regions are stronger than wall regions.

- (3) In wavelet analysis results, the negative values represent the passed bubble and positive peaks are the continuous motion of single bubbles.

## Nomenclature

$e$ : Particle restitution coefficient  
 $e_{\text{eff}}$ : Effective particle restitution coefficient  
 $f$ : Frequency  
 $g$ : Gravitational force  
 $g_0$ : Radial distribution function  
 $P$ : Pressure  
 $k$ : Kinetic energy  
 $t$ : Time  
 $V, v$ : Velocity.

## Greek Alphabets

$\alpha$ : Volume fraction  
 $\beta$ : Drag coefficient  
 $\delta$ : Kronecker-delta unit tensor  
 $\epsilon$ : Particle temperature  
 $\mu$ : Dynamic viscosity  
 $\nu$ : Kinematic viscosity  
 $\rho$ : Density  
 $\tau$ : Stress tensor.

## Subscripts

$i, j, k, l$ : Coordinates directions  
 coll: Collision  
 $g$ : Gas  
 $p$ : Particle  
 $r$ : Relaxation  
 sgs: Subgrid scale.

## Acknowledgment

The authors sincerely appreciate the financial support of Projects of National Natural Science Foundation of China under the Grant no. 20906014.

## References

- [1] J. R. Grace, "Reflections on turbulent fluidization and dense suspension upflow," *Powder Technology*, vol. 113, no. 3, pp. 242–248, 2000.
- [2] S. Elghobashi, "On predicting particle-laden turbulent flows," *Applied Scientific Research*, vol. 52, no. 4, pp. 309–329, 1994.
- [3] C. T. Crowe, M. Sommerfeld, and Y. Tsuji, *Multiphase Flows with Droplets and Particles*, CRC Press, Boca Raton, Fla, USA, 1998.
- [4] D. Gidaspow, *Multiphase Flows and Fluidization*, Academic Press, San Diego, Calif, USA, 1994.
- [5] S. Chapman and T. G. Cowling, *The Mathematical Theory of Non-Uniform Gases*, Cambridge University Press, 1970.
- [6] J. Ding and D. Gidaspow, "Bubbling fluidization model using kinetic theory of granular flow," *AIChE Journal*, vol. 36, no. 4, pp. 523–538, 1990.
- [7] J. L. Sinclair and R. Jackson, "Gas-particle flow in a vertical pipe with particle-particle interactions," *AIChE Journal*, vol. 35, no. 9, pp. 1473–1486, 1989.
- [8] S. Dasgupta, R. Jackson, and S. Sundaresan, "Turbulent gas-particle flow in vertical risers," *AIChE Journal*, vol. 40, no. 2, pp. 215–228, 1994.
- [9] C. M. Hrenya and J. L. Sinclair, "Effects of particle-phase turbulence in gas-solid flows," *AIChE Journal*, vol. 43, no. 4, pp. 853–869, 1997.
- [10] V. Mathiesen, T. Solberg, H. Arastoopour, and B. H. Hjertager, "Experimental and computational study of multiphase gas/particle flow in a CFB riser," *AIChE Journal*, vol. 45, no. 12, pp. 2503–2518, 1999.
- [11] G. Balzer, "Gas-solid flow modelling based on the kinetic theory of granular media: validation, applications and limitations," *Powder Technology*, vol. 113, no. 3, pp. 299–309, 2000.
- [12] S. Benyahia, H. Arastoopour, T. M. Knowlton, and H. Massah, "Simulation of particles and gas flow behavior in the riser section of a circulating fluidized bed using the kinetic theory approach for the particulate phase," *Powder Technology*, vol. 112, no. 1-2, pp. 24–33, 2000.
- [13] B. G. M. Van Wachem, J. C. Schouten, C. M. Van den Bleek, R. Krishna, and J. L. Sinclair, "Comparative analysis of CFD models of dense gas-solid systems," *AIChE Journal*, vol. 47, no. 5, pp. 1035–1051, 2001.
- [14] K. Agrawal, P. N. Loezos, M. Syamlal, and S. Sundaresan, "The role of meso-scale structures in rapid gas-solid flows," *Journal of Fluid Mechanics*, vol. 445, pp. 151–181, 2001.
- [15] M. J. V. Goldschmidt, J. A. M. Kuipers, and W. P. M. Van Swaaij, "Hydrodynamic modelling of dense gas-fluidised beds using the kinetic theory of granular flow: effect of coefficient of restitution on bed dynamics," *Chemical Engineering Science*, vol. 56, no. 2, pp. 571–578, 2001.
- [16] J. De Wilde, G. B. Marin, and G. J. Heynderickx, "The effects of abrupt T-outlets in a riser: 3D simulation using the kinetic theory of granular flow," *Chemical Engineering Science*, vol. 58, no. 3-6, pp. 877–885, 2003.
- [17] L. Huilin, D. Gidaspow, J. Bouillard, and L. Wentie, "Hydrodynamic simulation of gas-solid flow in a riser using kinetic theory of granular flow," *Chemical Engineering Journal*, vol. 95, no. 1, pp. 1–13, 2003.
- [18] J. Leboireiro, G. G. Joseph, and C. M. Hrenya, "Revisiting the standard drag law for bubbling, gas-fluidized beds," *Powder Technology*, vol. 183, no. 3, pp. 385–400, 2008.
- [19] N. Reuge, L. Cadoret, C. Coufort-Saudejaud, S. Pannala, M. Syamlal, and B. Caussat, "Multifluid Eulerian modeling of dense gas-solids fluidized bed hydrodynamics: influence of the dissipation parameters," *Chemical Engineering Science*, vol. 63, no. 22, pp. 5540–5551, 2008.
- [20] A. Passalacqua and L. Marmo, "A critical comparison of frictional stress models applied to the simulation of bubbling fluidized beds," *Chemical Engineering Science*, vol. 64, no. 12, pp. 2795–2806, 2009.
- [21] L. X. Zhou, *Theory and Numerical Simulation Modeling of Turbulent Gas-Particle Flows and Combustion*, Science Press and Florida, CRC Press, Beijing, China, 1993.
- [22] L. X. Zhou, C. M. Liao, and T. Chen, "Unified second-order-moment two-phase turbulence model for simulating gas-particle flows," in *Proceedings of the ASME Fluids Engineering Division Summer Meeting*, vol. 185, pp. 307–313, June 1994.

- [23] L. X. Zhou and T. Chen, "Simulation of swirling gas-particle flows using USM and  $k-\epsilon-k_p$  two-phase turbulence models," *Powder Technology*, vol. 114, no. 1-3, pp. 1-11, 2001.
- [24] Y. Yu, L. X. Zhou, B. T. Wang, and F. Cai, "USM- $\Theta$  two-phase turbulence model for simulating dense gas-particle flows," *Acta Mechanica Sinica/Lixue Xuebao*, vol. 21, no. 3, pp. 228-234, 2005.
- [25] Y. Liu, L. X. Zhou, and C. X. Xu, "Numerical simulation of instantaneous flow structure of swirling and non-swirling coaxial-jet particle-laden turbulence flows," *Physica A*, vol. 389, no. 23, pp. 5380-5389, 2010.
- [26] Y. Liu, X. Liu, S. Kallio, and L. X. Zhou, "Hydrodynamic predictions of dense gas-particle flows using a second-order-moment frictional stress model," *Advanced Powder Technology*, vol. 22, no. 4, pp. 504-511, 2011.
- [27] S. Ergun and A. A. Orning, "Fluid flow through packed columns," *Chemical Engineering Progress*, vol. 48, pp. 89-94, 1952.
- [28] C. Y. Wen and Y. H. Yu, "Mechanics of fluidization," *Chemical Engineering Progress Symposium*, vol. 62, pp. 100-113, 1966.
- [29] L. A. Giblaro, R. Difelice, and S. S. Waldram, "Generalized friction and drag coefficient correlations for flux particle interactions," *Chemical Engineering Science*, vol. 40, pp. 1817-1823, 1985.
- [30] R. Beetstra, M. A. Van Der Hoef, and J. A. M. Kuipers, "Drag force of intermediate reynolds number flow past mono- and bidisperse arrays of spheres," *AIChE Journal*, vol. 53, no. 2, pp. 489-501, 2007.
- [31] J. Van Der Schaaf, J. C. Schouten, and C. M. Van Den Bleek, "Origin, propagation and attenuation of pressure waves in gas-solid fluidized beds," *Powder Technology*, vol. 95, no. 3, pp. 220-233, 1998.
- [32] Z. He, W. Zhang, K. He, and B. Chen, "Modeling pressure fluctuations via correlation structure in a gas-solids fluidized bed," *AIChE Journal*, vol. 43, no. 7, pp. 1914-1920, 1997.
- [33] X. S. Lu and H. Z. Li, "Wavelet analysis of pressure fluctuation signals in a bubbling fluidized bed," *Chemical Engineering Journal*, vol. 75, no. 2, pp. 113-119, 1999.
- [34] J. Smagorinsky, "General circulation experiments with the primitive equation," *Journal of Chemical Physics*, no. 91, pp. 99-164, 1963.
- [35] S. Yuu, T. Umekage, and Y. Johno, "Numerical simulation of air and particle motions in bubbling fluidized bed of small particles," *Powder Technology*, vol. 110, no. 1-2, pp. 158-168, 2000.
- [36] T. McKeen and T. Pugsley, "Simulation and experimental validation of a freely bubbling bed of FCC catalyst," *Powder Technology*, vol. 129, no. 1-3, pp. 139-152, 2003.
- [37] J. Peltola, S. Kallio, and M. Honkanen P, "Saarenrinne. Image based measurement of particle phase Reynolds stresses in a laboratory scale circulating fluidized bed," in *Proceedings of the 7th International Conference on Multiphase Flow (ICMF '10)*, Tampa, Fla, USA, June2010.

## Research Article

# Solid Suspension by an Upflow Mixture of Fluid and Larger Particles

**Renzo Di Felice and Marco Rotondi**

*Dipartimento di Ingegneria Civile, Chimica ed Ambientale, Università degli Studi di Genova, 16145 Genova, Italy*

Correspondence should be addressed to Renzo Di Felice; [renzo.difelice@unige.it](mailto:renzo.difelice@unige.it)

Received 3 April 2013; Revised 19 June 2013; Accepted 20 June 2013

Academic Editor: Guan Heng Yeoh

Copyright © 2013 R. Di Felice and M. Rotondi. This is an open access article distributed under the Creative Commons Attribution License, which permits unrestricted use, distribution, and reproduction in any medium, provided the original work is properly cited.

In this paper new experimental observation is reported in order to shed light on the fluid dynamic interactions between the solid and the fluid phases in binary solid mixture suspensions. More specifically the case where a solid particle species is suspended by a slurry made up of fluid and larger particles has been investigated as there appear to be no previous studies on this type of systems. The effect of the presence of the larger solids in the fluidising media is quite evident from the experimental observation, and this effect can be quantified in first approximation by a very simple model based on the assumption that the larger solid restricts the available area for the fluid flow.

## 1. Introduction

When dealing with multiphase systems, such as solid-liquid systems, constitutive equations must include various terms to take into account the complex interphase interactions, with the solid-fluid drag, which arises when the phase velocities are different, being probably the most important one. Although it would be preferable to have exact theoretical approaches to estimate the drag force [1–7], nowadays its quantification is inferred mainly from experimental observations [8–10] with the homogenous suspension behaviour in vertical solid-fluid systems being the most common source. In fact, when a solid particle is suspended in steady-state conditions, the net force balance acting on it must be zero. This observation leads to an easy quantification of the solid-fluid drag force, which is obtained by neglecting other effects such as particle-particle interactions, as difference between the weight and the buoyant effect [11]. Therefore if the fluid dynamic conditions characterizing a suspension are known (phase velocities and phase volume concentrations), interphase drag can be expressed as a function of the previously mentioned conditions. This has been done when monocomponent solid-fluid systems have been considered with the homogeneous suspension behaviour being the main source of experimental evidence [8, 10]. However, when the

solid making up the suspension differs in size, experimental evidence is less abundant and the suggestion of a reliable universal drag law has been much more difficult as a consequence.

This aspect has been at the centre of a recent publication by the present authors [12] where empirical expressions for the drag force on large and small particles of a binary-solid suspension were suggested. In that work, however, it was pointed out that if, on one hand, the expression for the drag force on a large particle was supported by a substantial body of experimental evidence, on the other hand, the same could not be said for the drag force on the smaller particle of the binary-solid suspension, where the experimental evidence was quite limited. Therefore, aim of this paper is to contribute in filling that deficiency by concentrating on the smaller particles behaviour when suspended in the presence of larger particles.

## 2. Behaviour of Solid-Fluid Suspensions in Steady State Conditions

Given the importance of the knowledge of the suspension behaviour in steady-state for the determination of the drag

force acting on a solid particle, a short review is reported in the following section.

If all the particles are identical (e.g., with the same density and diameter), the equilibrium fluid dynamic condition of a suspension is usually expressed as

$$\frac{u}{u_t} = (1 - \phi)^n, \quad (1)$$

universally known as the Richardson-Zaki equation [13]. In (1)  $u$  is the superficial fluid velocity,  $u_t$  is the terminal velocity of a single particle settling in the pure fluid, and  $\phi$  is the solid volume concentration inside the column, defined as the volume occupied by the solid over the total suspension volume.

Using a large amount of experimental data obtained from fluidized beds and batch sedimentations Richardson and Zaki [13] suggested that the parameter  $n$  is a function of the terminal Reynolds number only

$$\text{Re}_t = \frac{\rho u_t d}{\mu}, \quad (2)$$

where  $\rho$  and  $\mu$  are, respectively, fluid density and viscosity, while  $d$  is the particle diameter. A simple expression for the estimation of  $n$  has given by Rowe [14]:

$$\frac{4.7 - n}{n - 2.35} = 0.175 \text{Re}_t^{0.75}. \quad (3)$$

If (1) is plotted on log-log scale, the behavior is linear with  $n$  as the slope and  $u_t$  as the intercept at solid volume concentration equal to zero.

However, further studies suggested that a different behaviour may be expected for large diameter particles, with high Reynolds number, fluidized by liquids [15–18], as depicted schematically in Figure 1. The velocity versus solid concentration relationship on double logarithmic coordinates is made up in this case of two linear sections, with the slope changing at a critical concentration  $\phi^*$ . The extrapolated velocity at zero solid concentration of the first segment is indicated as  $u_t^*$ , and it is below the true single unhindered particle settling velocity,  $u_t$ , with

$$k = \frac{u_t^*}{u_t}, \quad (4)$$

smaller than 1.

The slope of the first segment,  $n$ , is in good agreement with the Richardson and Zaki [13] coefficient, but after the critical value, it changes to a larger value  $n^*$ , with the velocity approaching this time  $u_t$  at  $\phi = 0$ . Rapagna et al. [15] proposed quantitative expressions for  $k$ ,  $\phi^*$ , and  $n^*$ , based on an empirical fitting of their experimental observations, as follows:

$$\begin{aligned} k &= 1.09 - 0.11 \log(\text{Re}_t), \\ \phi^* &= -0.05 + 0.06 \log(\text{Re}_t), \\ n^* &= 6.4 - 0.61 \log(\text{Re}_t). \end{aligned} \quad (5)$$

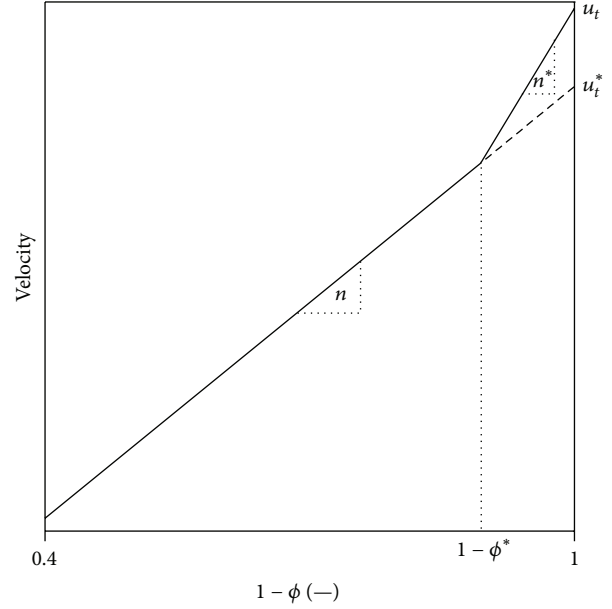


FIGURE 1: Schematic representation of large solid-liquid bed expansion characteristics [15].

The expressions reported are a simple elegant way to quantify the solid-fluid interaction for monocomponent systems and, as suggested by the authors, “little numerical significance can be ascribed to these relationships which do little more than indicate the trend” [15].

In binary-solid systems, where two solids (differing in size and/or density) are homogeneously suspended in a fluid, the presence of one solid is going to affect the expansion characteristics of the other.

As far as the effect due to the presence of small particles on the expansion characteristics of the larger particles, a limited experimental investigation has already been carried out in the past [19], where a larger solid was fluidized by a slurry made up of fluid and smaller particles. A typical result of that investigation is shown on Figure 2, where the fluid superficial velocity necessary to expand the larger solid to a fixed determined column height is plotted function of the smaller particle concentration.

From Figure 2 it appears evident that the effect brought about by the presence of the smaller particles is to “facilitate” the suspension of the larger ones, with experimental fluid velocity decreasing as the smaller particle concentration in the fluidizing slurry increases. A successful quantification of the observed behaviour has been done by the so-called “pseudo-fluid” approach [20, 21]. Basically the effect due to presence of the smaller particles is taken into account by properly modifying fluid physical properties (density and viscosity) so that previous relationships, such as the Richardson-Zaki [13] relationship, can still be formally applied. Therefore with this assumption, the binary mixture can be treated as monocomponent suspension, with the larger particles immersed in the pseudo-fluid made up of pure fluid and

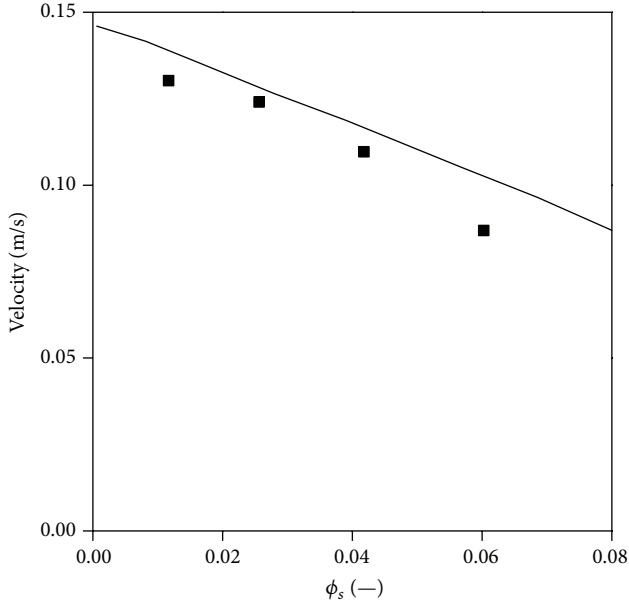


FIGURE 2: The effect of the presence of smaller particles on the fluidization velocity of larger solid as reported in [19]. The continuous line is the pseudo-fluid model approach.

smaller particles. The characteristics of the pseudo-fluid can be calculated as follows:

$$\rho_{pf} = \phi' \rho_S + (1 - \phi') \rho, \quad (6)$$

for the density

$$\mu_{pf} = \mu (1 - \phi')^{-2.8}, \quad (7)$$

and the viscosity, and

$$u_{pf} = \phi' u_S + (1 - \phi') u_f, \quad (8)$$

for the velocity, with the subscript pf referring to the pseudo-fluid, S referring to the smaller particle kind, and f referring to the fluid. In the previous expressions  $\phi'$  is the concentration of the smaller solid in the pseudo-fluid phase and is calculated as

$$\phi' = \frac{\phi_s}{1 - \phi_L}. \quad (9)$$

This model was validated through studies on binary-solid sedimentation next to the investigation of a circulating fluidized bed [19].

Unfortunately the mirror situation, that is, the effect brought about by the presence of larger particles on the expansion characteristics of smaller particles, has never been investigated before, and in this paper we make a first attempt to fill this gap.

As analogously done by [19], a circulating fluidized bed is purposely utilized. This time the attention is focussed on the smaller particles, and therefore they are fluidized by a suspension of larger particles transported by the fluid.

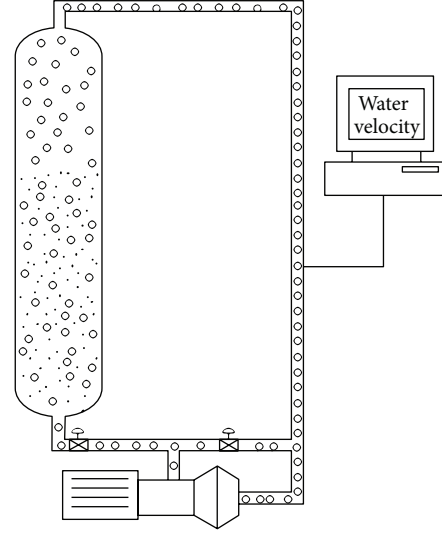


FIGURE 3: Schematic representation of the experimental apparatus.

### 3. Experimental

The experimental apparatus is schematized in Figure 3. The system allows the liquid to circulate in a closed loop; ambient water was used for all the experiments carried out in this work. The test section is a cylindrical vertical column of Perspex, 2000 mm tall, connected to a centrifugal pump via PVC tubing. The pump (T21-50 by TURO Italia srl) is specifically constructed so that solid-liquid slurries can be pumped, even at relatively high solid volume concentration (up to 20%). Two different vertical test sections were used, with internal diameter of 140 and 68 mm; on the other hand all the connecting tubes have an internal diameter of 40 mm.

The whole system could be filled with liquid through an opening situated in the most upper pipe. The liquid volumetric flow rate is regulated by manually setting two sphere valves, one situated just before the inlet of the test section and the other on the liquid bypass loop circuit. Liquid velocity is measured online with an electromagnetic probe (Alec Electronics) situated in the downcomer section of the closed loop. Superficial liquid velocity in the test section is then simply estimated by taking into account the relative flow area in the two sections, downcomer and test column.

Two main types of experiments were carried out, the first a simple monocomponent bed expansion which was used as a reference test and then a binary solid bed expansion where one type of particles was fluidized by a suspension made up of liquid and other larger solids. Obviously, in order to achieve the specific configuration wanted in this work the larger particle had to circulate while the smaller remains stationary in the test column, and therefore the larger solid had a density very close to that of the fluid so that their transport was facilitated. When the monocomponent test was carried out, a weighted amount of solid was charged into the system and the fluid flow rate was adjusted and varied in order to expand the solid in the vertical test section without circulating it. Different fluid superficial velocities were recorded

TABLE 1: Smaller solid material characteristics.

Material	Density (kg/m <sup>3</sup> )	Diameter (mm)	Re <sub>t</sub>
Glass 3.0	2500	3.0	922
Glass 5.0	2500	5.0	2171
Glass 8.0	2500	8.0	4594
Zirconia 2.2	3800	2.2	778

TABLE 2: Experimental parameters for monocomponent bed expansion.

Solid	$u_t^*$ (m/s)	$n$	$u_t$ (m/s)	$n^*$	$k$	$\phi^*$
Glass 8	0.434	2.14	0.640	5.21	0.68	0.114
Zirconia 2.2	—	2.22	0.379	—	1	—
Glass 3	0.302	2.26	0.355	4.11	0.85	0.084
Glass 5	0.320	2.14	0.373	4.06	0.86	0.077

TABLE 3: Binary-solid mixture investigated.

Smaller suspended	Larger circulating	$\phi_{L,max}$
Glass 5.0	Plastic 6 mm	0.134
Glass 3.0	Plastic 5 mm	0.109
Zirconia 2.2	Plastic 6 mm	0.157
Glass 8.0	Plastic 10 mm	0.109

together with the correspondent overall solid height, from which the velocity-concentration relationship could be easily estimated. On the contrary, parameter estimation for the binary-solid measurements was not so straightforward and some simplified assumption had to be made. First known weighted amount of the two solids were charged into the column. Then flow rate liquid was adjusted to values such as, while the larger solid would circulate together with the liquid, the smaller solid remained completely in the test section. Liquid superficial velocity was estimated as before, smaller solid concentration could be easily inferred from the height of the column occupied by the solid itself, whereas larger solid concentration was estimated assuming that it occupied homogeneously the whole systems. Moreover, while the smaller solid had zero velocity relative to the test tube wall, it was assumed that the difference in velocity between the liquid and the larger circulating solid is negligible. All the runs were carried out at ambient condition, and given that temperature did not change significantly a constant density of 1000 kg/m<sup>3</sup> and viscosity of 0.001 Pa s<sup>-1</sup> were used in the calculation. Solid fluidized material characteristics are summarized in Table 1, with the particles being practically spherical. The circulating material is always plastic with density very close to the density of water and diameters of 5, 6, and 10 mm.

#### 4. Result and Discussion

The first set of experimental run was carried out in order to verify monocomponent bed expansion and to have a reference point for the successive work. Figure 4 reports a typical result, referring to 5 mm glass beads, from which it can be

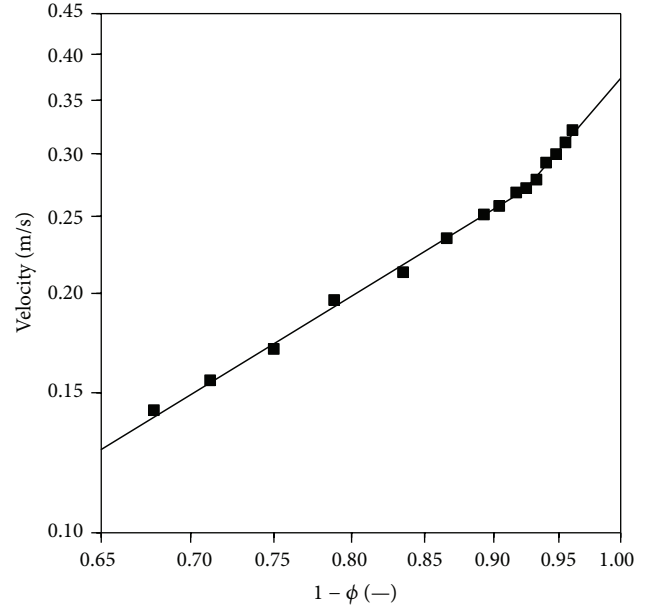


FIGURE 4: Monocomponent bed expansion characteristics. Solid: glass 5.0.

seen that bed expansion follows previously reported pattern and specifically that depicted in Figure 1. This behaviour was found to be true for every material investigated, with the exception of the smallest solid tested, zirconia, and the results are summarized in Table 2. The slopes ( $n$  and  $n^*$ ) and the terminal velocities ( $u_t$  and  $u_t^*$ ) reported in Table 2 were obtained by dividing the experimental voidage-velocity relationships in two sectors and fitting with a least square straight line the experimental points in each section. The intersection of the two straight lines yielded the critical particle concentration  $\phi^*$ , and the ratio of the two experimentally determined terminal velocities yielded the parameter  $k$ .

As can be seen from Figures 5, 6, and 7 the present results are in broad agreement with the empirical correlations recommended in [15]. The discrepancies, particular evident for the critical particle concentration reported in Figure 7, could well be due to the fact that the present data are well outside the range of validity of the data collected in [15]: in that paper the maximum terminal Reynolds number was just above 1000, whereas in the present work is larger than 4500.

Binary systems, with smaller particles suspended by larger particles circulating together with the fluid, were successively investigated. Table 3 reports the combination of larger-smaller solid utilized in this work. As already mentioned before, binary-solid pairs were chosen so that the smaller solid was fluidized stationary in the column, whereas the larger particles were transported by the fluid given their low density.

Figure 8 reports a typical experimental observation, referring to zirconia 2.2 suspended by water and 5 mm plastic particles, where the effect brought about by the presence of the larger particle in the fluidising fluid on the expansion characteristics of the smaller ones is depicted. More specifically it can be seen that as the larger particles volume concentration

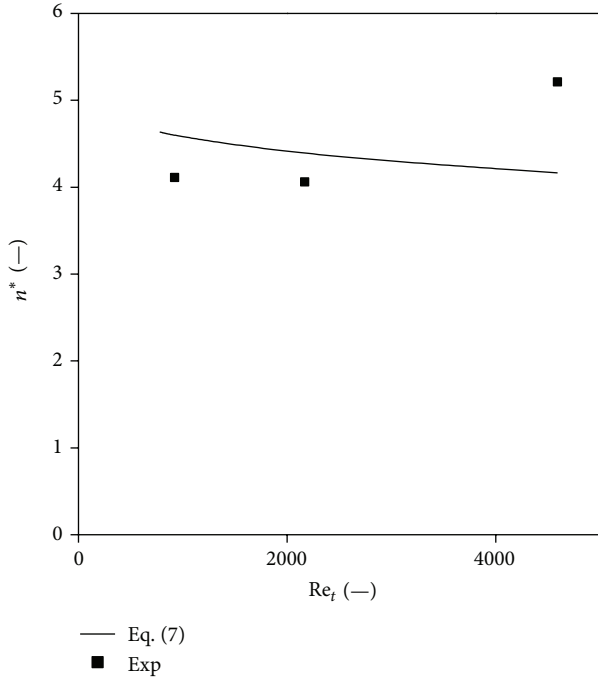


FIGURE 5: The parameter  $n^*$  function of  $Re_t$ .

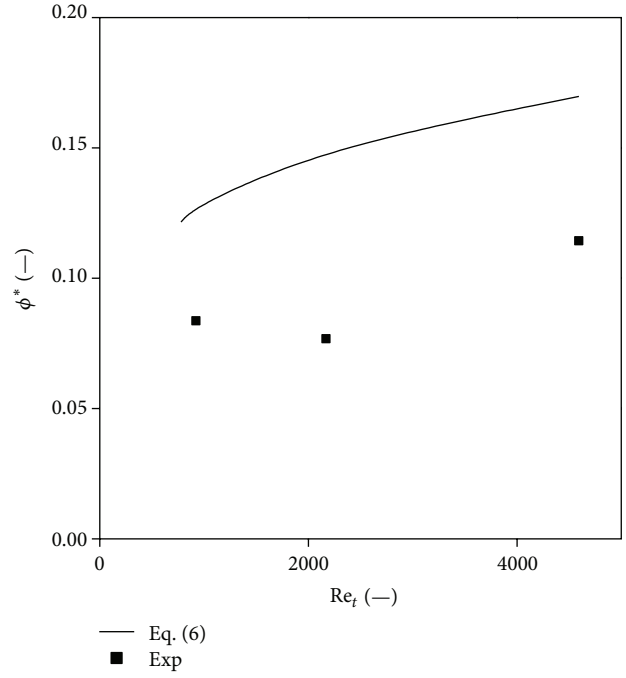


FIGURE 7: Critical particle concentration function of  $Re_t$ .

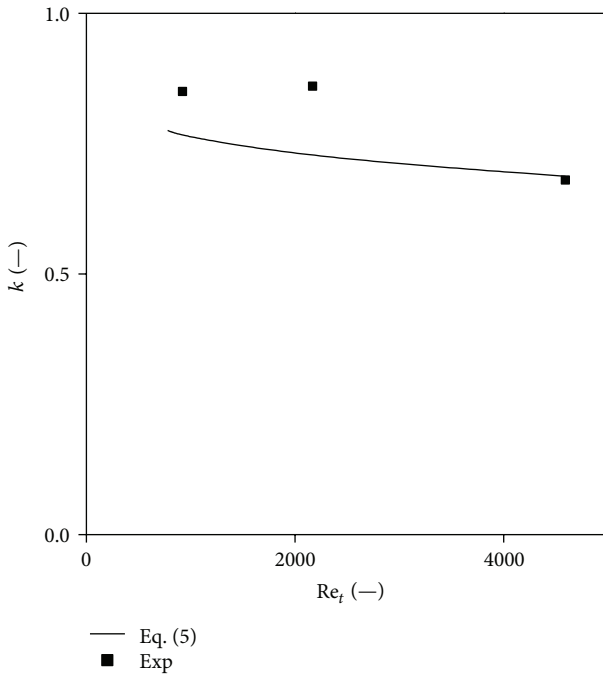


FIGURE 6: The parameter  $k$  function of  $Re_t$ .

increases, at a fixed water superficial velocity, the smaller particles bed height increases consequently. Therefore in this case also we can say that, qualitatively, the presence of the larger solid “facilitates” the fluidization of the smaller solid.

This observation was common for all the systems investigated, and a first attempt was made to quantify the effect arising from the presence of the larger particle. This situation

has been studied, in a different context, for example, by Moritomi et al. [22] who assumed, in their analysis, that the influence of the larger particle could be confined in a restriction of the area available for the flow of the liquid. With this simplification expansion characteristics law for the smaller solid system can be written again as

$$u = (1 - \phi_L) u_t^* (1 - \phi_S)^n, \quad (10)$$

when  $\phi_S > \phi_S^*$

$$u = (1 - \phi_L) u_t (1 - \phi_S)^{n^*}, \quad (11)$$

for  $\phi_S < \phi_S^*$ , with  $n$ ,  $u_t$ , and  $u_t^*$  being those determined from the monocomponent bed expansion earlier (Table 3).

Figures 9, 10, 11, and 12 show how this very simple approach fits the experimental observations. Considering the difficulties associated with this experimental measurement and the simplicity of the assumption made, the comparison between experiments and model can be defined satisfactory. The average error on the superficial velocity between experiments and model was smaller than 5%, with the smallest deviation being 2.1% for the 8 mm glass system (Figure 10) and the largest being 6.5% for the 5 mm glass system (Figure 11).

The question which arises at this point is if the pseudo-fluid approach, equations (6)–(9), which successfully describes the fluid dynamic effect brought about by the presence of the smaller particles on the larger particles could be applied on this case too. Unfortunately the present investigation cannot give a definite answer on this question. Three pseudo-effects were utilized in the pseudo-fluid simplification: the pseudo viscosity, the pseudo density, and

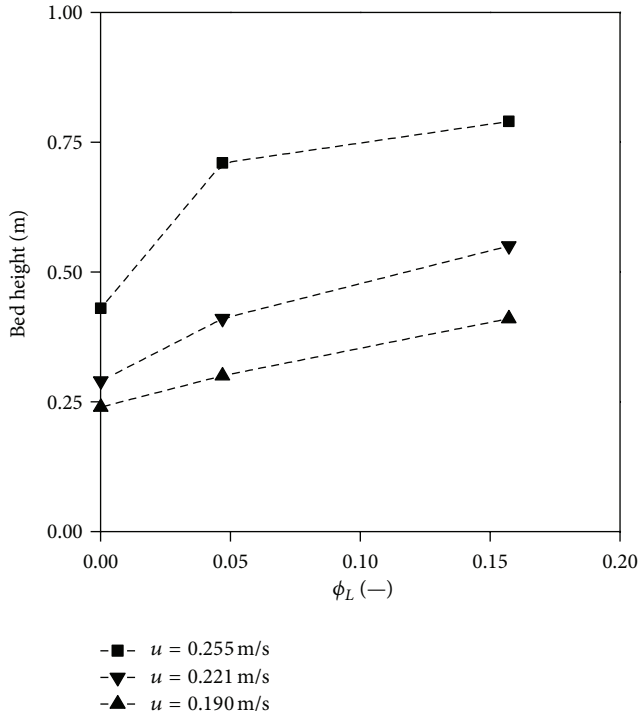


FIGURE 8: Experimental bed height function of larger particle concentration for three different water superficial velocities. System: zirconia 2.2 suspended by water and 5 mm plastic particles.

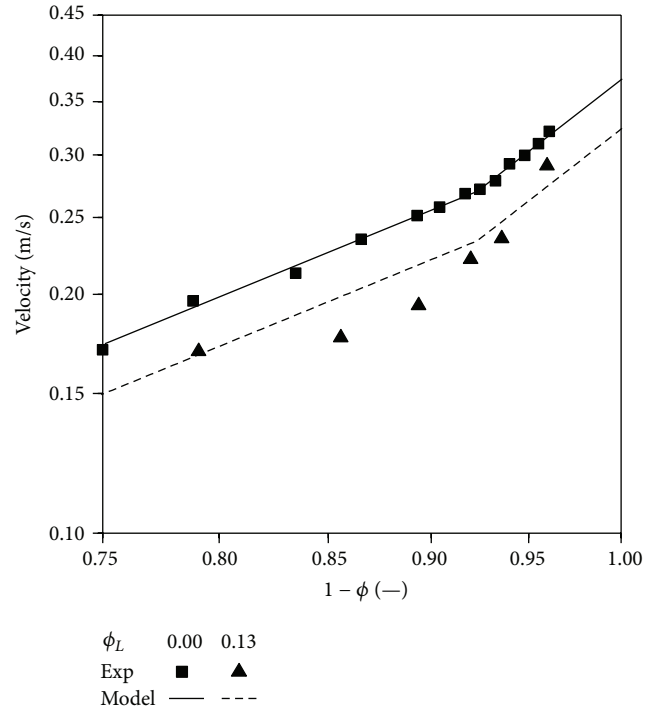


FIGURE 10: Comparison between experimental bed expansion characteristics and modelling. System: glass 5.0 suspended by water and 6 mm plastic particles.

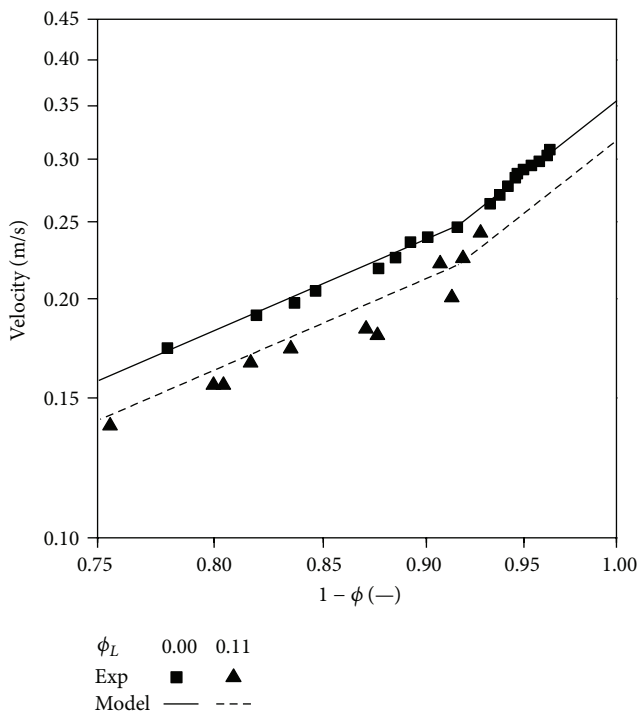


FIGURE 9: Comparison between experimental bed expansion characteristics and modelling. System: glass 3.0 suspended by water and 5 mm plastic particles.

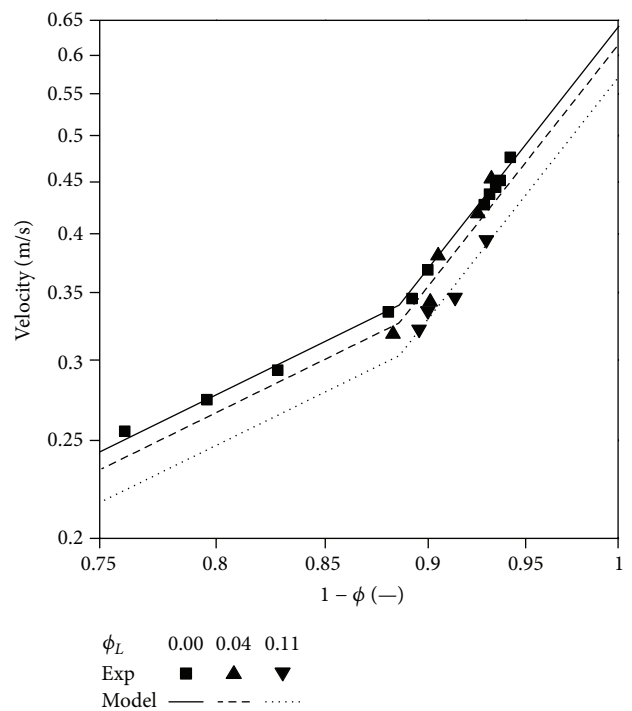


FIGURE 11: Comparison between experimental bed expansion characteristics and modelling. System: glass 8.0 suspended by water and 10 mm plastic particles.

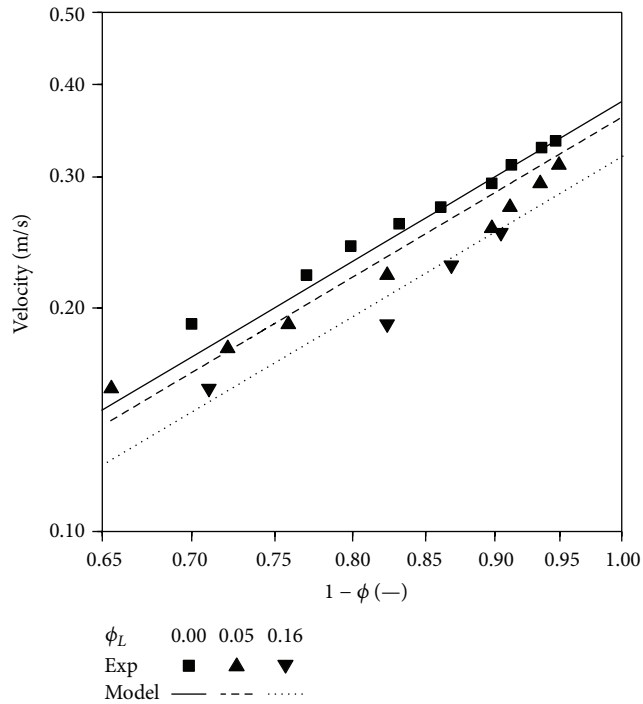


FIGURE 12: Comparison between experimental bed expansion characteristics and modelling. System: zirconia 2.2 suspended by water and 5 mm plastic particles.

the pseudo velocity, (5)–(7). It can be easily demonstrated that in this work the introduction of the restricted area for the fluid flow coincide with the pseudo-fluid velocity when the transported solid possesses a velocity equal to that of the fluid, a condition which can be assumed to hold in the systems investigated here. Unfortunately none of the other two pseudo effects (viscosity and density) could be properly validated in this work. Pseudo viscosity cannot be validated because our experiments were carried out at high Reynolds numbers, in the inertial flow regime, where the viscosity has no influence on the observed fluid dynamic behaviour so the use of (7) would make no practical difference. The other effect could not be tested either because we were forced to utilize nearly neutrally buoyant large particle, and therefore pseudo-fluid density, (6) coincides practically with the fluid density.

## 5. Conclusions

To the best of our knowledge in this work for the first time experiments on binary-solid suspensions, with the smaller particles fluidized by a mixture of larger neutrally buoyant particles and fluid, were carried out. Minding the effect described by Rapagna et al. [15], the observed bed expansion characteristics of the smaller particles, at different velocities and larger particle concentrations, could be satisfactorily reproduced by a simple approach based on the assumption that the influence of the larger particles is limited to a restricted area available for the fluid flow. Of note, at the same superficial velocity, the expansion of the fluidized bed

increases with the larger particles concentration. Due to the high particle Reynolds number ( $400 < Re < 4000$ ) and the neutrally buoyant spheres, it was not possible to verify if the pseudo-fluid model is applicable in our case, and future works will be directed to clarify this point. The experimental information reported in this paper will be useful in determining a proper relationship for the solid-fluid drag force in binary-solid suspensions, relationship of relevant importance when computational fluid dynamic works are carried out.

## References

- [1] G. K. Batchelor, "Sedimentation in a dilute dispersion of spheres," *Journal of Fluid Mechanics*, vol. 52, pp. 245–268, 1972.
- [2] G. K. Batchelor, "Sedimentation in a dilute polydisperse system of interacting spheres. Part 1: General theory," *Journal of Fluid Mechanics*, vol. 119, pp. 379–408, 1982.
- [3] G. K. Batchelor and C. S. Wen, "Sedimentation in a dilute polydisperse system of interacting spheres. Part 2: Numerical results," *Journal of Fluid Mechanics*, vol. 124, pp. 495–528, 1982.
- [4] D. L. Koch and A. S. Sangani, "Particle pressure and marginal stability limits for a homogeneous monodisperse gas-fluidized bed: Kinetic theory and numerical simulations," *Journal of Fluid Mechanics*, vol. 400, pp. 229–263, 1999.
- [5] A. J. C. Ladd, "Numerical simulations of particulate suspensions via a discretized Boltzmann equation. Part 1. Theoretical foundation," *Journal of Fluid Mechanics*, vol. 271, pp. 285–309, 1994.
- [6] A. J. C. Ladd, "Numerical simulations of particulate suspensions via a discretized Boltzmann equation. Part 2. Numerical results," *Journal of Fluid Mechanics*, vol. 271, pp. 311–339, 1994.
- [7] A. J. C. Ladd and R. Verberg, "Lattice-Boltzmann simulations of particle-fluid suspensions," *Journal of Statistical Physics*, vol. 104, no. 5–6, pp. 1191–1251, 2001.
- [8] C. Y. Wen and Y. H. Yu, "Mechanics of fluidization," in *Chemical Engineering Progress Symposium Series*, vol. 62, pp. 100–111, 1966.
- [9] D. Gidaspow, *Multiphase Flow and Fluidization: Continuum and Kinetic Theory Description*, Academic Press, New York, NY, USA, 1991.
- [10] R. Di Felice, "The voidage function for fluid-particle interaction systems," *International Journal of Multiphase Flow*, vol. 20, no. 1, pp. 153–159, 1994.
- [11] R. Di Felice, "Hydrodynamics of liquid fluidisation," *Chemical Engineering Science*, vol. 50, no. 8, pp. 1213–1245, 1995.
- [12] R. Di Felice and M. Rotondi, "Fluid-particle drag force in binary-solid suspensions," *International Journal of Chemical Reactor Engineering*, vol. 10, no. 1, pp. 1542–6580.
- [13] J. F. Richardson and W. N. Zaki, "Sedimentation and fluidization: Part I," *Transactions of the Institution of Chemical Engineers*, vol. 32, pp. 35–54, 1954.
- [14] P. N. Rowe, "A convenient empirical equation for estimation of the Richardson-Zaki exponent," *Chemical Engineering Science*, vol. 42, no. 11, pp. 2795–2796, 1987.
- [15] S. Rapagna, R. Di Felice, L. G. Gibilaro, and P. U. Foscolo, "Steady-state expansion characteristics of monosize spheres fluidized by liquids," *Chemical Engineering Communications*, vol. 79, pp. 131–140, 1989.
- [16] M. R. Dibouni, *The behaviour of liquid fluidised beds containing a wide size distribution of particles [Ph.D. thesis]*, University of London, 1975.

- [17] J. Garside and M. R. Al-Dibouni, "Velocity-voidage relationships for fluidization and sedimentation in solid-liquid systems," *Industrial and Engineering Chemistry Process Design and Development*, vol. 16, no. 2, pp. 206–214, 1977.
- [18] J. P. Riba and J. P. Couderc, "Expansion de couches fluidisées par des liquides," *Canadian journal of Chemical Engineering*, vol. 55, pp. 118–121, 1977.
- [19] R. Di Felice, L. G. Gibilaro, S. Rapagna, and P. U. Foscolo, "Particle mixing in a circulating liquid fluidized bed," in *Fluidization and Fluid Particle Systems: Fundamentals and Applications*, pp. 32–36, December 1988.
- [20] R. Di Felice, P. U. Foscolo, L. G. Gibilaro, and S. Rapagna, "The interaction of particles with a fluid-particle pseudo-fluid," *Chemical Engineering Science*, vol. 46, no. 7, pp. 1873–1877, 1991.
- [21] L. G. Gibilaro, K. Gallucci, R. Di Felice, and P. Pagliai, "On the apparent viscosity of a fluidized bed," *Chemical Engineering Science*, vol. 62, no. 1-2, pp. 294–300, 2007.
- [22] H. Moritomi, T. Yamagishi, and T. Chiba, "Prediction of complete mixing of liquid-fluidized binary solid particles," *Chemical Engineering Science*, vol. 41, no. 2, pp. 297–305, 1986.

## Research Article

# Modeling and Experimental Investigation of Pressure Field in the Grinding Zone with Nanoparticle Jet of MQL

C. H. Li, Z. L. Han, Q. Zhang, and S. Wang

School of Mechanical Engineering, Qingdao Technological University, Qingdao 266033, China

Correspondence should be addressed to C. H. Li; [sy\\_lichanghe@163.com](mailto:sy_lichanghe@163.com)

Received 31 March 2013; Revised 31 May 2013; Accepted 3 June 2013

Academic Editor: Guan Heng Yeoh

Copyright © 2013 C. H. Li et al. This is an open access article distributed under the Creative Commons Attribution License, which permits unrestricted use, distribution, and reproduction in any medium, provided the original work is properly cited.

*Solid nanoparticles* were added in minimum quantity lubrication (MQL) fluid medium to make nanofluids, that is, after the mixing and atomization of nanoparticle, lubricants and high pressure gas, to inject *solid nanoparticle* in the grinding zone with the form of jet flow. The mathematical model of two-phase flow pressure field of grinding zone with nanoparticle jet flow of MQL was established, and the simulation study was conducted. The results show that pressures in the grinding zone increased with the *acceleration* of grinding wheel, sharply decreased with the increased minimum clearance, and increased with the *acceleration* of jet flow. At three spraying angles of *nozzles*, when the *nozzle* angle was  $15^\circ$ , the pressure of grinding zone along the speed of grinding wheel was larger than the rest two angles. On the experimental platform built by KP-36 precision grinder and nanoparticle jet flow feed way, CY3018 pressure sensor was used to test the regularities of pressure field variations. The impact of the speed of grinding wheel, the gap between workpiece and grinding wheel, jet flow velocity, and spraying angles of *nozzles* on the pressure field of grinding zone was explored. The experimental result was generally consistent with the theoretical simulation, which verified the accuracy of the theoretical analysis.

## 1. Introduction

Minimum quantity lubrication (MQL) refers to the minimum quantity of lubricants that enters the high temperature grinding zone after being mixed in high pressure gas and atomized with high pressure draft (4.0–6.5 bar). The traditional poured and debridged feed liquid of grinding fluid is 60 L/h for a unit of the width of grinding wheel, while the consumption of MQL grinding fluid is 30–100 mL/h for a unit of the width of the grinding wheel [1–8]. High pressure draft serves as cooling and chip removal. Lubricants are attached to the finished surface of the workpiece, forming a layer of protective film and serving as the lubrication. This technology integrates the advantages of poured and debridged grinding and dry grinding, presenting similar lubrication effects compared with traditional poured and debridged grinding. Lubricants adopt vegetable oil as alkyl ester of base oil, which shows features such as excellent biodegradability, lubricating properties, high viscosity index, low volatility, recycling, short production cycle, and insignificant environmental diffusion. The consumption of lubricants is only parts per thousand

or a few hundredths of a percentage point compared with the traditional grinding approaches, which greatly improved the working environment. Thus, high pressure draft is an efficient low-carbon processing technology. However, studies show that cooling effect of high pressure draft is too limited to meet the needs of strengthened high temperature heat transfer of the grinding zone [8–12]. The processing quality of the workpiece and the grinding wheel life is worse than the traditional poured and debridged grinding, indicating that MQL technique requires further improvements.

According to strengthened heat transfer theory, the heat transfer ability of the solid greatly exceeds the liquid and gas. At room temperature, the coefficient of thermal conductivity of solid materials is greater than the fluid material by several orders of magnitude. It can be estimated that the coefficient of thermal conductivity of liquid with suspended metal, nonmetallic, or polymeric solid particles exceeded the pure liquid significantly. If solid particles are added in MQL medium, it is expected to greatly increase the coefficient of thermal conductivity of fluid medium so as to improve the convective heat transfer and offset the defects of insufficient

cooling effects of MQL. In addition, nano-particles (referring to ultrafine tiny solid particles with at least one dimension in the three-dimensional space, that is, in the nanoscale range (1–100 nm)) also present tribological features such as special antifriction and high carrying capacity in aspects of lubrication and tribology [13].

In this research, *solid nano* particles were added in MQL fluid medium to make nanofluids, that is, to inject *solid nano* particles after the mixing and atomization of nano-particle, lubricants (oil or oil-water mixture) and high pressure gas in the grinding zone with the form of jet flow. Nanofluids refer to the new heat transfer working medium with nanoscale metal or metallic oxide particles added in fluids at a certain way and ratio. In effect, from the aspect of its compositions, it is the two-phase suspension liquid formed by liquid and nano-particles and can be abbreviated as “nanofluids.” Due to the small size effect of nano-particle, its behavior is similar with that of the liquid molecules; the intensive Brownian motion of nano-particle maintains its stable suspension and keeps it from precipitation [5, 6].

There are few differences between Brownian motion of suspended particulates and the thermal motion of molecules in the true solution, and the most significant difference is the form of the thermal motion of molecules. The former involves the integrated effects of the thermal motion impact by many molecules while the latter involves the thermal motion of a single kind of molecules. Hence, in the research of three-phase flow (including compressed air, the grinding liquid, and nano-particles), nano-particles can be made suspending in the grinding liquid to form nanofluids, and transport parameters of nanofluids can be calculated based on related theories, which can thus be abbreviated into a study on two-phase flow.

When the grinding liquid was injected in the wedge-shaped zone between the grinding wheel and the workpiece surface, the fluid dynamic pressure of the grinding liquid was formed. Guo and Malkin [7] applied mass conservation equation and momentum conservation equation in the mathematical modeling, based on the consideration of the impact of the porosity of the grinding wheel. With theoretical calculation, the depth of the grinding liquid in the grinding wheel was obtained, indicating that the grinding wheel with pores has the function to pump the grinding liquid from the grinding zone. Chang [8] and others considered the impact from the porosity of the grinding wheel. According to conservation equation, mathematical model the dynamic pressure of grinding liquid during the gradual feeding was established, and the simulation results show that the larger the supply of grinding liquid is, the larger the dynamic pressure of grinding liquid will be. Ganesan et al. [9] applied Reynolds equation and Laplace equation to establish the cooling liquid equation for the infinite narrow grinding wheel and provided the analytical solution for calculating the dynamic pressure of fluid. Furutani et al. [10] considered the impact of degree of permeability of the grinding wheel and established the cooling liquid equation for the infinite wide grinding wheel, so as to solve the lifting force from the fluid pressure and the dynamic pressure. Engineer and others measured the flow of the grinding liquid.

With experimental measurements, the flow in the grinding zone was identified, indicating the significant role of porosity of the grinding wheel and the location of nozzles on the flow. Gviniashvili et al. [11] measured the depth of the grinding liquid in the grinding wheel and identified the relationship between the depth and the maximum temperature of the grinding workpiece. Ebbrell et al. [12], Li et al. [13], and Ganesan et al. [14] considered the impact of inertia force. Based on two-dimensional steady incompressible fluid Navier-Stokes equation, the fluid equation in grinding zone was deduced in planar grinding, and the dynamic pressure of the fluid was simulated and solved, which was verified in experiments. Hryniewicz et al. [15, 16] considered the influence of the roughness and established a two-dimensional mathematical model. The regularities of distribution of the dynamic pressure were simulated and solved, which was verified in experiments. They identified the relationship between the dynamic pressure and the speed of grinding wheel as well as minimum clearance between the grinding wheel and the workpiece. Based on theoretical and experimental analysis, the following conclusions were drawn: with other conditions identical, the larger the roughness, the larger the dynamic pressure of fluid will be. Furthermore, when the grinding wheel left the grinding zone, not all the grinding liquid was thrown from the grinding wheel. Only a part of the liquid left the grinding wheel, and the rest moved with the grinding wheel. In the experiment, Hryniewicz observed the following phenomenon: the grinding liquid left the grinding zone sticking to the grinding wheel surface rather than to the workpiece. Kim [17] and Lee et al. [18] designed experimental apparatus to test the effective flow rate of the grinding liquid in the grinding zone via the feeding with nozzles. They acquired the conclusion that the porosity of the grinding wheel and the position of the nozzles imposed a significant impact on the effective flow rate, while the feeding velocity and grinding depth of the workpiece has little impact over it. Klocke et al. [19] assumed that the radius of the grinding wheel was infinite, and the width of the workpiece and the grinding wheel was finite. Based on the assumption, a two-dimensional mathematical model of pressure distribution in the grinding zone was established according to the Navier-Stokes equation so as to calculate infinite width of the grinding wheel. The normal applied force generated by the dynamic pressure of grinding liquid was defined as Coolant induced force [20]. With the simulating calculation, the larger the velocity of grinding wheel is, the larger the normal force will be. Hryniewicz et al. [15] applied two types of nozzles in the experiment of cooling system. The first was formed by two nozzles, and the main nozzle was used to the feeding of the grinding liquid, and the assistant nozzle was used to break through “airbond” of air flow around the grinding wheel. The second only involves one nozzle for the feeding of the grinding liquid. It can be concluded from comparing the experimental results that the feeding nozzle of two nozzles has lower than that of one nozzle. Klocke [19] studied the percentage experiment of the grinding liquid in the grinding zone that accounts for the entire grinding liquid and summed up that when the flow of the grinding liquid was increased, Coolant induced force was enlarged. Yet when the ratio of

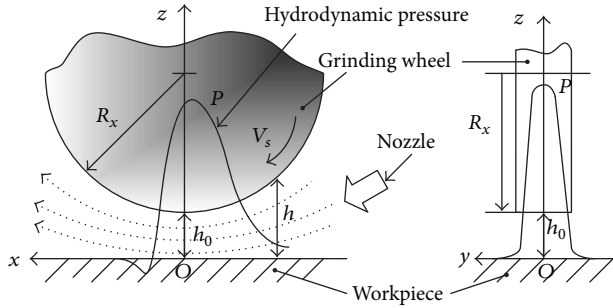


FIGURE 1: The sketch of geometrical model.

the grinding liquid in the grinding zone reached a certain value, it will increase with the increasing flow. Hryniewicz [15] conducted experiments of two grinding liquids (the oiliness grinding liquid and chemical synthetic fluids) and found that in the same experimental conditions, the maximum dynamic pressure generated by the oiliness of the grinding liquid was much larger than that from chemical synthetic fluids. In this research, the modeling and experimental investigation was conducted on nano-particle jet flow of MQL grinding pressure field.

## 2. Theoretical Modeling of Pressure Field in the Grinding Zone

Figure 1 shows the geometrical model. The three-dimensional system of coordinate was established, and the origin of coordinates was located at the workpiece surface between the grinding wheel and the minimum clearance. The direction of rotation of the workpiece surface along the grinding wheel was taken as  $X$  axis, and the direction vertical to the workpiece surface was taken as  $Y$  axis, that along the width of the grinding wheel as  $Z$  axis.

### 2.1. Modeling Conditions

(1) *Compressibility of Gas.* The room temperature was taken as  $T = 15^\circ\text{C}$ , the peripheral velocity of grinding wheel as  $V_s = 45 \text{ m/s}$ , and it was obtained that sound velocity:  $a = 20.05\sqrt{T} = 340 \text{ m/s}$ ; Mach number:  $M_a = V_s/a = 45/340 = 0.1323 < 0.3$ . As  $M_a < 0.3$ , the compressibility of gas can be excused from consideration in the fluid analysis.

(2) *Identification of Fluid State.*  $Re = (2b_0u_0)/\nu = (2 \times 45 \times 0.001)/(0.00105 \times 10^{-3}) = 85714.3 > 2300$ ; where  $2b_0$ —half width of outlet;  $u_0$ —outlet velocity;  $\nu$ —nanofluids dynamic viscosity.  $Re > 2300$ , so it is identified as turbulence flow. With the considerations of the following aspects (the fluid evenly flows in the grinding zone, the fluid is incompressible Newtonian flow, and the fluid in intervals is turbulence), for simplified calculation, the model was simplified as [21]:

- (i) to neglect the impact of temperature and pressure on fluid viscosity, or that of the inertial effect in the flow;

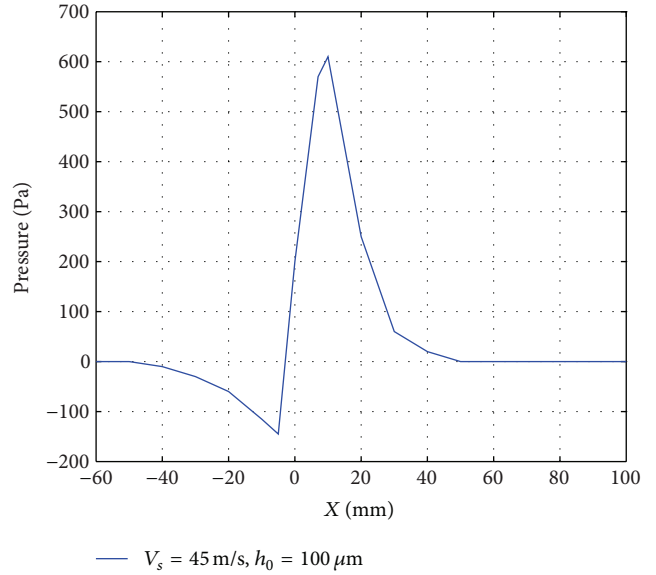


FIGURE 2: Pressure distribution of flow field in the  $X$  direction.

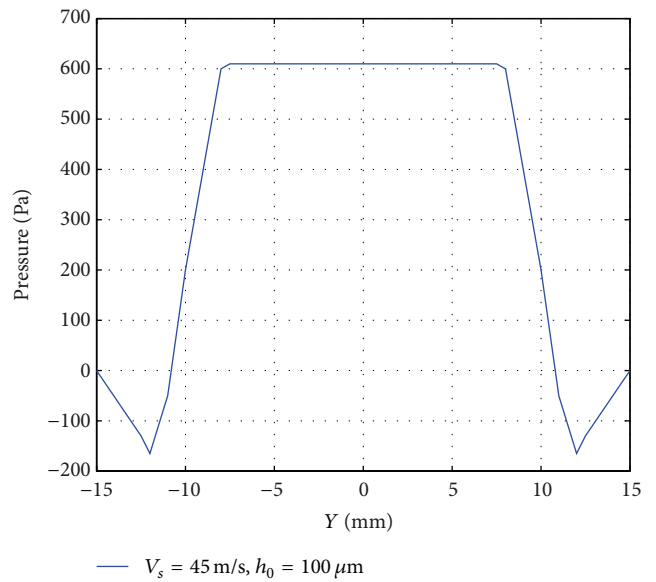


FIGURE 3: Pressure distribution of flow field in the  $Y$  direction.

- (ii) to not consider the impact of the workpiece surface roughness and elastic deformation;
- (iii) to neglect the ratio of feeding velocity of the workpiece and the peripheral velocity of grinding wheel;
- (iv) to neglect the ratio of fluid inertia force, body force, and surface force in nanofluid film.

2.2. *The Establishment of Mathematical Model.* According to the continuity equation, momentum conservation equation and energy conservation equation, of the hydromechanics, the mathematical model of the stress field of the grinding zone was established.

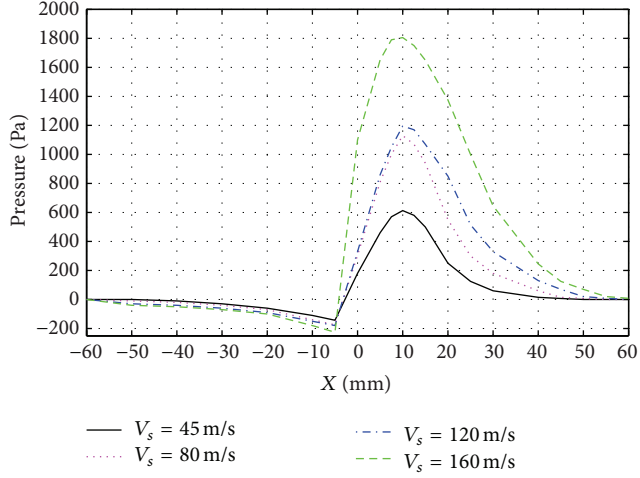


FIGURE 4: Pressure in grinding zone along the velocity change curve of wheel along the velocity direction of grinding wheel.

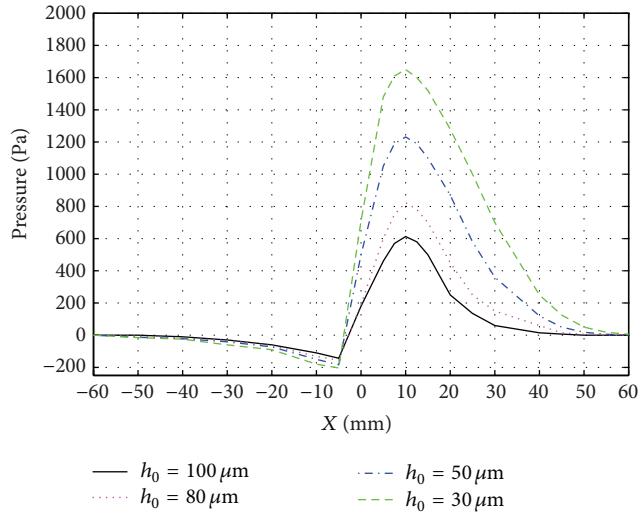


FIGURE 5: Pressure in grinding zone along the velocity change curve of wheel along the changing curve of minimum clearance.

(1) Continuity equation:

$$\frac{\partial \rho}{\partial t} + \frac{\partial u_i}{\partial X_i} = 0. \quad (1)$$

(2) Momentum conservation equation [22]:

$$\frac{\partial u_i}{\partial t} + u_j \frac{\partial u_i}{\partial X_j} = -\frac{1}{\rho} \frac{\partial \rho}{\partial x_i} + \gamma \frac{\partial^2 u_i}{\partial x_j \partial x_j} + \frac{1}{\rho} \frac{\partial (\overline{\rho \mu'_i \mu'_j})}{\partial X_j}, \quad (2)$$

where  $u_i$ ,  $u_j$ —average velocity of nanofluids along  $X_i$  and  $X_j$  direction;  $\rho$ —density of nanofluids;  $\overline{\rho \mu'_i \mu'_j}$ —Reynolds stress.

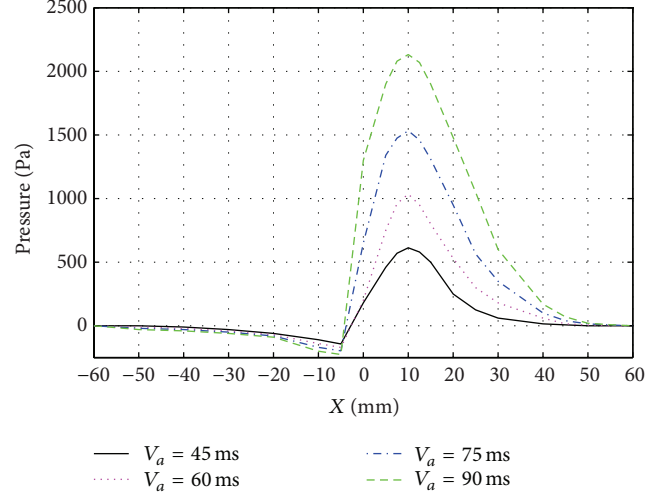


FIGURE 6: Pressure in grinding zone along the velocity change curve of wheel along the changing curve of jet flow velocity.

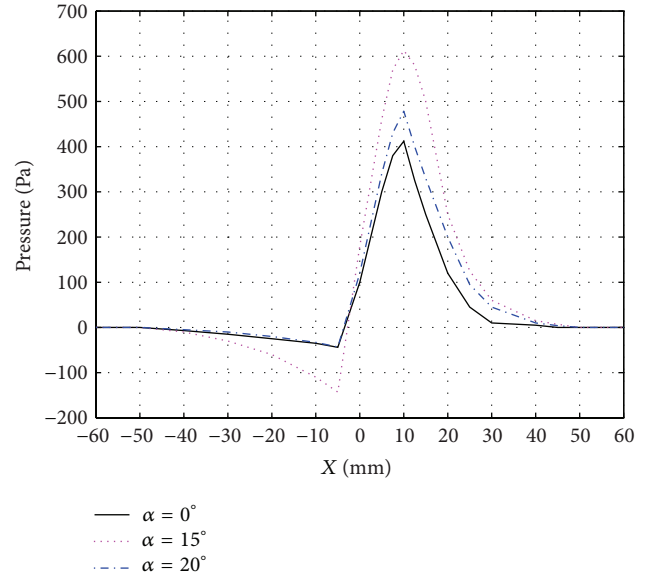


FIGURE 7: Pressure in grinding zone along the velocity change curve of wheel along the changing curve of positions and angles of nozzle.

(3) Energy conservation equation:

$$\left\{ \frac{\partial (\rho E)}{\partial t} + \frac{\partial}{\partial x_i} [u_i (\rho E + p)] \right\} = \frac{\partial}{\partial x_j} \left[ \left( k + \frac{c_p \mu_t}{Pr_t} \right) \frac{\partial T}{\partial x_j} + u_i (\tau_{ij})_{\text{eff}} \right], \quad (3)$$

where  $E$ —total energy;  $k$ —heat conductivity coefficient;  $T$ —temperature;

$$(\tau_{ij})_{\text{eff}} = \mu_{\text{eff}} \left( \frac{\partial u_i}{\partial x_j} + \frac{\partial u_j}{\partial x_i} \right). \quad (4)$$



FIGURE 8: Schematic diagram of the experimental device. (1) Nano-fluids jet flow device; (2) the CBN grinding wheel; (3) nano-fluids jet flow nozzles; (4) operative surface of pressure field test system; (5) numerical control grinder; (6) 24 V DC power supply; (7) pressure data acquisition.

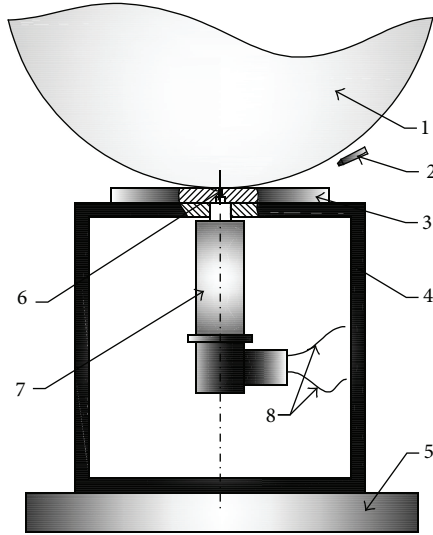


FIGURE 9: Diagram of pressure field test system. (1) The grinding wheel, (2) nozzles, (3) workpiece, (4) support, (5) grinder bench, (6) measuring hole, (7) pressure sensor, (8) cable.

In the previous equation, the amount of unknown numbers exceeded equations. To this end,  $k$ - $\epsilon$  turbulence model equation was introduced.

(4)  $k$ - $\epsilon$  turbulence model:

(a)  $K$  equation [23]:

$$\left[ \frac{\partial}{\partial t} (\rho k) + \frac{\partial}{\partial x_i} (\rho k u_i) \right] = \frac{\partial}{\partial x_j} \left[ \left( \mu + \frac{\mu_i}{\sigma_k} \right) \frac{\partial k}{\partial x_j} \right] + G_k - \rho \epsilon - Y_M. \quad (5)$$

(b)  $\epsilon$  equation:

$$\left[ \frac{\partial}{\partial t} (\rho \epsilon) + \frac{\partial}{\partial x_i} (\rho \epsilon u_i) \right] = \frac{\partial}{\partial x_j} \left[ \left( \mu + \frac{\mu_i}{\sigma_\epsilon} \right) \frac{\partial \epsilon}{\partial x_j} \right] + C_{1\epsilon} \frac{\epsilon}{k} G_k - C_{2\epsilon} \rho \frac{\epsilon^2}{k}, \quad (6)$$

where  $G_k$  shows the turbulence kinetic energy from the velocity gradient of laminar flow,  $G_b$  is the turbulence kinetic energy from the buoyancy force,  $Y_M$  is the fluctuations from transitional diffusion in the compressible turbulence.  $C_1$ ,  $C_2$ , and  $C_3$  are constants,  $\sigma_k$  and  $\sigma_\epsilon$  are the turbulence Prandtl numbers of  $k$  equation and  $\epsilon$  equation.

(c) Turbulence velocity model: the turbulence velocity  $\mu_i$  is determined by the following equation:

$$\mu_i = \rho C_\mu \frac{k^2}{\epsilon}, \quad (7)$$

where  $C_\mu$  is a constant; constants of the model include  $C_{1\epsilon} = 1.44$ ,  $C_{2\epsilon} = 1.92$ ,  $C_\mu = 0.09$ ,  $\sigma_k = 1.0$ ,  $\sigma_\epsilon = 1.3$ .

### 3. Simulation of Pressure Field in Grinding Zone

Figure 2 shows the pressure distribution of flow field of the grinding zone after the effects of compressed air continuous phase. It can be observed from the figure that the fluid pressure changes were only found at the entrance and exit of the wedge gap. There is a high pressure value, and the rapid pressure gradient occurs near the region where the gap between the grinding wheel and the work surface is minimal. The smaller the gap distance is, the higher the pressure gradient and the peak value pressure become. The pressure distribution is uniform in the direction of the width of the wheel except at the edge of wheel because of the side-leakage and becomes zero at the edge of the wheel, shown in Figure 3.

### 4. The Simulation Results

4.1. *The Impact of the Peripheral Velocity of Grinding Wheel on the Pressure in Grinding Zone.* By changing the peripheral velocity of grinding wheel, the pressure changes in the grinding zone can be obtained. The circumference velocity was taken as 45 m/s, 80 m/s, 120 m/s, and 160 m/s, and the corresponding changing curve was shown in Figure 4. In Figure 4, it can be seen that the pressure peak in direction  $x$  increased with the peripheral velocity of the grinding wheel. There is a high pressure value, and the rapid pressure gradient which occurred near the region where the gap between the wheel and the work surface was minimal, as shown in Figure 4. Along the  $X$  axis (the velocity of grinding wheel), the pressure gradually reached the maximum value from nothing, with the location close to the entrance of wedge gap. After this, it dropped sharply, even showing the negative pressure near minimum clearance. For *different velocities* of grinding wheel, two peak values of the pressure were almost at the same position, that is, close to the minimum clearance between the grinding wheel and the workpiece. Peak values of pressure were observed at the entrance near the wedge-shaped zone. The value was increased with rising velocity of

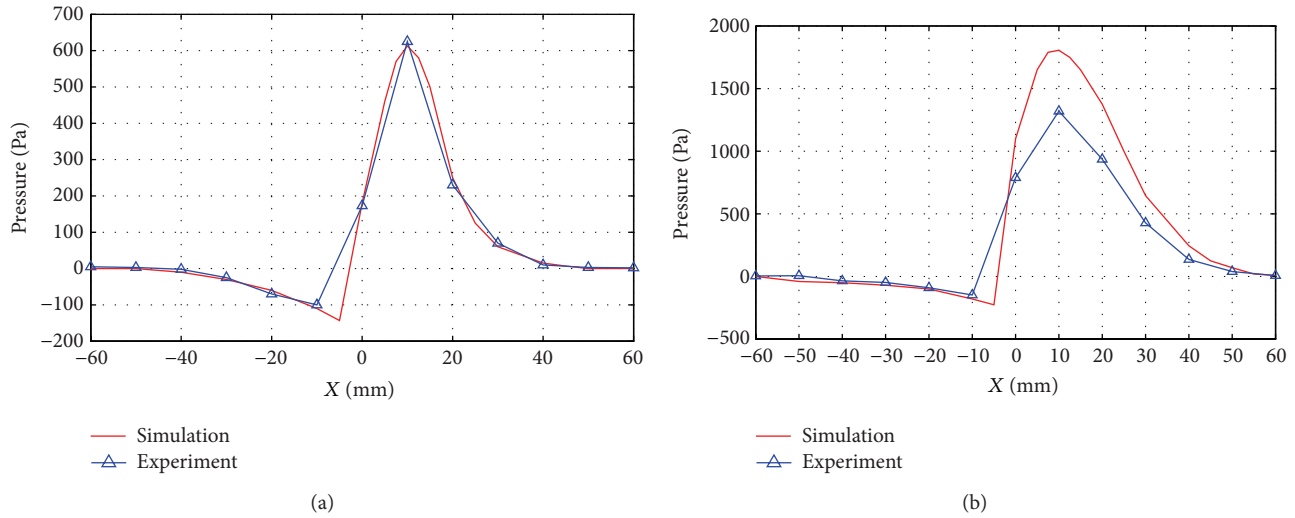


FIGURE 10: Comparison of pressure field theoretical simulation under different peripheral velocities of grinding wheel and the experimental results. (a) 45 m/s; (b) 160 m/s.

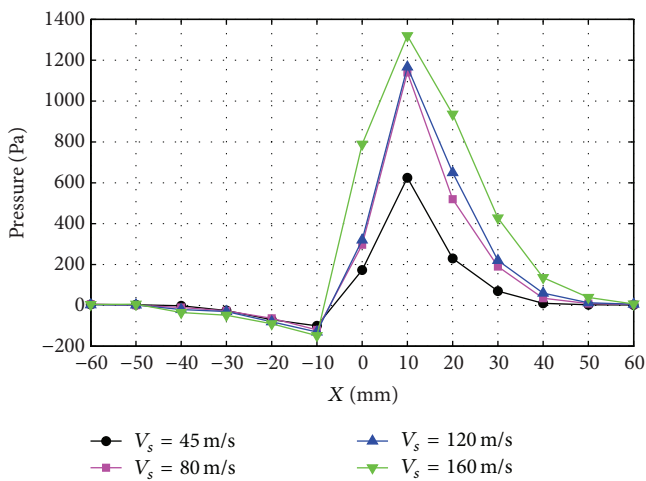


FIGURE 11: Comparison of pressure field experimental result under different peripheral velocities of grinding wheel.

grinding wheel, and the peak values of negative pressure were close to the exit of the wedge-shaped zone.

**4.2. The Impact of Minimum Clearance between the Grinding Wheel and the Workpiece on Pressure in the Grinding Zone.** By changing the minimum clearance between the grinding wheel and the workpiece, pressure changes of the grinding zone were obtained, and minimum clearance was taken as 100  $\mu\text{m}$ , 80  $\mu\text{m}$ , 50  $\mu\text{m}$ , and 30  $\mu\text{m}$ . The corresponding changing curve was shown in Figure 5.

As can be seen from Figure 5, peak values of pressure in grinding zone sharply reduce along the increase of minimum clearance. The smaller the gap distance was the higher the pressure gradient and the peak value pressure attained. It can

be inferred that the minimum clearance between the grinding wheel and the workpiece significantly influenced the pressure in the flow field of grinding zone.

**4.3. The Impact of Jet Flow Velocity on the Pressure of Grinding Zone.** By changing the jet flow velocity, pressure changes of the grinding zone were obtained. The jet flow velocity  $V_a$  was taken as 45 m/s, 60 m/s, 70 m/s, and 90 m/s. The corresponding changing curve was shown in Figure 6.

As can be seen from Figure 6, peak values of the pressure in grinding zone increase with increasing jet flow velocity, indicating that jet flow velocity influences the pressure in the flow field of grinding zone.

**4.4. The Impact of Positions and Angles of Nozzle on the Pressure in Grinding Zone.** By changing the positions and angles of nozzle, pressure changes of the grinding zone were obtained. The positions and angles of nozzle were taken as the intersection between the workpiece surface as 0°, 15°, and 20°, and corresponding changing curve was shown in Figure 7.

It can be seen from Figure 7 that at 15° the pressure in grinding zone was larger than the rest two angles because at 15°, the sprayed nanofluids were over the boundary of the return flux, when nanofluids can easily enter the wedge gap for cooling and lubricating. Hence, in the grinding with nanoparticle jet flow of MQL, the position of nozzles should be located beyond the boundary of the return flux.

## 5. The Experimental Study of Pressure Field in Grinding Zone

**5.1. Experimental Device.** Numerical control precision surface grinding machine and minimum quantity nano-particle jet flow feedway were used to establish minimum quantity

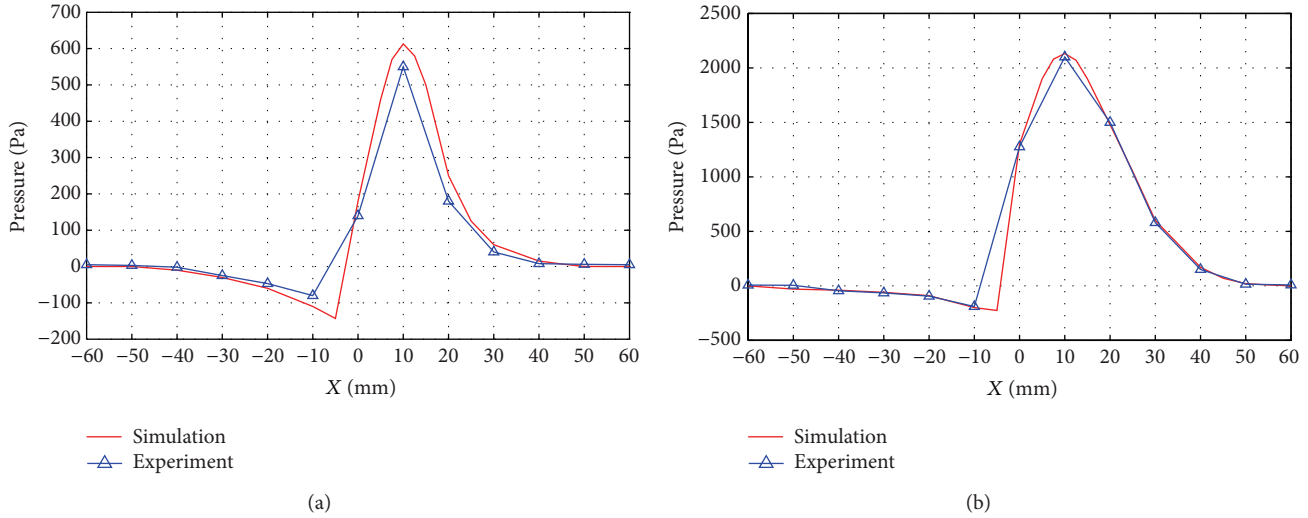


FIGURE 12: Comparison between pressure field theoretical simulation and experimental results at different jet flow velocities; (a) 45 m/s; (b) 90 m/s.

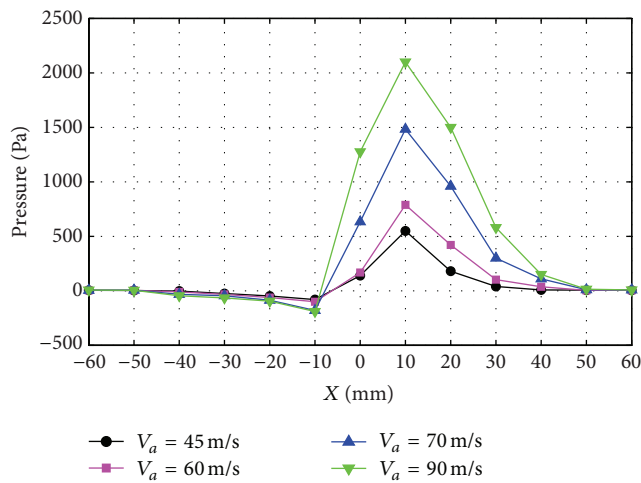


FIGURE 13: Comparison of pressure field experimental result under different at different jet flow velocities.

grinding bench. The jet flow pressure field applied workpiece-embedded CY3018 pressure sensor to measure and collect data. The schematic diagram of the experimental device was shown in Figure 8, and the diagram of pressure field test system was shown in Figure 9. The machining system of the experiment is composed of a rotating grinding wheel and a work surface, and the gap between them is MQL filled in with grinding coolant by a nozzle. The varied parameters included the grinding wheel velocity, nozzle jet velocity, minimum clearance between the grinding wheel and the work surface, and different angles of nozzle. A reciprocating table grinder with variable speed was used for the experiments. The wheels used were all of diameter  $D = 300$  mm and width  $b = 25$  mm. Each work specimen was 300 mm in length along

the grinding direction, 100 mm width, and 50 mm thickness. Parameters of nano-particle jet flow of MQL are carbon nanotube particles with the average diameter of 10–20 nm; oil base (vegetable oil); volume fraction: 1%; the MQL flow rates: 615 mL/h.

In the measurement of parameters, the sensor and transmitter transferred the measured values to the tester. The data was uploaded to the host computer via the serial port. After the conversion, the data was displayed in the form of tables and curves. Each experiment was repeated three times for averaging.

In the experiment, the numerical control ultrasonic oscillator was used to prepare stable oil-based nanofluids grinding liquid. The procedures are as follows: with the example of the preparation of 300 mL of oil-based nanofluids, the volume fraction was 1%. Assume the volume of nano-particle as  $V_n$  and the volume of base fluid as  $V_f$ . The volume fraction of nano-particles of nanofluids is

$$\phi = \frac{V_n}{V_n + V_f}. \quad (8)$$

According to the above equation, it can be calculated that the mass of nano-particles should be 0.74 g, with the volume of vegetable oil as 279 mL, the proportion of the dispersing agent as 7% (28 g). With the combination of nano-particle, base oil, and the dispersant, the ultrasonic vibration was used for the combination, with the vibration frequency as 70 Hz and the time as 15 min. After the mixture stabilized, the viscosity was measured.

## 6. Analysis of Experimental Results

Four different peripheral velocities of grinding wheel were adopted for the experiment. Among them, the experimental results of two grinding wheel velocities were compared with the theoretical simulation as shown in Figure 10. The contrast

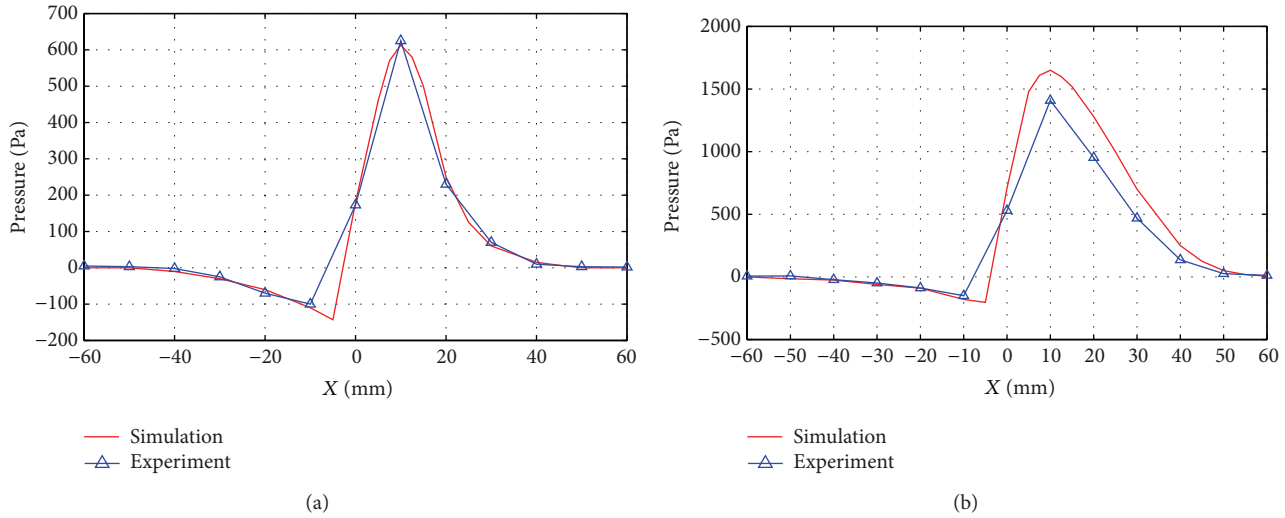


FIGURE 14: Comparison between pressure field theoretical simulation and experimental results with different minimum clearance; (a)  $100\ \mu\text{m}$ ; (b)  $30\ \mu\text{m}$ .

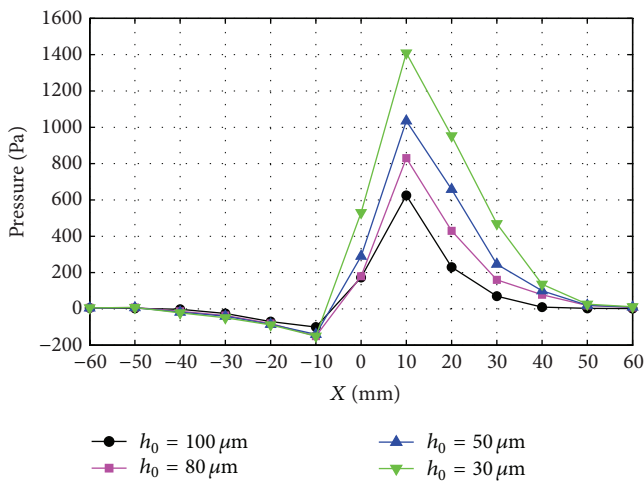


FIGURE 15: Comparison of pressure field experimental result with different minimum clearance.

of experimental result of the pressure in the grinding zone at two *different peripheral velocities* of grinding wheel was shown in Figure 11.

As shown in Figure 10, with lower the peripheral velocity of grinding wheel, the experimental result was relatively consistent with the theoretical simulation, when the velocity was 45 m/s; when the velocity was increased to 160 m/s, the experimental result at the entrance section of the wedge-shaped zone was lower than the theoretical simulation, which may be attributed to the increased difficulties of nanofluids breaking through the airbond with enlarged thickness. Figure 11 provides the contrast of experimental results of four *different peripheral velocities* of grinding wheel. The results show that the pressure in the grinding zone increased with the increases of the peripheral velocity of grinding wheel. With the velocity of 120 m/s, as the airbond layer prevented

nanofluids from entering the grinding zone, the pressure change was close to the curve when the grinding wheel velocity was 80 m/s.

Four different jet flow velocities were adopted for the experiment. Among them, the experimental results of two jet flow velocities were compared with the theoretical simulation as shown in Figure 12. The contrast of experimental result of the pressure in the grinding zone from different jet flow velocities from the nozzles was shown in Figure 13.

As shown in Figure 12, with higher jet flow velocity, the experimental result was relatively consistent with the theoretical simulation, when the velocity was 90 m/s; when the velocity was reduced to 45 m/s, the experimental result of the pressure in the grinding zone was lower than the theoretical simulation, which may be attributed to the influence from the airbond around the grinding wheel. With lower jet flow velocity, the sprayed nanofluids were insufficient to break through the airbond and enter the grinding zone. Figure 13 provides the contrast of experimental results of four different jet flow velocities, indicating that the pressure in the grinding zone increases with the jet flow velocity, and its regularities are basically consistent with those in the simulation analyze.

Four different minimum clearances were adopted for the experiment. Among them, the experimental results of two minimum clearances were compared with the theoretical simulation as shown in Figure 14. The contrast of experimental result of the pressure in the grinding zone with different minimum clearances was shown in Figure 15.

It can be observed from Figure 14 that with larger minimum clearance, the experimental result was relatively consistent with the theoretical simulation, when the minimum clearance was  $100\ \mu\text{m}$ ; yet when the minimum clearance was gradually reduced to  $30\ \mu\text{m}$ , the effective flow of nanofluids that enters the wedge gap was reduced, leading to lower experimental result of the pressure in the grinding zone than the theoretical simulation. Figure 15 shows the contrast of experimental curves with different minimum clearances. It

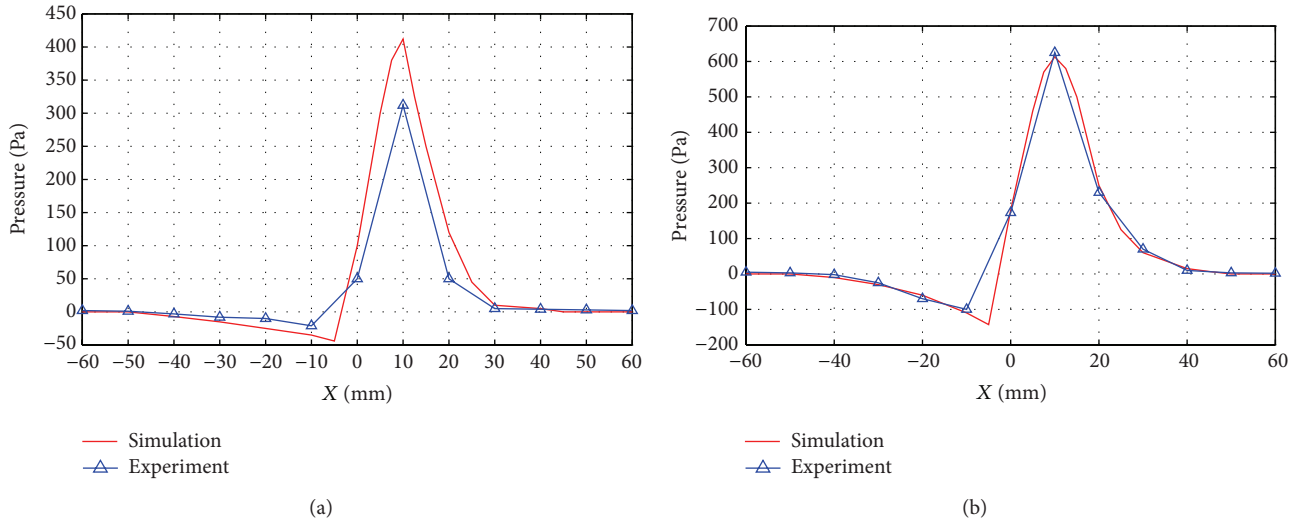


FIGURE 16: Comparison between pressure field theoretical simulation and experimental results with different positions and angles of nozzle; (a) 0°; (b) 15°.

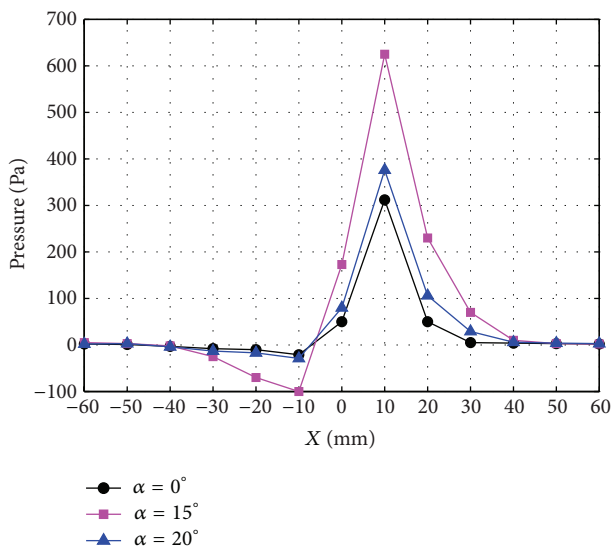


FIGURE 17: Comparison of pressure field experimental result with different positions of nozzles.

can be found that the regularities are basically consistent with the finding in our simulation. In other words, the pressure increases as wedge gap narrows. Along the velocity direction of grinding wheel, the pressure gradually increases, almost reaching the entrance of the wedge gap and then showing the tendency of declining. The negative pressure with a certain value was observed close to the wedge gap.

Three different spraying angles of nozzles were adopted for the experiment. The intersection between nozzle and the workpiece surface was taken as 0°, 15°, and 20°, respectively. Among them, the experimental results of two spraying angles of nozzle were compared with the theoretical simulation as shown in Figure 16. The contrast of experimental result of the

pressure in the grinding zone at different positions of nozzles was shown in Figure 17.

It can be observed from Figure 16 that when the spraying angle of nozzles was 15°, the experimental result was relatively consistent with the theoretical simulation; when the angle was 0°, the pressure in the grinding zone was lower than the theoretical simulation. It may be attributed to the lower spraying track of nanofluids at 0°. Figure 17 shows the contrast of experimental result of pressure at different spraying angles of nozzles. It can be observed that when the spraying angle of nozzles was 15°, the pressure was obviously higher than that at two different positions of nozzles, as the nanofluids were higher than the boundary of the return flux. At this angle, the nanofluids can easily enter the wedge-shaped zone.

## 7. Conclusions

In this paper, the theoretical model of nano-particle jet flow of MQL grinding zone pressure field was established for simulation and experiments. The results show the following.

- (1) With the velocity increase of grinding wheel, the pressure in the grinding zone gradually increases with a substantial range. For different velocities of grinding wheel, the peak values of the pressure were almost at the same position, that is, close to the minimum clearance between the grinding wheel and the workpiece. Peak values of pressure were observed at the entrance near the wedge-shaped zone. The value increases along rising velocity of grinding wheel. When the velocity was increased to 160 m/s, the experimental result at the entrance section of the wedge-shaped zone was lower than the theoretical simulation, which may be attributed to the increased difficulties of nanofluids breaking through the air-bond with enlarged thickness.

- (2) Peak values of pressure in grinding zone sharply reduce along the increase of minimum clearance with a substantial range, indicating that the minimum clearance between the grinding wheel and the workpiece significantly influences the pressure at the wedge gap of the flow field in grinding zone. When the minimum clearance was gradually reduced to 30  $\mu\text{m}$ , the effective flow of nanofluids that enters the wedge gap was reduced, leading to lower experimental result of the pressure in the grinding zone than the theoretical simulation.
- (3) Peak values of the pressure in grinding zone increase with increasing jet flow velocity with a substantial range, indicating that jet flow velocity influences the pressure in the flow field of grinding zone to a certain degree. For *different velocities* of jet flow, the peak values of the pressure were almost at the same position, that is, close to the minimum clearance between the grinding wheel and the workpiece. When the velocity was reduced to 45 m/s, the experimental result of the pressure in the grinding zone was lower than the theoretical simulation, which may be attributed to the influence from the airbond around the grinding wheel. With lower jet flow velocity, the sprayed nanofluids were insufficient to break through the airbond and enter the grinding zone.
- (4) When the spraying angle of *nozzles* was 15°, the pressure at the wedge gap was obviously higher than that at two different positions of nozzles. When the spraying angles of *nozzles* were 0° and 20°, the spraying track of nanofluids was lower than the boundary of the return flux. In this way, the nanofluids would encounter great obstacles to enter the wedge-shaped zone. Thus, the pressure became lower than the simulation results.

## Acknowledgments

This research was financially supported by the National Natural Science Foundation of China (50875138; 51175276) and the Shandong Provincial Natural Science Foundation of China (Z2008F11; ZR2009FZ007).

## References

- [1] J. Kopac and P. Krajnik, "High-performance grinding—a review," *Journal of Materials Processing Technology*, vol. 175, no. 1–3, pp. 278–284, 2006.
- [2] E. Brinksmeier and E. Minke, "High-performance surface grinding—the influence of coolant on the coolant process," *CIRP Annals*, vol. 42, no. 1, pp. 367–370, 1993.
- [3] E. Brinksmeier, Y. Mutlugünes, F. Klocke, J. C. Aurich, P. Shore, and H. Ohmori, "Ultra-precision grinding," *CIRP Annals*, vol. 59, no. 2, pp. 652–671, 2010.
- [4] J. F. G. Oliveira, E. J. Silva, C. Guo, and F. Hashimoto, "Industrial challenges in grinding," *CIRP Annals*, vol. 58, no. 2, pp. 663–680, 2009.
- [5] J. H. Liu, Z. J. Pei, and G. R. Fisher, "Grinding wheels for manufacturing of silicon wafers: a literature review," *International Journal of Machine Tools and Manufacture*, vol. 47, no. 1, pp. 1–13, 2007.
- [6] C. H. Li, G. Q. Cai, and S. C. Xiu, "Auto-correlation study on the surface profile finished by abrasive jet with grinding wheel as restraint," *International Journal of Computer Applications in Technology*, vol. 29, no. 2–4, pp. 262–266, 2007.
- [7] C. Guo and S. Malkin, "Analysis of fluid flow through the grinding zone," *Journal of engineering for industry*, vol. 114, no. 4, pp. 427–434, 1992.
- [8] C. C. Chang, "An application of lubrication theory to predict useful flow-rate of coolants on grinding porous media," *Tribology International*, vol. 30, no. 8, pp. 575–581, 1997.
- [9] M. Ganesan, C. Guo, R. A. Rafael, and S. Malkin, "Analysis of hydrodynamic forces in grinding," *Transactions of the North American Manufacturing Research Institute of SME*, vol. 24, pp. 105–110, 1996.
- [10] K. Furutani, N. Ohguro, N. T. Hieu, and T. Nakamura, "In-process measurement of topography change of grinding wheel by using hydrodynamic pressure," *International Journal of Machine Tools and Manufacture*, vol. 42, no. 13, pp. 1447–1453, 2002.
- [11] V. K. Gviniashvili, N. H. Woolley, and W. B. Rowe, "Useful coolant flowrate in grinding," *International Journal of Machine Tools and Manufacture*, vol. 44, no. 6, pp. 629–636, 2004.
- [12] S. Ebbrell, N. H. Woolley, Y. D. Tridimas, D. R. Allanson, and W. B. Rowe, "Effects of cutting fluid application methods on the grinding process," *International Journal of Machine Tools and Manufacture*, vol. 40, no. 2, pp. 209–223, 2000.
- [13] C. H. Li, J. Y. Li, S. Wang, and Q. Zhang, "Modeling and numerical simulation of the grinding temperature field with nanoparticle jet of MQL," *Advances in Mechanical Engineering*, vol. 2013, Article ID 986984, 9 pages, 2013.
- [14] M. Ganesan, C. Guo, and S. Malkin, "Measurement of hydrodynamic forces in grinding," *Transactions of the North American Manufacturing Research Institute of SME*, vol. 23, pp. 103–107, 1995.
- [15] P. Hryniewicz, A. Z. Szeri, and S. Jahanmir, "Application of lubrication theory to fluid flow in grinding: part I—flow between smooth surfaces," *Journal of Tribology*, vol. 123, no. 1, pp. 94–100, 2001.
- [16] P. Hryniewicz, A. Z. Szeri, and S. Jahanmir, "Application of lubrication theory to fluid flow in grinding: part II—influence of wheel and workpiece roughness," *Journal of Tribology*, vol. 123, no. 1, pp. 101–107, 2001.
- [17] J.-D. Kim, "Motion analysis of powder particles in EEM using cylindrical polyurethane wheel," *International Journal of Machine Tools and Manufacture*, vol. 42, no. 1, pp. 21–28, 2002.
- [18] S.-K. Lee, Y. Miyamoto, T. Kuriyagawa, and K. Syoji, "Effects of minimizing hydrodynamic pressure in ultra-precision mirror grinding," *International Journal of Machine Tools and Manufacture*, vol. 44, no. 10, pp. 1031–1036, 2004.
- [19] F. Klocke, E. Brinksmeier, and K. Weinert, "Capability profile of hard cutting and grinding processes," *CIRP Annals*, vol. 54, no. 2, pp. 557–580, 2005.
- [20] S. C. Xiu, C. X. Chao, and S. Y. Pei, "Experimental research on surface integrity with less or non fluid grinding process," *Key Engineering Materials*, vol. 487, pp. 89–93, 2011.
- [21] C. Li, Y. Hou, Y. Ding, and G. Cai, "Feasibility investigations on compound process: a novel fabrication method for finishing with grinding wheel as restraint," *International Journal of Computational Materials Science and Surface Engineering*, vol. 4, no. 1, pp. 55–68, 2011.

- [22] Y. Hou, C. Li, Z. Han, J. Li, and H. Zhao, "Examination of the material removal mechanisms during the abrasive jet finishing of 45 steel," *Advanced Science Letters*, vol. 4, no. 4-5, pp. 1478–1484, 2011.
- [23] Y. L. Hou, C. H. Li, and Q. Zhang, "Investigation of structural parameters of high speed grinder spindle system on dynamic performance," *International Journal Materials and Product Technology*, vol. 44, no. 1-2, pp. 92–114, 2012.

## Research Article

# Experimental Characterisation and Modelling of Homogeneous Solid Suspension in an Industrial Stirred Tank

Sébastien Calvo, Angélique Delafosse, Marie-Laure Collignon,  
Michel Crine, and Dominique Toye

Laboratory of Chemical Engineering, University of Liège, 15 Allée du 6 Août, 4000 Liège, Belgium

Correspondence should be addressed to Sébastien Calvo; scalvo@ulg.ac.be

Received 8 April 2013; Accepted 27 May 2013

Academic Editor: Guan Heng Yeoh

Copyright © 2013 Sébastien Calvo et al. This is an open access article distributed under the Creative Commons Attribution License, which permits unrestricted use, distribution, and reproduction in any medium, provided the original work is properly cited.

In this work, we study the conditions needed to reach homogeneous distribution of aluminium salts particles in water inside a torispherical bottom shaped stirred tank of 70 L equipped with a Pfaudler RCI type impeller and three equispaced vertical baffles. The aim of the present study is to develop a CFD model describing the quality of particle distribution in industrial scale tanks. This model, validated with experimental data, is used afterwards to develop scale-up and scale-down correlations to predict the minimum impeller speed needed to reach homogeneous solid distribution Nhs. The commercial CFD software Fluent 14 is used to model the fluid flow and the solid particle distribution in the tank. Sliding Mesh approach is used to take the impeller motion into account. Assuming that the discrete solid phase has no influence on the continuous liquid phase behaviour, the fluid flow dynamics is simulated independently using the well-known  $k-\varepsilon$  turbulence model. The liquid-solid mixture behaviour is then described by implementing the Eulerian Mixture model. Computed liquid velocity fields are validated by comparison with PIV measurements. Computed Nhs were found to be in good agreement with experimental measurements. Results from different scales allowed correlating Nhs values to the volumetric power consumption.

## 1. Introduction

Suspension of solid particles in a liquid is a key aspect of many processes, such as dissolution, crystallisation, adsorption, desorption, and catalytic or enzymatic reactions. Solid dispersion inside a stirred tank is a physical process where particles or aggregates are maintained in suspension and dispersed through a fluid by the action of an impeller. The main objective of this process is to avoid particle accumulation near the tank bottom and to obtain a solid distribution as uniform as possible to ensure a good quality mixing, that is, a homogeneous distribution of all components (catalyser, reacts, and products) inside the tank [1].

Depending on the application, the aim of mixing solid-liquid system is to obtain a “complete” suspension or a “homogeneous” suspension. In most published works, authors describe the solid dispersion process in stirred tanks using the just-suspended speed Njs which is the minimum speed of rotation of the impeller for which no particle deposits on the tank bottom and thus for which particles are

completely suspended [2, 3]. On the other hand, very few studies have described the stirring conditions for which the solid distribution is homogeneous in the whole tank. This is mainly due to the fact that small improvement in process performance is obtained by increasing agitation speed above Njs if compared to the corresponding increase of operating cost related to the dissipated power increase.

However, in some pharmaceutical and cosmetic processes, working with homogeneous suspensions is imperative. In this case, no correlation, similar to the Zwietering's one which allows the calculation of Njs [4], is available to predict the minimum impeller speed Nhs (homogeneous suspension speed) required to get an homogeneous distribution of solid particles. Experimental investigations and theoretical modelling are thus required to get robust scale-up and scale-down models allowing the prediction of Nhs. At the lab scale, several experimental methods allow the characterisation of solid dispersion in stirred tanks, such as electrical tomography [3], optical [5] or nephelometric probe [6], or direct visualisation of particle cloud [7]. In larger industrial vessels,

application of these methods may be problematic. Use of CFD codes, validated on the basis of experimental results collected at the lab scale, may be an appropriate alternative approach to characterise solid dispersion at the industrial scale.

During the last decade, computational fluid dynamics (CFD) has become a very powerful tool in the process industry not only for research and development of new processes but also for understanding and optimisation of existing ones. Number of authors have simulated turbulent fluid flow inside stirred tank, in many kinds of geometry and applications with commercial CFD codes (Fluent, CFX, ...). Reported results have shown the robustness of these codes to characterise the flow field in stirred tanks [8, 9]. Relevance of different simulation methods (LES,  $k-\epsilon$ , RSM, ...) used to describe turbulent quantities has been studied [10, 11]. Considering their results, we decided to use the well-known  $k-\epsilon$  model which allows sufficient accuracy on global turbulent quantities while keeping within a reasonable calculation time.

Concerning the modelling of the solid suspension, the literature mainly mentions two possible models: the “Eulerian Multiphase model” (MFM) and the “Eulerian Mixture model.” In the Eulerian Multiphase model, continuity and momentum balance equations are solved for each phases. The Eulerian Mixture model is a simplified version of the Eulerian Multiphase model suitable for dilute suspensions and small particle Stokes number. In this model continuity and momentum balance equations are solved for one mixture phase, the hydrodynamics parameters of which are computed from mass-averaged properties of each phase. Only one equation for the transport of volume fraction is added and solved for the dispersed phase. Consequently the dispersed phase is transported as a passive scalar in the tank. Interphase coupling term allows taking into account the relative motion of the dispersed phase from the continuous phase. This term consists of four different interphase forces: lift force, Basset force, virtual mass force, and drag force. Due to the very small influence of lift, Basset, and virtual mass forces on the simulated solid hold-dup profile [12], only the drag force may be considered in the interphase momentum exchange term (Schiller-Naumann). Results obtained using these two models are available in the literature and show that the Eulerian Multiphase model [13–15] is more accurate than the Eulerian Mixture model [16, 17] when working with particle size higher than  $100 \mu\text{m}$  and solid fraction ranging between 0.2 and 16%. Nevertheless, the Eulerian Mixture model is less time consuming and well adapted for low particle size ( $<10 \mu\text{m}$ ) and concentration ( $<0.1\%$ ) and should be suitable in our case.

## 2. Experimental Setup and Results

**2.1. Stirred Tank.** In the present work, experimental studies are performed in a pilot stirred tank of 70 L (Figure 1). It consists of a 430 mm diameter ( $D$ ) and 516 mm height ( $H/D = 1.2$ ) cylinder equipped with a torispherical bottom shape and three equispaced baffles with standard dimensions. Mixing is ensured by a 228 mm diameter ( $d/D = 0.53$ ) Pfaudler RCI (Retreat Curve Impeller) type impeller placed close to the tank bottom (clearance  $Y/D = 0.06$ ) in order to ensure a “single-loop” flow configuration. Working fluid

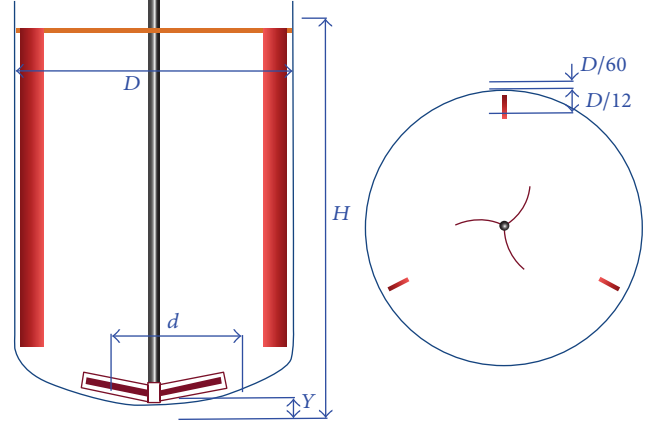


FIGURE 1: Schema of the pilot stirred tank.

is water in standard conditions ( $\rho_l = 998 \text{ kg}\cdot\text{m}^{-3}$  et  $\mu_l = 10^{-3} \text{ kg}\cdot\text{m}^{-1}\cdot\text{s}^{-1}$ ).

**2.2. Solid Suspension.** The solid phase used in this work is a mixture of aluminium salts (aluminium hydroxide and aluminium phosphate) commonly used in cosmetic and pharmaceutical processes. Only the properties of mixture will be considered in this study. Individual properties of each salt will not be taken into account. The density of the mixture is  $2500 \text{ kg}\cdot\text{m}^{-3}$  ( $\rho_s$ ) and the total particle load corresponds to an average volume fraction of  $0.74 \text{ cm}^3\cdot\text{L}^{-1}$ .

Size distribution of particles has been measured by LASER granulometry (Figure 2). This distribution has first been evaluated in a stirred cell. The measured mean particle size ranged between  $5$  and  $7 \mu\text{m}$ . Stopping agitation inside the measurement cell allows the visualisation of formation of aggregates due to the hydration of aluminium salts. As can be seen in Figure 2, after 60 min without agitation, the mean size of particles reached  $60 \mu\text{m}$ . Agitation resumption allows the breaking the aggregates and returning to the initial size of the particles. These results show that agitation has a significant influence on the particle size distribution with a tendency to reduce the average size.

The equivalent diameter of particle is a very commonly used quantity to describe their behaviour in suspension. It was determined by measuring their settling velocity, because, for a solid suspension composed of a wide range of particle sizes, an equivalent diameter can be expressed as a function of the particle settling velocity. The works of Perry and Green [18] give the correlation to express the settling velocity  $V_t$  for spherical particles:

$$V_t = \left( \frac{4gd_p^2(\rho_s - \rho_L)}{3C_D\rho_L} \right)^{1/2}, \quad (1)$$

where  $g$  is the gravitational constant ( $9.81 \text{ m}\cdot\text{s}^{-2}$ ) and  $C_D$  represents the drag coefficient which is a function of particle Reynolds number  $Re_p$  and particles shape:

$$Re_p = \frac{\rho_L V_t d_p}{\mu}. \quad (2)$$

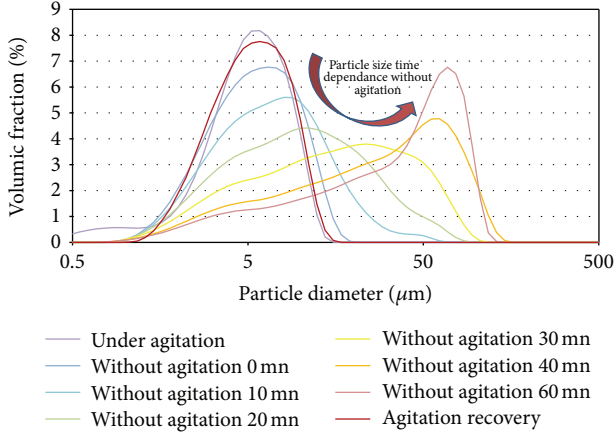


FIGURE 2: Particle size distribution and the impact of agitation on particle size.

TABLE I: Hydrodynamic regimes for settling particles.

Regime	Reynolds number	$C_D$ Expression
Stokes' law (laminar)	$Re_p < 0.3$	$C_D = 24/Re_p$
Intermediate law	$0.3 < Re_p < 1000$	$C_D = 18.5/Re_p^{3/5}$
Newton's law (turbulent)	$1000 < Re_p < 35 \times 10^4$	$C_D = 0.445$

Correlation for  $C_D$  covers several hydrodynamic regimes. The corresponding ranges for  $Re_p$  and the correlating expression of  $C_D$  are shown in Table 1 for three hydrodynamics regimes.

When the expressions for  $C_D$  are substituted in (1), the resulting expressions for the free settling velocity  $V_t$  are, respectively,

- (i) for the Stokes' law (laminar) regime,  $Re_p \leq 0.3$ :

$$V_t = \frac{gd_P(\rho_S - \rho_L)}{18\mu}, \quad (3)$$

- (ii) for the Newton's law (turbulent) regime,  $1000 \leq Re_p \leq 35.104$ :

$$V_t = 1.73 \left[ \frac{gd_P(\rho_S - \rho_L)}{\rho_L} \right]^{1/2}. \quad (4)$$

The settling velocity of the suspension has been estimated by observing the particle sedimentation front evolution inside a graduated tube (Figure 3). The settling velocity was found to be equal to  $23 \text{ cm}\cdot\text{h}^{-1}$  which corresponds to an equivalent diameter of  $9 \mu\text{m}$  considering that the particle flow regime was found to be ruled by the Stokes' law (laminar). If compared to the particle size distribution obtained by granulometry (Figure 2), this result shows that this size does not correspond to individual particles but corresponds to aggregates formed after the agitation stopped. Aggregates have

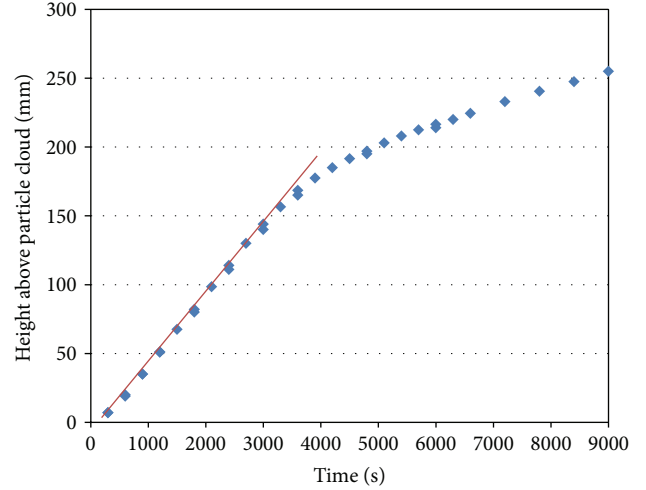


FIGURE 3: Time evolution of the particle sedimentation front: estimation of the settling velocity.

also been observed visually during the particle sedimentation front study.

In the case of our solid phase (mixture of aluminium salts), the estimation of the equivalent diameter of the suspension in a stirred tank seems to be difficult because the particle size directly depends on the surrounding hydrodynamic conditions. In the CFD model, this information is a key parameter to model the solid suspension. Considering the complex behaviour of our solid phase, we decide to use a pragmatic approach. We supposed that the particles are spherical and an equivalent diameter will be fitted to be representative of the experimental observations. The fitted value of the equivalent diameter will then be compared with previous results to check the soundness of our approach.

**2.3. Experimental Investigation of the Homogeneous Suspension Speed.** Homogeneous suspension is reached when the particle concentration is uniformly distributed inside the stirred tank. In the case of particles denser than the working fluid, heterogeneity first appears at the top of the tank.  $N_{hs}$  has thus been measured by a nephelometric probe (Figure 4) disposed near the liquid free surface. The probe is placed one centimetre below the liquid free surface to avoid disturbances due to the surface deformation.

The experimental method consists of two steps. First, the agitation speed is fixed at a high value to obtain a steady nephelometric signal which corresponds to a homogeneous suspension ( $N_{init} \gg N_{hs}$ ). The agitation speed is then decreased at a lower value ( $N_{test}$ ) and the nephelometric signal stability is controlled. We considered here that homogeneous suspension speed  $N_{hs}$  is reached when the oscillation of the signal does not exceed 2% of the value obtained at  $N_{init}$ . These two steps ( $N_{init} - N_{test}$ ) are then repeated increasing  $N_{test}$  value until  $N_{hs}$  is reached.

In this investigation, the position of the nephelometric probe remained constant and results may not be representative of the homogeneity in the entire volume of the tank. As

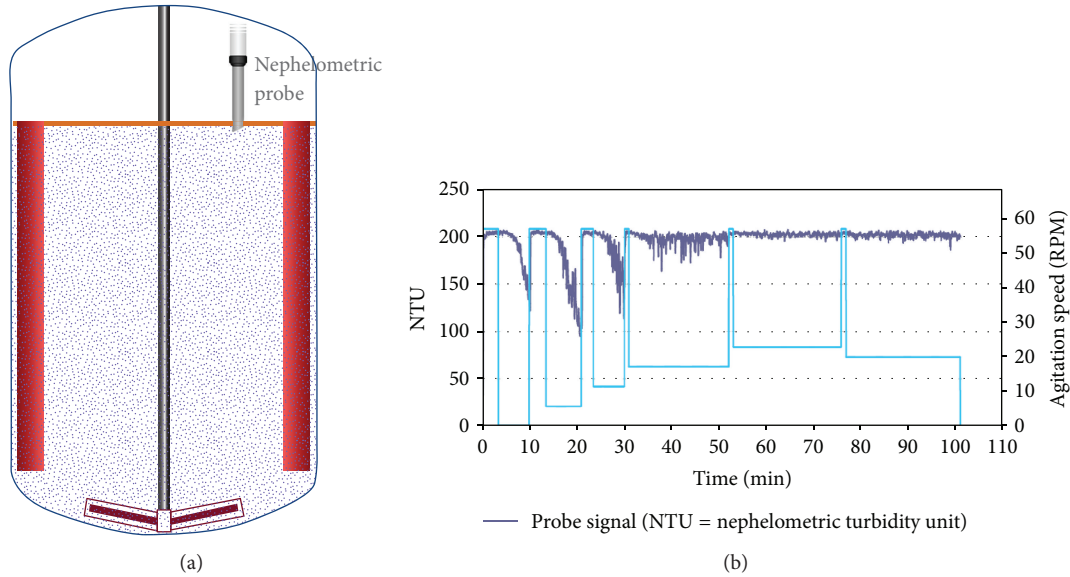


FIGURE 4: Experimental measurement of Nhs by nephelometric method.

nonhomogeneous zones were visually observed near the liquid free surface, we make here the hypothesis that measured Nhs corresponds to a homogeneous suspension within 95% of the tank volume. Assuming these considerations, Nhs was found to be equal to 20 RPM in the 70 L pilot tank.

### 3. CFD Modelling

**3.1. Liquid Flow Model:  $k-\varepsilon$ .** Geometry of the 70 L pilot tank and its meshing have been, respectively, performed with the commercial tools provide by Ansys Software “DesignModeler” and “Ansys Meshing” (Figure 5(a)). In order to use the Sliding Mesh (SM) method, two fluid zones were defined: an inner rotating cylindrical volume ( $4.3 \times 10^{-3} \text{ m}^3$ ) centred on the impeller which includes a part of bottom wall ( $Y/D = 0.06$ ) and an outer stationary zone ( $65.7 \times 10^{-3} \text{ m}^3$ ), containing the rest of the tank and the baffles. The interface is located at equal distance from the impeller Tip and the inside edge of the baffles so that the region of flow periodicity was contained within the sliding mesh. To counterbalance the rotation of the wall below the impeller, a “moving wall” condition is set in the direction opposite to the impeller rotation.

The mesh used consists of approximately 125,000 and 375,000 hexahedrons for the rotating and the stationary zones, respectively. An illustration of the meshed zones is given in Figure 5(a), which clearly shows that finer meshes have been used around the impeller and in the impeller discharge zone (inside the torispherical bottom), where the velocity spatial gradients are expected to be large. We also take care of keeping the same mesh dimension between the rotating and the stationary interface to ensure a good exchange of the hydrodynamic quantities between the two zones during the calculation. A “no-slip” condition is applied on all walls of the geometry. Assuming that the baffles limit the vortex formation, a symmetry condition was used at the liquid free surface.

Simulations of the turbulent single phase flow are then performed with the commercial CFD code Fluent 14 (Ansys 14) using the standard  $k-\varepsilon$  model [1]. The working fluid is water, with a density  $\rho_l = 998 \text{ kg}\cdot\text{m}^{-3}$  and a viscosity  $\mu_l = 10^{-3} \text{ kg}\cdot\text{m}^{-1}\cdot\text{s}^{-1}$ . As the SM method was used, the flow resolution is unsteady. At each time step, the position of the rotating zone relative to the stationary one is recomputed and the grid interface of the rotating zone slides along the interface of the stationary zone. For all simulations, the time step is set as a function of the impeller speed so that it rotates of a  $2^\circ$  angle per time step.

At the end of each time step, after a maximum of 20 iterations, the convergence criterion reaches  $10^{-4}$  for the continuity and  $10^{-5}$  for momentum and turbulence quantities. Simulations are performed in double precision with the segregated implicit solver. Temporal discretisation and spatial discretisation of all quantities (continuity, momentum and turbulence) are of the second order.

Finally, the analysis of the velocity field is performed after three or four complete revolutions of the impeller, when convergence of the Tip velocity is reached. For each time step, a velocity field is computed on a vertical plane which corresponds to one position of the impeller (phase average). To avoid the influence of the impeller position, an average is performed over a complete rotation of the impeller. The mean velocity field is thus obtained (Figures 5(b) and 5(c)).

**3.2. Experimental Validation of the Turbulent Flow Model.** Particle Image Velocimetry (PIV) is a nonintrusive optical technique which allows measuring instantaneous velocity fields in a plane of the flow. The 2D PIV technique is presented in Figure 6. To obtain the instantaneous velocity fields, fluid is previously seeded with fluorescent particles of the same density as the working fluid in order to follow the flow streamlines without disturbing it. The fluid is then highlighted by two light pulses provide by a vertical LASER



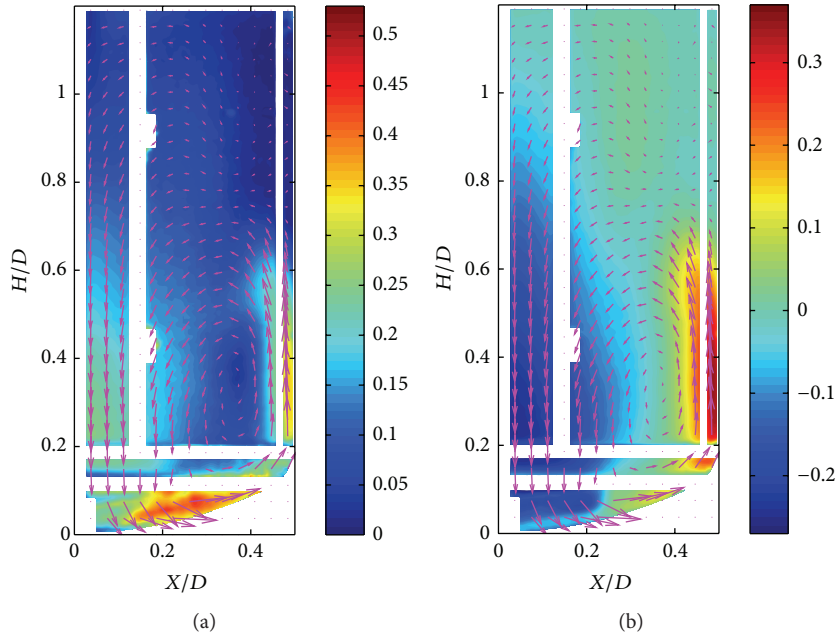


FIGURE 7: 3D PIV nondimensional velocity field: (a) mean velocity  $\bar{V}/V_{Tip}$  and (b) axial component  $V/V_{Tip}$ .

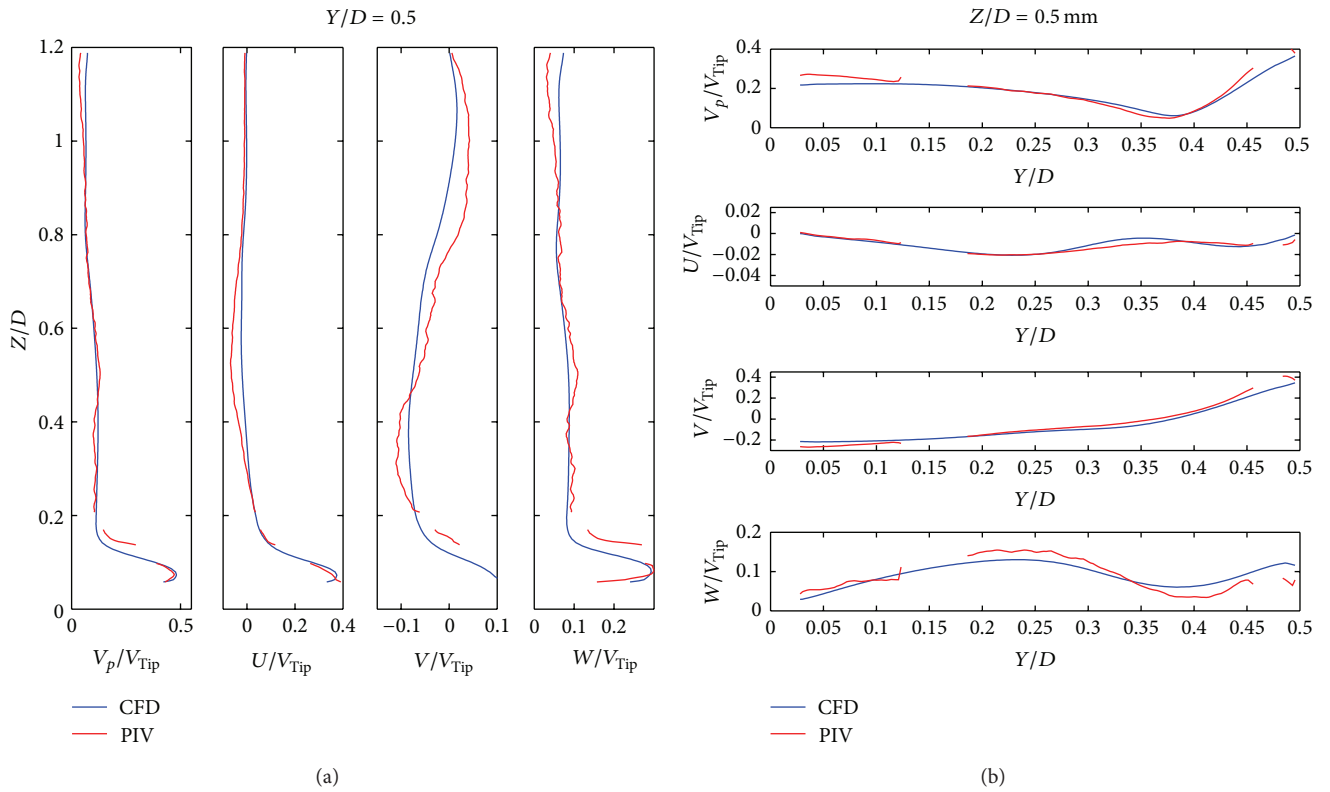


FIGURE 8: (a) axial and (b) radial evolution of non-dimensional mean velocity ( $V$ ) and the three non-dimensional components of the velocity: axial ( $V$ ), radial ( $U$ ), and tangential ( $W$ ).

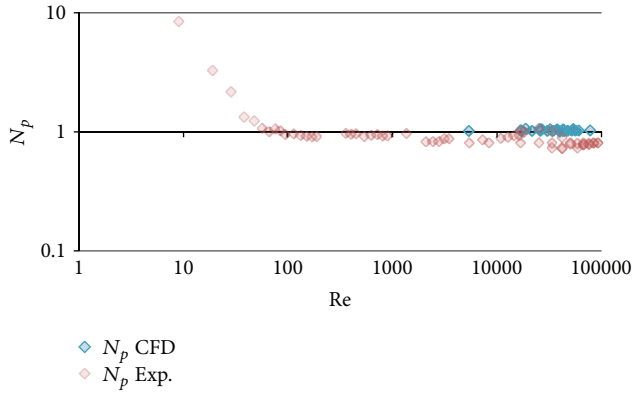


FIGURE 9: Power Number comparison.

model is thus able to provide representative values of the flow hydrodynamic quantities.

The CFD simulation results have been further validated by experimental measurement of the power number. The power number is deduced from the torque  $C$  measured or computed on the impeller axis and blades as follows:

$$P = 2\pi NC, \quad (5)$$

$$Np = \frac{P}{\rho N^3 d^5}.$$

The experimental torque has been measured with a torque meter installed on the agitation motor in the 70 L tank with several liquids of different viscosities in order to cover Reynolds number ranging from 10 to  $10^5$ . The numerical torque is computed from CFD simulations on the impeller and the agitation axis.

Comparison of the experimental and simulated power numbers is presented in Figure 9. These results show that the computed power number is greater than the experimental one due to the use of a moving wall at the bottom of the tank but remained in the same range, within the experimental error. The CFD model is then able to predict the power consumption in the turbulent regime ( $Re > 10^4$ ). On this figure, one can see that, in this geometry, the power number remained constant with the Reynolds in both transitional and turbulent regimes ( $Re > 10^3$ ).

**3.3. Modelling the Solid Suspension Behaviour.** Assuming that the solid particles have a negligible influence on the fluid flow (volume fraction less than 0.1%), the Eulerian Mixture model is implemented to the previously computed  $k-\epsilon$  model. Only drag force is considered in the interphase momentum exchange term with the Schiller-Naumann's drag correction available for spherical particles.

In order to compare experimental Nhs values to computed ones, we considered that the computed homogeneous suspension is reached when the local solid volume fraction reaches  $\pm 2\%$  of its averaged value ( $0.74 \text{ cm}^3 \cdot \text{L}^{-1}$ ) within 95% of the whole tank volume. To obtain a representative model of the experimental observation, the impeller speed is set to the experimental value of Nhs, 20 RPM, while the

particle equivalent diameter is fitted until the criterion of homogeneous suspension is reached.

In Figure 10(a), the spatial distribution of the solid volume fraction is computed on a vertical plan for an agitation speed of 20 RPM and a particle equivalent diameter of  $7 \mu\text{m}$ . For this equivalent diameter, integration of the local solid volume fraction on the entire volume shows that the suspension reaches the homogeneous criterion ( $0.74 \text{ cm}^3 \cdot \text{L}^{-1} \pm 2\%$ ) in more than 95% of the whole tank volume (Figure 10(b)). The model is thus representative of the experimental observations for a particle equivalent diameter equal to  $7 \mu\text{m}$ .

This adjusted value of the particle diameter is very close to the value measured by granulometry inside the stirred cell (Figure 2). According to these results, one may conclude that hydrodynamic conditions reached at Nhs are sufficient to avoid the formation of aluminium salts aggregates.

## 4. Results and Discussion

The numerical model of the solid suspension has been used to determine Nhs at three different scales in geometrically similar stirred tanks, the volume of which were 12.5 L, 70 L, and 375 L. Results are presented in Figure 11 (green circles). In order to reduce computing time, homogeneous suspension speed has been computed with an accuracy of 2.5 RPM. Experimental measurement of Nhs has also been performed at the same scales (blue marks). Results from CFD are in very good agreement with those experiment results.

Based on the literature [20], extrapolation of the just-suspended speed (Njs) can be performed according to two criteria: if the regime is controlled by the particle lift from the tank bottom, conservation of the Tip speed will be chosen as invariant parameter, whereas if the regime is controlled by the particle deposition on the tank bottom, the invariant parameter will be the volumetric power consumption. In the case of solid suspension denser than the working fluid, the process is controlled by sedimentation which can be expressed by analogy, as deposition. According to this analogy, a model based on the conservation of the volumetric power consumption will be able to predict Nhs at different scales as it is shown in Figure 11 (red curve). The CFD calculations have not been performed for Reynolds number lower than  $8 \cdot 10^3$  because the  $k-\epsilon$  model is only suited for fully developed turbulent regime. However, as shown in Figure 9, experimental study of the power consumption has shown that the power number remained constant in the transitional regime ( $Re > 10^3$ ). Consequently, Nhs has been measured at four different scales for Reynolds number lower than  $8 \cdot 10^3$  to evaluate the sensibility of the model in the transitional regime. These results show that the model is well suited to predict Nhs in the transitional regime as long as the power number is constant in this regime.

## 5. Conclusions

In this work, a CFD calculation was successfully used to model the global behaviour of a complex solid suspension. Turbulent flow inside the stirred tank was first simulated using the  $k-\epsilon$  model and the results have been validated by experimental PIV measurements. In order to model the

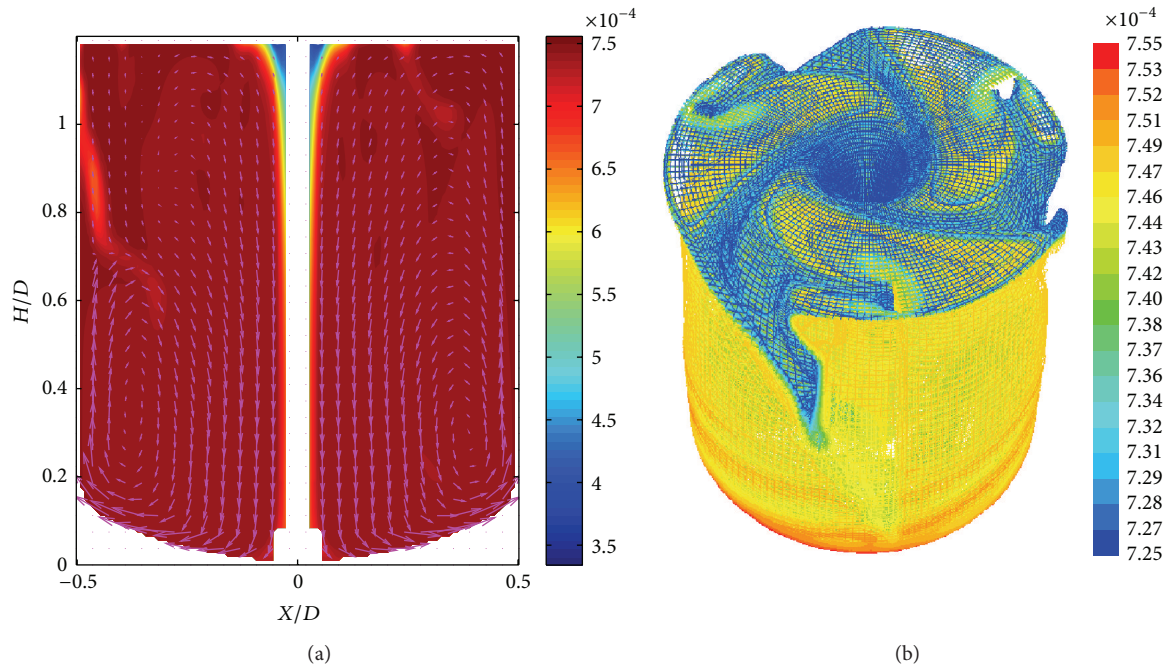


FIGURE 10: Spatial distribution of the computed solid volume fraction: (a) on a vertical plan and (b) within the whole volume.

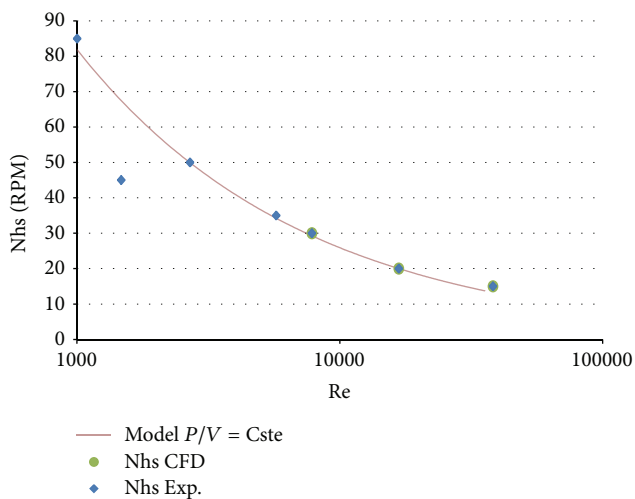


FIGURE 11: Estimation of  $N_{hs}$  at different scales.

solid suspension, the “Eulerian Mixture” model was then implemented in the previous model, assuming that due to the low concentration and to the very small size of particles, the solid phase would not affect the fluid flow. The equivalent diameter of the particles has been fitted inside the model to be representative of the experimental observations of the homogeneous suspension. Value of this diameter was then successfully compared to the value measured by granulometry under agitation. This result shows that the conditions needed to reach homogeneous suspension inside the tank avoid the formation of aggregates.

Finally, the model was used to compute  $N_{hs}$  at different scales. Corresponding results were successfully compared to  $N_{hs}$  values experimentally measured at the same scales.

These results allow the conclusion that the homogeneous suspension speed  $N_{hs}$  is directly correlated to the volumetric power consumption and that these quantities could thus be chosen as an invariant parameter in scale-up or scale-down operations.

## References

- [1] E. L. Paul, V. A. Atiemo-Obeng, and S. M. Kresta, *Handbook of Industrial Mixing*, John Wiley & Sons, Hoboken, NJ, USA, 2010.
- [2] R. Jafari, J. Chaouki, and P. A. Tanguy, “A comprehensive review of just suspended speed in liquid-solid and gas-liquid-solid stirred tank reactors,” *International Journal of Chemical Reactor Engineering*, vol. 10, no. 1, article R1, 2012.
- [3] F. Ricard, C. Brechtelsbauer, X. Y. Xu, and C. J. Lawrence, “Monitoring of multiphase pharmaceutical processes using electrical resistance tomography,” *Chemical Engineering Research and Design*, vol. 83, no. 7 A, pp. 794–805, 2005.
- [4] T. N. Zwietering, “Suspending of solid particles in liquid by agitators,” *Chemical Engineering Science*, vol. 8, no. 3-4, pp. 244–253, 1958.
- [5] R. Angst and M. Kraume, “Experimental investigations of stirred solid/liquid systems in three different scales: particle distribution and power consumption,” *Chemical Engineering Science*, vol. 61, no. 9, pp. 2864–2870, 2006.
- [6] R. Jafari, P. A. Tanguy, and J. Chaouki, “Experimental investigation on solid dispersion, power consumption and scale-up in moderate to dense solid-liquid suspensions,” *Chemical Engineering Research and Design*, vol. 90, no. 2, pp. 201–212, 2012.

- [7] S. Wang, D. V. Boger, and J. Wu, "Energy efficient solids suspension in an agitated vessel-water slurry," *Chemical Engineering Science*, vol. 74, pp. 233–243, 2012.
- [8] J. Aubin, D. F. Fletcher, and C. Xuereb, "Modeling turbulent flow in stirred tanks with CFD: the influence of the modeling approach, turbulence model and numerical scheme," *Experimental Thermal and Fluid Science*, vol. 28, no. 5, pp. 431–445, 2004.
- [9] D. A. Deglon and C. J. Meyer, "CFD modelling of stirred tanks: numerical considerations," *Minerals Engineering*, vol. 19, no. 10, pp. 1059–1068, 2006.
- [10] A. Delafosse, A. Line, J. Morchain, and P. Guiraud, "LES and URANS simulations of hydrodynamics in mixing tank: comparison to PIV experiments," *Chemical Engineering Research and Design*, vol. 86, no. 12, pp. 1322–1330, 2008.
- [11] B. N. Murthy and J. B. Joshi, "Assessment of standard  $k-\epsilon$ , RSM and LES turbulence models in a baffled stirred vessel agitated by various impeller designs," *Chemical Engineering Science*, vol. 63, no. 22, pp. 5468–5495, 2008.
- [12] G. R. Kasat, A. R. Khopkar, V. V. Ranade, and A. B. Pandit, "CFD simulation of liquid-phase mixing in solid-liquid stirred reactor," *Chemical Engineering Science*, vol. 63, no. 15, pp. 3877–3885, 2008.
- [13] G. Montante, G. Micale, F. Magelli, and A. Brucato, "Experiments and CFD predictions of solid particle distribution in a vessel agitated with four pitched blade turbines," *Chemical Engineering Research and Design*, vol. 79, no. 8, pp. 1005–1010, 2001.
- [14] G. Micale, F. Grisafi, L. Rizzuti, and A. Brucato, "CFD simulation of particle suspension height in stirred vessels," *Chemical Engineering Research and Design*, vol. 82, no. 9, pp. 1204–1213, 2004.
- [15] A. R. Khopkar, G. R. Kasat, A. B. Pandit, and V. V. Ranade, "Computational fluid dynamics simulation of the solid suspension in a stirred slurry reactor," *Industrial and Engineering Chemistry Research*, vol. 45, no. 12, pp. 4416–4428, 2006.
- [16] G. Micale, G. Montante, F. Grisafi, A. Brucato, and J. Godfrey, "CFD simulation of particle distribution in stirred vessels," *Chemical Engineering Research and Design*, vol. 78, no. 3, pp. 435–444, 2000.
- [17] D. Wadnerkar, R. P. Utikar, M. O. Tade, and V. K. Pareek, "CFD simulation of solid-liquid stirred tanks," *Advanced Powder Technology*, vol. 23, no. 4, pp. 445–453, 2012.
- [18] R. H. Perry and D. Green, *Chemical Engineer's Handbook*, McGraw-Hill, New York, NY, USA, 1984.
- [19] M.-L. Collignon, *Étude de l'hydrodynamique au sein d'un bioréacteur à cuve agitée utilise pour la culture de cellules animales adhérentes sur microporteurs: caractérisation expérimentale et théorique des écoulements via des outils eulériens et lagrangiens [Ph.D. report]*, 2012.
- [20] C. Xuereb, M. Poux, and J. Bertrand, *Agitation et Mélange: Aspects Fondamentaux et Applications Industrielles, L'Usine Nouvelle*, Dunod, Paris, France, 2006.

## Research Article

# Large-Eddy Simulation of Particle-Laden Turbulent Flows over a Backward-Facing Step Considering Two-Phase Two-Way Coupling

Wang Bing, Zhang Hui Qiang, and Wang Xi Lin

School of Aerospace, Tsinghua University, Beijing 100084, China

Correspondence should be addressed to Wang Bing; [wbing@mail.tsinghua.edu.cn](mailto:wbing@mail.tsinghua.edu.cn)

Received 22 January 2013; Revised 6 April 2013; Accepted 20 April 2013

Academic Editor: Guan Heng Yeoh

Copyright © 2013 Wang Bing et al. This is an open access article distributed under the Creative Commons Attribution License, which permits unrestricted use, distribution, and reproduction in any medium, provided the original work is properly cited.

Particle-laden turbulent flows over a backward-facing step were here numerically studied by means of a large-eddy simulation considering two-way coupling between particle and fluid phases. The modification of turbulence by particles was then analyzed based on the predicted results of mean and fluctuating velocities. The influencing factors of particle size and material density were also evaluated. Turbulence modifications are anisotropic and closely dependent on flow status. Stronger modulations were observed in the up-wall shear flow regions. Fluid laden with smaller size, low-density particles showed enhancement of turbulence in the streamwise direction, but this effect was less pronounced in the case of larger low-density particles. Particle dispersions were also investigated for comparison of particle instantaneous distributions in coherent structures. Particle modulations of turbulence were not found to change particle preferential distributions. The conclusions drawn in the present study were useful for further understanding of a two-phase turbulence physical mechanism and establishment of accurate prediction models for engineering applications.

## 1. Introduction

Two-phase turbulent flows occur in many technical processes in engineering, such as in chemical processes, pneumatic transport of particulates, air pollution control, circulating fluidized beds, and coal combustion. Turbulence plays a very important role in the transport of mass, momentum, and energy between particles and fluid phases. Studies on particle dispersion by turbulence and particle modulation to turbulence are very important for further understanding physical mechanisms of the interphase interactions between two phases.

The modulation of turbulence by particles has been studied in isotropic turbulence by Boivin et al. [1], Elghobashi and Truesdell [2], Michaelides and Stock [3], and Parthasarthy and Faeth [4, 5]. These teams have reported that dissipation and production of turbulent kinetic energy of the continuous fluid phase are modified by laden particles in homogeneous turbulence scenarios. Experimental investigations regarding the modification of turbulence have also been performed for

particle-laden turbulent flows in jets [6–10], vertical pipes [11–14], channels [15] and free shear layers [16, 17] and over a backward-facing step [18–20]. Gore and Crowe proposed a physical model that they used to determine whether particles enhance or attenuate the intensity of fluid turbulence by comparing the scales of particle and local vortices based on the results of previous studies on two-phase flow experiments [21]. Hetsroni summarized that turbulence can be enhanced or attenuated depending on the value of each particle's Reynolds number  $Re_p$  [22]. In addition, Yarin and Hetsroni proposed a simplified theory for the particles-turbulence interaction taking into account the carrier fluid velocity gradients and turbulent wakes behind coarse particles [23]. Kenning and Crowe developed a model of the modulation of turbulence for gas-particle flows based on previous work on particle drag and on the dissipation based on a length scale corresponding to the interparticle spacing [24]. In brief, particle modulation of turbulence can be affected by particle size and density.

However, the effective viscosity of the fluid phase can change, and turbulent and coherent eddies are generated in different ways, producing different increases in velocity gradients for specific flow configurations. In this way, even if the effects of particles on turbulence have been investigated by many researchers [25–30], modifications of turbulence characteristics by solid particles are not yet clearly understood. Whether particles enhance or attenuate the intensity of fluid-phase turbulence can differ under different study conditions. The influencing factors of particle phase on fluid phase in two-phase turbulent flows can vary considerably. For better application of gas-solid two-phase turbulent flows in industrial applications, more information should be provided to evaluate the factors affecting changes in turbulence.

In this paper, particle-laden two-phase turbulent flows over a backward-facing step were numerically predicted using a two-way coupling large-eddy simulation. Particle size and material density were investigated, and their influence on modulations in turbulence was evaluated. Quantitative comparisons of gas-phase mean and fluctuating velocities were carried out under different sets of flow conditions. Instantaneous large-scale turbulence structures in flows laden with different particles along with particle dispersion distributions in the flow field were also investigated.

## 2. Physical and Numerical Models

**2.1. Flow Configuration.** In this paper, the flow configuration was the same as the one used in a previous study [31], as shown in Figure 1. The backward-facing step height  $H$  was 0.0267 m, which was used as the reference length scale. The channel height  $h$  at inlet section was 0.04 m, representing an expansion ratio of 5 : 3. The computational domain was  $35 H$  in the streamwise direction,  $2.5 H$  in the transverse direction, and  $10 H$  in the spanwise direction. The inlet centerline velocity  $U_0$  is 10.5 m/s. The Reynolds number,  $Re = U_0 H / \nu$ , was 18,400. Here  $\nu$  was the kinematic viscosity.

**2.2. Continuous Phase Equations.** Applying the box-filtering operation to the incompressible Navier-Stokes equations, the equations governing the motion of the resolved scales in large-eddy simulation are given as follows:

$$\begin{aligned} \frac{\partial \bar{u}_i}{\partial x_i} &= 0, \\ \frac{\partial \bar{u}_i}{\partial t} + \frac{\partial}{\partial x_j} (\bar{u}_i \bar{u}_j) &= -\frac{\partial p}{\partial x_i} + \frac{1}{Re} \frac{\partial^2 \bar{u}_i}{\partial x_j \partial x_j} \\ &\quad - \frac{\partial \tau_{ij}}{\partial x_j} + \bar{S}_{pfi}. \end{aligned} \quad (1)$$

The unresolved scales are modeled using the subgrid-scale (SGS) stress term  $\tau_{ij}$ , which is approximated using the eddy viscosity hypothesis:

$$\tau_{ij} - \frac{1}{3} \delta_{ij} \tau_{kk} = -2\nu_T \bar{S}_{ij}. \quad (3)$$

The eddy viscosity  $\nu_T$  and strain rate tensor  $S_{ij}$  are defined as follows:

$$\begin{aligned} \nu_T &= C_{SGS} \Delta^2 |\bar{\mathbf{S}}|, \\ \bar{S}_{ij} &= \frac{1}{2} \left( \frac{\partial \bar{u}_i}{\partial x_j} + \frac{\partial \bar{u}_j}{\partial x_i} \right). \end{aligned} \quad (4)$$

The characteristic filter length is given as follows:

$$\Delta = \left[ \prod_{i=1}^3 \Delta x_i \right]^{1/3}. \quad (5)$$

Here  $\Delta x_i$  is the computational mesh size in the  $i$ th direction corresponding to the streamwise, transverse, and spanwise directions.  $C_{SGS}$  is the model coefficient, and it requires specification in order to be close to systems (1) and (2). In the present study,  $C_{SGS}$  was calculated using the dynamic approach developed by Germano et al. [32]. This method was calculated using the information from the resolved scales as a function of both time and space during the course of the simulation.

The two-phase two-way coupling is realized by the point-force model. As shown in (2),  $\bar{S}_{pfi}$  is the term that particles affect the fluid phase, as in a previous study [1],

$$\bar{S}_{pfi} = - \sum_{p=1}^{N_p} \int \bar{f}_i(\mathbf{x}_p, t) g(\mathbf{y} - \mathbf{x}_p) H_\Delta(\mathbf{x} - \mathbf{y}) d\mathbf{y}, \quad (6)$$

where  $\bar{f}_i(\mathbf{x}_p, t)$  is the fluid force acting on particle  $p$  centered at position  $\mathbf{x}_p$  at time  $t$ ,  $g$  is a weighted distribution function of the particle source term in the fluid flow field, and  $H_\Delta$  is a three-dimensional spatial low-pass filter with a characteristic width of the order of the mesh size  $\Delta x$ .

Equations (1) and (2) can be solved numerically using the fractional step method as described by Kim and Moin and by Wu et al. [33, 34]. A nonsolenoidal velocity field  $\mathbf{V}^{n+(1/2)}$  was projected onto a solenoidal field by a scalar quantity  $\Phi$ , which is related to the pressure term  $P$ . The continuity equation was satisfied through a Poisson equation for the pressure correction. Then the Poisson equation for pressure was solved using series expansions in the streamwise and spanwise directions with tridiagonal matrix inversion.

In order to reduce the aliasing errors and instability, the second-order hybrid scheme developed by Kravchenko and Moin was adopted for the advective term [35]. The central finite difference scheme for  $\partial(u_i u_j) / \partial x_j$  writes as

$$\delta^c = \frac{\partial (u_i u_j)}{\partial x_j} = \frac{(u_i u_j)_{j+1/2} - (u_i u_j)_{j-1/2}}{\Delta x_j}. \quad (7)$$

The forward finite difference scheme for  $\partial u_i / \partial x_j$  writes as

$$\delta^+ = \left( \frac{\partial u_i}{\partial x_j} \right)^+ = \frac{-3(u_i)_j + 4(u_i)_{j+1} - (u_i)_{j+2}}{2\Delta x_j} \quad (8)$$

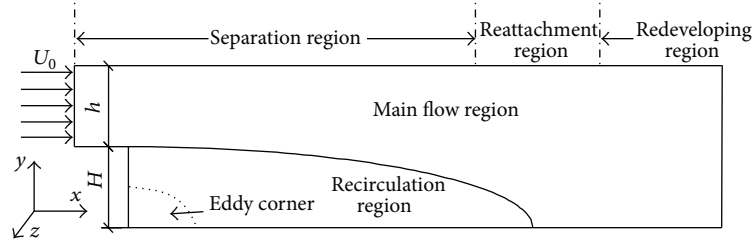


FIGURE 1: Sketch of the flow over a backward-facing step.

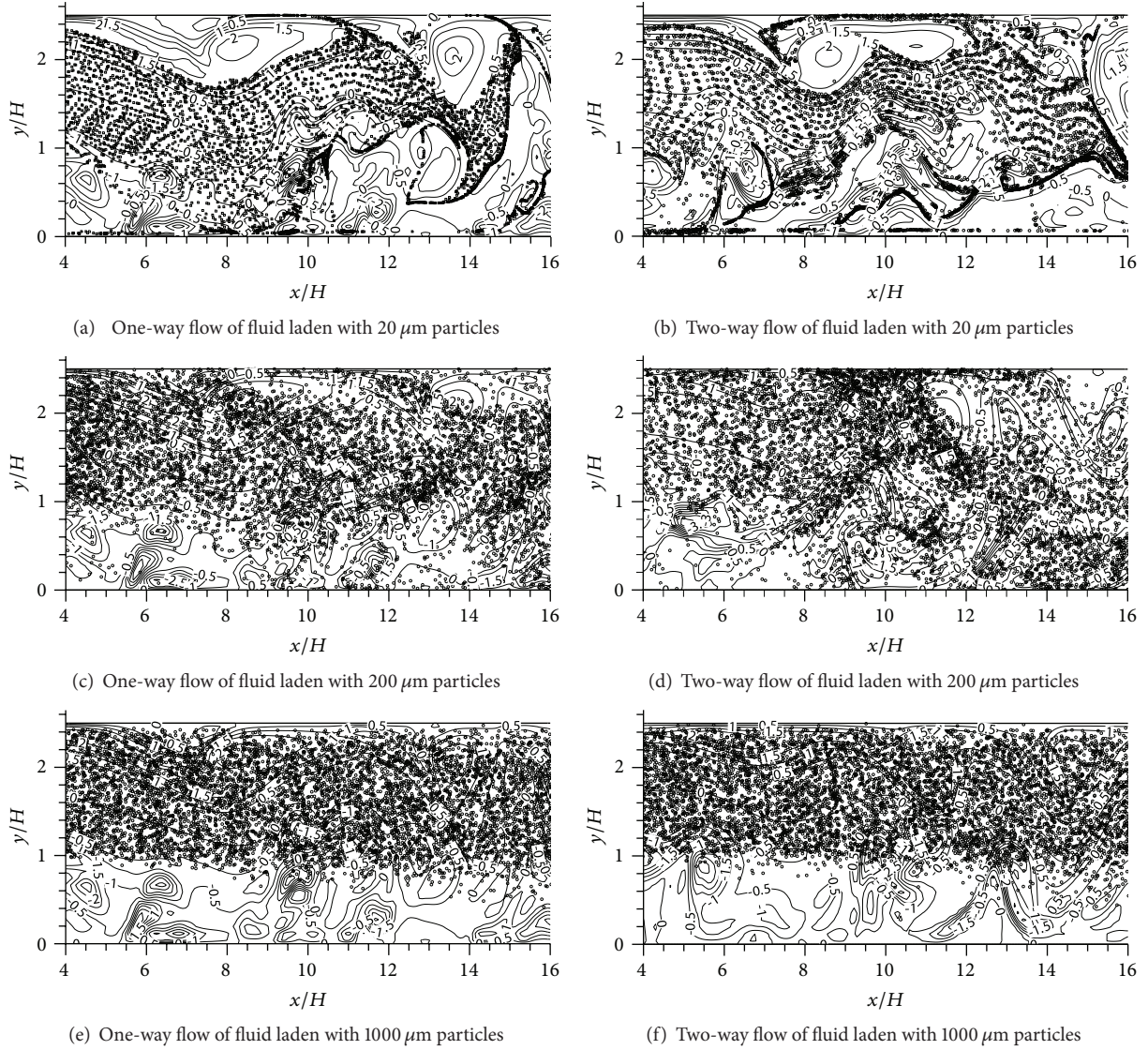


FIGURE 2: *Lycopodium* particle dispersion in large-scale turbulence structures.

and the backward one is

$$\delta^- = \left( \frac{\partial u_i}{\partial x_j} \right)^- = \frac{3(u_i)_j - 4(u_i)_{j-1} + (u_i)_{j-2}}{2\Delta x_j}. \quad (9)$$

In this way, the hybrid scheme for the advective term in the  $i$ th direction writes as

$$H_i = -\frac{1}{2} \left[ \delta^c + \frac{1}{2} (u_j + |u_j|) \cdot \delta^- + \frac{1}{2} (u_j - |u_j|) \cdot \delta^+ \right]. \quad (10)$$

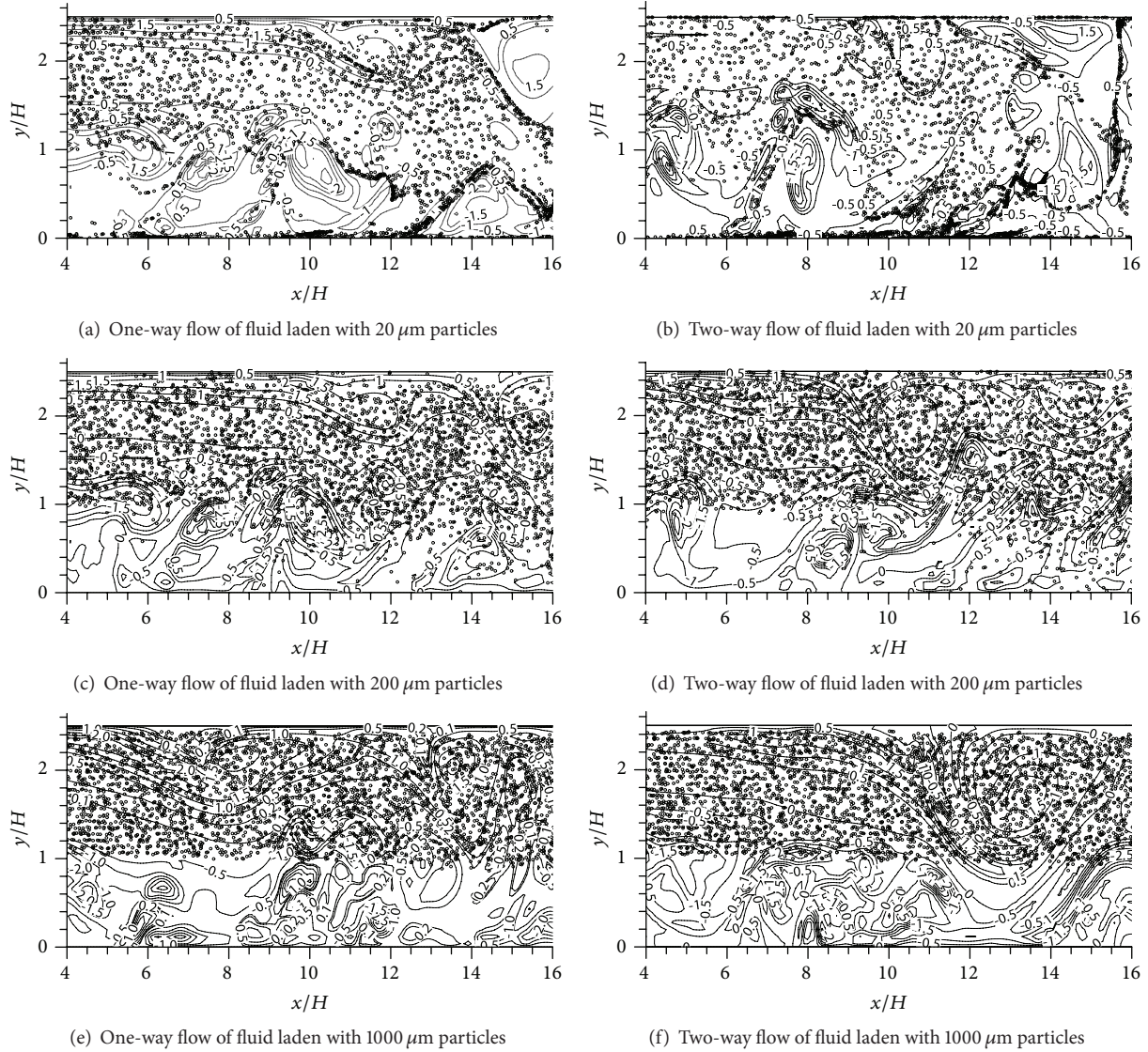


FIGURE 3: Glass particle dispersion in large-scale turbulence structures.

The viscous term is discretized using a second-order central difference.

The momentum equations were integrated explicitly using a third-order Runge-Kutta algorithm. The nondimensional calculation time step was taken as  $\Delta t = 10^{-5}$ . Because the time step yields to the stability condition, the numerical results are not affected by different time steps. This includes the statistical mean and fluctuating velocities for both phases.

The inlet flow condition is specified by a velocity distribution of  $U(y)$  with a white noise  $\xi$  superimposed.  $U(y)$  is assumed to obey the 1/7th power law, and the white noise is assumed to have a Gaussian distribution with a mean of zero and a variance of  $10^{-4}$ . Such white noises in the inlet plane are important for the development of unstable disturbances in the transverse and spanwise directions. An improved non-reflective Sommerfeld open boundary condition, as proposed by Dai et al. [36], was used at the exit so that the coherent structures could be transported downstream without any distortion.

The filtered equations were solved on a staggered Cartesian grid with 256 nodes in the streamwise direction. There were 34 nodes in the transverse direction and 35 nodes in the spanwise direction. The independence of grid resolution was examined in a previous study [31]. The consistency of the two-phase statistical velocities with the experimental data shows that the present grid resolution is suitable for an evaluation of flow physics.

**2.3. Dispersed Phase Equations.** A Lagrangian approach was used to track each particle. This requires the solution of the equation of the motion for each computational particle. Here, all particles were treated as nonevaporating rigid spheres. The particles are assumed to be denser than the fluid. In this way, relative to the viscous drag and lift forces, for high ratios of particle to gas densities, the Basset history term, added mass term, and pressure term are negligible. Particle collisions were not taken into account. The slip-shear lift force and slip-rotational lift force were negligible. With these assumptions,

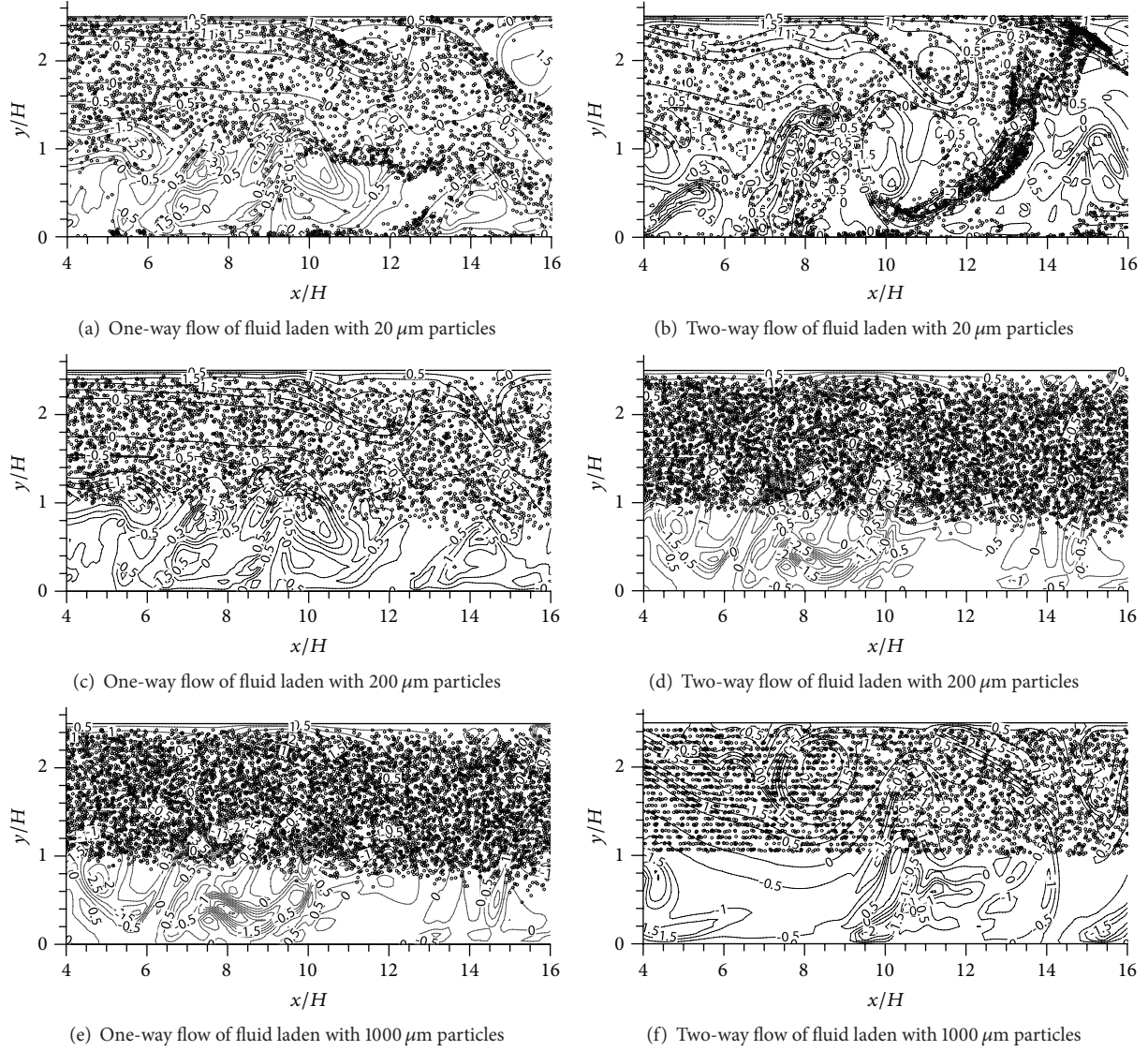


FIGURE 4: Copper particle dispersion in large-scale turbulence structures.

the dominant forces on each particle are the drag force and gravity.

The nondimensional dynamic equations for a particle along its trajectory are as follows:

$$\begin{aligned} \frac{d\mathbf{X}_p}{dt} &= \mathbf{V}_p, \\ \frac{d\mathbf{V}_p}{dt} &= \frac{\mathbf{F}}{(1/6)\pi d_p^3 \rho_p} + \frac{\mathbf{g}H}{U_0^2}. \end{aligned} \quad (11)$$

Here  $\mathbf{V}_p$  is the instantaneous particle velocity, and  $\mathbf{F}$  is the drag force on the particle such that the following is true:

$$\mathbf{F} = C_d \cdot \frac{1}{4}\pi d_p^2 \cdot \frac{1}{2} |\mathbf{V}_f - \mathbf{V}_p| (\mathbf{V}_f - \mathbf{V}_p). \quad (12)$$

$\mathbf{V}_f$  is the instantaneous fluid velocity, and  $C_d$  is the drag coefficient, as given in a previous study [37],

$$C_d = \begin{cases} \frac{24}{\text{Re}_p} \left( 1 + \frac{\text{Re}_p^{2/3}}{6} \right), & \text{Re}_p \leq 1000, \\ 0.44, & \text{Re}_p > 1000. \end{cases} \quad (13)$$

$\text{Re}_p$  is the particle Reynolds number defined as follows:

$$\text{Re}_p = \frac{\rho |\mathbf{V}_f - \mathbf{V}_p| d_p}{\mu}, \quad (14)$$

and  $\mu$  is the fluid viscosity. The Stokes number, which is used to characterize particle motion, is defined as follows:

$$St = \frac{\tau_p}{\tau}. \quad (15)$$

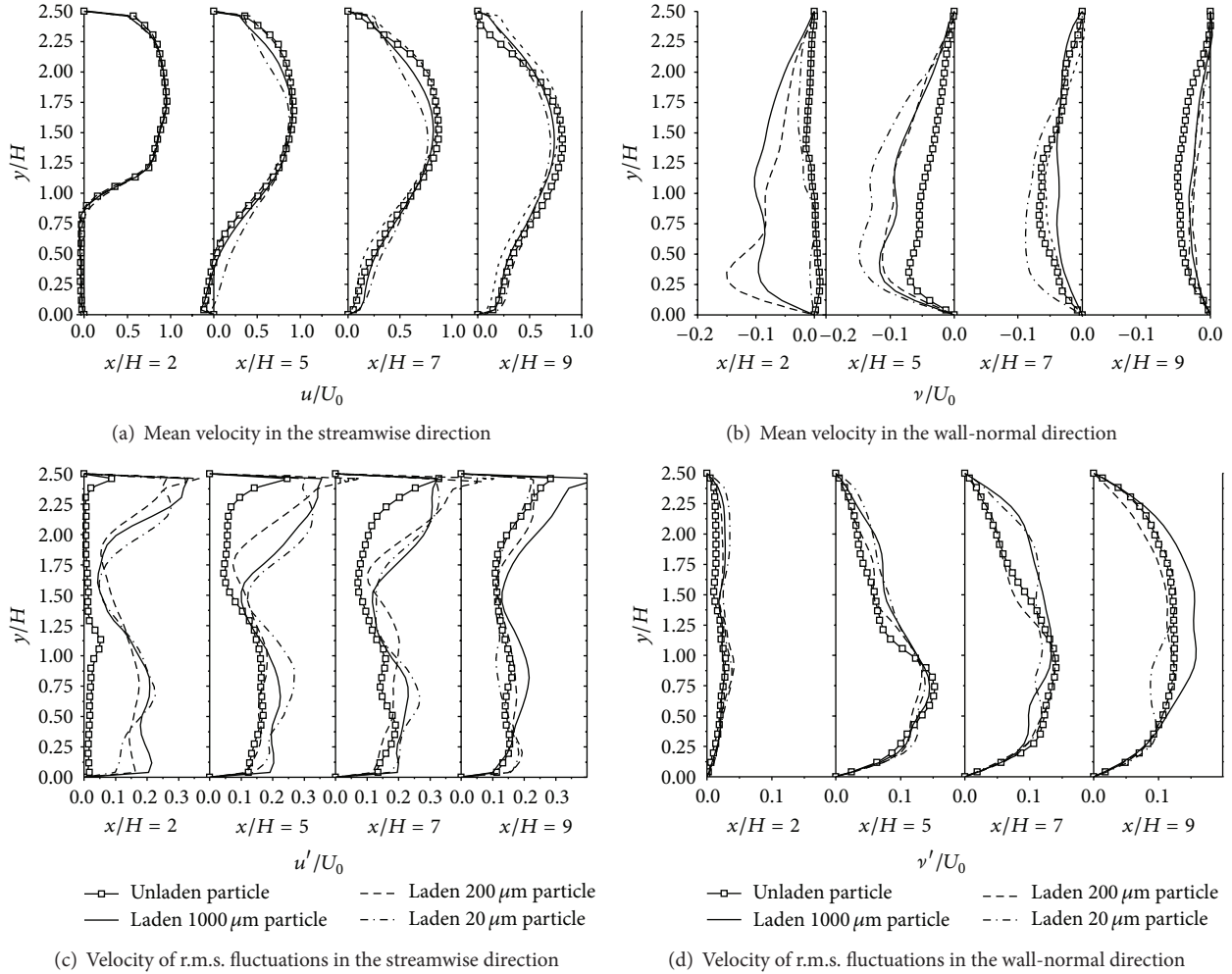


FIGURE 5: Mean and r.m.s. velocities at different sections laden with particles of different sizes.

Here  $\tau_p = \rho_p d_p^2 / (18\mu)$  is the particle relaxation or aerodynamic response time scale, and  $\tau = H/U_0$  is the fluid time scale.

The instantaneous fluid velocity at the location of each particle was determined using the local instantaneous fluid velocity interpolated from the neighboring grid points.

The boundary conditions of particles impacting on walls were here treated as perfectly elastic collisions; particles only changed velocity in the wall normal direction after impacting the wall, but the magnitudes of velocity in the three directions were not changed. The walls were considered smooth. Although both the particle-wall interactions and wall roughness influence particle dispersion, they are out of the scopes of the present work.

The particles are released into the flow fields at the inlet with the same local gas-phase velocities when the gas-phase flow is fully developed. In this way, there is no velocity slip between particles and fluid at the entrance of the flow.

These numerical methods were validated by means of comparing turbulence statistics of both phases with the experimental data collected by Eaton and Johnston [38]. The mean velocities and fluctuations in velocity were found to

be closely consistent with experimental measurements. The detailed validations of numerical procedures are described in a previous study [31].

In the present study, particles were released into the flow fields at the same rate, 16,000/s. Three kinds of particles were selected, *Lycopodium* ( $700 \text{ kg/m}^3$ ), glass ( $2500 \text{ kg/m}^3$ ), and copper ( $8900 \text{ kg/m}^3$ ). They had diameters of 20, 200, and  $1000 \mu\text{m}$ . In this way, the particle-mass-loading ratio was calculated according to the number of particles present. Those parameters are shown in Table 1.

### 3. Results and Discussion

**3.1. Particle Dispersion in Large-Scale Turbulence Structures.** The spanwise component of vorticity is used to visualize large-scale structures. The distributions of spanwise vortices in the regions of the shear layer and redevelopment are shown in Figures 2 and 3 for flows laden with particles of different diameters at the same instant. The lines represent the vortices, and the scattered points represent the particles.

The shedding vortices from the step develop and impinge onto the lower wall. The vortices that roll up by the upper

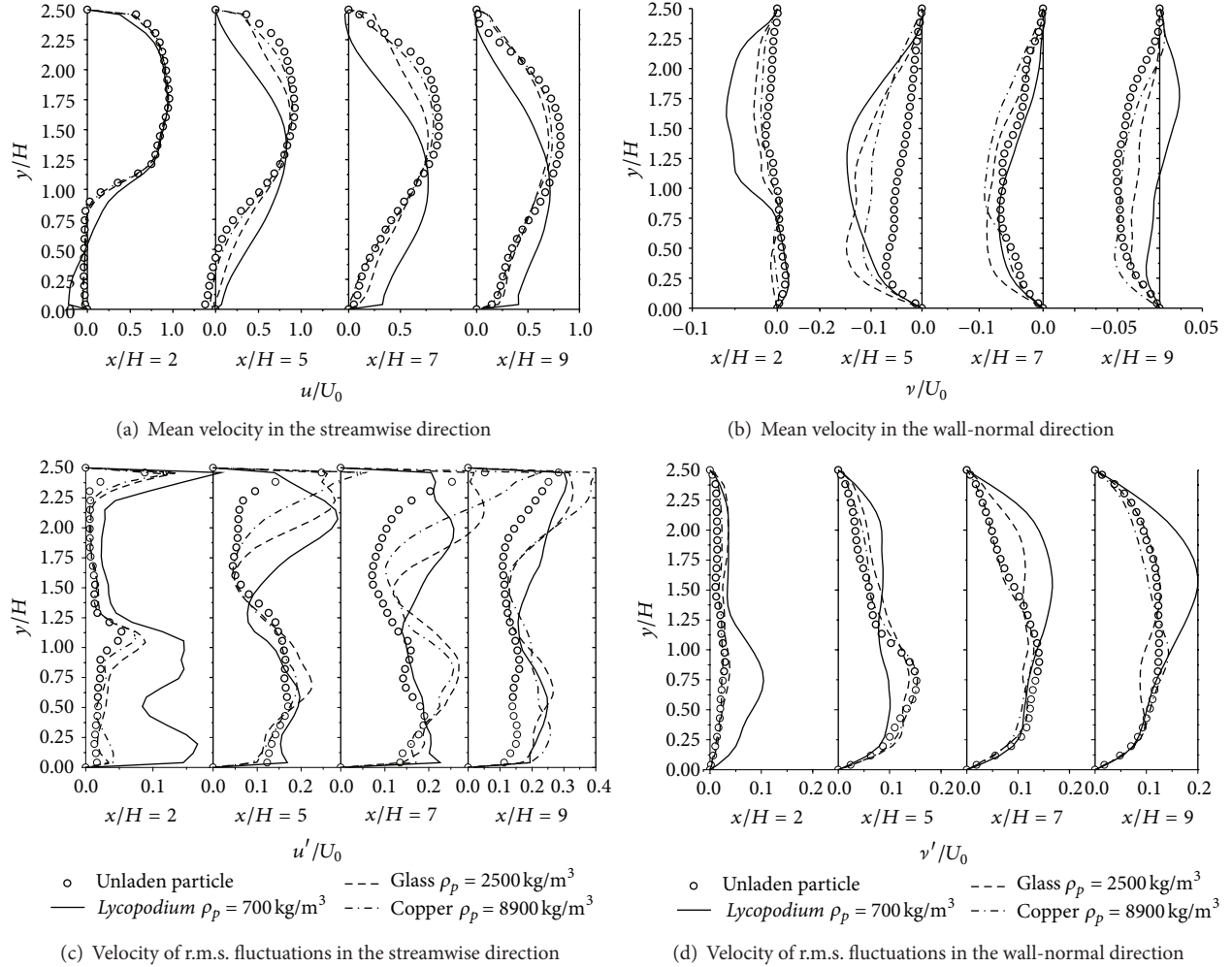
FIGURE 6: Modulations in turbulence modulations by particles  $20 \mu\text{m}$  in diameter.

TABLE 1: Calculation parameters of particles.

$d_p$ ( $\mu\text{m}$ )	Lycopodium		Glass			Copper		
	St	Mass-loading ratio	$d_p$ ( $\mu\text{m}$ )	St	Mass-loading ratio	$d_p$ ( $\mu\text{m}$ )	St	Mass-loading ratio
20	$\approx 0.3$		20	$\approx 1.1$		20	$\approx 4.0$	
200	$\approx 31.1$	0.1	200	$\approx 111.2$	0.1	200	$\approx 395.9$	0.1
1000	$\approx 778.4$		1000	$\approx 2779.6$		1000	$\approx 987.5$	

boundary layer interact with the vortices from the shear layer. All the vortices undergo a process of pairing, merging, and breaking up.

As shown in Figures 2(a) and 3(a), particles preferentially accumulate along the edges of vortices and concentrate in particle clusters. Particle modulations are visible in changes in the vortices and the scattering of particles in the same flow fields. However small particles with smaller Stokes numbers modulate turbulence in such a way that does not change the particle preferential distribution in the vortices.

Particle inertia increases with particle size, weakening their preferential distribution in the vortex edge, as shown in Figures 2(c) and 3(c). For the  $20 \mu\text{m}$  glass and copper

particles whose Stokes numbers were around unity, like those in Figures 2(a) and 3(a), preferential distribution is the most significant characteristic of dispersion. However, very large particles with large particle Stokes numbers disperse more uniformly within the flow fields, and they are hardly affected by the vortex structures, as shown in Figures 2(e), 2(f), 3(e), 3(f), 4(e), and 4(f).

Particle dispersion behavior changes accordingly. The motion of relatively small particles is mainly ruled by large-scale structures. Large eddies can be destroyed by large particles. This kind of effect is stronger when particles are larger, as shown in Figures 2(e), 3(e), and 4(e). However, even if large particles change more dramatically than smaller

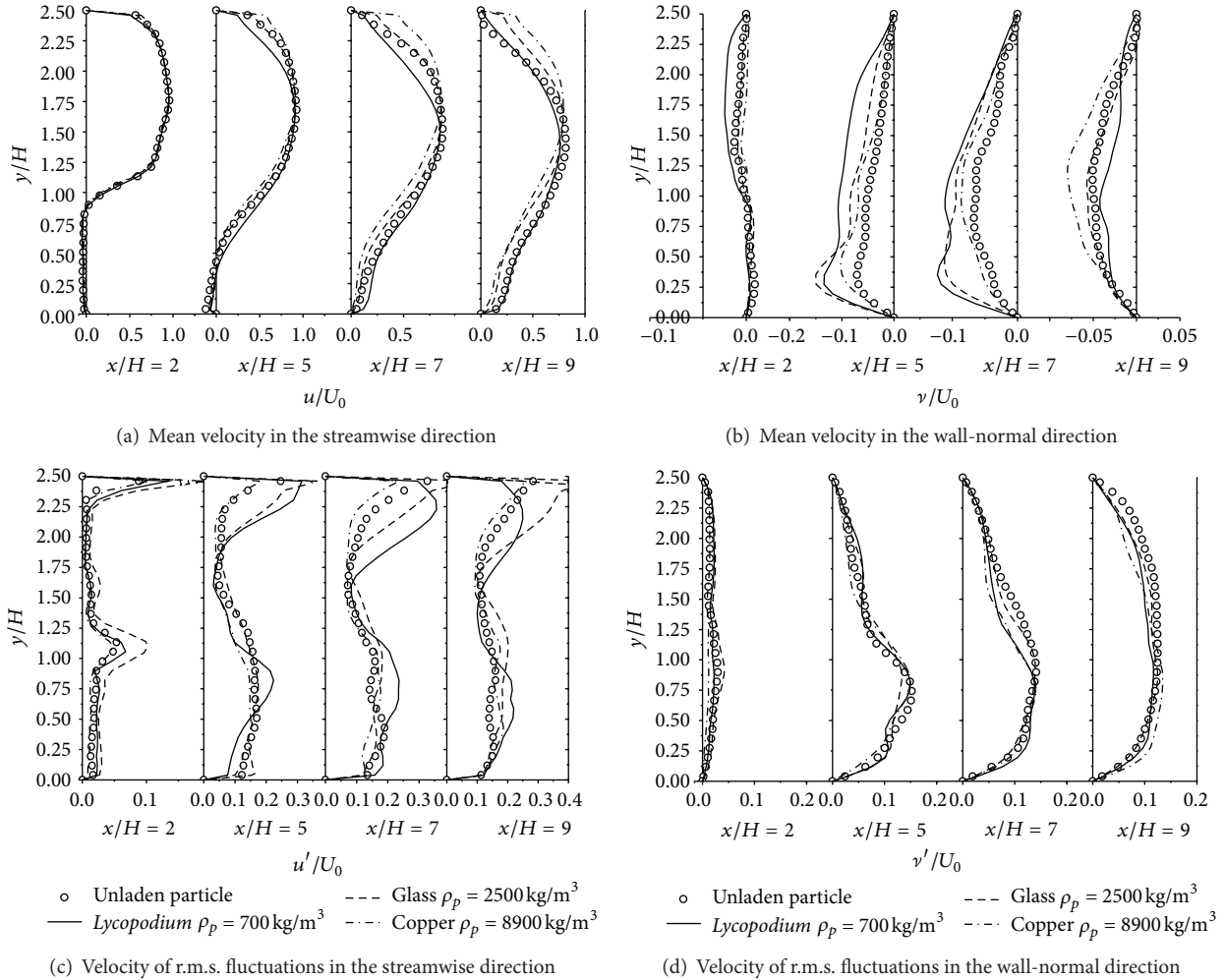


FIGURE 7: Modulations in turbulence modulations by particles  $200 \mu\text{m}$  in diameter.

ones, the large scale of the vortices in the flow field prevents their motion from being affected by the vortices. As shown in Figures 2(e), 3(e), and 4(e), particles were observed to maintain the directions of their initial velocity.

**3.2. Velocity Statistics.** The gas-phase velocity statistics, including the mean and root-mean-square (r.m.s.) velocities, were obtained for flows laden with different types of particles in four different areas to assess the modulation of turbulence.

**3.2.1. Effects of Particle Size.** Glass particles  $20$ ,  $200$ , and  $1000 \mu\text{m}$  in diameter were added to the flow at the same particle-mass-loading ratio. The results predicted for flow not laden with particles are also shown (Figure 5).

The degree to which particles modulate turbulence is shown not only for mean velocities but also for those of r.m.s. fluctuations. Close to the inlet, the effects of particles on mean velocity are negligible, regardless of particle size. However, for the wall-normal component, the mean velocities are modulated to smaller values. The mean velocities of the fluid phase are only slightly changed by particles downstream in

the streamwise direction. Particles of  $20 \mu\text{m}$  diameter were found to attenuate the mean velocity close to the upper wall much more than particles of  $200 \mu\text{m}$ . The changes in the wall-normal component of the mean velocity are complicated, depending on the way the flow develops. For example, the locations in the flow field can have a considerable effect. In general, upstream,  $x/H < 7$ , due to the presence of particles, the mean velocities in the wall-normal direction increased in modulus, but downstream they decreased in modulus.

The degree to which a given particle modulates turbulence depends on the flow status. The r.m.s. velocities in the streamwise direction were increased by particles in the regions close to the upper wall. Upstream,  $x/H < 7$ ,  $20 \mu\text{m}$  particles were found to enhance the degree of fluctuation in turbulence, but, downstream, those particles only modulate fluctuations in turbulence fluctuation very slightly. Unlike that of other particles, the degree to which  $1000 \mu\text{m}$  particles modulated turbulence became stronger along the flow direction.

For the wall-normal component of fluctuating velocities,  $1000 \mu\text{m}$  particles produce the strongest modulation of enhancement at the section of  $x/H = 9$ , but the other two

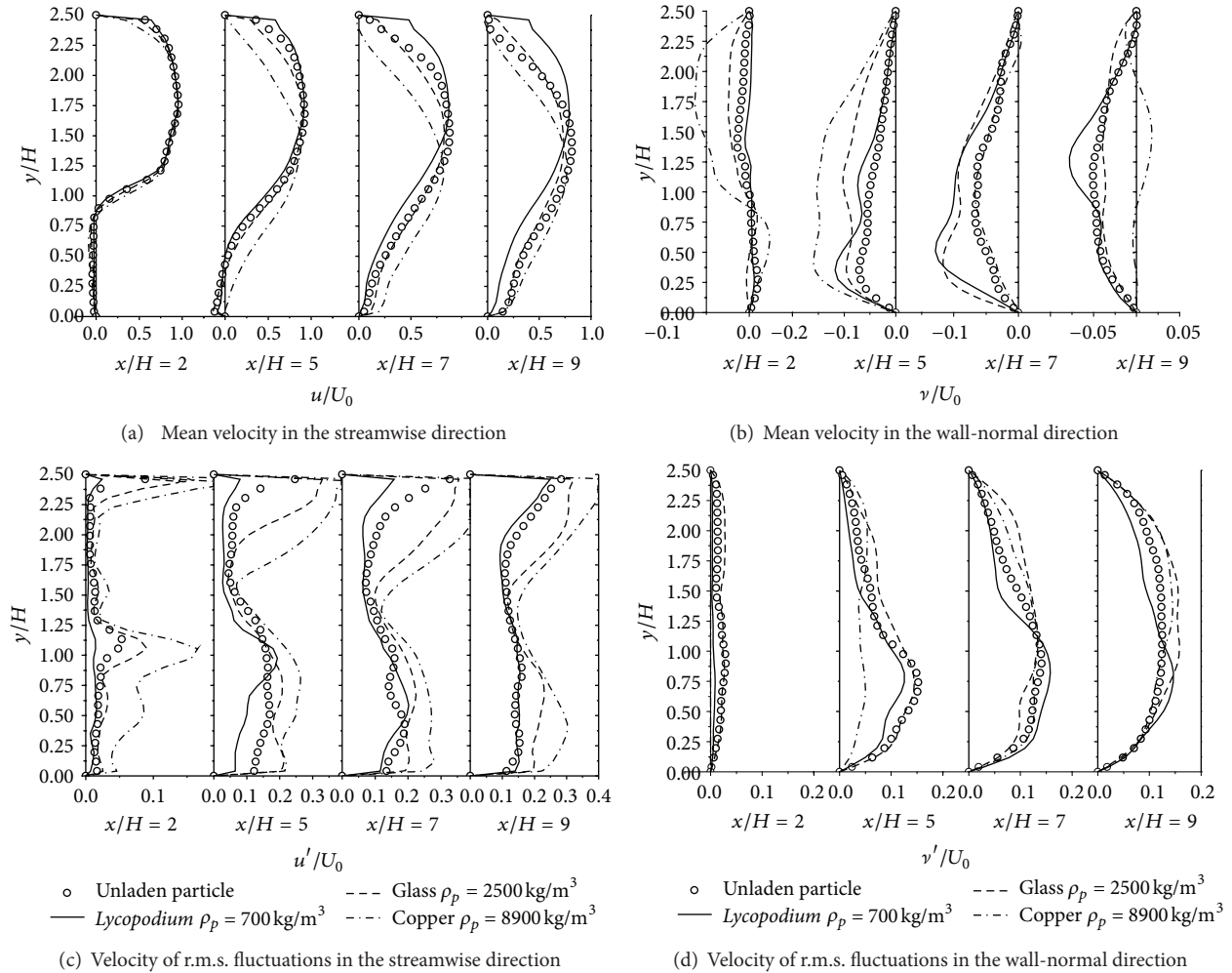


FIGURE 8: Modulations in turbulence modulations by particles  $1000 \mu\text{m}$  in diameter.

kinds of particles almost attenuate turbulence fluctuating levels.

In conclusion, the degree to which a given particle modulates turbulence is strongly dependent on the way the flow develops over the backward-facing step. In downstream regions, smaller particles exert weaker modulation, and larger particles exert stronger modulation.

**3.2.2. Effects of Particle Density.** At the same particle-mass-loading ratio, different particles with different material densities were loaded into the flows. Then, the effects of particle density on turbulence modulation were investigated. Particles with diameters of 20, 200, and  $1000 \mu\text{m}$  were chosen. Each group contained particles of 700, 2500, and  $8900 \text{ kg/m}^3$ .

Figure 6 shows the mean and fluctuating velocities for the flow laden with  $20 \mu\text{m}$  particles. Low-density particles were found to modulate mean velocities most strongly, and they even changed the velocity distribution profiles. High-density particles were found to produce slighter modifications in the mean velocities.

The degree to which particles modulate fluctuations in turbulence depends on the way the flow develops. As a whole, particles enhance fluctuations in turbulence in the

streamwise direction, especially near the upper wall. The velocities of the fluctuations in fluid laden with particles approach those of fluid not laden with particles in the wall-normal direction. In this way, denser particles do less to modulate turbulence than smaller particles.

As particles increases to  $200 \mu\text{m}$ , they do less to modulate to the mean velocities in the streamwise direction. Denser particles do less to modulate the fluctuations in turbulence. Those results are shown in Figure 7.

Large, low-density particles, as shown in Figure 8, enhance mean velocities close to the upper wall, but they attenuate the mean velocities in the regions close to the bottom wall. However, heavy particles, unlike those shown in Figure 6, change the distribution profiles of the mean velocity in the streamwise direction. As shown in Figures 8(c) and 8(d), large, low-density particles can attenuate the velocity of the turbulence in most parts of the flow fields.

#### 4. Conclusions and Remarks

A two-phase two-way coupling large-eddy simulation was used to numerically obtain particle-laden two-phase turbulent flows over a backward-facing step. Particles released into

the flow fields were tracked using a Lagrangian trajectory method. Particle dispersions in large-scale eddy coherent structures and statistical mean and fluctuating velocities were presented to show particle modulations to turbulence. The influences of particle size and material density on changes in turbulence were then analyzed. The main conclusions drawn were as follows.

- (1) Particles with smaller Stokes numbers preferentially accumulate in the coherent flow fields. Due to modulations, particles can change the vortices developing but do not change their preferential distribution within the vortices.
- (2) Particle modulations to turbulence depend on the flow status in the flow over a backward-facing step. Modifications of turbulence represent the variations of mean and fluctuating velocities. Smaller particles exert a weaker modulation in the downstream flow regions than larger particles do.
- (3) Effects of particle density on statistical mean and fluctuating velocities are dependent on particle size. Smaller, less dense particles can enhance the fluctuating velocities in the streamwise direction. Larger particles with lower density can, however, attenuate the fluctuations in turbulence.

Further studies of the effects of particle-mass-loading ratios and two-phase slip velocities on modulations in turbulence must be carried out in the future.

## References

- [1] M. Boivin, O. Simonin, and K. D. Squires, "Direct numerical simulation of turbulence modulation by particles in isotropic turbulence," *Journal of Fluid Mechanics*, vol. 375, pp. 235–263, 1998.
- [2] S. Elghobashi and G. C. Truesdell, "On the two-way interaction between homogeneous turbulence and dispersed solid particles. I: turbulence modification," *Physics of Fluids A*, vol. 5, no. 7, pp. 1790–1801, 1992.
- [3] E. E. Michaelides and D. E. Stock, *Turbulence Modification in Dispersed Multiphase Flows*, vol. 80 of *FED*, ASME, New York, NY, USA, 1989.
- [4] R. N. Parthasarathy and G. M. Faeth, "Turbulence modulation in homogeneous dilute particle-laden flows," *Journal of Fluid Mechanics*, vol. 220, pp. 485–514, 1990.
- [5] R. N. Parthasarathy and G. M. Faeth, "Turbulent dispersion of particles in self-generated homogeneous turbulence," *Journal of Fluid Mechanics*, vol. 220, pp. 515–537, 1990.
- [6] D. Modarress, H. Tan, and S. Elghobashi, "Two-component LDA measurement in a two-phase turbulent jet," *AIAA Journal*, vol. 22, no. 5, pp. 624–630, 1984.
- [7] A. A. Mostafa, H. C. Mongia, V. G. McDonnell, and G. S. Samuelsen, "Evolution of particle-laden jet flows: a theoretical and experimental study," *AIAA Journal*, vol. 27, no. 2, pp. 167–183, 1989.
- [8] C. J. Park and L. D. Chen, "Experimental investigation of confined turbulent jets, Part I: particle-laden flow data," *AIAA Journal*, vol. 27, no. 11, pp. 1506–1510, 1989.
- [9] C. J. Park and L. D. Chen, "Experimental investigation of confined turbulent jets. Part II. Particle-laden flow data," *AIAA Journal*, vol. 27, no. 11, pp. 1511–1516, 1989.
- [10] J. L. Cui, H. Q. Zhang, B. Wang, Y. Rong, and X. L. Wang, "Flow visualization and laser measurement on particle modulation to gas-phase turbulence," *Journal of Visualization*, vol. 9, no. 3, pp. 339–345, 2006.
- [11] S. S. Chandok and D. C. T. Pei, "Particle dynamics in solid-gas flows in a vertical pipe," *Progress in Heat and Mass Transfer*, vol. 6, pp. 465–474, 1972.
- [12] M. Meada, K. Hishida, and T. Furutani, "Optical measurements of local gas and solid velocity in an upward flowing dilute gas-solid suspension," in *Proceedings of the Polyphase Flow and Transport Technology, Century 2-ETC*, pp. 211–216, San Francisco, Calif, USA, 1980.
- [13] F. Durst, "REVIEW-combined measurements of particle velocities, size distributions, and concentrations," *Journal of Fluids Engineering, Transactions of the ASME*, vol. 104, no. 3, pp. 284–296, 1982.
- [14] Y. Tsuji, Y. Morikawa, and H. Shiomi, "LDV measurements of an air-solid two-phase flow in a vertical pipe," *Journal of Fluid Mechanics*, vol. 139, pp. 417–434, 1984.
- [15] J. D. Kulick, J. R. Fessler, and J. K. Eaton, "Particle response and turbulence modification in fully developed channel flow," *Journal of Fluid Mechanics*, vol. 277, pp. 109–134, 1994.
- [16] A. A. Mostafa and H. C. Mongia, "On the interaction of particles and turbulent fluid flow," *International Journal of Heat and Mass Transfer*, vol. 31, no. 10, pp. 2063–2075, 1988.
- [17] K. Hishida, A. Ando, and M. Maeda, "Experiments on particle dispersion in a turbulent mixing layer," *International Journal of Multiphase Flow*, vol. 18, no. 2, pp. 181–194, 1992.
- [18] J. R. Fessler and J. K. Eaton, "Turbulence modification by particles in a backward-facing step flow," *Journal of Fluid Mechanics*, vol. 394, pp. 97–117, 1999.
- [19] K. Hishida and M. Maeda, "Turbulence characteristics of particle laden flow behind a rearward facing step," *ASME, Gas-Solid Flows-FED*, vol. 121, pp. 207–212, 1991.
- [20] Y. Hardalupas, A. M. K. P. Taylor, and J. H. Whitelaw, "Particle dispersion in a vertical round sudden-expansion flow," *Philosophical Transactions of the Royal Society of London A*, vol. 341, pp. 411–442, 1992.
- [21] R. A. Gore and C. T. Crowe, "Effect of particle size on modulating turbulent intensity," *International Journal of Multiphase Flow*, vol. 15, no. 2, pp. 279–285, 1989.
- [22] G. Hetsroni, "Particles-turbulence interaction," *International Journal of Multiphase Flow*, vol. 15, no. 5, pp. 735–746, 1989.
- [23] L. P. Yarin and G. Hetsroni, *Combustion of Two-Phase Reactive Media*, Springer, 2004.
- [24] V. M. Kenning and C. T. Crowe, "On the effect of particles on carrier phase turbulence in gas-particle flows," *International Journal of Multiphase Flow*, vol. 23, no. 2, pp. 403–408, 1997.
- [25] K. Fukagata, S. Zahrai, and F. H. Bark, "Force balance in a turbulent particulate channel flow," *International Journal of Multiphase Flow*, vol. 24, no. 6, pp. 867–887, 1998.
- [26] Y. Yamamoto, M. Potthoff, T. Tanaka, T. Kajishima, and Y. Tsuji, "Large-eddy simulation of turbulent gas-particle flow in a vertical channel: effect of considering inter-particle collisions," *Journal of Fluid Mechanics*, vol. 442, pp. 303–334, 2001.
- [27] Q. Wang and K. D. Squires, "Large eddy simulation of particle deposition in a vertical turbulent channel flow," *International Journal of Multiphase Flow*, vol. 22, no. 4, pp. 667–683, 1996.

- [28] B. Wang, "Inter-phase interaction in a turbulent, vertical channel flow laden with heavy particles. Part II: two-phase velocity statistical properties," *International Journal of Heat and Mass Transfer*, vol. 53, no. 11-12, pp. 2522–2529, 2010.
- [29] B. Wang, "Inter-phase interaction in a turbulent, vertical channel flow laden with heavy particles. Part I: numerical methods and particle dispersion properties," *International Journal of Heat and Mass Transfer*, vol. 53, no. 11-12, pp. 2506–2521, 2010.
- [30] H. Q. Zhang, Y. Rong, B. Wang et al., "Large eddy simulation of 3-D spatially developing turbulent round jet," *Science China E*, vol. 54, no. 11, pp. 2916–2923, 2011.
- [31] H. Zhang, B. Wang, C. Chan, and X. Wang, "Large Eddy Simulation of a dilute particle-laden turbulent flow over a backward-facing step," *Science in China E*, vol. 51, no. 11, pp. 1957–1970, 2008.
- [32] M. Germano, U. Piomelli, P. Moin, and W. H. Cabot, "A dynamic subgrid-scale eddy viscosity model," *Physics of Fluids A*, vol. 3, no. 7, pp. 1760–1765, 1991.
- [33] J. Kim and P. Moin, "Application of a fractional-step method to incompressible Navier-Stokes equations," *Journal of Computational Physics*, vol. 59, no. 2, pp. 308–323, 1985.
- [34] X. Wu, K. D. Squires, and Q. Wang, "Extension of the fractional step method to general curvilinear coordinate systems," *Numerical Heat Transfer B*, vol. 27, no. 2, pp. 175–194, 1995.
- [35] A. G. Kravchenko and P. Moin, "On the effect of numerical errors in large Eddy simulations of turbulent flows," *Journal of Computational Physics*, vol. 131, no. 2, pp. 310–322, 1997.
- [36] Y. Dai, T. Kobayashi, and N. Taniguchi, "Large Eddy simulation of plane turbulent jet flow using a new outflow velocity boundary condition," *JSME International Journal B*, vol. 37, no. 2, pp. 242–253, 1994.
- [37] W. C. Hinds, *Aerosol Technology, Properties, Behavior and Measurement of Airborne Particles*, John Wiley & Sons, New York, NY, USA, 1982.
- [38] J. K. Eaton and J. P. Johnston, "An experimental study of the flow and structure behind a backward-facing step," Stanford University Report MD-39, 1980.